2016

Dilute-Anion III-Nitride Semiconductor Materials and Nanostructures

Chee-Keong Tan
Lehigh University

Dilute-Anion III-Nitride Semiconductor Materials and Nanostructures

by

Chee-Keong Tan

Presented to the Graduate and Research Committee
of Lehigh University
In Candidacy for the Degree of
Doctor of Philosophy

in

Electrical Engineering

Lehigh University

September 2016

Dissertation Signature Sheet

Approved and recommended for acceptance as a dissertation in partial fulfillment of the requirements for the degree of Doctor of Philosophy.

Date

Prof. Nelson Tansu
(Ph.D. Advisor)

Accepted Date

Committee Members:

Prof. Nelson Tansu
(Committee Chair)

Prof. Jonathan Wierer

Prof. Chao Zhou

Prof. Michael Stavola

Prof. Volkmar Dierolf

Acknowledgements

Discipline, focus and passion are perhaps the three terms I hear the most among many other positive words throughout my PhD study at Lehigh University. These words have played a key role in driving me step by step towards my dream, and strongly imprinted in my belief as the essential criteria of success. These words come from a wise man who has had a huge influence over my entire PhD study. Indeed, I am deeply indebted to Professor Nelson Tansu for his constructive advices and constant guidance during my PhD study at Lehigh University. He introduced me various research dimensions in the field of photonics and semiconductor materials, providing me the invaluable resources to conduct my research in various interesting topics. He taught me the skills to be an independent researcher and scholar, and helped to foster my skills of critical thinking and formal writing. His relentless support and willingness of sacrificing his time to help build up my career path are stunning that one could not easily duplicate. This dissertation could not be possibly completed without his support throughout my PhD study.

I am grateful to Prof. Jonathan Wierer, Prof. Chao Zhou, Prof. Michael Stavola, and Prof. Volkmar Dierolf for serving in my Ph.D. committee and providing valuable comments.

I would also like to thank Dr. Renbo Song, Anthony Jeffers, and Ray Filozof for the MOCVD and cleanroom equipment training and maintenance. I also would like to thank our past post-doctoral scientist Dr. Benjamin O. Tayo whom I have learnt a lot from.

I would like to express my sincere gratitude to my past and current laboratory colleagues for their assistance during my PhD studies at Lehigh: Dr. Guangyu Liu, Dr. Jing Zhang, Dr. Peifen Zhu, Wei Sun, Ioannis Fragkos, Damir Borovac, Xiongliang Wei, Liangyue Yan, Yiming Zhong, and Matthew Peart.

My appreciation also goes to other past and current members at Lehigh University: Dr. Kangbaek Kim, Dr. Yaoyao Zhu, Dr. Vitchanetra Hongpinyo, Chongzhao Wu, Le Zhao, Kanokwan Klinieam, Vahid Gholizadeh, and Zhangji Zhao. I would also like to thank our visiting scientist for constructive conversations: Dr. Te Li.

The research work was made possible by the financial support from various funding agencies especially the National Science Foundation and Daniel E. ’39 and Patricia M. Smith Endowed Chair Professorship fund.

Most importantly, I am beholden to my parents and siblings for their unconditional support and confidence in me, and timeless caring for my years of pursuit in academic career. I am forever indebted to my deceased mother, Madam Poh Choo Lim, for encouraging me and strengthening my resolve in pursuing my dream throughout the years. My mother was a wonderful and lovely lady who sacrifices everything for her family, and who I will never have the chance to repay for. I am also forever grateful to my father, Mr. Eng Lee Tan, for being supportive and taking care of the family including me. I am also greatly indebted to my brothers: Chee Loon Tan, and Chee Seng Tan. They are the aspiring role models, who attracted their youngest brother into the field of science and engineering since young. I am also deeply indebted to my lovely sister, Hui Lin Tan, for lending her listening ears and taking care of her younger brother throughout the years. Special thanks go to my sister-in-laws Li Zhou and Wei Min Lee, brother-in-law Alvin Lim, nephew Kai Boon Tan and nieces Kai Xin Tan and Kai Xia Lim for cheering up my ever-growing family life, who give me that extra determination to be a great and dependable brother and uncles.

Table of Contents

List of Tables

List of Figures

Abstract

In this dissertation, the work focuses on the development of the dilute-anion III-Nitride based semiconductor for device applications in visible and deep ultraviolet (UV) spectral regime. First-Principle Density-Functional Theory calculations are employed for the investigation of optoelectronic properties of the dilute-anion III-Nitride semiconductors, which includes the understanding of alloy band structures and related band parameters. Among the dilute-anion III-Nitride semiconductor material class, dilute-As GaNAs, dilute-P GaNP and dilute-As AlNAs are extensively studied in this work. The findings show that the incorporation of anion-content in the GaN or AlN alloy will result in significant changes in the electronic properties, leading to unique features as compared to the conventional III-Nitride alloys such as InGaN and AlGaN alloys. Specifically, the investigation in the electronic properties of dilute-As GaNAs and dilute-P GaNP alloys result in suppression of interband Auger recombination process – a known efficiency-limiting issue in the InGaN quantum well (QW) light emitting diode devices., Further analysis are performed to design novel active region nanostructure of InGaN / dilute-As GaNAs interface QW for visible light emission. The analysis tindicate significantly enhanced spontaneous recombination rate and optical gain across the visible spectral regime from blue to red by using InGaN / dilute-As GaNAs interface QW, as compared to conventional InGaN QW. In the case of dilute-As AlNAs semiconductor, the analysis shows that the incorporation of minute amount of As-content in the AlN alloy will result in the switching of crystal field field split-off band with the heavy hole / light hole band, potentially solving the valence band crossover issue persisting in the AlGaN deep ultraviolet light emitting devices.

In addition, extensive studies have been focused in the development of Auger recombination model taking into account the interface roughness in the QW, and analytical solutions for direct Auger recombination processes including interband Auger process for semiconductors. Specifically, the developed Auger model with interface roughness are important to provide intuitive insight of the role of Auger recombination process in the semiconductor devices employing nanostructures.

Chapter 1: Introduction to III-Nitride Semiconductors

1.1. Nitride Semiconductor Material and Device Applications

In the past decades, III-Nitride semiconductor alloys have been widely studied attributed to their potential in various technological applications. Up to present, the III-Nitride materials consisting of GaN, AlN and InN have had tremendous technological impacts. Specifically, advances in the III-Nitride based semiconductor devices have resulted in the solid-state lighting revolution over the past decade [1-25]. The ongoing revolution in the solid-state lighting applications coupled with the development in conventional III-Nitride materials promise to make breakthroughs in other applications including power electronics [26-30], solar cells [31-35] and thermoelectricity [36-41]. The progress and development in the aforementioned fields will be discussed in the following sections to provide a background on my research work.

1.1.1. Light-Emitting Diodes and Laser Diodes for Solid State Lighting

Solid-state lighting (SSL) has fulfilled the promise of the 'next-big-thing' in our illumination applications, bringing a lighting revolution that has changed the usual perception of light sources that exist in daily life [1]. SSL sources exhibit unique characteristics of high efficiency, long lifetime, high reliability, and environmentally friendly that are are impossible to achieve with conventional light sources such as incandescent light bulb and fluorescent lamps.

SSL sources consist of inorganic and organic light emitting diodes (LEDs), or the laser diodes. Currently, LEDs consisting of inorganic semiconductor materials are the most efficienct and reliable, and are leading the way in lighting applications [4]. More importantly, SSL technology has the potential to reduce light energy usage by nearly one half in the U. S. nation (Figure 1-1), which is a key contribution to the nation's climate change effort. As shown by the U. S. Department of Energy (DOE), the energy costs saving through switching from conventional sources to LEDs would reach more than $250 billion in the next decades [42] . As costs lower and efficiencies improve, the market of LED lighting is expected to increase significantly.

Specifically, the packaged LED revenue exceed $15 billion after year 2015 [43], as shown in Figure 1-2.

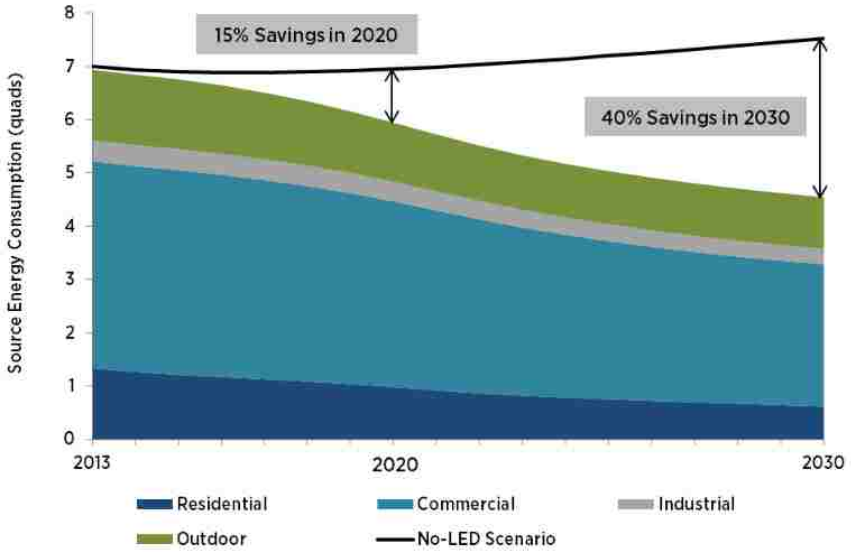

Figure 1-1: *Forecasted U.S. lighting energy consumption and savings from 2013 to 2030 [42].*

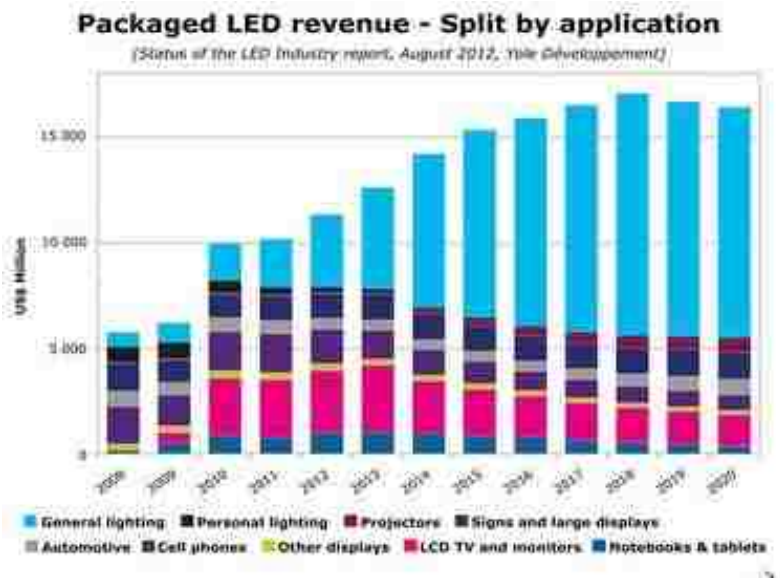

Figure 1-2: *Near-term forecast of packaged LED revenue in various consumer applications [43].*

The human eye response is sensitive to light emission from 360 nm to 770 nm, which means the coverage from blue to red region [see Figure 1-3], LEDs emitting white light (such as red, green, and blue) are required in most general lighting applications [4, 44]. There are different

approaches to generate]white light emission from the LEDs, as illustrated in Figure 1-4. The first and most commonly used approach in industry to generate white light is by using phosphor-converted LEDs (pc-LEDs), in which a blue LED is coated with a yellow phosphor [44]. A similar way is to use a UV LED coated with blue and yellow phosphors to achieve white light emission [44]. The second approach is the multi-chip LEDs that integrates multiple monochromatic color (red, green, and blue) LEDs to generate the white light emission. The multi-chip white LEDs will provide highly controllable color rendering index performance which is important in the indoor applications [44] and has the highest theoritcal luminious efficiacies]. The third approach is to use hybrid LED that combines both multi-chip and phosphor techniques. For example, a green phosphor material can be used together with red and blue LEDs, resulting in white light emission.

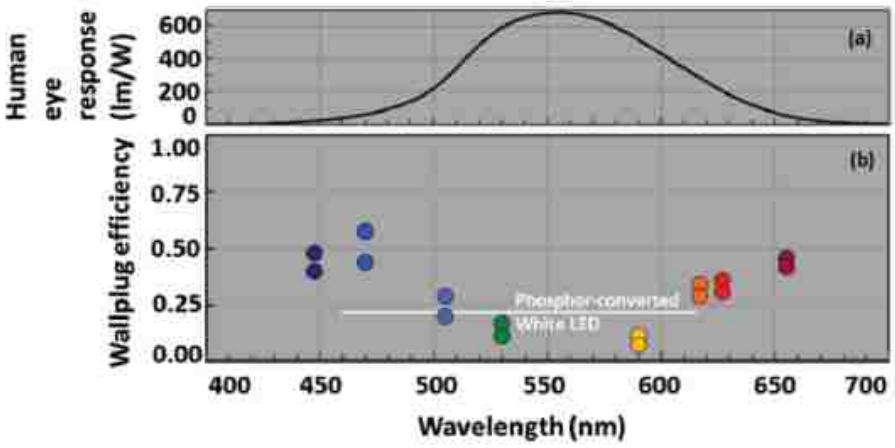

Figure 1-3: *(a) Human eye response towards the wavelength and (b) Wallplug efficiency of start-of-the-art commercial LEDs [4].*

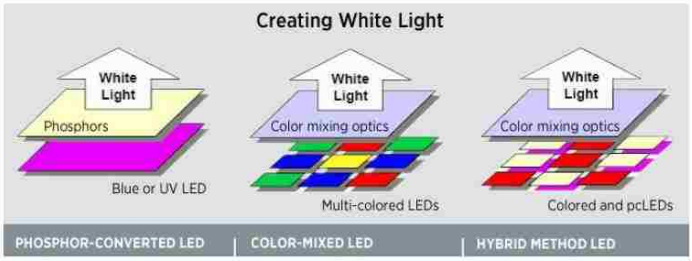

Figure 1-4: *Illustration of methods to generate white light emission from LEDs [44].*

The active materials widely used for state-of-the-art blue and green LEDs are based on III-Nitride semiconductor materials [4, 18]. The ternary InGaN compound possesses energy coverage from 0.7 eV to 3.4 eV that corresponds to 1.77 μm to 365 nm, respectively, and the InGaN alloy shows great promise and is arguably one of the most important semiconductor materials after silicon. The use of InGaN as the active region [45] in the LEDs [see Figure 1-5] has become the norm in the field of SSL, attributed to the relentless pursuit and performance breakthroughs in the early 1990s. The advances in GaN-based SSL devices have also led to the recognition of Nobel Prize in Physics in 2014 [46]. However, the challenges in the field of III-Nitride based LEDs still remains which limit the performance of the devices. These challenges will be further discussed in later chapters.

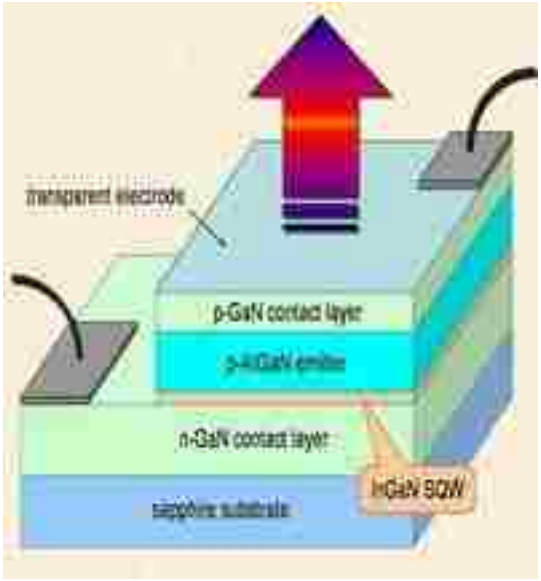

Figure 1-5: *Conventional LED device structure using InGaN material as the active region [45].*

Most recently, GaN-based laser diodes have also been developed with the promise to overcome fundamental challenges in LEDs. GaN-based laser diodes have been suggested as the next-generation SSL sources as a way to circumvent Auger recombination and achieve high efficiencies at high currents [16]. The research in the GaN-based laser diodes for green wavelengths and longer is however still ongoing, attributed to the challenges of high misfit dislocation density and phase separation issues in high In-content InGaN materials. The

challenges of using high In-content InGaN as the active region for long wavelength emission will be further discussed in later chapters.

1.1.2. High-Power Transistor for Power Electronics Applications

Power electronic applications are in high demand in the current world where controlling and converting electrical power is extremely important to ensure efficient power delivery in various appliances. However, the continuous power consumption of inefficient power supplies (standby electrical power) in most devices results in additional energy consumption that is simply wasted. The wide bandgap semiconductor materials such as GaN and AlN are now being explored as the next important semiconductor that will reduce wasted energy consumption. More importantly, the large critical electric fields (~4 MV/cm) and high electron mobility (~1500 cm^2/Vs) exhibited by GaN material implies that the electronic devices formed with GaN materials will have smaller for mactors, lower on-state resistance, low switching losses, and high power conversion efficiencies [48].

In addition, the use of AlGaN/GaN heterostructures [see Figure 1-6] is of great interest in high speed electron mobility transistors (HEMTs) as switching elements. The formation of large two-dimensional electron gas (2DEG) at the AlGaN/GaN heterointerface, attributed to the presence of polarization fields, is one of the key advantages in the AlGaN/GaN HEMT devices. Thus, GaN-based transistors are very promising for power electronics applications including microwave amplifiers, laptop power adaptors, and electronics to control batteries for electronics cars [49].

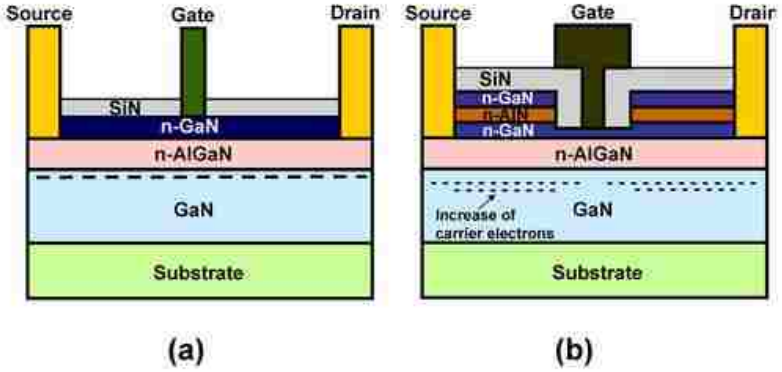

Figure 1-6: *Illustration of AlGaN / GaN device structure for power electronics applications [47].*

The research on GaN power electronics has led to commercial products [50, 51] as shown in Figure 1-7, and it is a matter of time before GaN material replaces the conventional material such as Si as the key element in the power electronics applications. It is also important to note that the market on the GaN power device is blooming, attributed to the huge potential of energy savings by using the GaN devices. As such, many companies started to get involved into developing the GaN power electronics devices, as shown in Figure 1-8. Figure 1-9 also shows that the market size of GaN based power electronic devices is expected to exceed $1 billion by year 2020 [53].

Figure 1-7: *GaN HEMT commercialized by major companies in global [50, 51].*

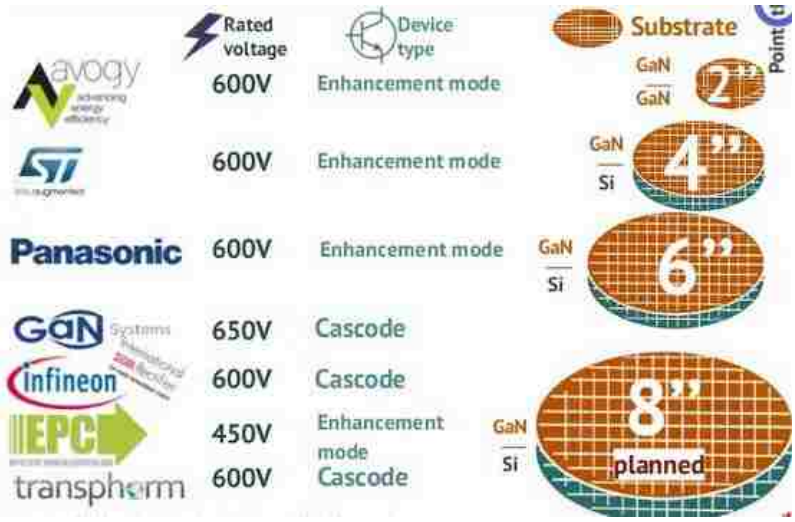

Figure 1-8: *Development of GaN power electronics devices by various companies [52].*

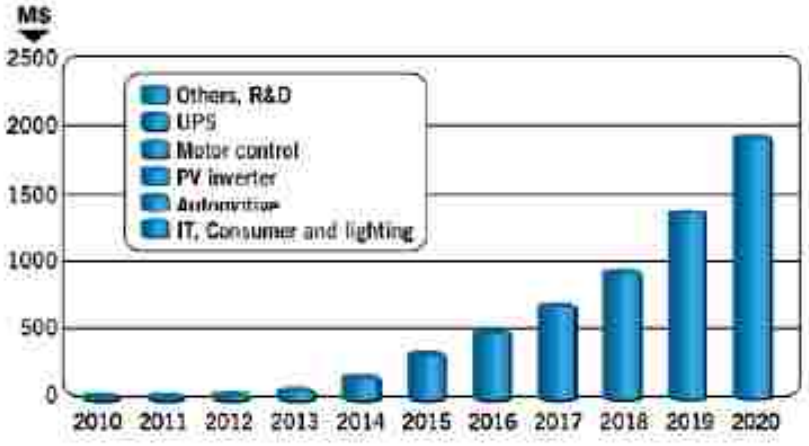

Figure 1-9: *Forecasted market size of GaN power electronics devices, provided by market research firm Yole Development [53].*

1.1.3. Nitride-Based Photovoltaic Cells

While III-Nitride materials are increasingly important in the field of solid-state lighting and power electronics, III-Nitride materials also have tremendous potential in the field of solar cells. In a world that increasingly demands the reduction of fossil fuel usage, renewable energy technologies such as solar energy, wind, geothermal, and biofuels will play a key role to generate the necessary electrical power for future applications.

Among all the renewable energy technology, photovoltaic cells has become one of the most widely studied research areas. The availability of 'unlimited' sunlight implies the unlimited usage of resources to generate electrical power, and thus photovoltaic cells have become extremely important as the method to produce the required energy. The incumbent solar cell technology are based on the low-cost silicon or III-V semiconductor multi-junction (MJ) solar cells as shown in Figure 1-10 [xx]. However, these devices are reaching their theoretical maximums and yield lower efficiencies of only ~20% for Si and ~45% for MJ. Also MJ solar cells are particarly expensive to fabricate. In comparison to these approaches, III-Nitride materials have advantage that the a large fraction of total spectrum of sunlight can be efficiently absorbed since the direct band gap of InGaN alloy could theoriticall cover from 0.7 eV to 3.4 eV.

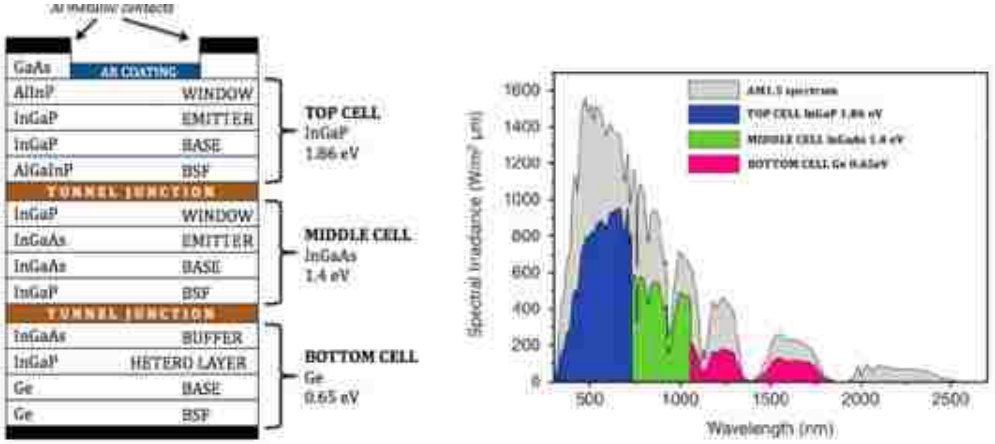

Figure 1-9: *Illustration of high efficiency III-V semiconductor multi-junction solar cell schematic structure[54].*

Up to present, different structure design such as p-i-n double heterojunction [35], InGaN/GaN multiple quantum wells (MQWs) [33] and nanowires [32] have been extensively investigated. However, the efficiency achieved in InGaN / GaN QWs is low at ~3% which is yet to be satisfactory for efficient solar cell performance. Further optimizations of materials and research work on how to improve the device design are still ongoing to improve the efficiency of InGaN solar cells.

1.1.4. Other Applications

III-Nitride materials are also important for several other applications including ultraviolet (UV) emission and detection, thermoelectricity, and sensor of toxic gas detection. As an example, III-Nitrides exhibit high sensitivity towards the combustible gases such as butane and carbon monoxide, which is suitable for toxic gas detection applications. Besides, III-Nitride-based devices can be used for thermoelectric [36-41] and solar hydrogen generations [55-56]. The thermoelectric effect allows the conversion from heat into electricity, implying that electrical power can be generated through temperature changes. One of the prime example of III-Nitride materials that can be used for the thermoelectricity applications is AlInN materials. AlInN alloy exhibits excellent thermoelectric properties with a figure of merit as high as 0.5 at room temperature.

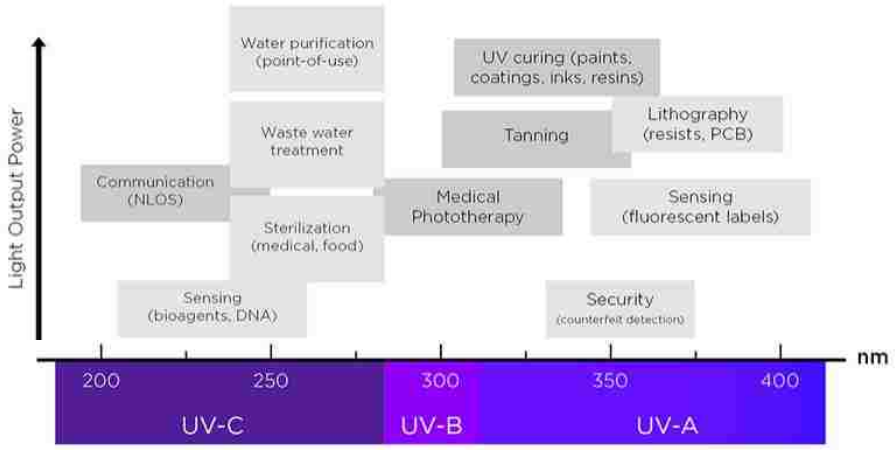

Figure1-10: *Various applications requiring the UV emission from 200 nm to 400 nm [57].*

The use of AlN-based materials also allow the generation of light at wavelengths of ~220 nm and longer, covering the deep UV and mid-UV spectrum regime. This allows the use of AlN-based materials as the active region for water purification, bio-agent detection and sterilization applications [see Figure 1-11]. The use of AlN-based material allows the replacement of conventional UV sources such as mercury lamps, help to reduce environmental pollution. Besides, high pressure mercury lamps operate at high temperatures (600-900°C) which renders it unsuitable for photo-chemical curing. The use of a solid state light-emitting devices based on AlN materials will lead to minimization of device size, low power consumption, low operating temperature and also environmental friendly UV sources.

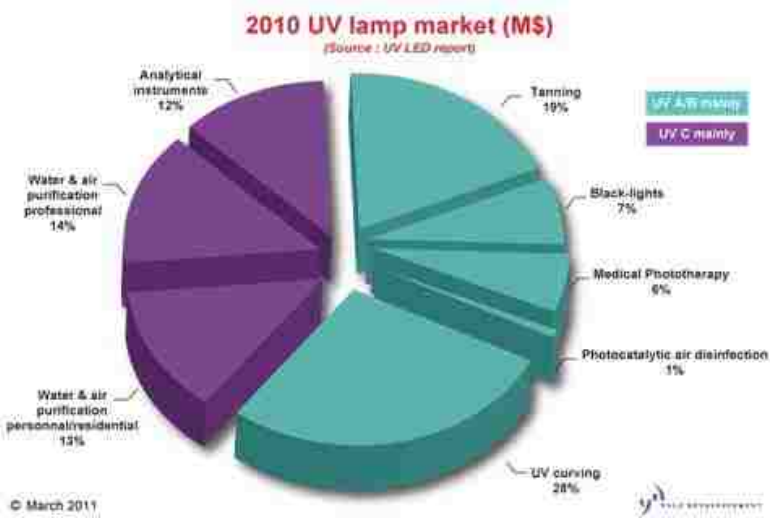

Figure 1-11: *UV lamp market for various applications in 2010 [58].*

It is also important to point out that the UV light market is expected to increase to more than $100 million in 2016 [see Figure 1-12], as predicted by market research firm Yole Development [58]. The UV emitters base on AlN semiconductor materias could potentially dominate the UV market attributed to their various advantages over that of conventional light sources. There are however challenges remaining in the AlN-based material and devices. One of the largest issues is the low efficiency yielded by the AlN-based UV devices, due to materials growth issues and the physics of light emission with the semiconductor. Research is still ongoing to resolve these challenges.

1.2. Research Work Accomplished

1.2.1. Novel Dilute-Anion III-Nitride Semiconductor Material Design

The electronic properties for dilute-As GaNAs materiasl including the band properties and band alignment were investigated in order to develop a novel material for light-emitting applications. The band properties studied for dilute-As GaNAs materiasl include band structure, band gap energy, effective masses, and split-off band energies. Dilute-As GaNAs materials exhibits peculiar yet interesting characteristics, in which the band gap energy can be reduced significantly by incorporating a small percentage of As-content into the GaN material. The large band gap coverage of GaNAs materials from 3.645 eV to 2.232 eV with up to 12.5% As-content shows strong potential for it to be used as an alternative for light emitting applications.

Investigations of the natural band alignment of dilute-As GaNAs materiasl with respect to GaN materials indicate a large valence band offset but a small conduction band offset. The studies show that dilute-As GaNAs can form a Type-I heterostructure with GaN materials, or Type-II heterostructure with InGaN material, attributed to their unique band offset characteristics.

The potential of dilute-As GaNAs materials is further evaluated by investigating Auger recombination process within the material. The findings show that the Auger recombination rates in the dilute-As GaNAs is two orders of magnitude smaller than InGaN, which potentially lead to a visible-emitting material that can overcome the so-called efficiency droop in conventional InGaN-

based LEDs. The lower Auger recombination rate in dilute-As GaNAs materials is attributed to the suppression of Auger resonant conditions in the interband Auger recombination process. Therefore, the combined features demonstrated in dilute-As GaNAs materials shows its strong potential as a next-generation material for the semiconductor device driven applications.

1.2.2. Novel Nanostructure Design for Visible Light Emitters

An interface quantum well (QW) structure design is proposed for visible light emitters. The interface QW structure can be formed using InGaN and dilute-As GaNAs materials. By employing the interface QW structure, electron-hole wavefunction overlap is significantly enhanced when compared to that of conventional InGaN QW, despite the existence of polarization field in the InGaN layer. High spontaneous emission rates can be achieved using an InGaN-GaNAs interface QW structure for red emission, whereas conventional InGaN QWs suffer from low spontaneous emission rates. Attributed to the deep hole localization and strong valence band discontinuity from the effect of dilute-As GaNAs layer in the interface QW structure, the findings show that the In-content in the InGaN material can be kept low (~15-20%) which is important for experimental demonstrations. This work shows promise to resolve some of the challenges faced by InGaN materials use for the long wavelength emission.

1.2.3. Novel Material and Nanostructure Engineering for Deep-Ultraviolet Light Emitters

Alternative III-Nitride materials have been proposed for deep ultraviolet emission. These materials include AlInN and dilute-As AlNAs materials. The incorporation of In into AlN semiconductor results in the reduction of energy band gap of the AlN. By employing AlInN material as the QW in the AlN-based nanostructures, the valence band crossover issue can be resolved when the In-content goes beyond ~12% in the AlInN QW. However, the spontaneous emission rates are low as expected in a conventional QW structure attributed to low electron-hole wavefunction overlap in the wavelength regime of 250-300 nm. Further studies have been carried

out to evaluate AlInN-delta-GaN QW structures sandwiched by AlN barriers. In this structure the delta-GaN layer is inserted into AlInN QW layer, resulting in a three-layer QW. The analysis show that a much higher spontaneous emission rate can be achieved for AlInN-delta-GaN QW structure in comparison to that of conventional AlInN QW, which is attributed to the significant enhancement of electron-hole wavefunction overlap in the AlInN-delta-GaN QW structure.

On the other hand, dilute-As AlNAs materiasl through the incorporation of As impurity in the AlN material is found to be a new material with strong potential for deep UV emission applications. Investigations have been carried out to analyze the electronic properties of dilute-As AlNAs. The band structure and related band parameters including effective mass and valence band energies were studied and analyzed. The findings on dilute-As AlNAs material show that the crystal field split-off band will be moved below the heavy-hole and light-hole bands when the As-content goes beyond ~1%. This implies that the valence band crossover issue persisting in deep UV AlGaN emitters can be resolved by using dilute-As AlNAs materials. Therefore, alternative III-Nitride materials and innovative nanostructure engineering provide attractive features that can be of important for use in deep-ultraviolet emitting applications.

1.2.4. Theoretical Modeling of Auger Recombination Process in III-Nitride Semiconductor

Analytical model has been developed for evaluating the Auger non-radiative recombination process in III-Nitride semiconductors. The analytical model takes into account the intraband and interband Auger recombination processes. The analytical model has been used to calculate the Auger recombination coefficients for InGaN alloy and dilute-anion GaN-based semiconductor alloys. The findings show that the analytically calculated interband Auger coefficients for InGaN alloy agrees considerably with the reported InGaN interband Auger coefficient values determined by numerical modeling. However, the advantage of the analytical model over the numerical model is that the compution time is much shorter. This allows quick and intuitive estimation of

determining Auger recombination rates and how potential changes in III-Nitride semiconductors will impact device performance.

Additionally, a numerical model has been developed to take into account the interface roughness in InGaN semiconductor quantum wells. The concept of how to include interface roughness in Auger recombination calculations is developed and described. The model holds significant importance, since the theory used by many globally assumes abrupt interface in the quantum well (QW) structure which is not the case in real-world quantum well structures. The findings show that Auger recombination rates without interface roughness yields Auger coefficiencts (C_{Auger}) ~ 10^{-34} cm^6s^{-1} for InGaN alloys, which agrees well with the reported calculated values in the literature. However, when an interface roughness of 1 nm is included in the calculation for 3 nm InGaN QW structure, the C_{Auger} ~ 10^{-30} cm^6s^{-1} which is large enough to agree with experimental findings and fully account for the Auger model of efficiency droop observed in the III-Nitride light emitting diodes. On the other hand, the C_{Auger} increases by conly two orders of magnitude for a QW structure with thickness of 20 nm. In comparison, the C_{Auger} increases by four orders of magnitude in a QW structure with thickness of 3 nm. More generally, the findings suggest that tinterface roughness is a critical factor that needs to be taken into account when calculating Auger recombination rates in semiconductor nanostructures.

As a result, an analytical solution has been provided that can take into account the direct band Auger recombination processes for III-Nitride semiconductor materials. Numerical modeling has also been developed for evaluating the Auger recombination process that takes into account the effect of interface roughness in the InGaN QW structure.

1.3. Dissertation Organization

This dissertation report comprises of nine chapters. The organization of this report is presented as follow.

- Chapter 1 consists of the introduction of III-Nitride materials and the relevant applications especially the solid state lighting.

- In Chapter 2, the review of current status of InGaN-based devices will be discussed. The current issues and efficiency limiting issues of III-Nitride light emitters will be reviewed. The development of novel dilute-anion III-Nitride semiconductor alloys will also be discussed.
- Chapter 3 provides the numerical simulation details for the investigation of electronic and optical properties in the III-Nitride semiconductors, which includes the band structure modeling, spontaneous emission characteristics calculation. The review of Density Functional Theory calculations and 6-band k.p method is provided.
- Chapter 4 discusses the Auger recombination theory in the III-Nitride semiconductors. The developed analytical for evaluating the Auger recombination processes for the III-Nitride semiconductor will be discussed. In addition, the concept of Auger recombination process in a realistic III-Nitride quantum well is described. The subsequent numerical Auger recombination model developed taking into account interface roughness effect in III-Nitride semiconductor is discussed as well.
- Chapter 5 discusses the electronic properties of the dilute-anion GaN-based semiconductor alloys, which include both the dilute-As GaNAs and dilute-P GaNP semiconductor alloys. The potential of the dilute-anion GaN-based semiconductor material for the light emitting applications will be discussed by analyzing the alloy electronic properties.
- Chapter 6 focuses in the intrinsic property calculation which is Auger recombination characteristics in the dilute-As GaNAs and dilute-P GaNP semiconductor materials.
- Chapter 7 focuses in the novel nanostructure design to implement the dilute-As GaNAs material into GaN-based active region structure. The spontaneous emission and optical gain characteristics of the GaNAs-based novel active region structure will be discussed.
- Chapter 8 focuses in the topic of deep ultraviolet applications, involving the discussion of current status and issues related to AlGaN-based deep ultraviolet emitters. In this chapter alternative material solutions involving the use of AlInN material and dilute-As AlNAs semiconductor material are also discussed.

Finally, in Chapter 9 the summary of the research performed is provided, and the future outlook of III-Nitride semiconductor materials and devices is discussed.

References for Chapter 1

[1] P. Pust, P. J. Schmidt, and W. Schnick, “A revolution in lighting”, Nature Mater., vol. 14, pp. 454-458, Apr. 2015.

[2] D. A. Steigerwald, J. C. Bhat, R. M. Fletcher, M. O. Holcomb, M. J. Ludowise, P. S. Martin, and S. L. Rudaz, “Illumation with solid state lighting technology”, IEEE Journal on Selected Topics in Quantum Electronics, vol. 8, no. 2, p. 310, Apr. 2002.

[3] J. Y. Tsao, “Solid-state lighting: lamps, chips, and materials for tomorrow”, Circuits and Devices Magazine, vol. 20, no. 3, pp. 28-37, 2004.

[4] J. Y. Tsao, M. H. Crawford, M. E. Coltrin, A. J. Fischer, D. D. Koleske, G. S. Subramania, G. T. Wang, J. J. Wierer, and R. F. Karlicek Jr., “Toward smart and ultra-efficient solid-state lighting”, Adv. Opt. Mat., vol. 2, pp. 809-836, 2014.

[5] E. F. Schubert, and J. K. Kim, “Solid-state light sources getting smart”, Science, vol. 308, pp. 1274-1278, May 2005.

[6] M. Krames, O. Shchekin, R. Mueller-Mach, G. Mueller, L. Zhou, et.al., “Status and future of high-power light-emitting diodes for solid-state lighting”, J. Disp. Technol., vol. 3, no. 2, pp. 160-175, Jun. 2007.

[7] S. Nakamura, “The roles of structural imperfections in InGaN-based blue light-emitting diodes and laser diodes”, Science, vol. 281, no. 5379, pp. 956-961, Aug. 1998.

[8] M. H. Crawford, “LEDs for solid-state lighting: performance challenges and recent advances”, IEEE J. Sel. Top. Quantum Electron., vol. **15**, no. 4, pp. 1028–1040, Aug. 2009.

[9] H. Zhao, G. Y. Liu, J. Zhang, J. D. Poplawsky, V. Dierolf, and N. Tansu, “Approaches for high internal quantum efficiency green InGaN light-emitting diodes with large overlap quantum wells”, Optics Express, vol. **19**, no. S4, pp. A991-A1007, Jul. 2011.

[10] H. Zhao, G. Liu, R. A. Arif, and N. Tansu, “Current Injection Efficiency Quenching Leading to Efficiency Droop in InGaN Quantum Well Light-Emitting Diodes,” *Solid-State Electronics*, vol. 54, pp. 1119–1124, 2010.

[11] S. P. DenBaars, D. Feezell, K. Kelchner, S. Pimputkar, C. C. Pan, C. C. Yen, S. Tanaka, Y. Zhao, N. Pfaff, R. Farrell, M. Iza, S. Keller, U. Mishra, J. S. Speck, S. Nakamura,

"Development of gallium-nitride-based light-emitting diodes (LEDs) and laser diodes for energy-efficient lighting and displays", Acta Materialia, vol. 61, no. 3, pp. 945-951, Feb. 2013.

[12] X. Li, S. Kim, E. E. Reuter, S. G. Bishop, and J. J. Coleman, "The incorporation of arsenic in GaN by metalorganic chemical vapor deposition", Appl. Phys. Lett, vol. **72**, no. 16, pp. 1990-1992, Feb. 1998.

[13] X. Li, S. G. Bishop, and J. J. Coleman, "GaN epitaxial lateral overgrowth and optical characterization", Appl. Phys. Lett., vol.**73**, no. 9, pp. 1179–1181, Jul. 1998.

[14] X. Li, H. Liu, X. Ni, U. Ozgur, H. Morkoc, "Effect of carrier spillover and Auger recombination on the efficiency droop in InGaN-based blue LEDs," Superlattices and Microstructures, vol. 47, pp. 118-122, 2010.

[15] X. H. Li, R. Song, Y. K. Ee, P. Kumnorkaew, J. F. Gilchrist, and N. Tansu, "Light extraction efficiency and radiation patterns of III-nitride light-emitting diodes with colloidal microlens arrays with various aspect ratios", IEEE Photon. J., vol. **3**, no. 3, pp. 489–499, Jun. 2011.

[16] J. J. Wierer, Jr., J. Y. Tsao, and D. S. Sizov, "The potential of III-Nitride laser diodes for solid-state lighting", Phys. Status Solidi C, vol. 11, no. 3-4, pp. 674-677, 2014.

[17] C. K. Tan, and N. Tansu, "Nanostructured lasers: Electrons and holes get closer", Nature Nanotech., vol. 10, no. 2, pp. 107-109, Feb. 2015.

[18] N. Tansu, H. P. Zhao, G. Y. Liu, X. H. Li, J. Zhang, H. Tong, and Y. K. Ee, "III-Nitride photonics", IEEE Photonics Journal, vol. 2, no. 2, pp. 241-248, Apr. 2010.

[19] A. C. Tamboli, E. D. Haberer, R. Sharma, K. H. Lee, S. Nakamura, and E. L. Hu, "Room-temperature continuous-wave lasing in GaN/InGaN microdisks," *Nature photonics,* vol. 1, pp. 61-64, Jan 2007.

[20] T. C. Lu, C. C. Kao, H. C. Kuo, G. S. Huang, and S. C. Wang, "CW lasing of current injection blue GaN-based vertical cavity surface emitting laser," *Applied Physics Letters,* vol. 92, Apr 7 2008.

[21] S.-H. Park, J. Park, and E. Yoon, "Optical gain in InGaN/GaN quantum well structures with embedded AlGaN delta layer," *Applied Physics Letters,* vol. 90, p. 023508, 2007.

[22] H. P. Zhao, R. A. Arif, Y. K. Ee, and N. Tansu, "Optical gain analysis of strain-compensated InGaN-AlGaN quantum well active regions for lasers emitting at 420-500 nm," *Optical and Quantum Electronics,* vol. 40, pp. 301-306, Apr-May 2008.

[23] A. Tyagi, R. M. Farrell, K. M. Kelchner, C. Y. Huang, P. S. Hsu, D. A. Haeger, M. T. Hardy, C. Holder, K. Fujito, D. A. Cohen, H. Ohta, J. S. Speck, S. P. DenBaars, and S. Nakamura, "AlGaN-Cladding Free Green Semipolar GaN Based Laser Diode with a Lasing Wavelength of 506.4 nm," *Applied Physics Express,* vol. 3, 2010.

[24] T. Miyoshi, S. Masui, T. Okada, T. Yanamoto, T. Kozaki, S. Nagahama, and T. Mukai, "510-515 nm InGaN-Based Green Laser Diodes on c-Plane GaN Substrate," *Applied Physics Express,* vol. 2, Jun 2009.

[25] M. R. Krames, J. Bhat, D. Collins, N. F. Gardner, W. Gotz, C. H. Lowery, M. Ludowise, P. S. Martin, G. Mueller, R. Mueller-Mach, S. Rudaz, D. A. Steigerwald, S. A. Stockman, and J. J. Wierer, "High-power III-Nitride emitters for solid state lighting", Phys. Stat. sol. (a), vol. 192, no. 2, pp. 237-245, 2002.

[26] Y. Uemoto, M. Hikita, H. Ueno, H. Matsuo, H. Ishida, M. Yanagihara, T. Ueda, T. Tanaka, and D. Ueda, "Gate injection transitor (GIT) – A normally-off AlGaN / GaN power transistor using conductivity modulation", IEEE Transactions on Electron Devices, vol. 54, no. 12, p. 3393, Dec. 2007.

[27] R. S. Pengelly, S. M. Wood, J. W. Milligan, S. T. Sheppard, and W. L. Pribble, "A review of GaN on SiC high electorn-mobility power transistors and MMICs", IEEE Transactons on Microwave Theory and Techniques, vol. 60, no. 6, Jun. 2012.

[28] W. Saito, Y. Takada, M. Kuraguchi, K. Tsuda, I. Omura, T. Ogura, and H. Ohasi, "High breakdown voltage AlGaN-GaN power-HEMT design and high current density switching behavior", IEEE Transactions on Electron Devices, vol. 50, no. 12, Dec. 2003.

[29] M. S. Shur, "GaN based transistors for high power applications", Solid-State Electronics, vol. 42, no. 12, pp. 2131-2138, 1998.

[30] U. K. Mishra, P. Parikh, and Y. F. Wu, "AlGaN/GaN HEMTs-an overview of device operation and applications," Proc. IEEE 90(6), 1022–1031 (2002).

[31] R. Dahal, B. Pantha, J. Li, J. Y. Lin, and H. X. Jiang, "InGaN/GaN multiple quantum well solar cells with long operating wavelengths", Appl. Phys. Lett., vol. 94, no. 6, p. 063505, Feb. 2009.

[32] Y. Dong, B. Tian, T. J. Kempa, and C. M. Lieber, "Coaxial Group III−Nitride Nanowire Photovoltaics," *Nano Letters,* vol. 9, pp. 2183-2187, 2009/05/13 2009.

[33] S. Y. Bae, J. P. Shim, D. S. Lee, S. R. Jeon, and G. Namkoong, "Improved Photovoltaic Effects of a Vertical-Type InGaN/GaN Multiple Quantum Well Solar Cell," *Japanese Journal of Applied Physics,* vol. 50, Sep 2011.

[34] C. J. Neufeld, N. G. Toledo, S. C. Cruz, M. Iza, S. P. DenBaars, and U. K. Mishra, "High quantum efficiency InGaN/GaN solar cells with 2.95 eV band gap," Appl. Phys. Lett. 93(14),143502 (2008).

[35] O. Jani, I. Ferguson, C. Honsberg, and S. Kurtz, "Design and characterization of GaN/InGaN solar cells," Appl. Phys. Lett. 91(13), 132117 (2007).

[36] J. Zhang, H. Tong, G. Y. Liu, J. A. Herbsommer, G. S. Huang, and N. Tansu, “Characterizations of Seebeck coefficients and thermoelectric figures of merit for AlInN alloys with various In-contents”, J. Appl. Phys., vol. 109, no. 05, p. 053706, Mar. 2011.

[37] B. N. Pantha, R. Dahal, J. Li, J. Y. Lin, H. X. Jiang, and G. Pomrenke, “Thermoelectric properties of InxGa1-xN alloys,” Appl. Phys. Lett. 92(4), 042112 (2008).

[38] H. Tong, J. Zhang, G. Y. Liu, J. Herbsommer, G. S. Huang, and N. Tansu, “Thermoelectric Properties of Lattice-Matched AlInN Alloy Grown by Metalorganic Chemical Vapor Deposition,” Appl. Phys. Lett., vol. 97, Art. 112105, September 2010.

[39] J. Zhang, S. Kutlu, G.Y.Liu, and N. Tansu, “High-Temperature Characteristics of Seebeck Coefficients for AlInN Alloys Grown by Metalorganic Vapor Phase Epitaxy,” J. Appl. Phys., vol. 110, Art. 043710, August 2011.

[40] N. Lu, and I. Ferguson, “III-nitrides for energy production: photovoltaic and thermoelectric applications”, Semiconductor Science and Technology, vol. 28, no. 7, p. 074023, 2013.

[41] G. Chen, M.S. Dresselhaus, G. Dresselhaus, J.-P. Fleurial, T. Caillat, “Recent developments in thermoelectric materials”, International Materials Reviews, vol. 48, pp. 45-66(22), 2003.

[42] http://apps1.eere.energy.gov/buildings/publications/pdfs/ssl/energysavingsforecast14.pdf DOE report “Energy Savings Forecast of Solid-State Lighting in General Illumination Applications”.

[43] http://www.led-professional.com/business/reports/packaged-led-market-report-from-yole-developpement-epic-forecasts-tremendous-growth-between-2012-and-2018

[44] http://www1.eere.energy.gov/buildings/ssl/sslbasics_ledbasics.html

[45] http://www.softimpact.ru/device.php

[46] http://www.nobelprize.org/nobel_prizes/physics/laureates/2014/

[47] http://phys.org/news/2008-10-fujitsu-world-gan-hemt-power.html

[48] J. Wuerfl, E. Bahat-Treidel, F. Brunner, E. Cho, O. Hilt, P. Ivo, A. Knauer, P. Kurpas, R. Lossy, M. Schulz, S. Singwald, M. Weyers, and R. Zhytnytska, "Reliability issues of GaN based high voltage power devices," *Microelectronics Reliability,* vol. 51, pp. 1710-1716, Sep-Nov 2011.

[49] http://indianexpress.com/article/technology/tech-news-technology/new-transistors-announced-by-mit-researchers-will-enable-power-efficient-electronics/

[50] http://www.cree.com/News-and-Events/Cree-News/Press-Releases/2014/May/plastic-HEMTs

[51] http://www.semiconductor-today.com/news_items/2013/APR/PANASONIC_040413.html

[52] http://www.slideshare.net/AlexandreAvron/sic-gan-wide-band-gap

[53] http://www.electroiq.com/articles/sst/2012/03/led-makers-could-diversify-with-gan-power-electronics-production.html

[54] http://sunlab.eecs.uottawa.ca/wp-content/uploads/2014/pdf/HiEfficMjSc-CurrStatusFuturePotential.pdf

[55] J. Li, J. Y. Lin, and H. X. Jiang, “Direct hydrogen gas generation by using InGaN epilayers as working electrodes”, Appl. Phys. Lett., vol. 93, p. 162107, 2008.

[56] J. Benton, J. Bai, and T. Wang, “Enhancement in solar hydrogen generation efficiency using a GaN-based nanorod structure”, Appl. Phys. Lett., vol. 102, p. 173905, 2013.

[57] http://www.koppglass.com/blog/uv-led-performance-improvements-accelerate-market-adoption/

[58] http://www.semiconductor-today.com/news_items/2011/MAR/YOLE_180311.html

Chapter 2: Development of III-Nitride Semiconductors in Device Applications

Significant progress has been achieved in the III-Nitride semiconductor devices for the solid-state lighting (SSL) applications over last couple of decades [1-24]. Despite advances in III-Nitride semiconductors, there are challenges that still remain that hinders fthe urther development of solid state lighting. These challenges include efficiency droop or the reduction of efficiencies at high currents, and the green-gap or the reduction of efficiencies at wavelengths longer than blue. These challenges need to be resolved before the next breakthrough in the SSL technology can be achieved, and one of the solutions being suggested is to develop new materials and design for III-Nitride semiconductors. In this chapter, some of the challenges and solutions of III-Nitride semiconductors for SSL are reviewed. In addition, the development of novel III-Nitride semiconductor material for device applications in the past decade are reviewed.

2.1. Low Efficiency of Green and Beyond InGaN-based LEDs

2.1.1. Greep Gap Issue and Approaches for High-Efficiency Green LEDs

The “green-gap” or the reduction of efficiency with increase wavelength has been one of the key issues in the field of LEDs. Figure 2-1 shows the external quantum efficiency (EQE) of LEDs covering wavelengths from blue to red [2]. As shown in Figure 2-1, the EQE of the blue LED, consisting of InGaN, and the red LED, consisting of the AlGaInP, are high high at approximately 50% at standard operating conditions. However, when the emission moves into wavelengths of ~550 nm, the EQE of the LEDs drops for both InGaN and AlInGaP semiconductors to ~20%. The luminous eye response is highest in the yellow spectral regime, which is contradictory to the efficiency of the LED devices (lowest at these wavelengths). This green-gap problem has resulted in significant research efforts aimed at increasing the efficiency of green and yellow emitters [5, 13, 15-16, 18]. In most cases, InGaN-based devices are being used, and suggested to be the solution in overcoming the green-gap issue. AlGaInP material is not feasible for green emission

because of immutable physical problems such as the crossover of direct band gap to indirect band gap of the alloys [1] and ther reduction of barrier height with decreasing wavelength. However, the utilization of InGaN / GaN quantum well (QW) system exhibits huge challenges in material growth and low performance, attributed to the phase separation problems during growth [25-26] and low recombination rates in the QW system when In-content becomes higher [21].

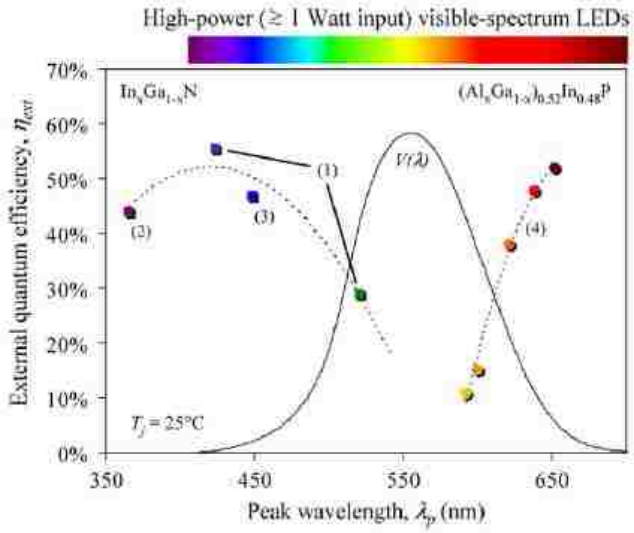

Figure 2-1: *External quantum efficiency of LEDs covering from blue to red spectral regime [2].*

Specifically, when the In-content increases in InGaN QWs, lattice-mismatch strain of InGaN to GaN layers increases. To overcome this strain defects are formed and the increasing defect density with increased In composition deters the performance of the LED devices at these longer wavelengths. Besides phase separation, higher In-content InGaN material will also lead to inhomogeneous In compositions in the QW and broader emission with lower spontaneous emission rates.

More importantly, the strain between the InGaN layer and GaN buffer layer leads to large piezoelectric polarization in the InGaN QW. The piezoelectric polarization along with the intrinsic spontaneous polarization in the InGaN QW then results in polarization-induced electric fields that spatially separate the electrons and holes from the center of the QW. These spatially separated electrons and holes wavefunctions resultin in the so called charge separation issue. Thus, the reduced optical matrix element due to charge separation eventually leads to lower radiative

recombination rates, implying lower efficiency in the devices, which is highly undesirable for LEDs. In the case of blue LEDs, such issues are less dominant since the In-content is much lower in the QW, leading to lesser charge separation, and phase separation, and defect formation. However, in the case of green LEDs, these aforementioned issues are challenging and high efficiency is difficult to realize.

Several approaches have been pursued to address charge separation, and to improve the InGaN LED efficiency [5, 15-24], including: nonpolar and semipolar InGaN QWs [15], staggered InGaN QWs [5, 16, 17], and InGaN QWs with AlGaN delta-layer [20]. The employment of nonpolar or semipolar InGaN QWs could address charge separation effectively, by minimizing the net polarization field in the active region. While there is significant progress in the nonpolar and semipolar InGaN QWs, their development still requires significant optimization in epitaxy and also reduction of production cost of the GaN substrates.

In the case of staggered InGaN QWs, the electron and hole wavefunction overlap can be significantly enhanced by centering the electron and hole wavefunctions in the active region [5]. The staggered InGaN QW structures [see Figure 2-2] are interesting in that the wavefunction overlap can be enhanced despite the existence of polarization-induced electric field. The use of a staggered InGaN QW is now one of the approaches used to improve the LED performance, attributed to the ease of growth and low production cost in comparison to the nonpolar and semipolar InGaN QWs.

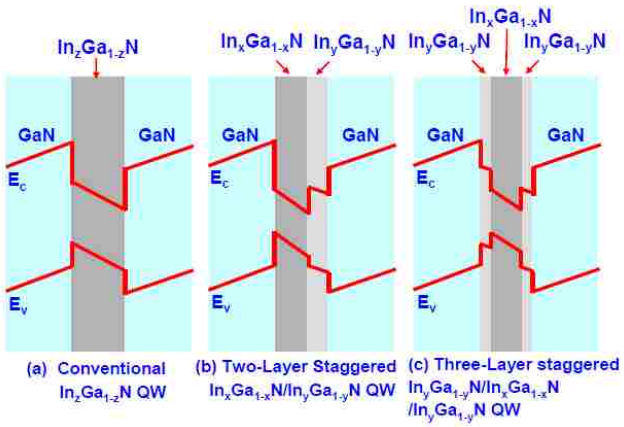

Figure 2-2: *Illustration of InGaN QW structure of (a) conventional QW, (b) two-layer staggered QW, and (c) three-layer staggered QW [5].*

2.1.2. Long-Wavelength Emission Issue

While the approaches such as nonpolar and semipolar QWs and staggered InGaN QWs could be used to improve efficiency in LEDs, those approaches are not necessarily applicable for longer wavelength emission in the amber and red. Figure 2-3 shows the electron-hole wavefunction overlap and emission wavelength as a function of In-content and thickness of InGaN QW [23]. As shown in Figure 2-3, the electron and hole wavefunction overlap reduces significantly as the In-content is increased in the InGaN active region to achieve emission in yellow and red spectral regime. Slight increases of the QW thickness will also result in a drop of the electron-hole wavefunction overlap, which is undesirable for achieving high efficiency in the LEDs.

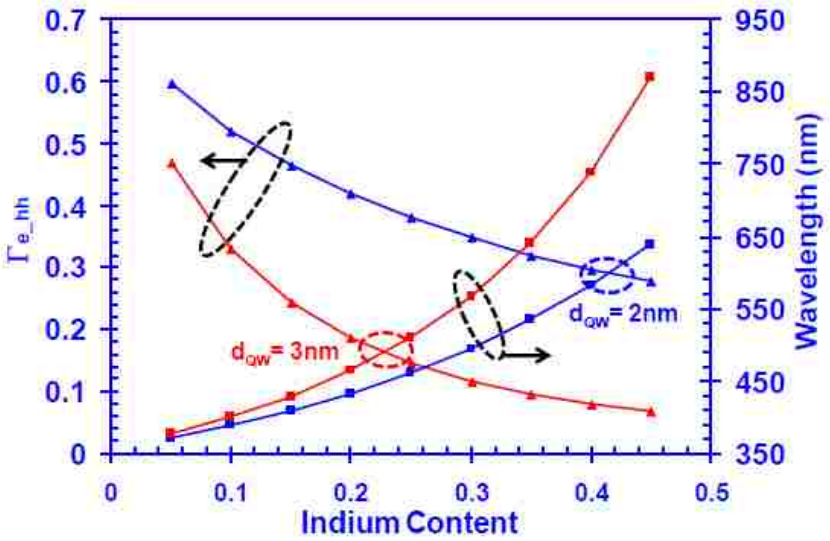

Figure 2-3: *Electron-hole wavefunction overlap (Γ_{e_hh}) for InGaN QW as a function of Indium content with QW thickness of 2nm and 3nm. Corresponding emission wavelength are also shown for comparison purpose [23].*

As the realization of monolithically integrated red-green-blue (RGB) GaN-based LEDs will be important towards achieving smart and ultra-efficient solid state lighting technology [1], it is critical to extend the efforts in developing high efficiency green and red LEDs. Efforts for red-emitting InGaN QWs up to present are still significantly lacking, even though there are several approaches being proposed lately to address them. These approaches include InGaN-delta-InN QWs [23], InGaN QWs with an AlGaN interlayer [30], Eu-doped GaN QWs [31, 32], lattice-relaxed InGaN

multiple QWs [33], and semipolar InGaN QWs [34]. To date the highest efficiencies for yellow-red use an AlGaN interlayer [29] which has shown to reduce defects within the InGaN QW to achieve higher efficiencies. However, research is still ongoing as these approaches still do not provide satisfactory efficiency for these LEDs. Our approach in addressing this issue will be described in Chapter 7.

2.2. Low Light Extraction Efficiency in GaN-based LEDs

In addition to radiative efficiency problems of InGaN-based emitters, light extraction efficiency is also a major challenge in the GaN-based LEDs. It is known that most of the light generated in the active regions of the LEDs are trapped within a higher refractive index (n) material when compared with air (n = 1). As indicated through Snell's Law, light rays incident from a higher index material to lower index material are subjected to total internal reflection, in which the critical angle is given by

$$\theta_{critical} = \sin^{-1}\left(\frac{n_{air}}{n_{semiconductor}}\right). \quad (2.1)$$

The $n_{semiconductor}$ is the refractive index of the material, while n_{air} is the refractive index of air. For material such as GaN, the refractive index is 2.4, resulting in a critical angle of 24.6°. This implies that a small fraction of light that can be extracted out of the semiconductor from within the critical angle, or commonly called the light escape cone. Note that the light extraction efficiency of a conventional top emitting GaN LEDs is ~4% [35-37]. This leads to a significant problem for LED devices, since the radiative efficiency coupled with the light extraction efficiency results in low efficiency from the device.

2.2.1. Approaches in Light Extraction Enhancement

Many approaches have been implemented in the past decade with the aim to increase the light extraction efficiency of III-nitride-based LEDs. These approaches include surface roughening [38], oblique mesa sidewalls [39], photonic crystals [40-42], sapphire microlens [43], patterned

GaN [44], graded refractive index layers [45], GaN micro-domes [46, 47], SiO_2 and TiO_2 microspheres and microlens [48-57], and nano-pyramid [58]. The state-of-the-art approach used in industry to maximize the light extraction efficiency of thin-film flip chip (TFFC) LEDs is based on surface roughening, in which the light extraction efficiency of the LEDs is extrememly high at 80-85%. The ease of forming the rough surface has lead to wide-spread adoption of this technique my many high-power LED manufactorors.

Another other method that leads to high light extraction efficiency is to use the photonic crystals [40-42], where extraction efficiency are as high as ~72%. The problem with the photonic crystals approach is the necessity of a nano-lithography technique, which can increase costs in large scale production of InGaN QW LEDs. Thus, finding a low cost and large area scalable method, such as nano-imprint lithography, in order to achieve a low-cost and practical LED with high extraction efficiency.

Previous work have also demonstrated the advantage of using SiO_2 microspheres or SiO_2 / polysterene (PS) microlens arrays on top of wafer surfaces, in which the light extraction efficiency can be significantly enhanced for InGaN LED devices [48]. In addition, TiO_2 microspheres and TiO_2 and PS microlens arrays have been recently investigated, and suggested as an improved approach over SiO_2 microspheres [54, 57]. For both SiO_2 and TiO_2 approaches, the microspheres and microlens arrays can be deposited via a rapid convective deposition (RCD) technique, as shown in Figure 2-4. RCD method is a colloidal lithography technique that can be used to form a monolayer of the concave microstructure arrays on top of the GaN-based LEDs [54]. This technique is also used for large area microsphere deposition, which is suitable for wafer scale deposition for GaN LEDs.

Figure 2-4: *Schematic of rapid convective deposition of TiO_2 microspheres on top of InGaN LED samples [54].*

The use of self-assembled SiO_2 microsphere and microlens arrays had been well studied for LEDs and organic LEDs in recent years [48-57, 59]. More importantly, the optimum light extraction efficiency of the LEDs can be achieved by optimizing the dimensions and refractive indices of the microspheres and microlens arrays. Very recently, the light extraction efficiency was shown to be as high as 86% by optimizing the PS thickness in the TiO_2 and PS microlens arrays for TFFC LEDs, as shown in Figure 2-5.

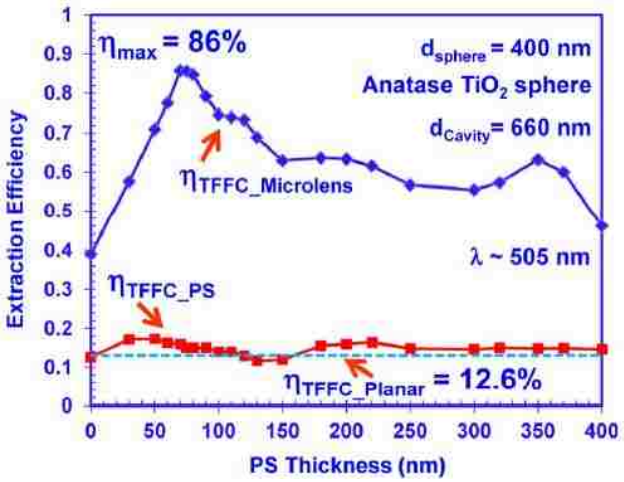

Figure 2-5: *Light extraction efficiency of thin film flip chip LED with TiO_2 microlens array in comparison with that of planar thin film flip chip LED [57].*

However, it is also undeniable that all the parameters including the PS thickness, the sphere diameter, packing density and packing geometry have to be optimized, or else the light extraction efficiency would be reduced significantly. The research stage for the use of TiO_2 microsphere or TiO_2 and PS microlens arrays is still in the early stage, and much work is needed to realize the use of TiO_2 spheres.

2.3. Efficiency Droop Phenomenon in InGaN-based LEDs

While achieving high efficiency in LEDs is an important requirement for SSL, maintaining high efficiency when operating at high current densities is another important criteria. This is especially required in applications that demand high brightness from the lamp, which means high current density is needed to generate the necessary high powers [2]. However, the quantum efficiency of

III-nitride LEDs reduces significantly when the operating current density increases. As shown in Figure 2-6, the EQE and light output power reduces as a function of DC forward currents [2] for both the blue and green LEDs. This 'efficiency-droop' phenomenon shown in Figure 2-6 still exists in the state-of-the-art LEDs and yet to be resolved.

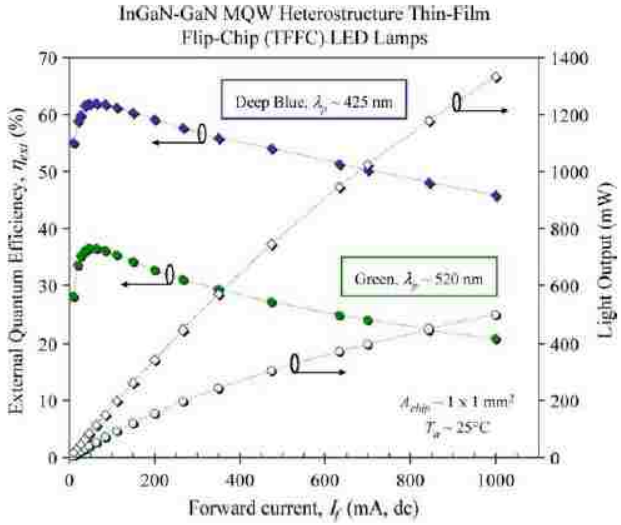

Figure 2-6: *External quantum efficiency and light output power of blue and green InGaN-based LEDs as a function of dc forward currents [1].*

2.3.1. Possible Causes and Suggested Solutions for Droop Suppression

Extensive studies have been carried out to determine the original cause behind the efficiency droop in LEDs. The suggested loss mechanisms for the droop phenomenon include carrier leakage [6, 60-61], Auger recombination [62-70], junction heating effects [71-73], high dislocation density [74], current crowding effects [75-76], carrier loss via indirect absorption [77], hole transport impediment [78-79] and decreased carrier localization at In-rich regions [80]. The original cause of the efficiency-droop phenomenon in the InGaN LEDs is still inconclusive up to present, but the research work in recent years have been narrowed down to carrier leakage and Auger recombination.

Most recently, Iveland and co-workers have managed to detect the Auger electron which correlates with the droop current through direct measurement under electrical excitation [70]. The finding sheds light on the role of Auger recombination in efficiency droop of InGaN-based LEDs,

showing that Auger recombination process plays an important role in the droop issue. On the other hand, there are still some researchers in the LED community believing that carrier injection efficiency is low in the devices through their theoretical analysis, indicating that the carrier leakage could play a role in the droop issue as well. However, such a theory is difficult to measure in practice as there is no known way to separate injection efficiency in the measurement of external quantum efficiency of LEDs.

Various solutions on the nanostructure configuration have been explored to enhance the injection efficiency of the InGaN LEDs. For example, the use of different design in barrier layers and electron blocking layers would help to provide a more uniform current density distribution and to enhance hole injection. The use of electron blocking layer includes thick AlGaN or AlGaInN layers, or thin large band gap AlInN layers [10]. Figure 2-7 shows schematic diagrams of InGaN QWs without polarization-induced electric fields, a conventional InGaN QW, and a large-bandgap thin barriers in InGaN QW. As shown in Figure 2-7, the effective barrier heights for both electrons and holes in conventional InGaN QW are reduced compared to that of nonpolar InGaN QW. This leads to higher thermionic carrier escape rate from the QW to the barrier layers. On the other hand, as shown in Figure 2-7(c), by inserting thin large-bandgap barriers around the InGaN QW layer, the effective barrier heights are increased, resulting in lower thermionic escape rates. This will help to improve the injection efficiency when the current density increases.

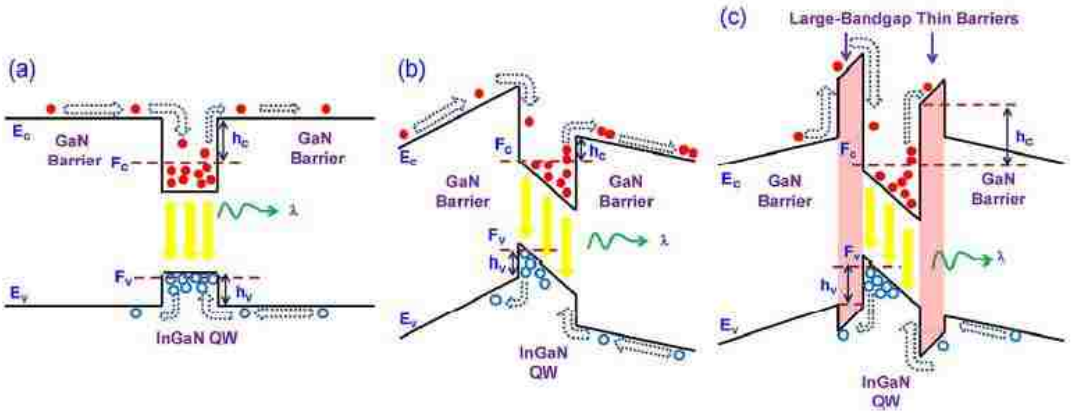

Figure 2-7: *Illustration of band diagrams and carrier flow in the InGaN QW structures [10].*

On the other hand, Auger recombination is a fundamental to InGaN active material itself and plays a large role in efficiency droop. As shown in Figure 2-8, the interband Auger recombination processes result in large Auger recombination coefficients, which are more than sufficient to describe the efficiency droop phenomenon observed in the LEDs [63]. The interband Auger recombination process involves the recombination of carriers in the conduction and valence band, with the Auger recombination rate depending on the intrinsic band property of the corresponding material. This implies that InGaN material has a fundamental issue that is intrinsic and not be easily engineered [63]. Increasing the QW thickness would help to reduce the Auger recombination rates by lowering carrier densities, but this option is difficult in practice because increased strain and defect formation with increased InGaN thickness.

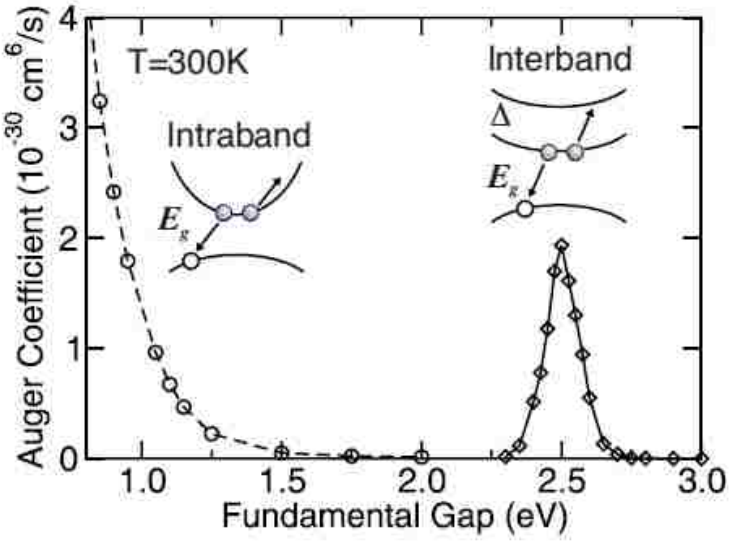

Figure 2-8: *Auger recombination coefficients in InGaN semiconductor material [63].*

2.4. Development in Dilute-Anion III-Nitride Semiconductor Alloys

As discussed in Chapter 2.3.1, Auger recombination is intrinsic to InGaN semiconductors, and it difficult to engineer a solution to overcome it. One of the methods that has been suggested is to use new materials with lower Auger recombination rates. Our most recent work in dilute-As GaNAs material shows that the semiconductor could be used as a low Auger recombination rates

material that emits a visible wavelengths; lower by two orders of magnitude compared to III-nitride semiconductors [81, 82].

However, the field of dilute-As GaNAs material is still in the early stages [8, 81-91]. In fact, the dilute-impurity III-Nitride semiconductor class that dilute-As GaNAs belongs to is still relatively unexplored. One of the reasons is because the dilute-impurity III-Nitride semiconductor would be a highly-mismatched material alloy if grown on GaN or sapphire, implying a complexity and difficulty in the realization of these materials. Besides, conventional InGaN material has been well established as one of the most important semiconductors in recent history, leading to less attention into developing new materials for SSL. However, in current situation where InGaN semiconductors have the intrinsic issue such as phase separation and Auger recombination (leading to efficiency droop that is yet to solve), we may need to begin looking at new semiconductors. The dilute-impurity III-Nitride semiconductor alloy is a very attractive option for the current SSL research community. Thus, in this section, we review the past achievements in the material synthesis and development of dilute-As GaNAs alloys.

2.4.1. Material Synthesis and Growth Development

Among the dilute-anion GaN-based semiconductors, the dilute-As GaNAs is considerably more developed and there are experimental realizations of this semiconductor. Thus, the growth development available in the dilute-anion GaN-based semiconductors is centered around dilute-As GaNAs alloy. Specifically, the arsenic impurity was first successfully incorporated by Li and co-workers into a thin film GaN through metal-organic chemical vapor deposition (MOCVD) [8]. As shown in figure 2-9, the dilute-As GaNAs alloy grown by the MOCVD exhibits strong As-related emission similar to that of the GaN material. This is the first time a redshift of wavelength emission by adding As impurities into the GaN material was shown.

Building on the first successful synthesis of dilute-As GaNAs alloy by Li and co-workers [8], Kimura and co-workers reported growth of dilute-As GaNAs alloy with As-content up to 6.7% As-content with MOCVD [85]. This work is very important in the field of dilute-As GaNAs

semiconductor alloy, since the As-content is now present in the MOCVD-grown GaNAs material. As a result, a map of the band gap energy as a function of the As-content can be determined, showing that a significant energy band gap reduction is achieved by using the dilute-As GaNAs alloy. On the other hand, up to present, the As-content in the GaNAs alloy reaches maximum ~7% with MOCVD. It is yet to know if MOCVD can use used to successfully grow dilute-As GaNAs alloys with As-content more than 7%.

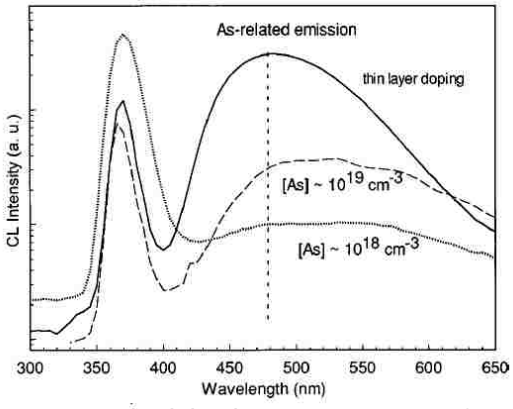

Figure 2-9: *Room-temperature cathodoluminescence spectra for GaNAs alloy grown by using MOCVD technique [8].*

Most recently, Yu and co-workers reported synthesis of dilute-As GaNAs alloy by using nonequilibrium low temperature molecular beam epitaxy (MBE) [86, 87]. The studies show that the energy band gap of the dilute-As GaNAs alloy is significantly reduced when the As-content increases in the GaNAs semiconductor [see Figure 2-10], which is consistent with the findings shown in MOCVD grown GaNAs materials [85].

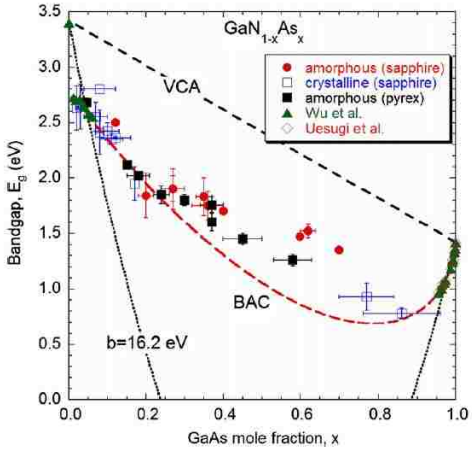

Figure 2-10: *Energy band gap versus the As-composition in the GaNAs material grown by MBE technique [86].*

Interestingly, from the MBE growth studies [see Figure 2-11], it is shown that the hexagonal phase of the dilute-As GaNAs material shifts to amorphous and becomes cubic phase when the As-content increases to 86% [86].

All these works represent key developments of the dilute-As GaNAs alloy in the past decades. The studies demonstrated that the band gap of GaNAs alloy reduces, as the As-content increases. The band gap reduction in dilute-As GaNAs alloy enables the wavelengths over the entire visible spectrum [15]–[17], which shows it is a good potential alternative novel semiconductor for the visible light applications.

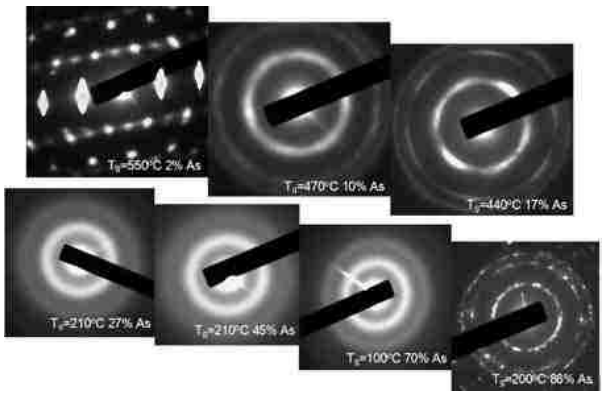

Figure 2-11: *Selective area electron diffraction pattern from GaNAs layer with increasing As-content up to 86% [85].*

However, along with the material synthesis of dilute-As GaNAs alloys, the theoretical studies of this material are still highly limited. The understanding of the electronic and optical properties of dilute-As GaNAs semicoductors and the motivation behind utilizing the dilute-anion GaN-based semiconductor alloys are still significantly lacking. The work in understanding the optoelectronic properties of the dilute-anion GaN-based semiconductor alloys have just been initiated, and various research work is ongoing to provide further understanding of the alloy properties and also the motivation in employing these materials for applications.

2.5. Summary

In this chapter, the challenges and solutions of III-Nitride LED technology are reviewed. The green gap problem in LEDs is yet to be resolved, attributed to the phase separation and charge

separation issues in InGaN QW LEDs. Besides, the efficiency droop phenomenon in the InGaN LED devices is yet to be fully understood, and efforts are still ongoing to determine the original cause of the droop issue. The suggested cause of the efficiency droop phenomenon is likely related to the carrier-related mechanism which involve carrier leakage and Auger recombination. Some solutions have been suggested to resolve green-gap and efficiency droop in the InGaN LEDs. However, the fundamental causes in these issues for the InGaN devices imply the importance of looking beyond InGaN semiconductors to find the suitable solutions. One of the material class of interest is the dilute-impurity nitride semiconductor material. Specifically, the development in dilute-As GaNAs semiconductor material is discussed. Further details on dilute-As GaNAs semiconductors and its potential as an alternative semiconductor for light-emitting applications will be discussed in later chapters.

References for Chapter 2

[1] J. Y. Tsao, M. H. Crawford, M. E. Coltrin, A. J. Fischer, D. D. Koleske, G. S. Subramania, G. T. Wang, J. J. Wierer, and R. F. Karlicek Jr., "Toward smart and ultra-efficient solid-state lighting", Adv. Opt. Mat., vol. 2, pp. 809-836, 2014.

[2] M. Krames, O. Shchekin, R. Mueller-Mach, G. Mueller, L. Zhou, et.al., "Status and future of high-power light-emitting diodes for solid-state lighting", J. Disp. Technol., vol. 3, no. 2, pp. 160-175, Jun. 2007.

[3] S. Nakamura, "The roles of structural imperfections in InGaN-based blue light-emitting diodes and laser diodes", Science, vol. 281, no. 5379, pp. 956-961, Aug. 1998.

[4] M. H. Crawford, "LEDs for solid-state lighting: performance challenges and recent advances", IEEE J. Sel. Top. Quantum Electron., vol. **15**, no. 4, pp. 1028–1040, Aug. 2009.

[5] H. Zhao, G. Y. Liu, J. Zhang, J. D. Poplawsky, V. Dierolf, and N. Tansu, "Approaches for high internal quantum efficiency green InGaN light-emitting diodes with large overlap quantum wells", Optics Express, vol. **19**, no. S4, pp. A991-A1007, Jul. 2011.

[6] H. Zhao, G. Liu, R. A. Arif, and N. Tansu, "Current Injection Efficiency Quenching Leading to Efficiency Droop in InGaN Quantum Well Light-Emitting Diodes," *Solid-State Electronics*, vol. 54, pp. 1119–1124, 2010.

[7] S. P. DenBaars, D. Feezell, K. Kelchner, S. Pimputkar, C. C. Pan, C. C. Yen, S. Tanaka, Y. Zhao, N. Pfaff, R. Farrell, M. Iza, S. Keller, U. Mishra, J. S. Speck, S. Nakamura, "Development of gallium-nitride-based light-emitting diodes (LEDs) and laser diodes for energy-efficient lighting and displays", Acta Materialia, vol. 61, no. 3, pp. 945-951, Feb. 2013.

[8] X. Li, S. Kim, E. E. Reuter, S. G. Bishop, and J. J. Coleman, "The incorporation of arsenic in GaN by metalorganic chemical vapor deposition", Appl. Phys. Lett, vol. **72**, no. 16, pp. 1990-1992, Feb. 1998.

[9] X. Li, S. G. Bishop, and J. J. Coleman, "GaN epitaxial lateral overgrowth and optical characterization", Appl. Phys. Lett., vol.**73**, no. 9, pp. 1179–1181, Jul. 1998.

[10] G. Y. Liu, J. Zhang, C. K. Tan, and N. Tansu, "Efficiency-Droop Suppression by Using Large-Bandgap AlGaInN Thin Barrier Layers in InGaN Quantum Wells Light-Emitting Diodes", IEEE Photonics Journal, vol. 5, no. 2, Art. 2201011, April 2013.

[11] X. H. Li, R. Song, Y. K. Ee, P. Kumnorkaew, J. F. Gilchrist, and N. Tansu, "Light extraction efficiency and radiation patterns of III-nitride light-emitting diodes with colloidal microlens arrays with various aspect ratios", IEEE Photon. J., vol. **3**, no. 3, pp. 489–499, Jun. 2011.

[12] J. J. Wierer, Jr., J. Y. Tsao, and D. S. Sizov, "The potential of III-Nitride laser diodes for solid-state lighting", Phys. Status Solidi C, vol. 11, no. 3-4, pp. 674-677, 2014.

[13] C. K. Tan, and N. Tansu, "Nanostructured lasers: Electrons and holes get closer", Nature Nanotech., vol. 10, no. 2, pp. 107-109, Feb. 2015.

[14] N. Tansu, H. P. Zhao, G. Y. Liu, X. H. Li, J. Zhang, H. Tong, and Y. K. Ee, "III-Nitride photonics", IEEE Photonics Journal, vol. 2, no. 2, pp. 241-248, Apr. 2010.

[15] D. F. Feezell, J. S. Speck, S. P. DenBaars, and S. Nakamura, "Semipolar ($20\bar{2}\bar{1}$) InGaN/GaN light emitting diodes for high-efficiency solid-state lighting", J. Disp. Tech., vol. 9, no. 4, pp. 190-198, Apr. 2013.

[16] R. A. Arif, Y. K. Ee, and N. Tansu, "Polarization engineering via staggered InGaN quantum wells for radiative efficiency enhancement of light emitting diodes", Appl. Phys. Lett., vol. 91, no. 9, p. 091110, Aug. 2007.

[17] R. A. Arif, H. P. Zhao, Y. K. Ee, and N. Tansu, "Spontaneous emission and characteristics of staggered InGaN quantum-well light-emitting diodes", IEEE J. Quantum Electron., vol. 44, no. 6, pp. 573-580, Jun. 2008.

[18] J. Zhang, and N. Tansu, "Improvement in spontaneous emission rates for InGaN quantum wells on ternary InGaN substrate for light-emitting diodes", J. Appl. Phys., vol. 110, no. 11, p. 113110, Dec. 2011.

[19] M. R. Krames, J. Bhat, D. Collins, N. F. Gardner, W. Gotz, C. H. Lowery, M. Ludowise, P. S. Martin, G. Mueller, R. Mueller-Mach, S. Rudaz, D. A. Steigerwald, S. A. Stockman, and J. J. Wierer, “High-power III-Nitride emitters for solid state lighting”, Phys. Stat. sol. (a), vol. 192, no. 2, pp. 237-245, 2002.

[20] H. P. Zhao, R. A. Arif, Y. K. Ee, and N. Tansu, "Optical gain analysis of strain-compensated InGaN-AlGaN quantum well active regions for lasers emitting at 420-500 nm," *Optical and Quantum Electronics,* vol. 40, pp. 301-306, Apr-May 2008.

[21] H. P. Zhao, G. Y. Liu, and N. Tansu, “Analysis of InGaN-delta-InN quantum wells for light-emitting diodes”, Appl. Phys. Lett., vol. 97, no. 13, p. 131114, Oct. 2010.

[22] R. A. Arif, H. Zhao, and N. Tansu, “Type-II InGaN-GaNAs quantum wells for lasers applications”, Appl. Phys. Lett., vol. 92, no. 1, p. 011104, Jan. 2008.

[23] H. Zhao, R. A. Arif, and N. Tansu, “Self-consistent gain analysis of type-II ‘W’ InGaN-GaNAs quantum well lasers”, J. Appl. Phys., vol. 104, no. 4, p. 043104, Aug. 2008.

[24] J. Daubler, T. Passow, R. Aidam, K. Kohler, L. Kirste, M. Kunzer, and J. Wagner, “Long wavelength emitting GaInN quantum wells on metamorphic GaInN buffer layers with enlarged in-plane lattice parameter”, Appl. Phys. Lett., vol. 105, no. 11, p. 111111, Sep. 2014.

[25] K. G. Belyaev, M. V. Rakhlin, V. N. Jmerik, A. M. Mizerov, Ya. V. Kuznetsova, M. V. Zamoryanskaya, S. V. Ivanov, and A. A. Toropov, “Phase separation in InxGa1-xN (0.10 < x< 0.40), Phys. Status Solidi C, vol. 10, no. 3, pp. 527-531, Feb. 2013.

[26] M. D. McCluskey, L. T. Romano, B. S. Krusor, D. P. Bour, N. M. Johnson, and S. Brennan, “Phase separation in InGaN multiple quantum wells”, Appl. Phys. Lett., vol. 72, no. 14, pp. 1730-1732, Apr. 1998.

[27] J. Zhang, and N. Tansu, “Improvement in spontaneous emission rates for InGaN quantum wells on ternary InGaN substrate for light-emitting diodes”, J. Appl. Phys., vol. 110, no. 11, p. 113110, Dec. 2011.

[28] J. Daubler, T. Passow, R. Aidam, K. Kohler, L. Kirste, M. Kunzer, and J. Wagner, “Long wavelength emitting GaInN quantum wells on metamorphic GaInN buffer layers with enlarged in-plane lattice parameter”, Appl. Phys. Lett., vol. 105, no. 11, p. 111111, Sep. 2014.

[29] J. Hwang, R. Hashimoto, S. Saito, and S. Nunoue, “Development of InGaN-based red LED grown on (0001) polar surface”, Appl. Phys. Express, vol. 7, no. 7, p. 071003, Jun. 2014.

[30] J. Heikenfeld, M. Garter, D. S. Lee, R. Birkhahn, and A. J. Steckl, “Red light emission by photoluminescence and electroluminescence from Eu-doped GaN”, Appl. Phys. Lett.,vol. 75, no. 9, pp. 1189-1191, Aug. 1999.

[31] A. Nishikawa, N. Furukawa, T. Kawasaki, Y. Terai, and Y. Fujiwara, “Room-temperature red emission from light-emitting diodes with Eu-doped GaN grown by organometallic vapor phase epitaxy”, Optical Materials, vol. 33, no. 7, pp. 1071-1074, May 2011.

[32] A. Nishikawa, T. Kawasaki, N. Furukawa, Y. Terai, and Y. Fujiwara, “Room-temperature red emission from a p-type/Europium-doped/n-type gallium nitride light-emitting diode under current injection”, Appl. Phys. Express, vol. 2, no. 07, p. 071004, Jun. 2009.

[33] K. Ohkawa, T. Watanabe, M. Sakamoto, A. Hirako, and M. Deura, “740-nm emission from InGaN-based LEDs on c-plane sapphire substrates by MOVPE”, J. Crys. Growth, vol. 343, no. 1, pp. 13-16, Mar. 2012.

[34] Y. Kawaguchi, C. Y. Huang, Y. R. Wu, Y. Zhao, S. P. DenBaars, and S. Nakamura, “Semipolar (2021) single-quantum-well red light-emitting diodes with a low forward voltage”, Jap. J. Appl. Phys., vol. 52, no. 8S, p. 08JC08, Jun. 2013.

[35] H. Benisty, H. De Neve, and C. Weisbuch, “Impact of planar microcavity effects on light extraction—Part I: Basic concepts and analytical trends,” IEEE J. Quantum Electron. vol. 34, pp. 1612–1631, 1998.

[36] H. Benisty, H. De Neve, and C. Weisbuch, “Impact of planar microcavity effects on light extraction—Part II: Selected exact simulations and role of photon recycling,” IEEE J. Quantum Electron., vol. 34, pp. 1632–1643, 1998.

[37] D. Delbeke, R. Bockstaele, P. Bienstman, R. Baets, and H. Benisty, “High-efficiency semiconductor resonant-cavity light-emitting diodes: a review,” IEEE J. Sel. Top. Quantum Electron., vol. 8, pp. 189–206, 2002.

[38] T. Fujii, Y. Gao, R. Sharma, E. L. Hu, S. P. DenBaars, and S. Nakamura, “Increase in the extraction efficiency of GaN-based light-emitting diodes via surface roughening,” Appl. Phys. Lett., vol. 84, pp. 855–857, 2004.

[39] J. S. Lee, J. Lee, S. Kim, and H. Jeon, “Fabrication of reflective GaN mesa sidewalls for the application to high extraction efficiency LEDs,” *Phys. Status Solid. (c)*, vol. 4, pp. 2625–2628, 2007.

[40] J. Jewell, D. Simeonov, S. C. Huang, Y. L. Hu, S. Nakamura, J. Speck, and C. Weisbuch, “Double embedded photonic crystals for extraction of guided light in light-emitting diodes,” Appl. Phys. Lett., vol. 100, p. 171105, 2012.

[41] K. H. Li, K. Y. Zang, S. J. Chua, and H. W. Choi, “III-nitride light emitting diode with embedded photonic crystals,” Appl. Phys. Lett., vol. 102, p. 181117, 2013.

[42] J. J. Wierer, A. David, and M. M. Megens, “III-nitride photonic-crystal light-emitting diodes with high extraction efficiency,” Nat. Photonics, vol. 3, pp. 163–169, 2009.

[43] H. W. Choi *et al.*, “GaN micro-light-emitting diode arrays with monolithically integrated sapphire microlenses,” *Appl. Phys. Lett.*, vol. 84, pp. 2253–2255, Mar. 2004.

[44] S. Chhajed, W. Lee, J. Cho, E. F. Schubert, and J. K. Kim, “Strong light extraction enhancement in GaInN light-emitting diodes by using self-organized nanoscale patterning of p-type GaN,” *Appl. Phys. Lett.*, vol. 98, p. 071102, Feb. 2011.

[45] J. Q. Xi *et al.*, “Optical thin-film materials with low refractive index for broadband elimination of Fresnel reflection,” *Nat. Photon.*, vol. 1, pp. 176–179, Mar. 2007.

[46] P. Zhao and H. P. Zhao, “Analysis of light extraction efficiency enhancement for thin-film-flip-chip InGaN quantum wells light-emitting diodes with GaN micro-domes,” Opt. Express, vol. 20, pp. A765–A776, 2012.

[47] L. Han, T. A. Piedimonte, and H. Zhao, “Experimental exploration of the fabrication of GaN microdome arrays based on a self-assembled approach,” Opt. Mater. Express, vol. 3, pp. 1093–1100 2013.

[48] Y. K. Ee, R. A. Arif, N. Tansu, P. Kumnorkaew, and J. F. Gilchrist, “Enhancement of light extraction efficiency of InGaN quantum wells light emitting diodes using SiO2 / polystyrene microlens arrays,” Appl. Phys. Lett., vol. 91, p. 221107, 2007.

[49] Y. K. Ee, P. Kumnorkaew, R. A. Arif, H. Tong, H. P. Zhao, J. F. Gilchrist, and N. Tansu, “Optimization of light extraction efficiency of III-nitride light emitting diodes with self-assembled colloidal-based microlenses,” IEEE J. Sel. Top. Quantum Electron., vol. 15, pp. 1218–1225, 2009.

[50] P. Kumnorkaew, Y. K. Ee, N. Tansu, and J. F. Gilchrist, “Deposition of microsphere monolayers for fabrication of microlens arrays,” Langmuir, vol. 24, pp. 12150–12157, 2008.

[51] X. H. Li, R. B. Song, Y. K. Ee, P. Kumnorkaew, J. F. Gilchrist, and N. Tansu, “Light extraction efficiency and radiation patterns of III-nitride light-emitting diodes with colloidal microlens arrays with various aspect ratios,” IEEE Photon. J., vol. 3, pp. 489–499, 2011.

[52] Y. K. Ee, P. Kumnorkaew, R. A. Arif, H. Tong, J. F. Gilchrist, and N. Tansu, “Light extraction efficiency enhancement of InGaN Quantum wells light-emitting diodes with polydimethylsiloxane concave microstructures,” Opt. Express, vol. 17, pp. 13747–13757, 2009.

[53] P. F. Zhu, G. Y. Liu, J. Zhang, and N. Tansu, “FDTD analysis on extraction efficiency of GaN light-emitting diodes with microsphere arrays,” J. Disp. Technol., vol. 9, pp. 317–323, 2013.

[54] X. H. Li, P. F. Zhu, G. Y. Liu, J. Zhang, R. B. Song, Y. K. Ee, P. Kumnorkaew, J. F. Gilchrist, and N. Tansu, “Light extraction efficiency enhancement of III-nitride light-emitting diodes by using 2-D closepacked TiO2 microsphere arrays,” J. Disp. Technol., vol. 9, pp. 324–332, 2013.

[55] P. F. Zhu and N. Tansu, “Effect of packing density and packing geometry on light extraction of III-nitride light-emitting diodes with microsphere arrays,” Photon. Res., vol. 3, pp. 184–191, 2015.

[56] P. F. Zhu and N. Tansu, “Resonant cavity effect optimization of III-nitride thin-film flip-chip light-emitting diodes with microsphere arrays,” Appl. Opt., vol. 54, pp. 6305–6312, 2015.

[57] P. F. Zhu, C. K. Tan, W. Sun, and N. Tansu, “Aspect ratio engineering of microlens arrays in thin-film flip-chip light-emitting diodes”, Appl. Optics, vol. 54, no. 34, pp. 10299-10303, Nov. 2015.

[58] J. Q. Xi, H. Luo, A. J. Pasquale, J. K. Kim, and E. F. Schubert, “Enhanced light extraction in GaInN light-emitting diode with pyramid reflector,” *IEEE Photon. Technol. Lett.*, vol. 18, pp. 2347–2349, Nov.-Dec. 2006.

[59] W. H. Koo, W. Youn, P. F. Zhu, X. H. Li, N. Tansu, and F. So, “Light extraction of organic light emitting diodes using defective hexagonalclose-packed array,” Adv. Funct. Mater. 22, 3454–3459 (2012).

[60] M. H. Kim, M. F. Schubert, Q. Dai, J. K. Kim, E. F. Schubert, J. Piprek, and Y. Park, “Origin of efficiency droop in GaN-based light-emitting diodes”, Appl. Phys. Lett., vol. 91, no. 18, p. 183507, Oct. 2007.

[61] H. P. Zhao, G. Y. Liu, J. Zhang, R. A. Arif, and N. Tansu, “Analysis of internal quantum efficiency and current injection efficiency in III-nitride light-emitting diodes”, J. Display Technol., vol. 9, no. 4, pp. 212-225, Apr. 2013.

[62] Y. C. Shen, G. O. Mueller, S. Watanabe, N. F. Gardner, A. Munkholm, and M. R. Krames, “Auger recombination in InGaN measured by photoluminescence”, Appl. Phys. Lett., vol. 91, no. 14, p. 141101, Oct. 2007.

[63] K. T. Delaney, P. Rinke, and C. G. Van de Walle, “Auger recombination rates in nitrides from first principles”, Appl. Phys. Lett., vol. 94, no. 19, p. 191109, May 2009.

[64] F. Bertazzi, M. Goano, and E. Bellotti, “A numerical study of Auger recombination in bulk InGaN”, Appl. Phys. Lett., vol. 97, no. 23, p. 231118, Dec. 2010.

[65] E. Kioupakis, P. Rinke, K. T. Delaney, and C. G. Van de Walle, “Indirect Auger recombination as a cause of efficiency droop in nitride light-emitting diodes”, Appl. Phys. Lett., vol. 98, no. 16, p. 161107, Apr. 2011.

[66] F. Bertazzi, M. Goano, and E. Bellotti, “Numerical analysis of indirect Auger transitions in InGaN”, Appl. Phys. Lett., vol. 101, no. 1, p. 011111, Jul. 2012.

[67] G. Hatakoshi and S. Nunoue, “Analysis of Auger Recombination for Wurtzite InGaN”, Appl. Phys. Express, vol. 5, no. 7, p. 071001, Jun 2012.

[68] F. Bertazzi, X. Zhou, M. Goano, G. Ghione, and E. Bellotti, “Auger recombination in InGaN/GaN quantum wells: A full-Brillouin-zone study”, Appl. Phys. Lett., vol. 103, no. 08, p. 081106, Aug. 2013.

[69] R. Vaxenburg, E. Lifshitz, and Al. L. Efros, “Suppression of Auger-stimulated efficiency droop in nitride-based light emitting diodes”, Appl. Phys. Lett., vol. 102, no. 03, p. 031120, Jan. 2013.

[70] J. Iveland, L. Martinelli, J. Peretti, J. S. Speck, and C. Weisbuch, “Direct measurement of Auger electrons emitted from a semiconductor light-emitting diode under electrical injection: Identification of the dominant mechanism for efficiency droop”, Phys. Rev. Lett., vol. 110, no. 17, p. 177406, Apr. 2013.

[71] A. A. Efremov, N. I. Bochkareva, R. I. Gorbunov, D. A. Lavrinovich, Y. T. Rebane, D. V. Tarkhin, Y. G. Shreter, “Effect of the joule heating on the quantum efficiency and choice of thermal conditions for high-power blue InGaN/GaN LEDs”, Semiconductors, vol. **40**, pp. 605-610, 2006.

[72] W. W. Chow, M. H. Crawford, J. Y. Tsao, and M. Kneissl, “Internal efficiency of InGaN light-emitting diodes: Beyond a quasiequilibrium model”, Appl. Phys. Lett., vol. 97, no. 12, pp. 121105-1-121105-3, Sep. 2010.

[73] J. Hader, J. V. Moloney, and S. W. Koch, “Temperature-dependence of the internal efficiency droop in GaN-based diodes”, Appl. Phys. Lett., vol. 99, no. 18, pp. 181127-1-181127-3, Oct. 2011.

[74] M. F. Schubert, S. Chhajed, J. K. Kim, E. F. Schubert, D. D. Koleska, M. H. Crawford, S. R. Lee, A. J. Fischer, G. Thaler, and M. A. Banas, “Effect of dislocation density on efficiency droop in GaInN/GaN light-emitting diodes”, Appl. Phys. Lett., vol. 91, no. 23, pp. 231114-1-231114-3, Dec. 2007.

[75] X. Guo, and E. F. Schubert, “Current crowding in GaN/InGaN light emitting diodes on insulating substrates”, J. Appl. Phys., vol. 90, no. 8, pp. 4191-4195, Oct. 2001.

[76] V. K. Malyutenko, S. S. Bolgov, and A. D. Podoltsev, “Current crowding effect on the ideality factor and efficiency droop in blue lateral InGaN/GaN light emitting diodes”, Appl. Phys. Lett., vol. 97, no. 25, pp. 251110-1-251110-3, Dec. 2010.

[77] E. Kioupakis, P. Rinke, A. Schleife, F. Bechstedt, and C. G. Van de Walle, “Free-carrier absorption in nitrides from first principles”, Phys. Rev. B, Condens. Matter, vol. 81, no. 24, pp. 241201-241201-4, Jun. 2010.

[78] J. Xie, X. Ni, Q. Fan, R. Shimada, U. Ozgur, and H. Morkoc, “On the efficiency droop in InGaN multiple quantum well blue light emitting diodes and its reduction with p-doped quantum well barriers”, Appl. Phys. Lett., vol. **93**, no. 12, pp. 121107-1-121107-3, Sep. 2008.

[79] X. Ni, Q. Fan, R. Shimada, U. Ozgur, and H. Morkoc, “Reduction of efficiency droop in InGaN light emitting diodes by coupled quantum wells”, Appl. Phys. Lett., vol. 93, no. 17, pp. 171113-171113-3, Oct. 2008.

[80] S. F. Chichibu, T. Azuhata, M. Sugiyama, T. Kitamura, Y. Ishida, H. Okumura, et. al., “Optical and structural studies in InGaN quantum well structure laser diodes”, J. Vac. Sci. Technol. B: Microelectronics and Nanometer Structures, vol. **19**, no. 6, pp. 2177-2183, Nov. 2001.

[81] C. K. Tan, J. Zhang, X. H. Li, G. Y. Liu, B. O. Tayo, and N. Tansu, “First-Principle Electronic Properties of Dilute-As GaNAs Alloy for Visible Light Emitters”, Journal of Display Technology, vol. 9, no. 4, pp. 272-279, April 2013

[82] C. K. Tan, and N. Tansu, "Auger Recombination Rates in Dilute-As GaNAs Semiconductor", AIP Advances, vol. 5, no. 5, Art. 057135, May 2015.

[83] C. K. Tan and N. Tansu, “First-Principle Natural Band Alignment of GaN / Dilute-As GaNAs Alloy,” AIP Advances, vol. 5, no. 1, Art. 017129, January 2015.

[84] C. K. Tan, D. Borovac, W. Sun, and N. Tansu, “InGaN/Dilute-As GaNAs Interface Quantum Well for Red Emitters,” Scientific Reports, vol. 6, Art. 19271, January 2016.

[85] A. Kimura, C. A. Paulson, H. F. Tang, and T. F. Kuech, “Epitaxial layers with high As content grown by metalorganic vapor phase epitaxy and their band gap energy,” *Appl. Phys. Lett.*, vol. 84, no. 9, pp. 1489–1491, Mar. 2004.

[86] K. M. Yu, S. V. Novikov, R. Broesler, C. R. Staddon, M. Hawkridge, Z. Liliental-Weber, I. Demchenko, J. D. Denlinger, V.M. Kao, F. Luckert, R. W. Martin, W. Walukiewicz, and C. T. Foxon, “Non-equilibrium GaNAs alloys with band gap ranging from 0.8–3.4 eV,” *Physica Status Solidi (c)*, vol. 7, no. 7–8, pp. 1847–1849, May 2010.

[87] S. V. Novikov, C. R. Staddon, C. T. Foxon, K. M. Yu, R. Broesler, M. Hawkridge, Z. Liliental-Weber, J. Denlinger, I. Demchenko, F. Luckert, P. R. Edwards, R. W. Martin, and W. Walukiewicz, “Growth by molecular beam epitaxy of amorphous and crystalline GaNAs alloys with band gaps from 3.4 eV to 0.8 eV for solar energy conversion devices”, J. Crys. Growth, vol. 323, pp. 60-63, 2011.

[88] T. Mattila and A. Zunger, “P-P and As-As isovalent impurity pairs in GaN: Interaction of deep t2 levels,” *Phys. Rev. B, Condens. Matter*,vol. 59, no. 15, pp. 9943–9953, Apr. 1999.

[89] C. G. Van de Walle, “Arsenic impurities in GaN,” *Appl. Phys. Lett.*, vol. 76, no. 8, pp. 1009–1011, Feb. 2000.

[90] K. Laaksonen, H.-P. Komsa, E. Arola, T. T. Rantala, and R. M. Nieminen, “Computational study of and alloys and arsenic impurities in GaN,” *J. Phys.: Condens. Matter*, vol. 18, pp. 10097–10114, Oct. 2006.

[91] J. Wu, W. Walukiewicz, K. M. Yu, J. D. Denlinger, W. Shan, J. W. Ager, III, A. Kimura, H. F. Tang, and T. F. Kuech, “Valence band hybridization in N-rich alloys,” *Phys. Rev. B, Condens. Matter*, vol. 70, no. 11, p. 115214, Sep. 2004.

Chapter 3: Theory and Calculations for Electronic and Optical Properties of III-Nitride Semiconductors

The use of modeling of III-Nitride semiconductors to predict the electronic and optical properties is very important in order to gain understanding of their properties, and to also help to induce a need for later practical growth optimization and device realization. The accurate prediction of electronic and optical properties is especially important when the semiconductor material is still unavailable via synthesis. These prediction will help to save the experimental cost and time required to optimize the semiconductor nanostructure.

There are two different methods in computing the electronic band structure for semiconductors. The first method is First-Principle Density-Functional Theory (DFT), and second method is the empirical method. Empirical methods include empirical pseudopotential method, tight-binding (TB) method, and the ***k·p*** method. All methods have their own advantages, however the DFT method provides an accurate description of the ground state properties with the additional computational cost, while ***k·p*** method is useful for modeling semiconductor nanostructures with fairly short computational time.

In this chapter, the details of the simulation for electronic properties of III-Nitride semiconductors using the DFT method are presented. After that, the theoretical and numerical formalism of the 6-band ***k·p*** method for III-Nitride based nanostructures taking into account the valence band mixing, strain effect, and spontaneous and piezoelectric polarization are presented. The calculations of spontaneous radiative recombination rate for semiconductor nanostructures are then presented.

3.1. Density-Functional Theory (DFT) Calculations

3.1.1. Born-Oppenheimer Approximation

Electronic structure theory describes the motion of electrons in atoms or molecules through the Born-Oppenheimer approximation. An assumption is made that electron motion and nuclei

motion in molecules can be separated. Further assumptions are the electrons move much faster than the nuclei since they are much lighter, and nuclei can 'feel' the potential energy of the electrons at each nuclear configuration [1].

Since electrons possess the wave-particle duality characteristic, they can be best thought of as waves that can interfere. The wavefunction can be determined by solving the time-independent Schrodinger's equation. Referring to the assumption made in the Born-Oppenheimer approximation, in atomic units, the Hamiltonian for the electron and nuclei in a system is as shown below [1, 2],

$$\hat{H} = -\frac{\hbar^2}{2m_e}\sum_i \nabla_i^2 - \sum_{i,I}\frac{Z_I e^2}{|r_i - R_I|} + \frac{1}{2}\sum_{i\neq j}\frac{e^2}{|r_i - r_j|} - \sum_I \frac{\hbar^2}{2M_I}\nabla_I^2 + \frac{1}{2}\sum_{I\neq J}\frac{Z_I Z_J e^2}{|R_I - R_J|}. \quad (3.1).$$

The m_e is the electron effective mass, m_I is the nuclei effective mass Z is the charge of the atom, r is the position of the atom. Since the nuclei is fixed in the approximation, the kinetic energy of the nuclei can be considered negligible. This leaves the Hamiltonian as

$$\hat{H} = \hat{T} + \hat{V}_{ext} + \hat{V}_{int} + E_{II} \quad (3.2),$$

where $\hat{T}$ is the electron kinetic energy operator, $\hat{V}_{ext}$ is the external potential acting on the electrons due to the nuclei, $\hat{V}_{int}$ is the internal potential possessed by the electrons. E_{II} is the classical interaction of the nuclei with one another and any other terms that contribute to the total energy of the system. Note that the relativistic effects are not included in the above equation.

3.1.2. Hartree-Fock (HF) Approximation

As an independent particle approximation, the purpose of HF approximation is to determine the ground state wavefunction and the ground state energy of a quantum many-body system. A few assumptions are made in this HF approximation, for example the Born-Oppenheimer approximation is inherently assumed, the relativistic effect is neglected, and the electrons correlation effect are not included for electrons with opposite spin. If there is no spin-orbit interaction, the Slater determinant is used as shown below,

$$\Phi = \frac{1}{(N!)^{1/2}}\begin{vmatrix} \phi_1(r_1,\sigma_1) & \phi_1(r_2,\sigma_2) & \cdots \\ \phi_2(r_1,\sigma_1) & \phi_2(r_2,\sigma_2) & \cdots \\ \cdots & \cdots & \cdots \end{vmatrix} \quad (3.3),$$

where the $\phi_i(r_j,\sigma_j)$ are single particle "spin-orbitals" each of which is a product of a function of the position ${\psi_i}^{\sigma}(r_j)$ and a function of the spin variable $\alpha_i(\sigma_j)$.

The Hartree-Fock approach is to minimize the total energy with respect to all degrees of freedom in the wavefunction with the restriction of Slater determinant form. In atomic units, the Hartree-Fock equation is

$$\left[-\frac{1}{2}\nabla^2 + V_{ext}(r) + \sum_{j,\sigma_j}\int dr' {\psi_j}^{\sigma_{j^*}}(r')\,{\psi_j}^{\sigma_j}(r')\frac{1}{|r-r'|}\right]{\psi_i}^{\sigma}(r) - \sum_j \int dr' {\psi_j}^{\sigma_*}(r')\,{\psi_i}^{\sigma}(r')\frac{1}{|r-r'|}{\psi_j}^{\sigma}(r) \quad (3.4),$$

where the exchange term (the last term in equation (3.4)) is summed over all orbitals of the same spin including the self-term i=j that cancels the unphysical self-term included in the direct term. If the exchange term is modified by multiplying and dividing by ${\psi_i}^{\sigma}(r)$, the equation can be written in the form

$$\hat{H}_{eff}{}^{i}{\psi_i}^{\sigma}(r) = \left[-\frac{\hbar^2}{2m_e}\nabla^2 + \hat{V}_{eff}{}^{i,\sigma}(r)\right]{\psi_i}^{\sigma}(r) = {\varepsilon_i}^{\sigma}{\psi_i}^{\sigma}(r) \quad (3.5),$$

with the effective potential including the external, exchange and Hartree potential.

$$\hat{V}_{eff}{}^{i,\sigma}(r) = V_{ext}(r) + V_{Hartree}(r) + \hat{V}_x{}^{i,\sigma}(r) \quad (3.6),$$

where the exchange potential is

$$\hat{V}_x{}^{i,\sigma}(r) = -\sum_j \int dr' {\psi_j}^{\sigma_*}(r')\,{\psi_i}^{\sigma}(r')\frac{1}{|r-r'|}\frac{{\psi_j}^{\sigma}(r)}{{\psi_i}^{\sigma}(r)} \quad (3.7),$$

and the Hartree potential is

$$V_{Hartree}(r) = \sum_{j,\sigma_j}\int dr' {\psi_j}^{\sigma_{j^*}}(r')\,{\psi_j}^{\sigma_j}(r')\frac{1}{|r-r'|} \quad (3.8).$$

3.1.3. Density functional Theory

Density functional theory (DFT) is a modeling method using quantum mechanics to investigate the electronic structure of atoms and molecules in many-body systems. Within this theory, functionals of electron density are used to determine the many-electron system. While the Thomas-Fermi model has provided the conceptual roots for the DFT, Hohenberg-Kohn Theorems

contribute a solid theoretical footing for DFT. Further work on DFT was extended by Kohn-Sham equations and the Kohn-Sham work is popularly used by researchers nowadays for its well established theory. Since these are the pioneer works that have developed DFT, it is vital to discuss about their theorems in order to provide a better understanding of DFT.

A general description of the functional for DFT, namely total-energy functional, is given as below,

$$E[n] = T[n] + E_H[n] + E_{xc}[n] + \int d^3r\, V_{ext}(r)n(r) \quad (3.9),$$

where $T[n]$ is the kinetic energy, $E_H[n]$ is the classical electrostatic Hartree energy and $E_{xc}[n]$ is the exchange and correlation energies, and $V_{ext}(r)$ is the external potential acting on the system.

3.1.4. Kohn-Sham Equations

The Kohn-Sham approach is to replace the difficult interacting many-body system. While it is obeying the Hamiltonian with a different system, this approach can provide an easier solution to solve [2]. The approach assumes that the ground state density of the original interacting system is equal to that of some chosen non-interacting system. This leads to independent-particle equations for the non-interacting system that can be considered exactly soluble with all the difficult many-body terms incorporated into an exchange-correlation functional of the density. By solving the equations one finds the ground state density and the energy of the original interacting system with the accuracy limited only by the approximations in the exchange-correlation functional. Two assumptions are used in the Kohn-Sham construction of an auxiliary system.

The actual calculations are performed on the auxiliary independent-particle system defined by the auxiliary Hamiltonian.

$$\hat{H}_{aux}{}^{\sigma} = -\frac{1}{2}\nabla^2 + V^{\sigma}(r) \quad (3.12).$$

At this point the $V^{\sigma}(r)$ is not specified and the expressions must apply for all $V^{\sigma}(r)$ in some range, in order to define the functionals. The density of the auxiliary system is given by sums of squares of the orbitals for each spin

$$n(r) = \sum_\sigma n(r,\sigma) = \sum_\sigma \sum_{i=1}^{N^\sigma} |\psi_i{}^\sigma(r)|^2 \quad (3.13).$$

The independent-particle kinetic energy T_s is given by

$$T_s = -\frac{1}{2}\sum_\sigma \sum_{i=1}^{N^\sigma} \langle \psi_i{}^\sigma | \nabla^2 | \psi_i{}^\sigma \rangle = \frac{1}{2}\sum_\sigma \sum_{i=1}^{N^\sigma} d^3r |\nabla \psi_i{}^\sigma(r)|^2 \quad (3.14).$$

The classical Coulomb interaction energy of the electron density $n(r)$interacting with itself is given by

$$E_{Hartree}[n] = \frac{1}{2}\int d^3r d^3r' \frac{n(r)n(r')}{|r-r'|} \quad (3.15).$$

For the Kohn-Sham approach,

$$E_{KS} = T_s[n] + \int dr\, V_{ext}(r)n(r) + E_{hartree}[n] + E_{II} + E_{xc}[n] \quad (3.16),$$

where $V_{ext}(r)$ is the external potential due to the nuclei and any other external fields and E_{II} is the interaction between the nuclei.

For the exchange-correlation energy E_{xc}

$$E_{xc}[n] = \langle \hat{T} \rangle - T_s(n) + \langle \hat{V}_{int} \rangle - E_{Hartree}[n] \quad (3.17).$$

Note that $[n]$ here denotes a functional of the density $n(r,\sigma)$that depends on both position in space and spin.

Since T_s is expressed as a functional of the orbitals but all other terms are considered to be the functionals of the density, variational equations can be derived.

$$\frac{\delta E_{KS}}{\delta \psi_i{}^{\sigma*}(r)} = \frac{\delta T_s}{\delta \psi_i{}^{\sigma*}(r)} + \left[\frac{\delta E_{ext}}{\delta n(r,\sigma)} + \frac{\delta E_{Hartree}}{\delta n(r,\sigma)} + \frac{\delta E_{XC}}{\delta n(r,\sigma)}\right]\frac{\delta n(r,\sigma)}{\delta \psi_i{}^{\sigma*}(r)} = 0 \quad (3.18),$$

where

$$\frac{\delta T_s}{\delta \psi_i{}^{\sigma*}(r)} = -\frac{1}{2}\nabla^2 \psi_i{}^\sigma(r)$$

$$\frac{\delta n^\sigma(r)}{\delta \psi_i{}^{\sigma*}(r)} = \psi_i{}^\sigma(r) \quad (3.19).$$

From the Schrodinger equations:

$$V_{KS}{}^\sigma(r) = V_{ext}(r) + V_{Hartree}(r) + V_{XC}{}^\sigma(r) \quad (3.20).$$

The exchange-correlation potential $V_{XC}{}^\sigma(r)$ is the functional derivative of E_{xc} and it can be written as

$$V_{XC}{}^{\sigma}(r) = \epsilon_{XC}([n], r) + n(r)\frac{\delta\epsilon_{XC}([n],r)}{\delta n(r,\sigma)} \quad (3.21),$$

where $\epsilon_{XC}([n], r)$ is an energy per electron at point r that depends only upon the density $n(r, \sigma)$ in some neighborhood of point r. $\epsilon_{XC}([n], r)$ is given by

$$\epsilon_{XC}([n], r) = \frac{1}{2}\int d^3r' \frac{\bar{n}_{xc}(r,r')}{|r-r'|} \quad (3.22).$$

Here $\bar{n}_{xc}(r, r')$ is the coupling-constant-averaged hole.

3.1.5. Projector Augmented Wave method (PAW)

Projector augmented wave method (PAW) is a general approach to solution of the electronic structure problem by reformulating orthogonalized plane wave (OPW) method [1]. It introduces projectors and auxiliary localized functions, as well as defining a functional for the total energy that involves auxiliary functions. PAW approach also keeps the full all-electron wavefunctions since the full wavefunction varies rapidly near the nucleus. The advantage of PAW is that it allows the density functional theory calculation to be performed with greater computational efficiency.

The all-electron function is given by

$$|\psi\rangle = T|\tilde{\psi}\rangle = \sum_m c_m|\psi_m\rangle \quad (3.23),$$

where T is the linear transformation to relate all-electron valence functions to the smooth function. The full wavefunction in all space is given by

$$|\psi\rangle = |\tilde{\psi}\rangle + \sum_m c_m\{|\psi_m\rangle - |\tilde{\psi}_m\rangle\}$$

$$T = 1 + \sum_m c_m\{|\psi_m\rangle - |\tilde{\psi}_m\rangle\}\langle p_m| \quad (3.24),$$

where c_m and p_m is the coefficient and projection operator respectively.

The relation between Kohn-Sham equations and PAW method can be related to

$$H = -\frac{1}{2}\nabla^2 + V_{Hartree}(r) + V_{XC}(r) + v(r) \quad (3.25),$$

$$T^*HT = -\frac{1}{2}\nabla^2 + V_{Hartree}(r) + V_{XC}(r) + \sum_m\sum_{i,j}|p_{m,i}\rangle H_{i,j}\langle p_{m,j}| \quad (3.26).$$

It is important to note here that PAW method is typically combined with frozen core approximation, implying that the core states are assumed to be unaffected by the ion's environment.

3.1.6. Calculation Methods and Computational Details

With the use of simple approximations, it eases the complexity of the exact functional $E_{xc}[n]$. The popular approximations include the local density approximation (LDA) and various classes of generalized-gradient approximation (GGA) [2]. The details of both approximations are discussed.

LDA is the most general local approximation. The exchange-correlation energy is simply an integral over all space with the exchange-correlation energy density at each point assumed to be the same.

$$E_{XC}{}^{LDA}\left[n^{\uparrow}, n^{\downarrow}\right] = \int d^3 r n(r) \epsilon_{XC}{}^{hom}\left(n^{\uparrow}(r), n^{\downarrow}(r)\right) \quad (3.27),$$

where ϵ_X is the exchange energy and ϵ_C is the correlation energy.

Kohn-Sham potential can be expressed directly through the LDA and GGA functionals. In the LDA, the form is shown as below,

$$\delta E_{XC}[n] = \sum_{\sigma} \int dr \left[\epsilon_{XC}{}^{hom} + n \frac{\partial \epsilon_{XC}{}^{hom}}{\partial n^{\sigma}}\right] \delta n(r, \sigma) \quad (3.28),$$

$$V_{XC}{}^{\sigma}(r) = \left[\epsilon_{XC}{}^{hom} + n \frac{\partial \epsilon_{XC}{}^{hom}}{\partial n^{\sigma}}\right] \quad (3.29).$$

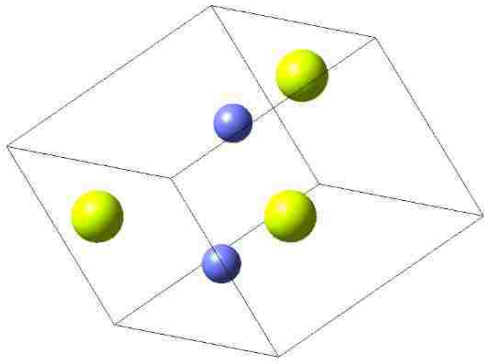

Figure 3-1*: GaN supercell structure constructed using VASP software.*

The band structure calculations based on the Density Functional Theory are computed using the MedeA Vienna Ab initio Simulation Package (VASP) software [3]. Supercell approach is required to construct the crystal structure for a particular material. Based on the supercell, structure optimization is performed to obtain the relaxed structure of the material, with the atom positions with the Hellmann-Feynman force set to 0.02 eV/Å. The external stress was set to 0 GPa, and the energy convergence tolerance was set to 1 10 eV atom. The Gamma centered Monkhorst-Pack grid and high symmetry k-points were used for the band structure calculations. Different Monkhorst-Pack k-point meshes were generated in the calculations attributed to the use of different supercell sizes. The structure shown in figure 3-1 is a simple GaN supercell structure consisting of 2 Ga atoms and 2 N atoms. It is expected that the supercell structure needs to be larger in order to take into account of ternary semiconductor alloy. Further details are discussed in Chapter 4.

3.2. Band Structure and Wave Function Calculations with 6-Band *k·p* Method

3.2.1. 6x6 *k·p* Hamiltonian Matrix

The calculations of band structure and electron and hole wavefunctions are carried out based on a 6-band ***k·p*** formalism for wurtzite semiconductors. The six bands correspond to the heavy hole, light hole, and the crystal-field split-off bands which have double degeneracy with spin counterparts. The electron energy bands are assumed to be parabolic in the calculations. The full Hamiltonian for the Schrondinger equation is given as

$$H = \begin{bmatrix} F & -K^* & -H^* & 0 & 0 & 0 \\ -K & G & H & 0 & 0 & 0 \\ -H & H^* & \lambda & 0 & 0 & 0 \\ 0 & 0 & 0 & F & -K & H \\ 0 & 0 & 0 & -K^* & G & -H^* \\ 0 & 0 & 0 & H^* & -H & \lambda \end{bmatrix} \quad (3.30),$$

Where

$$F = \Delta_1 + \Delta_2 + \lambda + \theta$$

$$G = \Delta_1 - \Delta_2 + \lambda + \theta$$

$$\lambda = \frac{\hbar^2}{2m_0}[A_1 k_z^2 + A_2 k_t^2]$$

$$\theta = \frac{\hbar^2}{2m_0}[A_3 k_z^2 + A_4 k_t^2]$$

$$K_t = \frac{\hbar^2}{2m_0}\left[A_5 (k_x + ik_y)^2\right]$$

$$H_t = \frac{\hbar^2}{2m_0}\left[A_6 (k_x + ik_y) k_z\right]$$

$$\Delta = \sqrt{2}\Delta_3 \qquad (3.31).$$

It is important to note that III-Nitride quantum wells (QWs) often exhibit strain and a reulsting polarization field. As such, taking into account strain and polarization into the calculations is important in order to provide a more accurate prediction of the optical and electronic properties [4-8]. For a strained-layer wurtzite crystalline semiconductor material grown along the z-axis direction, the strain tensor is obtained as

$$\varepsilon_{xx} = \varepsilon_{yy} = \frac{a_0 - a}{a}$$

$$\varepsilon_{zz} = -\frac{2C_{13}}{C_{33}}\varepsilon_{xx}$$

$$\varepsilon_{xy} = \varepsilon_{yz} = \varepsilon_{zx} = 0 \qquad (3.32),$$

where a_0 and a are the lattice constants of the substrate and the layer material, while C_{13} and C_{33} are the elastic constants of the corresponding materials. For tensile strain, the substrate has a larger lattice constant than the layer material, leading to lattice expansion of the layer material to fit with the substrate. For compressive strain, the substrate has smaller lattice constant than the layer material, leading to lattice compression of the layer material to fit with the substrate. In the case of InGaN layer on top of the GaN material, the InGaN layer experiences compressive strain, since InGaN has larger lattice constant than the GaN layer.

The strain effect can be included into the Hamiltonian matrix as shown below:

$$H_{6x6} = \begin{bmatrix} F & K_t & -iH_t & 0 & 0 & 0 \\ K_t & G & \Delta + iH_t & 0 & 0 & 0 \\ iH_t & \Delta + iH_t & \lambda & 0 & 0 & 0 \\ 0 & 0 & 0 & F & K_t & iH_t \\ 0 & 0 & 0 & K_t & G & \Delta + iH_t \\ 0 & 0 & 0 & -iH_t & \Delta - iH_t & \lambda \end{bmatrix} \quad (3.33),$$

Where

$$F = \Delta_1 + \Delta_2 + \lambda + \theta$$

$$G = \Delta_1 - \Delta_2 + \lambda + \theta$$

$$\lambda = \frac{\hbar^2}{2m_0}[A_1 k_z^2 + A_2 k_t^2] + D_1 \varepsilon_{zz} + D_2(\varepsilon_{xx} + \varepsilon_{yy})$$

$$\theta = \frac{\hbar^2}{2m_0}[A_3 k_z^2 + A_4 k_t^2] + D_3 \varepsilon_{zz} + D_4(\varepsilon_{xx} + \varepsilon_{yy})$$

$$K_t = \frac{\hbar^2}{2m_0}[A_5 k_t^2]$$

$$H_t = \frac{\hbar^2}{2m_0}[A_6 k_t k_z]$$

$$\Delta = \sqrt{2}\Delta_3 \quad (3.34).$$

The electrostatic field resulting from the spontaneous polarization field (P_{sp}) and piezoelectric polarization field is then taken into account in the numerical calculation model [8]. The calculation of piezoelectric uses linear interpolation for the piezoelectric coefficients and elastic coefficients [8]. The piezoelectric polarization field can be expressed as

$$P_{pz} = 2d_{31}\left(C_{11} + C_{12} - \frac{2{C_{13}}^2}{C_{33}}\right), \quad (3.35),$$

where $d_{31}$is piezoelectric coefficient and the C's are the elastic coefficients.

By incorporating both the spontaneous polarization field and piezoelectric polarization fields, the electrostatic fields in each layer (j_{th}) can be written as [8]

$$E_j = \frac{\sum_k l_k P_k/\varepsilon_k - P_j \sum_k l_k/\varepsilon_k}{\varepsilon_j \sum_k l_k/\varepsilon_k} \quad (3.36),$$

where P is the total macroscopic polarization, ε is the dielectric constant, and l is the thickness of each layer. The electrostatic field also needs to satisfy the periodic boundary condition to ensure zero average electric field in the layer

$$\sum_k l_k E_k = 0 \quad (3.37),$$

where the summation sums up the layers including the active region and barrier region.

3.2.2. Carrier Screening Effect in Calculation

The carrier screening effect is taken into account for the eigen energies and wavefunctions calculations, by solving the Poisson equation [6, 8]:

$$\frac{\partial}{\partial z}\left(\varepsilon \frac{\partial V_{sc}}{\partial z}\right) = -\rho(z) \quad (3.38),$$

where the potential V_{sc} includes the polarization field effects.

The charge distribution is then given as

$$\rho(z) = |e|[p(z) - n(z)] \quad (3.39),$$

where

$$n(z) = \sum_n |\phi_n(z)|^2 N_n$$

$$p(z) = \sum_m |g_m(z)|^2 P_m \quad (3.40).$$

The surface electron and hole concentration in the conduction band and valence band respectively are expressed as

$$N_n = 2\int_0^\infty \frac{2\pi k_t}{(2\pi)^2} \frac{1}{1+e^{[Een(k_t)-F_c]/k_B T}} dk_t$$

$$P_m = 2\int_0^\infty \frac{2\pi k_t}{(2\pi)^2} \frac{1}{1+e^{[F_v - E_{hm}(k_t)]/k_B T}} dk_t \quad (3.41).$$

As a result, the potential profile for electrons and holes for a III-Nitride nanostructure will be affected by the inclusion of self-consistent electrostatic potential:

$$U_e(z) = U_0^e(z) - |e|V_{sc}(z)$$

$$U_h(z) = U_0^h(z) - |e|V_{sc}(z) \quad (3.42).$$

The self-consistent Schrodinger equations taking into account the carrier screening effect for electrons and holes can then be expressed as

$$\left[-\frac{\hbar^2}{2m_e}\frac{d^2}{dz^2} + U_e(z)\right]\phi(z) = E_e\phi(z)$$

$$\left[-\frac{\hbar^2}{2m_h}\frac{d^2}{dz^2}+U_h(z)\right]g(z)=E_h g(z) \quad (3.43).$$

3.3. Spontaneous Radiative Recombination Rate and Optical Gain Calculation

The Hamiltonian shown in section 3.2 can be split into two 3 x 3 matrices:

$$H^U=\begin{bmatrix} F & K_t & -iH_t \\ K_t & G & \Delta-iH_t \\ iH_t & \Delta+iH_t & \lambda \end{bmatrix}$$

$$H^L=\begin{bmatrix} F & K_t & iH_t \\ K_t & G & \Delta+iH_t \\ -iH_t & \Delta-iH_t & \lambda \end{bmatrix} \quad (3.44).$$

As a result of the calculated envelop functions, the optical transition matrix element can then be computed.

For Transverse electric (TE)-polarization:

$$|(M_x)^v_{\sigma m}(k_t)|^2=\frac{|\langle S|p_x|X\rangle|^2}{4}\left\{\langle\phi_n|g_m^{(1)}\rangle^2+\langle\phi_n|g_m^{(2)}\rangle^2\right\}, \text{for } \sigma=U$$

$$|(M_x)^v_{\sigma m}(k_t)|^2=\frac{|\langle S|p_x|X\rangle|^2}{4}\left\{\langle\phi_n|g_m^{(4)}\rangle^2+\langle\phi_n|g_m^{(5)}\rangle^2\right\}, \text{for } \sigma=L \quad (3.45).$$

For Transverse magnetic (TM)-polarization:

$$|(M_x)^v_{\sigma m}(k_t)|^2=\frac{|\langle S|p_x|Z\rangle|^2}{4}\left\{\langle\phi_n|g_m^{(3)}\rangle^2\right\}, \text{for } \sigma=U$$

$$|(M_x)^v_{\sigma m}(k_t)|^2=\frac{|\langle S|p_x|Z\rangle|^2}{4}\left\{\langle\phi_n|g_m^{(6)}\rangle^2\right\}, \text{for } \sigma=L \quad (3.46).$$

Where ϕ_n is the n^{th} conduction band confined state and g_m is the m^{th} valence band confined state.

Based on the Fermi's Golden rule, the optical gain for the semiconductor nanostructures can be calculated by taking into account all interband transitions between n^{th} conduction subbands and m^{th} valence subbands as follow [4, 8]

$$g_{sp}(\hbar\omega)=\frac{2q^2\pi}{n_r c\varepsilon_0 {m_0}^2\omega L_\omega}\sum_{\sigma=U,L}\sum_{n,m}\int\frac{k_t dk_t}{2\pi}|(M_e)^\sigma_{nm}|^2.\frac{f_n^c(k_t)\left(1-f_{\sigma m}^v(k_t)\right)(\gamma/\pi)}{\left(E^{cv}_{\sigma,nm}(k_t)-\hbar\omega\right)^2+\gamma^2} \quad (3.47),$$

where q is the electron charge, m_0 is the mass of a free electron, c is the speed of light and ε_0 is the permittivity in free space. The n_r is the refractive index of the material used for the QW, while L_w is the thickness of the well. In addition, $\hbar\gamma$ is the half line width of the Lorentzian function with the linewidth broadening time used in our calculations as 0.1 ps. Note that the $f_n^c(k_t)$ and $f_{\sigma m}^v(k_t)$ are the Fermi-Dirac distribution probabilities for the electrons in conduction band and valence band, which are given as

$$f_n^c(k_t) = \frac{1}{1+exp\left(\frac{E_n^c(k_t)-F_c}{k_BT}\right)} \quad (3.48),$$

$$f_{\sigma m}^v(k_t) = \frac{1}{1+exp\left(\frac{E_{\sigma m}^v(k_t)-F_v}{k_BT}\right)} \quad (3.49).$$

The calculation of the spontaneous emission rate takes into account both the TE and TM polarizations. The total momentum matrix element is taken by averaging of two TE-polarized components and one TM-polarized component, which is expressed as following:

$$\left|M_{sp}\right|^2 = \frac{1}{3}(2|M_x|^2 + |M_z|^2) \quad (3.50).$$

The total spontaneous emission rate per unit volume per unit energy interval ($s^{-1}cm^{-3}eV^{-1}$) can be written as

$$r^{spon}(E = \hbar\omega) = \frac{{n_e}^2\omega^2}{\pi^2\hbar c^2}\frac{2\left(2g_{sp}^x+g_{sp}^z\right)}{3} \quad (3.51).$$

The g_{sp}^x and g_{sp}^z are the optical gain with TE and TM polarizations respectively, as expressed below:

$$g^{TE}(\hbar\omega) = g_{sp}^x(\hbar\omega)\left[1 - exp\left(\frac{\hbar\omega-\Delta F}{k_BT}\right)\right],$$

$$g^{TM}(\hbar\omega) = g_{sp}^z(\hbar\omega)\left[1 - exp\left(\frac{\hbar\omega-\Delta F}{k_BT}\right)\right] \quad (3.52),$$

where ΔF the represents the energy separation between the quasi-Fermi levels of the electrons and holes.

The total spontaneous emission rate per unit volume R_{sp} can then be obtained by integrating Equation (3.51) over the entire frequency range as shown below

$$R_{sp} = \int_0^{\infty} r^{spon}(\hbar\omega) d(\hbar\omega) \quad (3.53).$$

Based on the total spontaneous emission rate per unit volume, the radiative recombination current density can then be obtained by

$$J_{rad} = qL_w R_{sp} \quad (3.54).$$

The calculations of the spontaneous emission rates for InGaN heterostructures include all possible transitions between electron and hole confined states. The existence of polarization-induced electric field band bending in III-Nitride QW structures, leads to the break of orthogonality between states with different quantum numbers. This means that the transitions between different states such as that of conduction 1st state and heavy hole 2nd state will occur with a certain transition probability. Therefore, all transition states are needed to be taken into account for the calculation.

3.4. Summary

The electronic structure theory for the DFT calculations is discussed, with the simulation details presented along for completeness. The band structure and wavefunctions calculations for the III-Nitride heterostructure are also presented, which are important for the calculation of spontaneous emission rates. Lastly, the calculation of spontaneous emission rates is also presented. The simulation methods for the band structures of the III-Nitride semiconductor material and heterostructure are important, attributed to the accurate prediction of the electronic and optical properties which can provide insightful information for realization in the future.

References for Chapter 3

[1] R. Martin, Electronic Structure: Basic Theory and Practical Methods, *Cambridge University Press* (2004).

[2] E. Kaxiras, Atomic and Electronic Structure of Solids, *Cambridge University Press* (2003).

[3] MedeA-VASP, Material Designs Inc.

[4] S. L. Chuang, “Optical gain of strained wurtzite GaN quantum-well lasers”, IEEE J. Quantum Electron., vol. 32, no. 10, pp. 1791-1800, Oct. 1996.

[5] S. L. Chuang, and C. S. Chang, “A band-structure model of strained quantum-well wurtzite semiconductors”, Semicond. Sci. Technol., vol. 12, no. 3, pp. 252-263, Mar. 1997.

[6] S. L. Chuang, Physics of Photonic Devices 2nd ed. Wiley, New York, 2009.

[7] S. L. Chuang, and C. S. Chang, “k.p method for strained wurtzite semiconductors”, Phys. Rev. B, vol. 54, pp. 2491-2504, Jul. 1996.

[8] H. Zhao, R. A. Arif, Y. K. Ee and N. Tansu, “Self-consistent analysis of strain-compensated InGaN-AlGaN quantum wells for lasers and light-emitting diodes”, IEEE J. Quntum Electron., vol. 45, no. 1, pp. 66-78, Jan. 2009.

Chapter 4: Auger Recombination Theory in III-Nitride Semiconductors

In the recent decade, III-Nitride based semiconductor alloys are extensively studied for prospective applications in solid state lighting, thermoelectric and photovoltaic solar cells [1-13]. In order to advance the GaN-based technology in general illumination applications such as automotive headlights, high external quantum efficiencies (EQE) of the nitride-based light emitting diode (LED) devices are essentially required at high operating power (high current density with >200 Acm^{-2}). Nevertheless, the EQE of InGaN-based LED device has been found to be declining when the current density is increased. Studies in recent years have pointed towards the reduction of internal quantum efficiency (IQE) at high current density as the main cause responsible for the EQE reduction of InGaN-based LED devices [3].

The reduction of IQE of the InGaN-based device at high operating current density is classified as efficiency droop. The extensive studies suggested that the efficiency droop phenomena is related to various loss mechanisms, which include carrier leakage [14-16], Auger recombination process [17-25], junction heating effects [26-28], high dislocation density [29], current crowding effect [30-31], carrier loss via indirect absorption [32], hole transport impediment [33-34] and decreased carrier localization at In-rich regions [35]. The origin of the efficiency droop cause is inconclusive, but carrier-related mechanisms such as carrier leakage and Auger recombination process are being narrowed down as the dominant reasons.

Apart from the vast discussions on the remedies [36-41] in which the efficiency droop issue still exists, the discussions on Auger recombination process are mainly focused in determining the role of Auger recombination mechanism in the efficiency droop issue as well as determining the Auger coefficient value in the semiconductor device [17-25, 42]. Most recently, Iveland and co-workers have managed to detect the Auger electron which linearly correlates with the droop current through direct measurement under electrical injection condition [25]. The finding shed the light on the role of Auger recombination process in the efficiency droop issue of the InGaN-based LED device, since it has been difficult to distinguish the loss channels through experimental

works. A determination of the Auger coefficient in the device is however not provided in the work by Iveland and co-workers. In the case of determining the Auger coefficient value, most notably the reported value of Shen and coworkers (2 x 10^{-30} cm^6s^{-1}) through photoluminescence study [17] is in huge discrepancy with the value obtained by Hader and coworkers (3.5 x 10^{-34} cm^6s^{-1}) through theoretical calculation [42]. Finding the causes that would bring the discrepancy closer is an important step towards addressing the original cause of the efficiency droop issue in the InGaN LEDs.

In this work, we focus in the Auger recombination model concerning the direct band Auger processes. Two separate analysis have been performed for investigating the interband Auger process in InGaN and investigating the intraband Auger process that includes realistic interface in the InGaN semiconductor. For the analysis of the interband Auger recombination, the theoretical model with closed-form analytical expressions were developed and presented. For the analysis of the intraband Auger process involving realistic interface, the calculation approach by taking into account the interface roughness and the numerical formulation of the Auger coefficient were developed and presented. In addition, the possible ways to suppress the Auger process based on the analysis were discussed.

4.1. Auger Recombination Processes and the Role of Auger

4.1.1. Direct Auger Recombination Processes – Interband and Intraband

The band-to-band Auger recombination processes are classified into intraband and interband Auger processes according to the related bands. The intraband Auger process has been well studied, and it has been found to have insignificant effect on large band gap semiconductor alloys, which should apply for visible-light emitters (around the region of 2-3 eV band gap) [23]. However there is a huge discrepancy between theoretically calculated [42] and experimentally estimated [17] Auger recombination coefficient values (ranging from 10^{-34} cm^6s^{-1} to 10^{-30} cm^6s^{-1}) in the InGaN alloy. On the other hand, the interband Auger process involving second upper conduction band is recently suggested to contribute considerably in the droop for green-emitting InGaN

quantum wells [18]. In contrast to intraband Auger process, interband Auger process is comparably less studied and the literature available through the published manuscripts are severely limited up to present [18-23, 43]. It is thus important and also interesting to elucidate the physics behind the interband Auger recombination mechanism.

For intraband Auger recombination process, the energy released from the recombination between an electron and a hole is transferred to another carrier resulting in excitation of the carrier into a higher-energy state, as illustrated in figure 4-1(a). For the interband Auger recombination process, the carrier receiving the energy is excited to the second conduction band instead of the higher-energy state in the first conduction band, as illustrated in figure 4-1(b). In both cases, non-radiative recombination processes occurred under the energy and momentum conservation conditions.

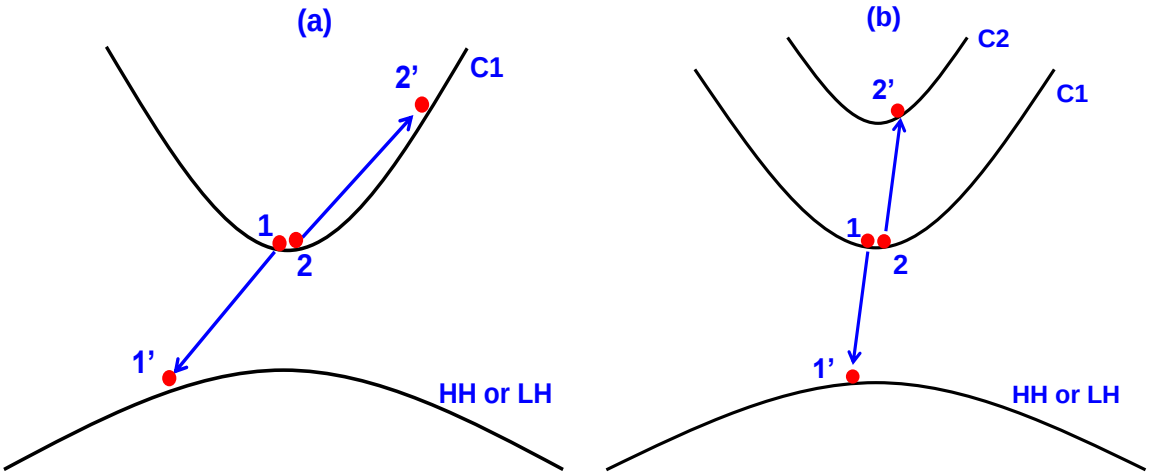

Figure 4-1: *Illustration of (a) CHCC2 Auger recombination process involving heavy hole (HH) and two conduction bands. The valence band can also be light hole band (LH). (b)CHSH Auger recombination process involving two valence bands, one conduction band and one split-off band (SO).*

4.1.2. Previous Work in Interband Auger Process

The interband Auger process was discussed by Delaney and co-workers on InGaN ternary alloy using first-principle density functional theory calculation to obtain the electronic structures of the alloys [18]. Building on this finding, Bertazzi and co-workers followed up the investigation on

this interband Auger process with the InGaN electronic structures obtained through nonlocal empirical pseudopotential method [19]. Both studies employed the Monte Carlo method to simulate the result, which is computational exhaustive method. While the works are completed based on InGaN material, Heinemann and co-workers carried out Monte Carlo simulation of interband Auger recombination on a different material which is ZnMgO ternary alloy by using first-principle approach for band structure information [43]. All the studies have demonstrated that when the energy band gap is equal or close to the interband separation energy (energy difference between the first and second conduction band at gamma-point) of the understudied ternary alloy, Auger resonance occurs leading to large Auger coefficient of the ternary alloy.

Although the finding on the interband Auger process in InGaN-based alloy is interesting, significant computational efforts are required to obtain the calculated results. This elaborate computational resource is required for Auger coefficient calculation attributed to the use of Monte Carlo simulation method which requires huge calculation time [18]. In other words, it is not feasible to perform Monte Carlo simulations on all under-test semiconductor materials in a remarkably short period. In contrast, analytical solutions can be used to address this issue while providing physical intuitive insight of the particular Auger process. Hence a closed-form analytical expression without any integral involved is highly desirable to carry out the Auger rate calculations in an efficient and fast way.

4.2. Analytical Solution Development for Interband Auger Process

The development of the close-form expression for interband Auger recombination rate will be presented in this section. In general, the Auger recombination rate can be obtained by the following expression [44-45]:

$$R_{Auger} = 2\frac{2\pi}{\hbar}\left(\frac{V}{8\pi^3}\right)^3 \int\int\int\int \left|M_{1,1',2,2'}\right|^2 P_{1,1',2,2'} x\delta(E_{sum}) x\delta\left(\vec{k}_{sum}\right) d\vec{k}_1 d\vec{k}_{1'} d\vec{k}_2 d\vec{k}_{2'} \quad (4.1),$$

where the states 1 and 2 are for electrons in the first conduction band, the state 1' is for a heavy hole in the valence band, the state 2' is for an electron in the second upper conduction band. The E_{sum} and $\vec{k}_{sum}$ stand for $E_{1'} + E_{2'} - E_1 - E_2$ and $\vec{k}_{1'} + \vec{k}_{2'} - \vec{k}_1 - \vec{k}_2$ (k-selection rule),

respectively. The probability factor $P_{1,1',2,2'}$ is the term that accounts for the occupation probabilities of the carriers and $M_{1,1',2,2'}$ is the Auger matrix element.

As shown in figure 4-1(b), the interband Auger process involves two conduction bands and one valence band. The valence band can be either heavy hole band or light hole band. Due to the energy and momentum conservation, when an electron in the first upper conduction band recombines with a hole from valence band, the energy is transferred to a random electron in the first upper conduction band. This electron which receives the energy will then be excited into second upper conduction band. Intuitively this process is similar to CHSH process, which is a process involving the conduction band, heavy hole / light hole band, and the split-off band.

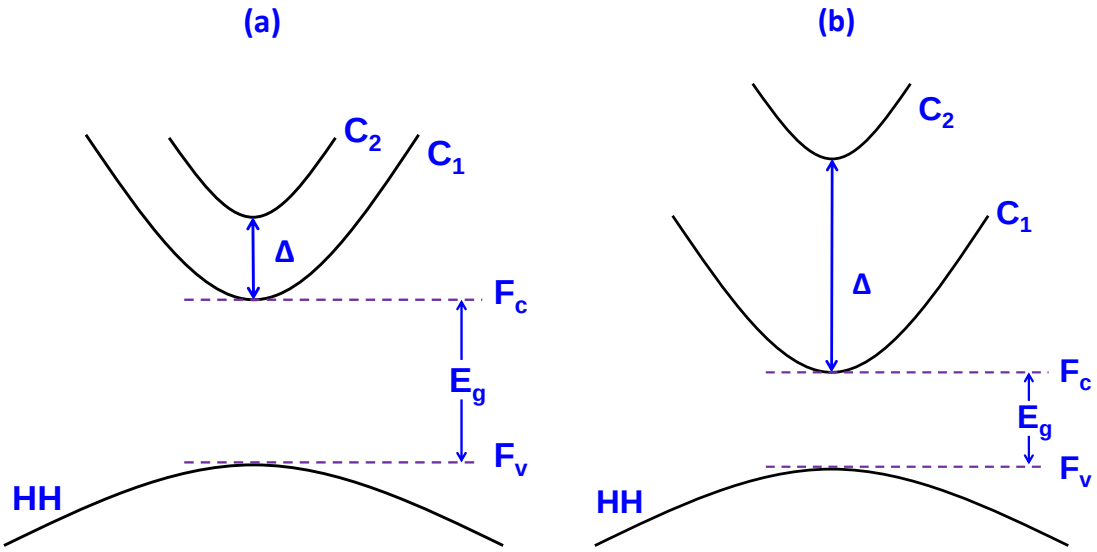

Figure 4-2: *Illustration of the energy conditions resulted from momentum and energy conservation laws, where (a) $E_g > \Delta$ condition and (b) $E_g < \Delta$ condition. F_c and F_v are meant for lowest conduction band level and uppermost valence band level, while E_g is the difference between F_c and F_v.*

The similarity between CHCC2 and CHSH process is presented in the energy conditions existing in the process. The parameter Δ is the separation energy between first conduction band and second conduction band, while the parameter E_g refers to the energy band gap (energy difference between valence band and conduction band). Under the restriction of momentum and energy conservation, this will lead to two energy conditions of interest in the context of interband

Auger analysis, as presented in figure 4-2. The two energy conditions include the energy range for $E_g > \Delta$ [figure 4-2(a)] and $E_g < \Delta$ [figure 4-2(b)] conditions. When the Δ energy is larger than the energy band gap, the energy transferred from the recombination energy to an electron in first conduction band is insufficient to excite the electron to second conduction band. The threshold energy is literally zero and the energy conservation condition is not satisfied. However, in the case when the energy band gap is larger than the Δ energy, the momentum and energy conservation rules are satisfied and a certain threshold energy to excite the electron comes into play. The derivation of the threshold energy for CHCC2 process starts from the momentum and energy conservation law, which is shown below.

For the CHCC2 process in figure 4-1(b), the momentum and energy conservation relations can be expressed as follow [46]:

$$\vec{k}_1 + \vec{k}_2 = \vec{k}_3 + \vec{k}_4 \quad (4.2),$$

$$\Delta E_4 - (E_g - \Delta) = \Delta E_1 + \Delta E_2 + \Delta E_3 \quad (4.3),$$

where $\vec{k}$ is the wave vector and E is the energy. Note that E_v is set as the reference energy level in the analysis presented here. Two new variables are introduced to represent the m_c, m_h and m_{c2}, shown as

$$u_h = \frac{m_c}{m_h} \ , u_{c2} = \frac{m_c}{m_{c2}} \quad (4.4).$$

By following along the outlined procedures [46], in which the most probably transition corresponds to the minimum possible energy of state 4, the minimum energy for ΔE_4 (threshold energy) is expressed as

$$E_t \equiv \Delta E_4 = \left(\frac{m_h + 2m_c}{m_h + 2m_c - m_{c2}}\right).\left(E_g - \Delta\right) \quad (4.5).$$

The threshold energy derivations have shown that the effect of band effective mass needs to be considered in CHCC2 process. Besides, it also proves that the threshold energy expressions for CHCC2 and CHHS process are indeed similar, with only notations of effective mass change from m_s to m_{c2}, m_c to m_h and vice versa.

The expression presented earlier is meaningful but the analytical expression for interband Auger recombination coefficient is yet to be sorted out, which is needed to calculate the interband Auger coefficient in a semiconductor alloy. Thus, the derivation of the interband Auger recombination coefficient will be presented starting from equation (4.1). Based on the interband Auger process, the basic relations for the interband Auger recombination coefficient are first defined. Non-degenerate carrier densities and parabolic energy bands are considered in the calculation. The matrix elements of the electron-electron interaction consists of Coulomb term and can be evaluated in the following expression [44]:

$$|M|^2 = \frac{4\beta}{\varepsilon^2}\left(\frac{4\pi q^2}{V}\right)^2 \left|\frac{F_{1'1}F_{2'2}}{\left(\vec{k}_{1'}-\vec{k}_1\right)^2+\lambda^2}\right|^2 \quad (4.6),$$

where the parameter F are overlap integrals of the wave functions in the aforementioned states and β $(1 \leq \beta \leq 2)$ takes into account the contribution of the exchange term, the parameter λ is the Debye screening wavenumber, the parameter ε is the static dielectric constant, and the q is the electric charge. In the Boltzmann approximation for the non-degenerate semiconductor systems, the statistical factor can be written as [47]

$$P = \frac{p}{\bar{p}}\left(\frac{np}{n_0 p_0}-1\right)e^{\frac{E_2-E_v}{k_b T}} \;, \bar{p} = \frac{1}{4}\left(\frac{2m_v k_b T}{\pi\hbar^2}\right)^{\frac{3}{2}} \quad (4.7),$$

where n and p are the electron and hole densities while n_0 and p_0 are the equilibrium values. k_b is the Boltzmann constant and T is the temperature.

In order to obtain the expression for Auger coefficient, first the relation between the Auger lifetime and Auger coefficient is defined as [44]:

$$\frac{p-p_0}{\tau} = \frac{R}{V} \quad (4.8),$$

$$\frac{1}{\tau} = C{p_0}^2 \quad (4.9),$$

where τ is the Auger lifetime. By combining equation (4.8) and equation (4.9) and ${p_0}^2(p-p_0) \approx p(np-n_0p_0)$, the Auger relation between Auger recombination rate and Auger coefficient is found as,

$$R = p(np-n_0p_0)CV \quad (4.10).$$

By substituting equation (4.6), equation (4.7) and equation (4.10) into equation (4.1), the Auger recombination coefficient equation is obtained, as shown in the following:

$$C = \frac{\hbar^{12} q^4 \beta f_{CH} f_{CC2}}{2\varepsilon^2 {m_0}^2 \left|E_{1'} - E_1\right|^2 \left(2\pi {m_v}^2 m_h {k_b}^3 T^3\right)^{\frac{3}{2}}} \times \exp\left(\frac{E_g - \Delta}{k_b T}\right) \times H \quad (4.11),$$

$$H = \int exp\left(\frac{E_2 - E_v + \Delta}{k_b T}\right) \delta(E_{1'} + E_{2'} - E_1 - E_2) \delta\left(\vec{k}_{1'} + \vec{k}_{2'} - \vec{k}_1 - \vec{k}_2\right) d\vec{k}_1 d\vec{k}_2 d\vec{k}_{1'} d\vec{k}_{2'} \quad (4.12),$$

where H is the integral that requires huge calculation time due to the twelvefold integral required in the calculation, f is the oscillator strength, ħ is the reduced Planck constant, m_v is the valence band effective mass and m_0 is the free electron effective mass.

The H integral needs to be evaluated in order to obtain the expression for interband Auger coefficient. The discussion here follows the treatment developed in Ref. 44. Starting from equation (4.12) by considering the elimination of integration of $\vec{k}_{2'}$ through wave vector δ-function in which $\vec{k}_{2'} = \vec{k}_1 + \vec{k}_2 - \vec{k}_{1'}$ and by defining parabolic energy relation as shown below,

$$E_1 = E_c + \alpha {k_1}^2,\ E_2 = E_v - \Delta - \mu_s \alpha {k_2}^2,\ E'_{1,2} = E_v - \mu_H \alpha {k'_{1,2}}^2 \quad (4.13),$$

$$\alpha = \frac{\hbar^2}{2m_H}, \mu_s = \frac{m_H}{m_{c2}}, \mu_H = \frac{m_H}{m_c} \quad (4.14),$$

the H integral can be simplified as

$$H = \int e^{-\frac{\mu_s \alpha {k_2}^2}{k_B T}} \delta\left[\alpha(-h - \mu_H {k_{1'}}^2 - {k_1}^2 + \mu_s {k_2}^2 - \mu_H\left(\vec{k}_1 + \vec{k}_2 - \vec{k}_{1'}\right)^2\right] d\vec{k}_1 d\vec{k}_2 d\vec{k}_{1'} \quad (4.15),$$

$$h = \frac{E_g - \Delta}{\alpha} \quad (4.16).$$

Further simplifications of H integral can be obtained by using definition of $\vec{k} = \vec{k}_1 - \vec{k}_{1'}$, and transformation of the spherical coordinates of $\vec{k}$, $\vec{k}_1$ and $\vec{k}_2$. The introduction of several substitution variables and step functions [44] into the H integral of equation (4.12) thus leads to the expression of

$$H = \frac{2\pi^4 \hbar^2}{\alpha[\mu_H(2+\mu_H)]^{\frac{3}{2}}} \int e^{-a{k_2}^2} \left(\frac{{k_2}^6}{K^2} - 2\frac{{k_2}^4}{K} + {k_2}^2\right) dk_2 \quad (4.17).$$

Note that a and K in equation (4.17) has the dependency on the effective mass of the conduction and valence bands in which the definitions of a and K are given as

$$a = \frac{\mu_s \alpha}{k_B T}, K = \frac{2+\mu_H}{\mu_s(2+\mu_H)-\mu_H} h \quad (4.18).$$

As shown in equation (4.17), the H integral is still dependent on k_2 in which the dependence on k_2 can be further simplified through asymptotic expansion incomplete Γ-function [44]. In the case of $E_g > \Delta$ condition, the boundaries are set to be K and ∞. As a result of the asymptotic expansion of the Γ-function for equation (4.17), the H integral can then be found as

$$H = \frac{2\pi^4 \hbar^2}{\alpha[\mu_H(2+\mu_H)]^{\frac{3}{2}}} . \frac{1}{a^3 K^{\frac{3}{2}}} e^{-aK} \quad (4.19).$$

In the case of $E_g < \Delta$ condition, the boundary of the integral in equation (4.17) is 0 and ∞. As a result, the H integral can be given as

$$H = \frac{\pi^{\frac{9}{2}} \hbar^2 a^{-\frac{3}{2}}}{2\alpha[\mu_H(2+\mu_H)]^{\frac{3}{2}}} \left\{ \frac{15}{4} \frac{1}{a^2 K^2} - \frac{3}{aK} + 1 \right\} \quad (4.20).$$

In order to provide a brief explanation of the derivation of the Auger coefficient value, figure 4-3 presents the flowchart of the outline of the derivation. Firstly, the basic relations of matrix element, statistical factor and non-degenerate carrier densities are defined. The equation (4.1) is simplified using the definitions presented earlier, and the equation (4.11) with leftover H integral is obtained. The k-vector components in the H integral are transformed into scalar-k component using spherical coordinates. Several substitution variables are then being introduced into the derivation to simplify the angle integration resulted from the spherical coordinate transformation in the H integral. Finally, by setting up the boundary conditions of the energy conditions described earlier, the analytical expressions for interband Auger recombination coefficient are obtained for both energy conditions.

As a result from the derivations shown above, the interband Auger recombination coefficient is given followed in the case of $E_g > \Delta$:

$$C = \frac{f_{CH} f_{CC2}}{{m_0}^2 \varepsilon^2} \frac{8\hbar^3 \pi^{\frac{5}{3}} q^4}{E_g \Delta} \frac{\sqrt{E_g - \Delta}}{(k_b T)^{\frac{3}{2}}} \left(\frac{m_c}{m_h}\right)^3 \left(\frac{m_{c2}(2m_c + m_h - m_{c2})}{(2m_c + m_h)^2}\right)^{\frac{3}{2}} \times exp\left[-\frac{m_{c2}}{2m_c + m_h - m_{c2}} \frac{E_g - \Delta}{k_b T}\right] \quad (4.21).$$

In the case of $E_g < \Delta$, the interband Auger recombination coefficient is given in the following expression:

$$C = \frac{f_{CH} f_{CC2}}{{m_0}^2 \varepsilon^2} \frac{2\hbar^3 \pi^3 q^4}{E_g \Delta} \frac{(\Delta - E_g)^2}{(k_b T)^3} \left(\frac{m_c}{m_h}\right)^3 \left(\frac{m_{c2}}{2m_c + m_h}\right)^{\frac{3}{2}} \left\{1 + \frac{3\mu k_b T}{\Delta - E_g} + \frac{15}{4}\left(\frac{\mu k_b T}{\Delta - E_g}\right)^2\right\} \times exp\left[-\frac{\Delta - E_g}{k_b T}\right] \quad (4.22),$$

$$\mu = \frac{2m_c + m_h - m_{c2}}{2m_c + m_h} \quad (4.23).$$

The above equations are in agreement with the finding just from the threshold energy expression. In the case for $E_g < \Delta$ condition, both the momentum and energy conservation rules have restricted the successful excitation of an electron from first conduction band into second conduction band. In the case for $E_g > \Delta$ condition, threshold energy exists and band effective masses affect the threshold energy, so as the interband Auger recombination coefficient. This justifies the physical explanation of the two energy conditions suggested earlier. A more fascinating thought from the expressions is that when the energy band gap is equal to the Δ energy, the interband Auger recombination coefficient reaches the peak value leading to the interband Auger resonance phenomena.

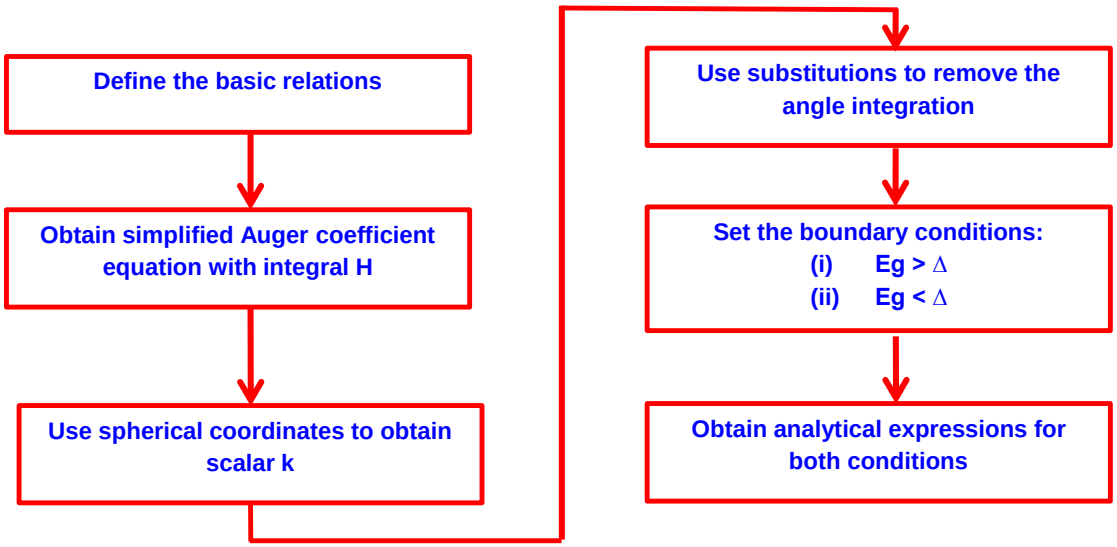

Figure 4-3: *Flow chart of the outline procedure for the interband Auger calculation.*

4.3. Interband Auger Recombination Analysis for InGaN Alloy

In this section, the interband Auger recombination coefficients of technologically important semiconductor materials are determined by using interband Auger recombination coefficient expressions developed in section 4.2. Based on the interband Auger coefficient expressions, the

band parameters of the semiconductor materials are required to calculate the interband Auger recombination coefficient of the materials.

The information of semiconductor materials that are available from published literature regarding to interband Auger recombination CHCC2 process are InGaN alloys [18-19, 22-23] and ZnMgO alloys [43]. Hence, InGaN alloys and ZnMgO alloys are used as the materials for our interband Auger coefficient calculation and for the purpose of our result comparison with published works.

Ternary alloy ($A_xB_{1-x}C$)	InGaN	ZnMgO	GaN	InN
Alloy composition x	0.148	0.5		
E_g (eV)	2.80	4.64	3.24	0.69
Δ (eV)	2.90	5.00	2.50	3.12
m_e (m_0)	0.155	0.544	0.183	0.102
m_{hh} (m_0)	1.523	2.325	1.713	1.331
m_{lh} (m_0)	0.449	0.656	0.586	0.347
m_{c2} (m_0)	0.722	0.925	0.501	0.680

Table 4-1: *Band parameters extracted from available band structures for GaN, InN, InGaN and ZnMgO ternary alloys.*

Table 4-1 displays the band parameters, as well as the energy band gap and the interband separation energy of the $In_{14.8}Ga_{85.2}N$ and $Zn_{0.5}Mg_{0.5}O$ alloys. The energy band gap value is obtained by taking the energy difference between the valence band maximum and the conduction band minimum, while delta energy (Δ) is obtained by taking the energy difference between the first and second conduction bands from alloy band structures at gamma symmetry point in Brillouin Zone. The parabolic line fitting method is used to extract the effective mass parameters from the alloy band structures [43].

Figure 4-4 shows the interband Auger coefficient values for $In_{14.8}Ga_{85.2}N$ and $Zn_{0.5}Mg_{0.5}O$ alloys. For the $In_{14.8}Ga_{85.2}N$ alloy, the calculated result of the interband Auger recombination coefficient is 3.13×10^{-30} cm^6s^{-1}, while the available published Auger coefficient values ranged from 1×10^{-29} cm^6s^{-1} to 1×10^{-32} cm^6s^{-1} [18-19, 22]. Our result falls within the range of reported values, similar to the results obtained by Delaney et al [18] and Hatakoshi et al [22].

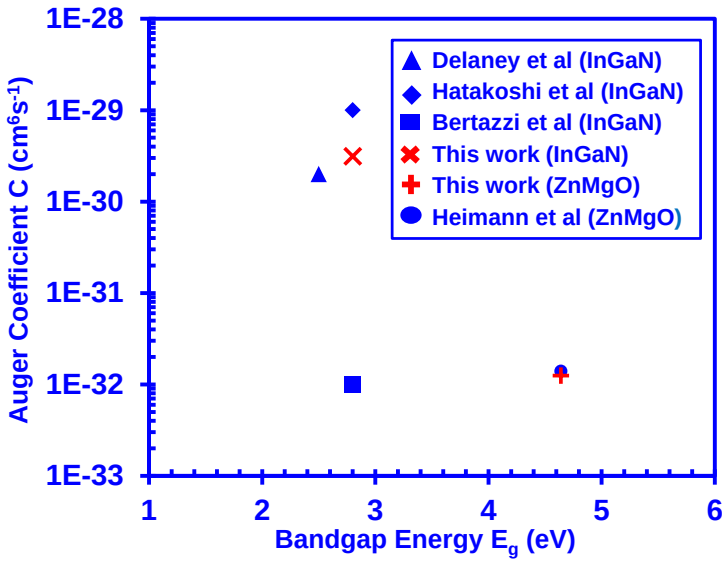

Figure 4-4: *Interband Auger coefficient values from calculation and reported literature of InGaN alloy and ZnMgO alloy. Note that the results from Ref. 19 and Ref. 22 include conventional intraband Auger recombination for the InGaN alloys.*

The results reported in Ref. 19 and Ref. 22 have considered intraband Auger recombination mechanism and interband Auger recombination processes, but intraband Auger recombination is known to be negligible in the InGaN alloys [18], which means that the interband Auger recombination is the dominant mechanism in the reported result. Note that the position of the Auger interband peak coefficient value in Ref. 18 is different from this work. The discrepancy is primarily due to the difference in the energy band gap of the InGaN alloys, in which E_g = 2.8 eV in the present work while E_g = 2.5 eV in Delaney work. In addition, different methods were used to calculate the InGaN alloy band structures, resulting in relatively different band parameters which possibly leads to discrepancy in the interband Auger coefficient values. On the other hand, as shown in figure 4-4, the calculated interband Auger coefficient for ZnMgO alloy is 1.25 x 10^{-32} cm^6s^{-1} which agrees considerably well with the result reported by Heinemann and co-workers [43].

4.3.1. Effect of Band Parameters on Interband Auger in InGaN

Previously, the study performed by Sugimura suggested that the most sensitive parameter for the Auger recombination coefficient in CHSH process is the exponential form in the Auger

coefficient expression [48]. Intuitively the same applies for CHCC2 and CLCC2 interband Auger processes since these two processes are similar in regards to the CHSH process. As a result, the exponential form consisting of energy band gap and Δ energy of an alloy plays a primary role in determining the interband Auger coefficient for both $E_g > \Delta$ and $\Delta > E_g$ energy conditions.

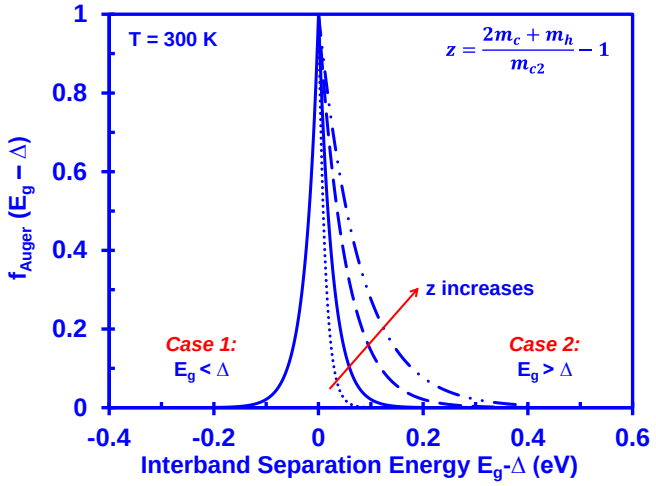

Figure 4-5: *Auger function as a function of interband separation energy. Two energy conditions are taken into account and z (a function of effective mass) is important as a tuning factor for the upper limit of interband separation energy range.*

A simple analytical function is presented in Figure 4-5 as a function of interband separation energy. The analytical function is introduced as a Auger function model. The dominant factor determining the Auger coefficient is the exponential term of interband separation energy. Since the Auger function model is directly proportional to the exponential term of interband separation energy, the interband Auger coefficient is also directly proportional to the Auger function model. Under the $E_g < \Delta$ condition, the carrier effective masses are excluded from the expression and hence the Auger function is proportional to the exponential term of $[-(\Delta-E_g)/kT]$. For the case of $E_g > \Delta$ condition, the Auger function is proportional to the exponential term of $[-(E_g-\Delta)/zkT]$. The parameter k and T correspond to the Boltzmann constant and temperature (T = 300K) respectively. The parameter z refers to an effective mass expression that is given as follow:

$$z = \frac{2m_c+m_h}{m_{c2}} - 1 \tag{4.24}$$

The above expression shows that the changes in effective masses value of a semiconductor alloy have secondary effect on the Auger function, and ultimately the interband Auger

recombination rate. For instance, if the hole effective mass increases in the InGaN alloy, the hole band will be modified leading to a smaller band curvature which is likely to allow additional carrier transitions to occur due to energy and momentum conservation rule. As such there is a slightly different exponential decaying function in the Auger function that results in higher interband Auger recombination rate which can be seen through the changes in parameter z in figure 4-5. In other words, the carrier effective masses also play as a tuning factor to determine the upper limit of the resonant energy condition, implying the amount of interband separation energy that can be allowed to result in the interband Auger recombination resonance. It is important to note that the changes in second conduction band effective mass also have secondary effect on the Auger function, and thus the interband Auger recombination rate. The information on the second conduction band effective mass is unavailable in the literature and more in-depth research is necessary to harness the required data.

Nevertheless, this is only an approach to provide quick intuitive explanation of how the interband Auger coefficient will change with regards to the interband separation energy. In order to examine the effect of interband separation energy on Auger coefficient value at whole composition range of a material, as mentioned earlier, the material parameters of each composition have to be known. Since not all band structures at each alloy composition are presented in the literature, approximations utilizing the band parameters in binary alloys can be used to determine the band parameters of ternary alloys for interband Auger coefficient calculations. InGaN ternary alloy is used as the example. The approximations are made as following. The energy band gap is extrapolated using Vegard's law with bowing parameter set at 2.5 eV. Linear interpolation is used to obtain Δ value of GaN and InN alloys. The effective mass parameters of GaN and InN are extrapolated using the virtual crystal approximation equation [45]. The information of the GaN and InN alloy listed in Table 4-1 are extracted from Delaney band structures [18]. The parameter data extraction method was described in section 4.3.

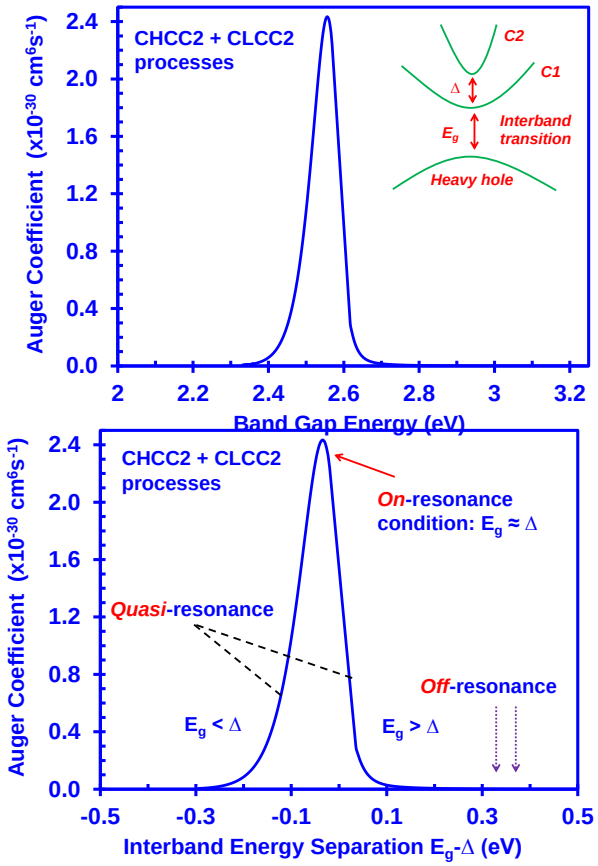

Figure 4-6: *Auger coefficient as a function of (a) band gap energy and (b) interband energy separation.*

Figure 4-6(a) and figure 4-6(b) present the interband Auger coefficient value as a function of band gap energy and interband separation energy respectively. The calculated Auger recombination values agree reasonably with the result reported by Delaney and coworkers [18]. As shown in figure 4-6(a), the interband Auger peak reaches 2.4 x 10^{-30} cm^6s^{-1} at 2.55 eV which is similar as compared to the interband Auger peak of 1.2 x 10^{-30} cm^6s^{-1} at 2.5 eV [18]. Figure 7(b) shows the interband Auger coefficient result as a function of interband energy separation (E_g-Δ). As shown in figure 4-6(b), the result exhibits similar characteristics as shown in the simple model presented earlier in this section indicating that the most sensitive parameter in the interband Auger recombination is the exponential form of interband energy separation.

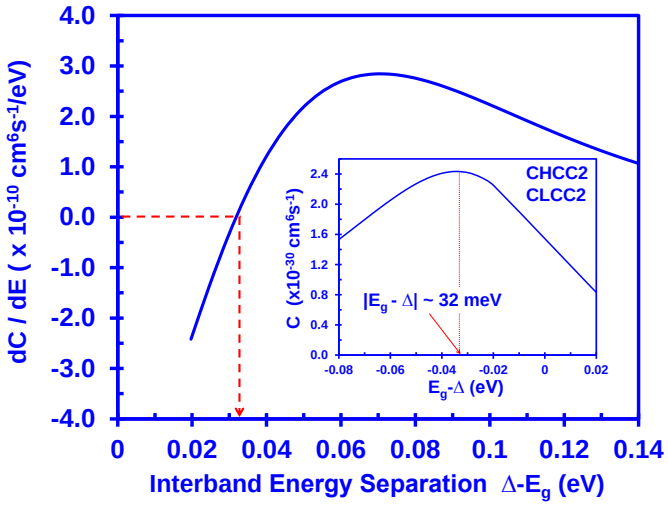

Figure 4-7: *Differentiation of the interband Auger coefficient with energy as a function of interband energy separation Δ-E_g. It shows that the Auger resonance occurs at a small corrected energy difference.*

In addition, as shown in figure 4-7, by setting dC/dE as zero, the interband Auger peak is achieved when the interband separation energy is equal to roughly 1.25 times of thermal energy (25.6 meV) at room temperature. The finding can be explained that when energy band gap is close to the Δ energy, the existence of thermionic energy contributes to the carrier excitation leading to successful interband Auger recombination process under energy conservation condition. The approximations that have been made in the interband Auger calculations would also possibly contribute as part of the explanations in the findings. Further analysis on the interband Auger recombination calculations in semiconductor alloy will be required to provide a more complete understanding of the finding shown in figure 4-7.

4.3.2. Methods to Suppress the Interband Auger Process in Semiconductor

Interband Auger recombination is an undesirable carrier mechanism existing in a semiconductor alloy which hinders the performance of the devices utilizing the alloys, provided that the resonance energy conditions are satisfied. As such, the interband Auger coefficient of a semiconductor alloy ought to be kept as small as possible. For visible light emitting devices utilizing InGaN alloys, interband Auger coefficient value in the magnitude of 10^{-30} cm^6s^{-1} is detrimental to the device performance at high current density [17]. Based on the analysis

provided in earlier sections, several approaches are suggested as the possible measures to reduce the interband Auger coefficient value of InGaN alloy.

First, interband separation energy as the most sensitive parameter in the interband Auger recombination needs to be kept larger than 0.15 eV in a semiconductor alloy such as InGaN alloy to avoid the resonance energy condition. Moving second conduction band further away from the first conduction band of the alloy to provide larger Δ value has been briefly discussed by Delaney and co-workers for nitride alloys which include using the zinc-blend phase nitrides, strain engineering the band structure and tuning the AlInGaN alloy compositions [18]. Here in figure 4-8, an analysis of how changing the Δ value would affect the interband Auger coefficient value of InGaN ternary alloy is presented. An increment of Δ energy value of roughly 150 meV from 2.85 eV to 3 eV leads to 60 times reduction in the interband Auger coefficient value of InGaN alloy, thus suppressing the interband Auger coefficient value of InGaN alloy by more than one order of magnitude.

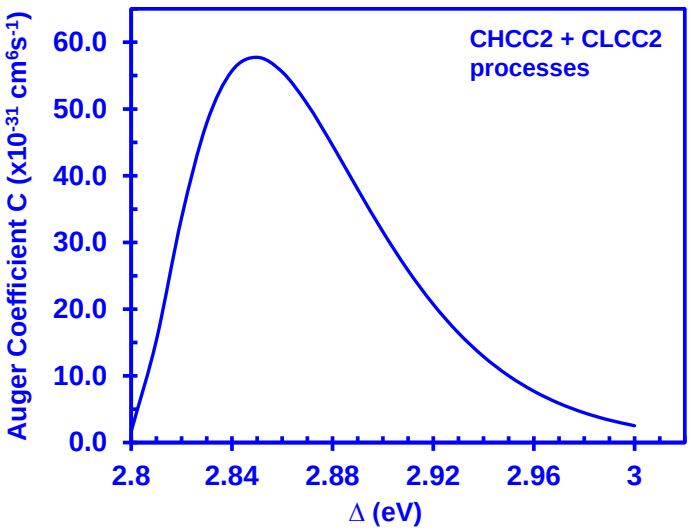

Figure 4-8: *Interband Auger coefficient as a function of Δ energy. The tuning of Δ energy value results in the different interband Auger coefficient value.*

In addition, an alternative way is to employ novel media to achieve visible light emission which is the dilute arsenic (As) GaNAs ternary alloy. Most studies were focused on dilute-nitride GaNAs ternary alloy [50-56], and the study on the dilute-arsenic GaNAs is still on its early stage [7, 57-60]. A recent study based on first principle approach showed that dilute-As GaNAs ternary

alloy has the potential to be used as a green-emitting device while having a large interband separation energy (>0.5 eV) [60]. This suggests that dilute-As GaNAs ternary alloy possibly has lower interband Auger coefficient compared to InGaN ternary alloy.

Second, the effective mass of a semiconductor alloy plays an important role in determining the interband Auger coefficient of the alloy. Thus it is important to modify the alloy effective mass in order to reduce the interband Auger coefficient. Strain engineering semiconductor alloy band structure is a method that has been extensively studied [61-70], especially in the laser applications [61-64]. Strain engineering method can be implemented through internal strain [65] or external pressure [66] onto the alloy. The studies based on equibiaxial strain tuning onto a semiconductor alloy showed the significant band structure changes in the alloy such as silicon [67] and GaN [68-69] alloys, which leads to modification in the effective mass. In particular, the first-principle calculations of the study in GaN alloy showed that the second conduction band is heavily modified under the equibiaxial strain effect [68-69]. This means that if the right amount of strain is induced, the effective mass of conduction and valence bands can be modified accordingly to suppress the interband Auger coefficient of the InGaN alloy.

Furthermore, quantum confinement can be incorporated to modify the conduction or valence effective mass. Few studies have been carried out to determine the effect of quantum confinement that is quantum well on the conduction effective mass [56, 70-71] and the hole effective mass [72]. The in-plane conduction effective mass was found to increase when the well width decreases in the InGaAs/InP quantum well [70] and GaAsN/GaAs quantum well [56]. Note that the information regarding to the change of C2 band effective mass as a function of the well width is still unavailable through literature. For the hole effective mass, it decreases when the well width decreases [72].

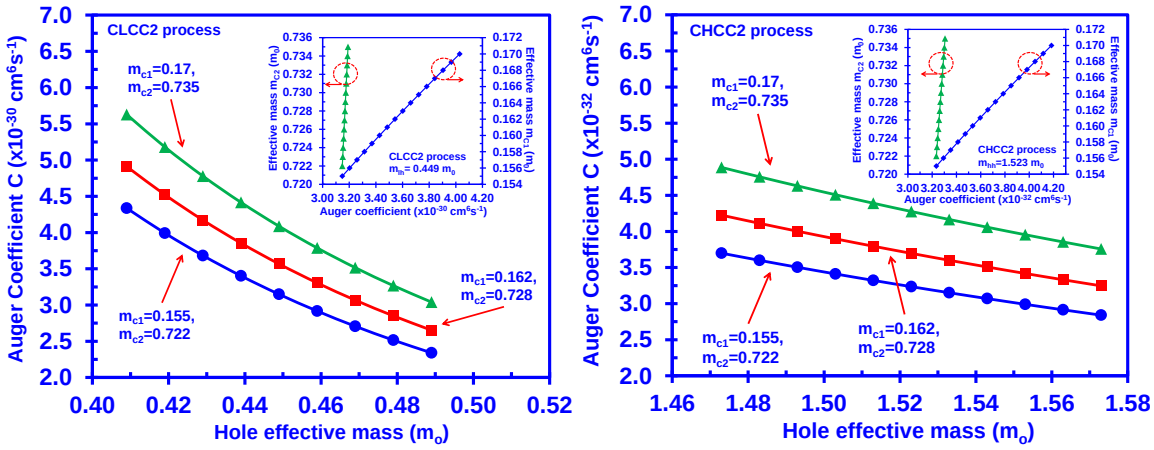

Figure 4-9: *(a) Auger coefficient value of CLCC2 Auger process as a function of light hole effective mass. Figure subset is Auger coefficient value of CLCC2 Auger process as a function of C1 and C2 band effective mass. (b) Auger coefficient value of CHCC2 Auger process as a function of heavy hole effective mass. Figure subset is Auger coefficient value of CHCC2 Auger process as a function of C1 and C2 band effective mass.*

While the carrier effective mass of a semiconductor alloy can be modified to change the interband Auger coefficient, it is important to provide the understanding on the effect of effective mass on the interband Auger coefficient. Figure 4-9(a) and 4-9(b) present the interband Auger coefficient of CHCC2 and CLCC2 processes respectively when there is an increment of conduction band effective mass or a reduction of valence band effective mass. InGaN alloy is used as an example in both figures. Note that the interband Auger coefficient result in figure 10 is calculated based on the case of $E_g < \Delta$ condition since the energy band gap value of InGaN alloy in our example is smaller than the Δ energy in the InGaN alloy, as shown in Table 4-1. In figure 4-9(a), the interband Auger coefficient of the InGaN alloy reduces from 4.34 x 10^{-30} cm^6s^{-1} to 2.34 x 10^{-30} cm^6s^{-1} when the hole effective mass increases from 0.41 m_0 to 0.49 m_0 with m_{c1} set at 0.155 m_0 and m_{c2} set at 0.722 m_0. The reduction rate of interband Auger coefficient as a function of hole effective mass is similar when m_{c1} increases from 0.155 m_0 to 0.17 m_0 and m_{c2} increases from 0.722 m_0 to 0.735 m_0. The figure subset in figure 4-9(a) shows that the interband Auger coefficient of the InGaN alloy increases from 3.15 x 10^{-30} cm^6s^{-1} to 4.03 x 10^{-30} cm^6s^{-1} when m_{c1} increases from 0.155 m_0 to 0.17 m_0. The interband Auger coefficient of the InGaN alloy increases

slightly from 3.15 x 10^{-30} cm^6s^{-1} to 3.19 x 10^{-30} cm^6s^{-1} when m_{c2} increases from 0.722 m_0 to 0.735 m_0. Similar trend can be observed in figure 4-9(b) for CHCC2 process for InGaN alloy.

In overall, the results from figures 4-9 have shown that the increment of conduction band effective mass of either first or second conduction band will result in the increment of the interband Auger coefficient in the InGaN alloy. In the opposite, the increment of hole effective mass leads to the reduction in the interband Auger coefficient value of the InGaN alloy. It is important to note that the analytical solution is developed for calculation of the interband Auger coefficient in bulk material rather than quantum well. Thus the result presented in figure 4-9(a) and figure 4-9(b) only indicates that the quantum confinement such as quantum well can be used to modify the band effective mass and consequently the interband Auger coefficient of semiconductor alloy. Further analysis of interband Auger coefficient in a quantum well are required to clarify the effect of quantum well thickness and effective mass on the interband Auger coefficient in lower dimensional system.

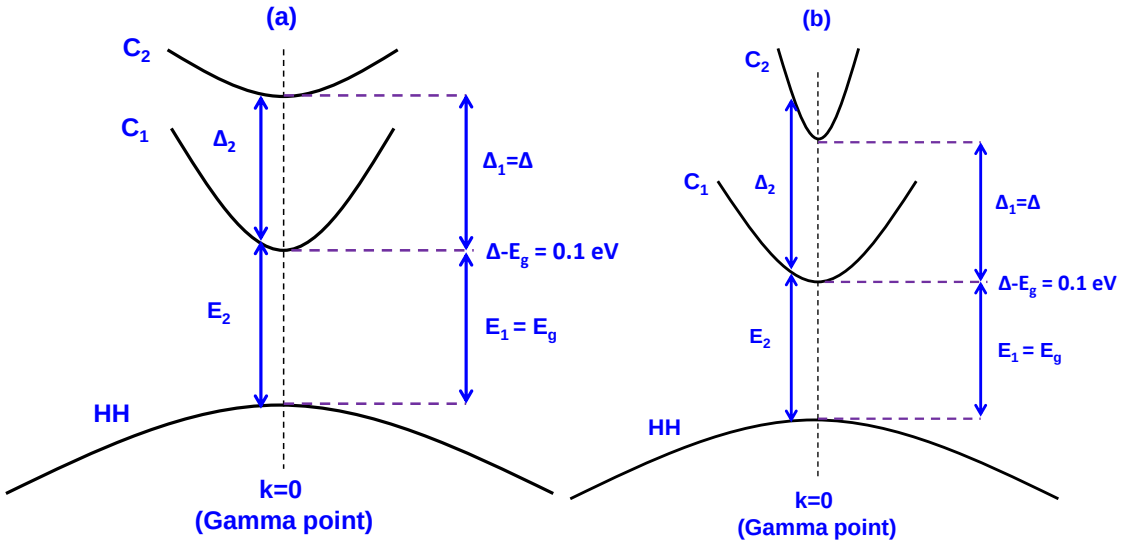

Figure 4-10: *Illustration of a band structure for the case of $E_g < \Delta$ condition ($\Delta - E_g = 0.1$ eV) in which (a) C2 band curvature is smaller than C1 band curvature and (b) C2 band curvature is larger than C1 band curvature. For case (a), when k > 0 in Brillouin Zone, Δ_2 is not necessarily larger than E_2 and thus interband Auger process could happen in this situation while satisfying the momentum and energy conservation rule. For case (b), Δ_2 will be larger than the E_2 and thus the interband Auger process is less likely to occur due to the restriction of momentum and energy conservation condition.*

It is important to note that in the case for $E_g < \Delta$ condition, the argument of the restriction of momentum and energy conservation rule on the interband Auger process holds true if the interband Auger recombination is considered only at the gamma-point in the Brillouin Zone. However if the k-wave vector is considered beyond gamma point in the Brillouin Zone and if the C2 band curvature is smaller than the C1 band curvature as shown in figure 4-10(a), the Δ_2 energy is not necessarily larger than E_2 energy and therefore the interband Auger process can occur by satisfying the momentum and energy conservation rule. On the other hand, as shown in figure 11(b), if the C2 band curvature is larger than the C1 band curvature, the Δ_2 energy will be larger than E_2 energy at k-wave vector beyond gamma point which means that the interband Auger process is less likely to occur due to the restriction of momentum and energy conservation rule.

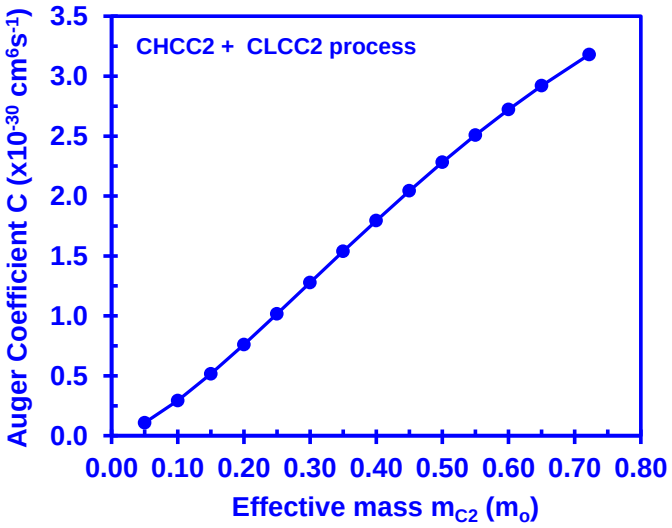

Figure 4-11: *Interband Auger coefficient of InGaN alloy as a function of C2 band effective mass.*

Figure 4-11 shows the interband Auger coefficient value of InGaN alloy as a function of C2 band effective mass. When the C2 band effective mass reduces from 0.722 m_0 to 0.01 m_0, the interband Auger coefficient value of the InGaN alloy reduces from 3.18 x 10^{-30} cm^6s^{-1} to 1 x 10^{-32} cm^6s^{-1}. Intuitively the result in figure 4-11 agrees with figure 4-10 that if the C2 band effective mass reduces (C2 band curvature increases), the interband Auger process will be less likely to occur which leads to lower interband Auger coefficient. Therefore reducing the C2 band effective

mass in semiconductor alloy is also important to suppress the interband Auger recombination process in the alloy.

4.4. Auger Recombination Theory with Interface Roughness

4.4.1. Existence of Interface Roughness in Semiconductors

Auger recombination is a fundamental nonradiative recombination process that exists in all semiconductors [73], and is theoretically determined by using the appropriate band structure and quantum states in Fermi's Golden Rule. In homogeneous, or "bulk", semiconductors Auger recombination is limited, because of conservation of energy and momentum. However, when a lower bandgap semiconductor is restricted in space by higher bandgap semiconductors (or barriers) to form quantum states, Auger recombination rates can become appreciable. The most widely used and technologically important restriction method for semiconductors is the quantum well (QW), where quantum states are formed and the density of states is reduced via layering of different bandgap semiconductors. QWs not only increase favorable carrier recombination processes such as spontaneous emission and optical gain over bulk semiconductors, but also affects Auger recombination. Understanding Auger recombination in QWs is important, particularly for QW-based optical devices, because at high carrier densities it can become the dominant (and detrimental) recombination mechanism.

Although Auger recombination has been studied extensively in various technologically important semiconductors [17-25, 42-45, 48, 73-80], the convergence of experimental and theoretical results is lacking. This discrepancy is most notable in III-nitride semiconductor alloys, and complicates their advancement in important applications such as solid-state lighting and lasers. It is now becoming clearer via experimental results that Auger recombination is present in III-nitrides [17], and causes a detrimental decrease in radiative efficiency of light-emitting diodes (LEDs) operating at high operating current densities [18]. However, this result is non-intuitive because simplified models of Auger recombination rates predict a decrease in Auger recombination rates with increased bandgap, and therefore, Auger recombination should not be a

concern in wide bandgap III-nitrides [42]. Complex theoretical studies have confirmed this simplification with calculated Auger recombination rates at much lower values when compared to experimental predictions [42]. The disconnect between theoretical and experimental results has created confusion and has hindered progress in III-nitride research.

In theoretical calculations of Auger recombination abrupt heterointerfaces are assumed between the quantum well and barrier layers [23, 24, 74-78]. However, in practice the roughness of this heterointerface is always present, in spite of advances in epitaxial crystal growth techniques such as molecular beam epitaxy (MBE) and metal organic chemical vapor deposition (MOCVD). Specifically, for GaAs QWs with AlGaAs energy barrier layers the interface roughness is one to two monolayers (3-5 Å) [81], for InGaAs/InP QW/barriers it is one to four monolayers [82], and InGaN/GaN QW/barriers it is one to six monolayers (3-18 Å) [83-84]. The variation in the InGaN QW is notable because it is considerably large when compared to the typical quantum well thickness (L_{QW}) that is in the range of 2-3 nm. Clearly, interface roughness is a feature of all semiconductor QWs, yet interface roughness is ignored in Auger recombination calculations, and is not discussed qualitatively and quantitatively. One would expect rougher interfaces will affect the quantum states and subsequently the recombination probability between states. However, it is an unknown exactly how interface roughness impacts the Auger recombination process in QWs.

The interface roughness always exists owing to the local alloy fluctuations or growth process conditions in the MOCVD or MBE. Besides, due to the polarization existence between two different materials, interfacial reconstruction will be in place leading to alloy disordering and stoichiometry change at the interface [85]. Interface roughness is detrimental to the device performance such as reducing the electron mobility of the device, which has been theoretically shown through the photoluminescence line width broadening effect [86-87]. However, the study of interface roughness on the Auger recombination process is not discussed qualitatively and quantitatively in details. Since InGaN/GaN quantum well semiconductor device has the interface roughness of at least one monolayer and efficiency droop issue possibly caused by Auger

recombination process, it is thus important to elucidate the effect of the interface roughness on the Auger recombination process in the quantum well.

In this section, we present a theoretical analysis of Auger recombination in semiconductor QWs, comparing QWs with varying degrees of interface roughness. The interface roughness is shown to play an important role, causing a large increase in the Auger recombination rate because of the additional energy states that can participate in the process. In the technologically important III-nitride semiconductors the increase can be four orders of magnitude over a QW with perfect heterointerfaces illustrating the importance of including interface roughness when calculating Auger recombination rates.

4.4.2. Development of Auger Recombination Model with Interface Roughness

Figure 4-12 schematically represents the interface roughness between the QW and barrier materials. The real interface of the two materials fluctuated around the ideal interface forming imperfections at the interface due to the intrinsic reasons (e.g. strain between materials, and alloy disorder) and extrinsic factors (e.g. growth technique, and growth condition) [88]. As illustrated in figure 4-12, by setting $z = 0$ at the ideal interface, the interface roughness can be characterized by the fluctuations of the well width $\Delta L(\lambda)$ at different lateral position λ. Note that the small imperfections are formed with different sizes at random locations resulting in variations of well width fluctuations at different positions. It is thus difficult to precisely characterize the interface roughness at each position.

In order to address the variations of the interface roughness at different positions, an average interface roughness is used to summarize the variety of interface roughness existing at the interface. The average interface roughness can be estimated by taking the root mean square of the interface roughness along the lateral direction. The expression to calculate the average interface roughness ΔL is given in equation (4.25) as following:

$$\Delta L = \sqrt{\frac{1}{\lambda_T}\int_0^{\lambda_T}[\Delta L(\lambda)]^2\, d\lambda} \qquad (4.25),$$

where λ is the lateral position, λ_T is the length of the active region, $\Delta L(\lambda)$ is the interface roughness at different lateral position λ. Since the total lateral thickness of a device structure is usually more than a few hundred angstroms [88], the average interface roughness could be effectively smaller than one monolayer depending on the material quality.

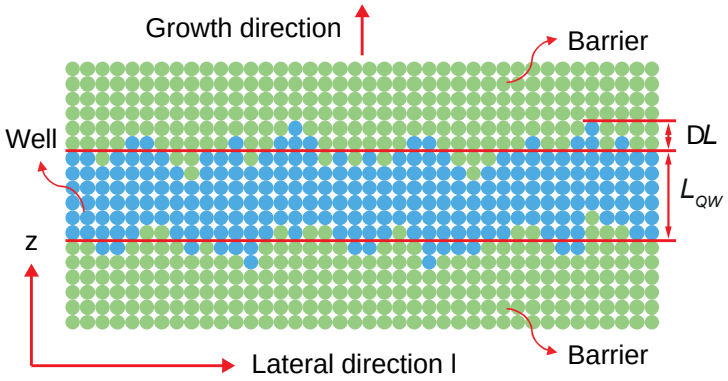

Figure 4-12: *Illustration of the interface roughness at the interface of the well and barrier. The curved line represents the rough interface while the dotted line represents the ideal interface.*

In the direct Auger recombination process (e.g. CHCC process), as described in earlier section, the energy released from recombination of an electron-hole pair is transferred to a third carrier. As a result, the carrier receiving the released energy is excited to a higher-energy final state that also satisfies conservation of energy and momentum. The Auger recombination rate R_{Auger} can be expressed as [23]:

$$R_{Auger} = 2\frac{2\pi}{\hbar}\left(\frac{A}{8\pi^3}\right)^3 \int\int\int\int \left|M_{1,1',2,2'}\right|^2 P_{1,1',2,2'} \times \delta(E_{sum}) \times \delta(\vec{k}_{sum}) d\vec{k}_1 d\vec{k}_{1'} d\vec{k}_2 d\vec{k}_{2'}\,, \qquad (4.26)$$

where ħ is the Planck's constant, *A* is the quantum well area, $M_{1,1',2,2'}$ is the matrix element, and $P_{1,1',2,2'}$ accounts for the occupation probabilities of the carriers. E_{sum} and $\vec{k}_{sum}$ stand for $E_{1'} + E_{2'} - E_1 - E_2$ and $\vec{k}_{1'} + \vec{k}_{2'} - \vec{k}_1 - \vec{k}_2$ (k-selection rule), respectively. In equation (1), state 1 and 2 (represented by subscripts) are for electrons in the lower states of the conduction band, while state 1' is for a heavy hole in the valence band and state 2' is for an excited electron in the higher

state of the conduction band. The $\delta(k)$ and $\delta(E)$ correspond to the Dirac-delta function of momentum and energy, respectively.

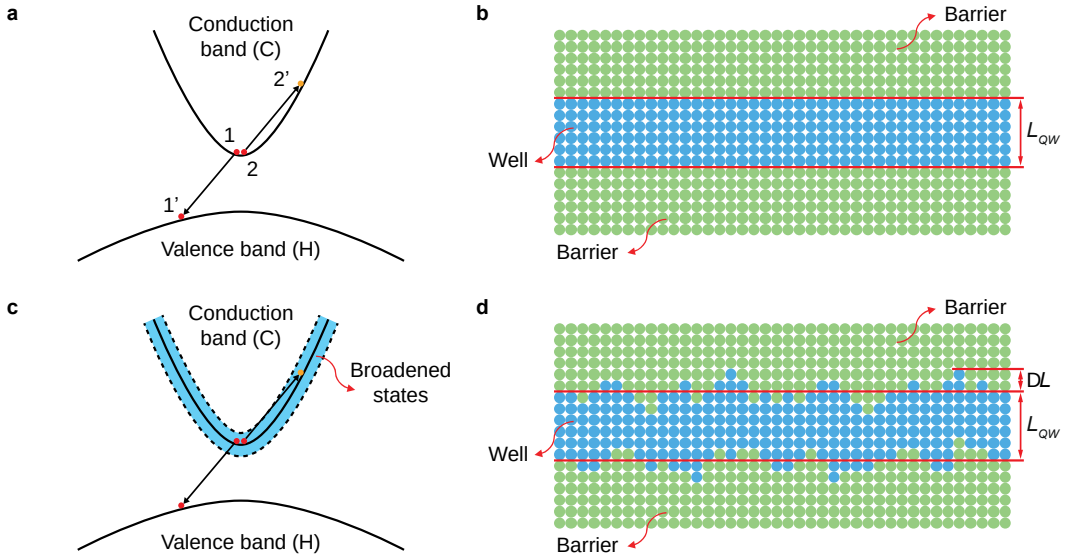

***Figure 4-13: Auger process and QW structure. a**, E-k diagram showing a typical band-to-band CHCC Auger recombination process for a QW without interface roughness. **b**, Illustration of a QW without interface roughness sandwiched by two barrier layers, where the L_{QW} represents the thickness of quantum well. **c**, E-k diagram showing the broadened states in the conduction band for the CHCC Auger process of a QW with interface roughness. **d**, Illustration of a QW with interface roughness between the well and the barriers, where the □L represents the average interface roughness.*

Our analysis of interface roughness in QWs uses Equation (4.26), and we begin with describing the interface roughness for a QW with barrier layers of infinite potential energy, in order to gain a qualitative understanding of Auger recombination. Figs. 4-13b and 4-13d show the schematic representation of this QW system with and without interface roughness between the QW and barrier layers. The average interface roughness, ΔL, is the fluctuation of the interface around the ideal (flat) interface. This roughness is formed by imperfections caused by intrinsic reasons such as strain between materials and alloy disorder, and extrinsic factors such as flaws in epitaxial growth [88].

Under the circumstances of sharp and abrupt interface between the quantum well and the barrier – in "ideal QW", a simple and ideal energy dispersion relation can be used as shown in equation (4.27):

$$E = \frac{\hbar^2({k_z}^2+{k_x}^2+{k_y}^2)}{2m^*} = \frac{\hbar^2({k_z}^2)}{2m^*} + \frac{\hbar^2({k_{||}}^2)}{2m^*} \quad (4.27),$$

where ħ is the Planck's constant, m^* is the effective mass, k_z denotes the wave number in growth direction (representing the perpendicular momentum), and $k_{||}$ denotes the wave number in in-plane direction (representing the in-plane momentum).

Under the infinite potential well approximation, the perpendicular momentum is inversely proportional to the quantum well thickness as specified in equation (4.28),

$$k_z = \frac{\pi}{L_{QW}} \quad (4.28).$$

However, since various degrees of roughness exist in a "real QW", the fluctuation of well thickness (ΔL) directly results in the perpendicular momentum uncertainty (Δk_z), as shown in equation (4.29):

$$\frac{\Delta k_z}{\Delta L} = -\frac{\pi}{{L_{QW}}^2} \quad (4.29).$$

Thus the perpendicular momentum uncertainty has to be taken into account in the energy dispersion relation as shown in equation (4.30):

$$E = \frac{\hbar^2(k_z \pm \Delta k_z)^2}{2m^*} + \frac{\hbar^2({k_{||}}^2)}{2m^*} \quad (4.30).$$

The equation 4.305) can then be expanded and rewritten into

$$E = \frac{\hbar^2{k_z}^2}{2m^*} + \frac{\hbar^2}{2m^*}\left({k_{||}}^2 \pm 2k_z\Delta k_z + {\Delta k_z}^2\right) \quad (4.31),$$

where the perpendicular momentum uncertainty Δk_z is relatively small, so that the square term of Δk_z is negligible in comparison to the two terms of ${k_{||}}^2$ and $2k_z\Delta k_z$. Thus ${\Delta k_z}^2$ term can be dropped in equation (4.31), leading to

$$E \cong \frac{\hbar^2{k_z}^2}{2m^*} + \frac{\hbar^2{k_{||}}^2}{2m^*}\left(1 \pm \frac{2k_z\Delta k_z}{{k_{||}}^2}\right) \quad (4.32).$$

Equation (4.32) can then be approximated into

$$E \cong \frac{\hbar^2 {k_z}^2}{2m^*} + \frac{\hbar^2 {k_{||}}^2}{2m^*}\left(1 \pm \frac{k_z \Delta k_z}{{k_{||}}^2}\right)^2 \quad (4.33),$$

which can be rewritten as following:

$$E = \frac{\hbar^2 {k_z}^2}{2m^*} + \frac{\hbar^2}{2m^*}\left(k_{||} \pm \frac{k_z \Delta k_z}{k_{||}}\right)^2 \quad (4.34).$$

Afterwards, a comparison between equation (4.27) and equation (4.34) gives the insight that the fluctuation of well thickness also results in the in-plane momentum uncertainty ($\Delta k_{||}$), which is specified in equation (4.35):

$$\Delta k_{||} = \pm \frac{k_z \Delta k_z}{k_{||}} \quad (4.35).$$

By substituting the equation (4.28) and equation (4.29) into the equation (4.35), the expression for the absolute value of the in-plane momentum uncertainty can then be obtained as shown below,

$$\left|\Delta k_{||}\right| = \frac{\pi^2}{k_{||}} . \frac{\Delta L}{{L_{QW}}^3} \quad (4.36).$$

The resulted in-plane momentum uncertainty from the interface roughness as shown in equation (4.36) implies that the governing momentum conservation condition (Dirac-delta function) in Auger recombination process is relaxed. It is thus important to take into account the effect of interface roughness in the Auger recombination calculations.

In the quantum well without interface roughness, $\delta(k)$ is replaced with the sinc function of $\sin(k/a)/\pi k$, where a is known as $2/L_{QW}$ [74]. In the case of non-ideal quantum well, the interface roughness has to be taken into consideration in the derivation of a. As the uncertainty of interface roughness results in the uncertainty of final quantum states, the summation of momentum conservation leads to a net momentum vector $\vec{k}$, which can be described as shown below:

$$\vec{k} = \Delta k_{2'z}\vec{k}_z + \Delta k_{2'||}\vec{k}_{||} \ . \quad (4.37)$$

The absolute value of the net momentum vector can then be expressed as follow,

$$k = \sqrt{(\Delta k_{2'z})^2 + (\Delta k_{2'||})^2} \ . \quad (4.38)$$

From equation (4.35), the $\Delta k_{||}$ can be incorporated into equation (4.38). The net momentum vector value can then be described as shown below:

$$k = \Delta k_{2'z} \sqrt{1 + \left(\frac{k_{2'z}}{k_{2'||}}\right)^2} \quad . \tag{4.39}$$

Assuming that the ratio of $k_{2'z}/k_{2'||}$ is much larger than 1, and by replacing $\Delta k_{2'z}$ and $k_{2'z}$ term through equation (4.28) and (4.29), the net momentum value can then be expressed in equation (4.40):

$$k = \frac{\pi^2}{{L_{QW}}^3} . \frac{\Delta L}{k_{2'||}} \quad . \tag{4.40}$$

The root of $\sin(k/a)/\pi k$ where k is the variable would yield $na\pi$. Thus, by using equation (4.40) and taking $n = 1$, the a can then be expressed in equation (4.41):

$$a = \frac{\pi}{{L_{QW}}^3} . \frac{\Delta L}{k_{2'||}} \quad . \tag{4.41}$$

The $k_{2'||}$ represent the quasi-momentum for the in-plane wave number in the final state. This results in the linewidth broadening of the sinc function, increasing the number of possible Auger transition states attributed to the relaxation of momentum conservation.

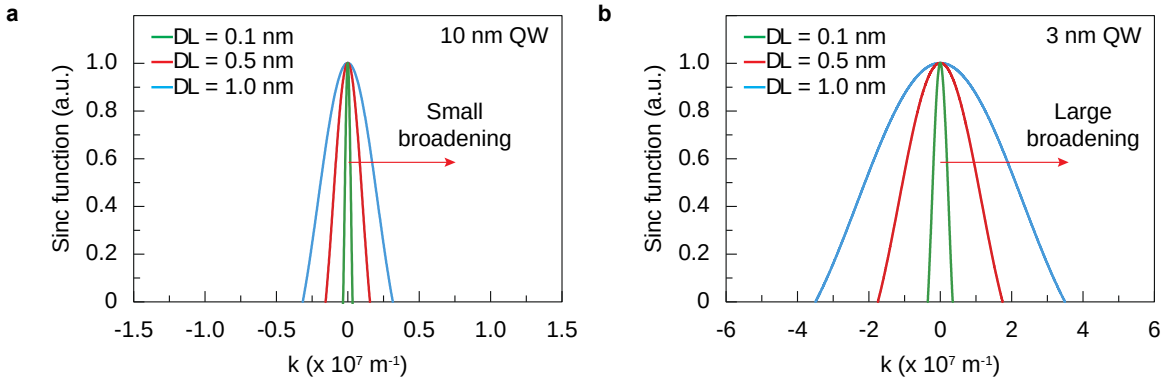

***Figure 4-14: The broadening of k-selection in a QW with interface roughness. a**, Increment of interface roughness in a 10 nm QW yields relatively small broadening of the sinc function. **b**, Increment of interface roughness in a 3 nm QW results in larger broadening of the sinc function. The broadening of the k-selection results in larger number of possible Auger transition states, and the comparison of **(a)** and **(b)** shows the effect of interface roughness is more significant in thin QWs compared to thicker QWs.*

Further understanding on the effect of interface roughness on the Auger transition states can be seen from figure 4-14. Figure 4-14(a) and 4-14(b) illustrate the line shapes of the sinc functions in the 3 nm QW and 10 nm QW with varying degree of roughness as a function of momentum k. As shown in figure 4-14, the line width of both QWs assembles the Dirac-delta line shape when the interface roughness is small (attributed to small ΔL / L_{QW}). When the roughness increases, the linewidth of the sinc function also broadens. The implication behind the line width broadening is that the k-selection limit has sprouted into a wider range, indicating the increase in the possible Auger transition states. Consequently, this gives the extra choices of k-value to allow for the successful Auger processes. By comparing figure 4-14(a) and 4-14(b), the linewidth of sinc function has a larger broadening in the thin QW (3 nm) than that in the thick QW (10 nm), which is attributed to larger ΔL / L_{QW} in the thin QW. This shows that the ΔL / L_{QW} plays an important role in determining the impact of interface roughness in the thin QW as compared to that of thick QW.

4.4.3. Numerical Formulation of Auger Recombination with Interface Roughness

To be more specific, the probability factor is a term accounting for the Fermi-Dirac distribution of carriers occupying the available states for transitions. It is the difference between the product of the occupation probability of the four states 1,1',2,2' for an Auger process to occur and intuitively the inverse process of impact ionization. The quantity is given as following:

$$P = f_1 . f_2 . f_{1'} . [1 - f_{2'}] . \left[1 - \exp\left(\frac{-E_g - E_{fc} - E_{fv}}{k_b T}\right)\right] \quad (4.42).$$

For most cases, E_g is much larger than the $k_b T$ term, and thus the exponential term will be negligible compared to the unity. Also, the state 2' is usually located at a higher energy level which means that the Fermi-Dirac distribution for that particular term will be insignificant. This leaves the quantity into the following [89]:

$$P = \frac{1}{exp\left(\frac{E_1 - E_{fn}}{k_b T}\right)+1} \cdot \frac{1}{exp\left(\frac{E_{1'} - E_{fp}}{k_b T}\right)+1} \cdot \frac{1}{exp\left(\frac{E_2 - E_{fn}}{k_b T}\right)+1} \quad (4.43),$$

where E_j stands for the energy band level of the electrons and holes in which subscript j denotes the carrier band, $E_{fn}$and $E_{fp}$are quasi Fermi levels for electrons and holes respectively. k_b is Boltzmann constant and T is the room temperature.

Assume that the structure is of charge neutrality and zero external applied electric field, the electron and hole quasi-Fermi levels should remain constant throughout the structure. Under the circumstances that temperature, conduction and hole band energy are determined, evaluation of the quasi-Fermi levels for electrons and holes depend on the determination of the density of states of carriers.

The density of states for two-dimensional heterostructure are given as following:

For electron:

$$N_c = \frac{m_e{}^* k_b T}{\pi \hbar} \quad (4.44),$$

For hole:

$$N_v = \frac{m_h{}^* k_b T}{\pi \hbar} \quad (4.45),$$

where m_e denotes for the electron effective mass while m_h denotes for hole effective mass. The other terms are previously described.

Quasi-Fermi level can now be obtained using the Joyce-Dixon approximation and is given as followings:

$$E_{fn} = E_c + k_b T.\left[ln\left(\frac{n}{N_c}\right) + \frac{1}{\sqrt{8}}.\frac{n}{N_c}\right] \quad (4.46),$$

For electron:

$$E_{fp} = E_v + k_b T.\left[ln\left(\frac{p}{N_v}\right) + \frac{1}{\sqrt{8}}.\frac{p}{N_v}\right] \quad (4.47),$$

For hole:

where n and p denotes the carrier density for electrons and holes respectively. Here E_c is defined as the minimum conduction band energy and E_v is defined as the maximum valence band energy.

The matrix element can be defined as following [90-91]:

$$M_{1,2,1',2'} = \frac{2\pi e^2}{4\pi\epsilon A q_{xy}} F_{ijfg} \quad (4.48),$$

where

$$F_{ijfg} = \int\int \phi_i(z)\phi_j(z')\phi_f{}^*(z)\phi_g{}^*(z')e^{-q_{xy}|z-z'|}dz\,dz' \quad (4.49)$$

are form factors. A is the quantum well area, e is the electron charge, ϵ is the dielectric constant and q_{xy} is the in-plane momentum vector. The computational challenges in calculating the Auger rates have been discussed by Laks et al [45]. The scales with the fourth power of the number of k points within the Auger recombination rate equation leads to prohibitively expensive computational resources. Therefore this multidimensional integration is tackled through the use of Monte Carlo approach. Statistically an average over 40 000 000 Monte Carlo steps are computed in the approach. The numerical calculation procedure is summarized in the following flowchart.

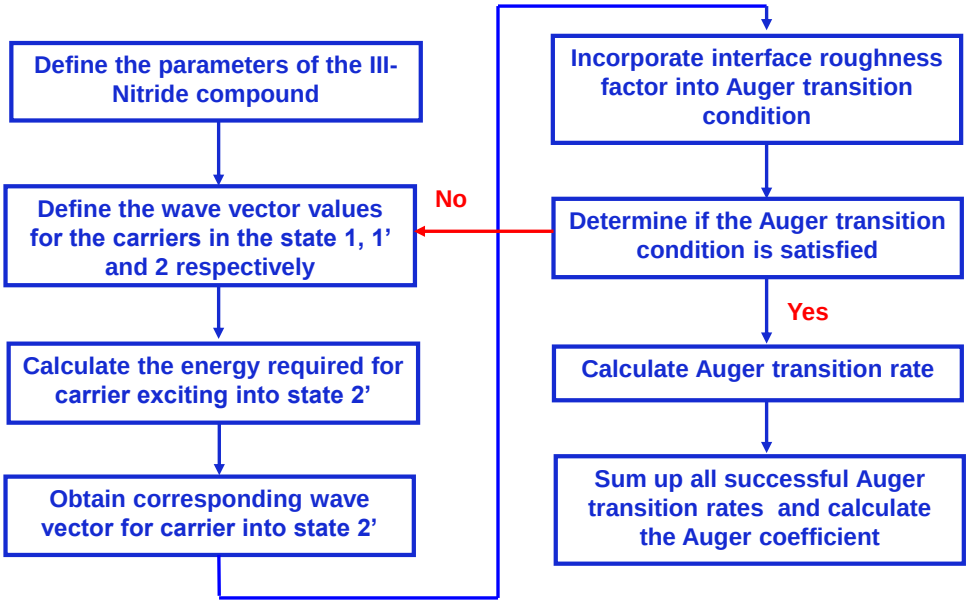

Figure 4-15: *Flowchart of the numerical calculation for the Auger recombination coefficient evaluation in III-Nitride QW.*

It is already shown that the parameters from the band structure are required for the calculation. Here the band parameters are listed in Table 4-2. For the band gap of the alloy under investigation, a composition-dependent energy band gap equation is employed. The bowing parameter used in the equation is set as 1.4 eV. The alloy composition in our study is set at 28%

In, leading to energy band gap of 2.372 eV by following the composition-dependent energy band gap equation as shown in equation (4.50):

$$E_{g,InGaN} = E_{g,GaN}(1-x) + E_{g,InN}(x) - b(1-x)(x) \quad (4.50).$$

For the effective mass, the electron and hole effective mass of binary alloy GaN and InN are obtained through available literature [92-93]. Linear interpolation is used to obtain the electron and hole effective mass for the particular InGaN ternary alloy, as shown in the following equations:

$$\frac{1}{m_{c,InGaN}} = \frac{x}{m_{c,InN}} + \frac{1-x}{m_{c,GaN}} \quad (4.51).$$

For the carrier concentration, under equilibrium condition the electron concentration is assumed to be exactly the same as the hole concentration. Thus, the carrier concentration is used as 1 x 10^{19} cm^{-3} for both electron and hole concentrations. The Auger coefficient is defined as $C = R_{Auger}/n^3$and the calculated result will be extensively discussed in section 4.5.

	GaN	InN	$In_{0.28}Ga_{0.72}N$
E_g (eV)	3.437	0.6405	2.372
m_c (m_0)	0.210	0.070	0.137
m_h (m_0)	1.400	1.563	1.442

Table 4-2: *The band parameters listed are used for the calculation in the Auger coefficient for the InGaN semiconductor.*

4.5. Auger Recombination Analysis with Interface Roughness in InGaN Semiconductor

To demonstrate the effect of interface roughness on Auger recombination rates in QWs we use the III-nitride semiconductor system. The choice of this system, and in particular InGaN QWs, is of interest because they are not only technologically interesting for applications such as high brightness LEDs, but also because strain and epitaxial growth constrains limit QW thicknesses to ~ 3 nm where we believe interface roughness plays an important role. Additionally, QWs formed from InGaN are much thinner than those formed in other semiconductor systems, and have relatively high interface roughness (ΔL ~ 0.6-1.5 nm) [83-84].

The Auger coefficient (C_{Auger}) is plotted as a function of interface roughness (Fig. 4-16(a)) and ratio of interface roughness (Fig. 4-16(b)) for InGaN QWs with thickness of 3 nm, 10 nm, and 20 nm. For the 3 nm thick QW without interface roughness (ΔL=0) the C_{Auger} is 3.1 x 10^{-34} cm^6s^{-1}, which is in close agreement with previous theoretical results [42]. More importantly, the C_{Auger} for 3 nm thick QW increases abruptly from 3.1 x 10^{-34} cm^6s^{-1} to 1.7 x 10^{-31} cm^6s^{-1} when only 0.1 nm of interface roughness is introduced. Increases hold for thicker QWs too, with increases of C_{Auger} from 1.6 x 10^{-35} cm^6s^{-1} to 1.5 x 10^{-34} cm^6s^{-1} and from 1.3 x 10^{-36} cm^6s^{-1} to 2.8 x 10^{-35} cm^6s^{-1} for 10 nm and 20 nm thick InGaN QWs, respectively. The dramatic increase of C_{Auger} with increased ΔL in the InGaN quantum well is attributed to the increased number of available final states for the excited carrier created by the interface roughness. As the number of available final states increases due to the interface roughness, the probability of an Auger transition is enhanced. Additionally, we find as the ratio of interface roughness to quantum well thickness is increased, Auger recombination is significantly enhanced. At larger interface roughness, from 0.1 nm to 1 nm, the C_{Auger} of all three QWs increases at a slower rate.

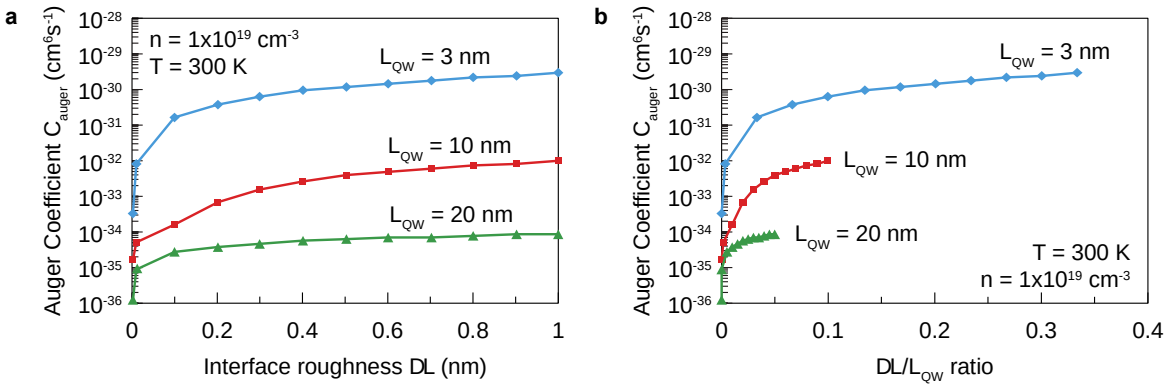

***Figure 4-16: The effect of interface roughness. a**, Calculated Auger recombination coefficients in InGaN QWs as function of the interface roughness ΔL with QW thickness of 3 nm, 10 nm, and 20 nm represented by the blue, red and green lines, respectively. **b**, Auger recombination coefficients in InGaN QWs as function of the ratio of interface roughness to QW thickness $\Delta L/L_{QW}$. The QW thickness corresponding to blue, red, and green lines are 3 nm, 10 nm, and 20 nm, respectively.*

These results are interesting because they can explain the discrepancy in theoretical and experimental results for III-nitride QWs. Experimental Auger recombination coefficients are at a much higher value compared to theoretical results that does not consider interface roughness.

While including electron-phonon coupling and alloy scattering in Auger recombination calculations [20] can lead to higher theoretical values, we show that including interface roughness can also provide higher values. Including this interface roughness in the calculations is paramount because all realistic III-nitride quantum wells have interface roughness. If we use an interface roughness that is greater than 0.5 nm than for a typical 3 nm thick QW the Auger coefficient is on the order of 10^{-30} cm^6s^{-1} which is much closer to experimental values [17].

The value of the C_{Auger} also exhibits a large variation with changing QW thickness. Fig. 4-17 plots the C_{Auger} of InGaN QW as a function of QW thickness with various fixed interface roughness of 0.1 nm, 0.3 nm, 0.5 nm and 1 nm. The C_{Auger} is reduced by ~ 4 orders of magnitude when the InGaN QW thickness increases from 3 nm to 20 nm for each value of interface roughness (This can also be observed in Fig. 4-16). This phenomenon is caused by the weakening of the momentum relaxation when the QW thickness increases, and is separated from the expected reduction in carrier density with thicker wells [12]. This distinction is important because this result suggests that thicker quantum wells will lead to lower Auger recombination rates by *both* lower carrier densities and from a weakening of the momentum relaxation.

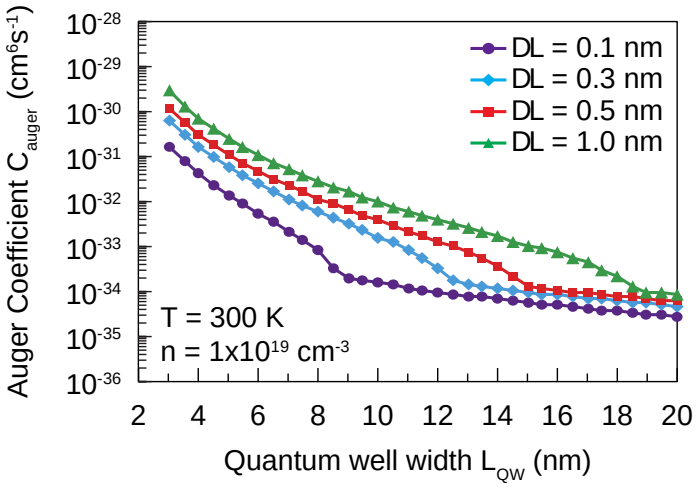

Figure 4-17: The effect of QW thickness on Auger recombination. *Auger recombination coefficients in the InGaN QW are shown as a function of QW thickness from 3 nm to 20 nm with fixed interface roughness. The interface roughness in the case of the purple, blue, red, and green lines equals to 0.1 nm, 0.3 nm, 0.5 nm, and 1 nm, respectively.*

Fig. 4-17 also shows that the C_{Auger} asymptotes to a minimum value with increased QW thickness, and this asymptote value depends on the interface roughness. For example, at an interface roughness of 0.3 nm, the C_{Auger} decreases rapidly from 6.5 x 10^{-31} cm^6s^{-1} to 3.3 x 10^{-34} cm^6s^{-1} when the QW thickness increases from 3 nm to 12 nm, and decreases at a lower rate for thicknesses greater than 12 nm. A similar trend can be observed for all values of interface roughness. Our analysis indicates that increasing the QW thickness (i.e. reducing the ΔL / L_{QW} ratio) is also important for reducing the Auger rates. However, the effect of suppressing the Auger recombination by using thicker InGaN QW becomes less significant when the QW thickness increases beyond a specific level, thus reducing the role interface roughness plays in controlling and suppressing Auger recombination.

This theoretical study shows the importance of interface roughness in the Auger recombination process of semiconductor QWs. For InGaN QWs this study is particularly interesting, because the thin QWs and large interface roughness will result in C_{Auger} values that are much higher than what is predicted by using perfect heterointerfaces. For example, assuming a typical InGaN QW thickness of ~ 3 nm, and interface roughness of ~ 0.5 nm the C_{Auger} is ~ 1.2 x 10^{-30} cm^6/s. This value is large enough to cause high Auger recombination rates in visible III-InGaN-based LEDs, and confirms the notion that Auger recombination produces the observed reduced efficiency at high carrier densities (efficiency droop). Additionally, our Auger calculations assume direct transitions and do not employ phonons to achieve higher values [15] simplifying the message that Auger recombination is appreciable in III-nitride semiconductors.

4.6. Potential Experimental Verification Methods and Solutions

The question naturally arises as to the method of revealing the effect of interface roughness on Auger recombination process experimentally. Thus two simple experiments are proposed as following to verify the effect of interface roughness on the Auger recombination process in a QW structure. The first proposed experiment can be carried out to verify the effect of interface roughness in a thin QW as compared to that of a thick QW by using a well-established

AlGaAs/GaAs QW system. As illustrated in figure 4-18(a), the heterostructure formed by AlGaAs (barriers) and GaAs (QW) is known for small interface roughness (~ 1 monolayer), attributed to the advanced epitaxial techniques and lattice-matched condition between the two materials [86]. By varying the well thickness from 3 nm to 20 nm without changing the interface roughness, the QW structures can be measured through photoluminescence technique in a similar manner performed by Shen and co-workers [17]. Consequently, the Auger recombination coefficients for the QW structures can be obtained and compared through data fitting with total recombination rate equations.

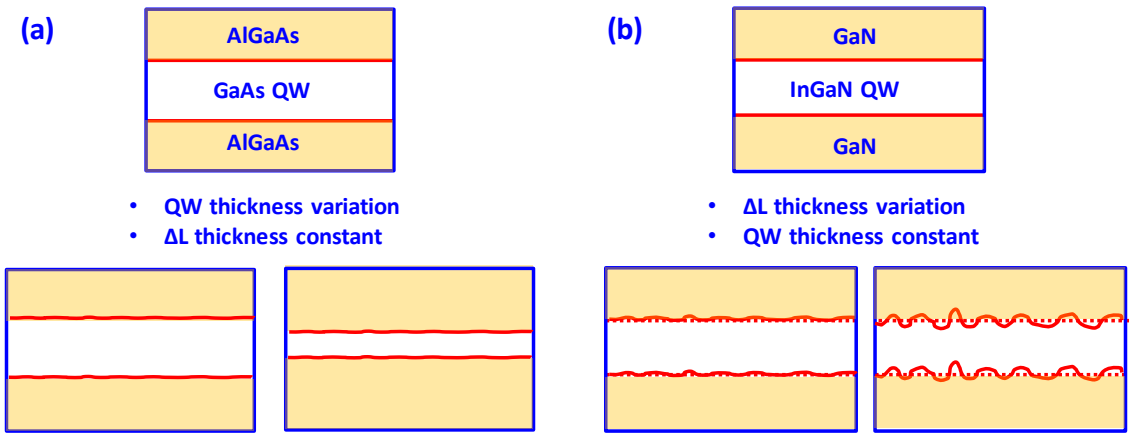

Figure 4-18: *(a) First proposed experiment with different QW widths but constant interface roughness by using AlGaAs/GaAs QW system, and (b) second proposed experiment with constant QW width but different interface roughness using GaN/InGaN QW system.*

On the other hand, the second proposed experiment can be carried out through GaN/InGaN or GaAs/InGaAs QW systems. This experiment is proposed with the aim of verifying the effect of interface roughness in a fixed QW as discussed in the findings of section 4.5. The interface roughness in the QW systems can be reduced from ~ four monolayers to ~ one monolayer through optimizations of the experiment conditions [82]. Assuming that experiments condition can be modified intentionally, the interface roughness could potentially be tuned from one monolayer to four monolayers in the QW structure while the QW thickness is kept constant, as illustrated in figure 4-18(b). Under the same measurement suggested in the first proposed experiment, the

Auger coefficient of the QW structures with different roughness can then be obtained and compared.

It is important to note that the current study is aimed to provide the key insight on the role of interface roughness in affecting the Auger recombination process in a semiconductor QW structure. In addition, if the effect of interface roughness in the QW can be experimentally verified via the first or second proposed experiment, it is remarkable that a simple theoretical model with the inclusion of interface roughness effect should provide an insightful explanation on the discrepancy of the Auger recombination coefficients between the theoretical and experimental works. Correspondingly, potential solutions to suppress the roughness effect could also be allowed to reduce the large Auger recombination coefficient in the semiconductor devices.

These findings also offer an alternative technological solution for controlling and suppressing Auger recombination, and several experimental pathways could be considered. First and foremost, optimizing the material epitaxial growth technique (MOCVD or MBE) could be a useful experimental path to reduce the interface roughness and Auger recombination. Previous studies have demonstrated that the modulation of growth pauses between layers can be used to reduce the interface roughness in the InGaAs QWs [82], and similar innovations in the growth techniques might also be applied in other semiconductors such as InGaN QWs. Secondly, utilizing thicker QW could suppress the effect of interface roughness on the Auger recombination process, resulting in lower Auger recombination rates. Typically, thicker QWs are desired for lower carrier densities, but the lower Auger recombination rates from a weakening of the momentum relaxation in thicker QWs may also be of benefit too. (Note: For strained and polar materials such as III-nitrides there will be a trade-off with thicker QWs and radiative efficiency because of increased charge separation as the QW becomes thicker.) Finally, developing and implementing surfactant techniques could be important experimental pathway in order to reduce the interface roughness [94-95]. A combination of the aforementioned methods would potentially minimize interface roughness in semiconductor QWs, and controlling Auger recombination processes for improved device performance.

4.7. Summary

In summary the analysis on the interband Auger recombination of semiconductor alloys were carried out with closed-form analytical expressions. The closed-form analytical solutions give physical insight of the interband Auger recombination mechanism in a semiconductor alloy efficiently with the result compared to those obtained through computationally expensive Monte-Carlo simulation method. InGaN and ZnMgO ternary alloys were used as the examples in the analytical calculations for their availability of band structures and band parameters in published literature. Our analysis shows that interband Auger recombination is heavily affected by the alloy band parameters which are the energy band gap, the interband separation energy and the band effective masses. In addition, analysis on the methods to suppress the interband Auger recombination rate in semiconductor alloy were presented. Band structure engineering such as the use of alternative material and low-dimensional systems (quantum well) are suggested for its capability in modifying the band parameters, which could be useful to suppress the interband Auger recombination rate in ternary alloys.

In addition, theoretical studies were carried out to evaluate the impact of interface roughness on the Auger recombination process in semiconductor QWs. Our analysis shows that the existence of interface roughness results in a significant enhancement of the Auger recombination process, leading to a large Auger recombination coefficient. The ratio of interface roughness and QW thickness has a strong contribution to the Auger recombination rate in a realistic QW structure with interface roughness. Further analysis shows that the effect of interface roughness on the Auger recombination process is much more significant in a thin QW as compared to a thick QW. Specifically, when considering a InGaN QW with interface roughness, the Auger recombination coefficient is enhanced by two orders of magnitude in the 3 nm thin QW over that in the 20 nm thick QW. In addition, a 3 nm InGaN QW with interface roughness ranging from 0.5 nm to 1 nm, has an C_{Auger} ~ 10^{-30} cm^6s^{-1}. This work identifies the importance of interface roughness on the Auger recombination process in the semiconductor QW devices.

References for Chapter 4

[1] S. Nakamura, “The roles of structural imperfections in InGaN-based blue light-emitting diodes and laser diodes”, Science, vol. 281, no. 5379, pp. 956-961, Aug. 1998.

[2] M. H. Crawford, “LEDs for solid-state lighting: performance challenges and recent advances”, IEEE J. Sel. Top. Quantum Electron., vol. **15**, no. 4, pp. 1028–1040, Aug. 2009.

[3] M. Krames, O. Shchekin, R. Mueller-Mach, G. Mueller, L. Zhou, et.al., “Status and future of high-power light-emitting diodes for solid-state lighting”, J. Disp. Technol., vol. 3, no. 2, pp. 160-175, Jun. 2007.

[4] H. Zhao, G. Y. Liu, J. Zhang, J. D. Poplawsky, V. Dierolf, and N. Tansu, “Approaches for high internal quantum efficiency green InGaN light-emitting diodes with large overlap quantum wells”, Optics Express, vol. **19**, no. S4, pp. A991-A1007, Jul. 2011.

[5] D. F. Feezell, J. S. Speck, S. P. DenBaars, and S. Nakamura, “Semipolar (2021) InGaN/GaN light-emitting diodes for high-efficiency solid-state lighting”, J. Display Tech., vol. 9, no. 4, pp. 190-198, Apr. 2013.

[6] S. P. DenBaars, D. Feezell, K. Kelchner, S. Pimputkar, C. C. Pan, C. C. Yen, S. Tanaka, Y. Zhao, N. Pfaff, R. Farrell, M. Iza, S. Keller, U. Mishra, J. S. Speck, S. Nakamura, “Development of gallium-nitride-based light-emitting diodes (LEDs) and laser diodes for energy-efficient lighting and displays”, Acta Materialia, vol. 61, no. 3, pp. 945-951, Feb. 2013.

[7] X. Li, S. Kim, E. E. Reuter, S. G. Bishop, and J. J. Coleman, “The incorporation of arsenic in GaN by metalorganic chemical vapor deposition”, Appl. Phys. Lett, vol. **72**, no. 16, pp. 1990-1992, Feb. 1998.

[8] X. Li, S. G. Bishop, and J. J. Coleman, “GaN epitaxial lateral overgrowth and optical characterization”, Appl. Phys. Lett., vol.**73**, no. 9, pp. 1179–1181, Jul. 1998.

[9] X. Li, H. Liu, X. Ni, U. Ozgur, H. Morkoc, “Effect of carrier spillover and Auger recombination on the efficiency droop in InGaN-based blue LEDs,” Superlattices and Microstructures, vol. 47, pp. 118-122, 2010.

[10] X. H. Li, R. Song, Y. K. Ee, P. Kumnorkaew, J. F. Gilchrist, and N. Tansu, “Light extraction efficiency and radiation patterns of III-nitride light-emitting diodes with colloidal microlens arrays with various aspect ratios”, IEEE Photon. J., vol. **3**, no. 3, pp. 489–499, Jun. 2011.

[11] I. H. Brown, P. Blood, P. M. Smowton, J. D. Thomson, S. M. Olaizola, A. M. Fox, P. J. Parbrook, and W. W. Chow, “Time evolution of the screening of piezoelectric fields in InGaN quantum wells,” IEEE J. Quantum Electron., vol. 42, no. 12, pp. 1202–1208, Nov-Dec. 2006.

[12] N. F. Gardner, Blue-emitting InGaN-GaN double-heterostructure light-emitting diodes reaching maximum quantum efficiency above 200 A/cm2. *Appl. Phys. Lett.*, **91**, 243506 (2007).

[13] R. Dahal, B. Pantha, J. Li, J. Y. Lin, and H. X. Jiang, "InGaN/GaN multiple quantum well solar cells with long operating wavelengths", Appl. Phys. Lett., vol. 94, no. 6, p. 063505, Feb. 2009.

[14] M. H. Kim, M. F. Schubert, Q. Dai, J. K. Kim, E. F. Schubert, J. Piprek, and Y. Park, "Origin of efficiency droop in GaN-based light-emitting diodes", Appl. Phys. Lett., vol. 91, no. 18, p. 183507, Oct. 2007.

[15] H. P. Zhao, G. Y. Liu, R. A. Arif, and N. Tansu, "Current injection efficiency quenching leading to efficiency droop in InGaN quantum well light-emitting diodes," Solid State Electron., vol. 54, no. 10, pp. 1119-1124, Oct. 2010.

[16] H. P. Zhao, G. Y. Liu, J. Zhang, R. A. Arif, and N. Tansu, "Analysis of internal quantum efficiency and current injection efficiency in III-nitride light-emitting diodes", J. Display Technol., vol. 9, no. 4, pp. 212-225, Apr. 2013.

[17] Y. C. Shen, G. O. Mueller, S. Watanabe, N. F. Gardner, A. Munkholm, and M. R. Krames, "Auger recombination in InGaN measured by photoluminescence", Appl. Phys. Lett., vol. 91, no. 14, p. 141101, Oct. 2007.

[18] K. T. Delaney, P. Rinke, and C. G. Van de Walle, "Auger recombination rates in nitrides from first principles", Appl. Phys. Lett., vol. 94, no. 19, p. 191109, May 2009.

[19] F. Bertazzi, M. Goano, and E. Bellotti, "A numerical study of Auger recombination in bulk InGaN", Appl. Phys. Lett., vol. 97, no. 23, p. 231118, Dec. 2010.

[20] E. Kioupakis, P. Rinke, K. T. Delaney, and C. G. Van de Walle, "Indirect Auger recombination as a cause of efficiency droop in nitride light-emitting diodes", Appl. Phys. Lett., vol. 98, no. 16, p. 161107, Apr. 2011.

[21] F. Bertazzi, M. Goano, and E. Bellotti, "Numerical analysis of indirect Auger transitions in InGaN", Appl. Phys. Lett., vol. 101, no. 1, p. 011111, Jul. 2012.

[22] G. Hatakoshi and S. Nunoue, "Analysis of Auger Recombination for Wurtzite InGaN", Appl. Phys. Express, vol. 5, no. 7, p. 071001, Jun 2012.

[23] F. Bertazzi, X. Zhou, M. Goano, G. Ghione, and E. Bellotti, "Auger recombination in InGaN/GaN quantum wells: A full-Brillouin-zone study", Appl. Phys. Lett., vol. 103, no. 08, p. 081106, Aug. 2013.

[24] R. Vaxenburg, E. Lifshitz, and Al. L. Efros, “Suppression of Auger-stimulated efficiency droop in nitride-based light emitting diodes”, Appl. Phys. Lett., vol. 102, no. 03, p. 031120, Jan. 2013.

[25] J. Iveland, L. Martinelli, J. Peretti, J. S. Speck, and C. Weisbuch, “Direct measurement of Auger electrons emitted from a semiconductor light-emitting diode under electrical injection: Identification of the dominant mechanism for efficiency droop”, Phys. Rev. Lett., vol. 110, no. 17, p. 177406, Apr. 2013.

[26] A. A. Efremov, N. I. Bochkareva, R. I. Gorbunov, D. A. Lavrinovich, Y. T. Rebane, D. V. Tarkhin, Y. G. Shreter, “Effect of the joule heating on the quantum efficiency and choice of thermal conditions for high-power blue InGaN/GaN LEDs”, Semiconductors, vol. **40**, pp. 605-610, 2006.

[27] W. W. Chow, M. H. Crawford, J. Y. Tsao, and M. Kneissl, “Internal efficiency of InGaN light-emitting diodes: Beyond a quasiequilibrium model”, Appl. Phys. Lett., vol. 97, no. 12, pp. 121105-1-121105-3, Sep. 2010.

[28] J. Hader, J. V. Moloney, and S. W. Koch, “Temperature-dependence of the internal efficiency droop in GaN-based diodes”, Appl. Phys. Lett., vol. 99, no. 18, pp. 181127-1-181127-3, Oct. 2011.

[29] M. F. Schubert, S. Chhajed, J. K. Kim, E. F. Schubert, D. D. Koleska, M. H. Crawford, S. R. Lee, A. J. Fischer, G. Thaler, and M. A. Banas, “Effect of dislocation density on efficiency droop in GaInN/GaN light-emitting diodes”, Appl. Phys. Lett., vol. 91, no. 23, pp. 231114-1-231114-3, Dec. 2007.

[30] X. Guo, and E. F. Schubert, “Current crowding in GaN/InGaN light emitting diodes on insulating substrates”, J. Appl. Phys., vol. 90, no. 8, pp. 4191-4195, Oct. 2001.

[31] V. K. Malyutenko, S. S. Bolgov, and A. D. Podoltsev, “Current crowding effect on the ideality factor and efficiency droop in blue lateral InGaN/GaN light emitting diodes”, Appl. Phys. Lett., vol. 97, no. 25, pp. 251110-1-251110-3, Dec. 2010.

[32] E. Kioupakis, P. Rinke, A. Schleife, F. Bechstedt, and C. G. Van de Walle, “Free-carrier absorption in nitrides from first principles”, Phys. Rev. B, Condens. Matter, vol. 81, no. 24, pp. 241201-241201-4, Jun. 2010.

[33] J. Xie, X. Ni, Q. Fan, R. Shimada, U. Ozgur, and H. Morkoc, “On the efficiency droop in InGaN multiple quantum well blue light emitting diodes and its reduction with p-doped quantum well barriers”, Appl. Phys. Lett., vol. **93**, no. 12, pp. 121107-1-121107-3, Sep. 2008.

[34] X. Ni, Q. Fan, R. Shimada, U. Ozgur, and H. Morkoc, “Reduction of efficiency droop in InGaN light emitting diodes by coupled quantum wells”, Appl. Phys. Lett., vol. 93, no. 17, pp. 171113-171113-3, Oct. 2008.

[35] S. F. Chichibu, T. Azuhata, M. Sugiyama, T. Kitamura, Y. Ishida, H. Okumura, et. al., “Optical and structural studies in InGaN quantum well structure laser diodes”, J. Vac. Sci. Technol. B: Microelectronics and Nanometer Structures, vol. **19**, no. 6, pp. 2177-2183, Nov. 2001.

[36] H. J. Chung, R. J. Choi, M. H. Kim, J. W. Han, Y. M. Park, Y. S. Kim, H. S. Paek, C. S. Sone, Y. J. Park, J. K. Kim, and E. F. Schubert, “Improved performance of GaN-based blue light emitting diodes with InGaN/GaN multilayer barriers”, Appl. Phys. Lett., vol. 95, no. 24, pp. 241109-1-241109-3, Dec. 2009.

[37] C. S. Xia, Z. M. Simon Li, Z. Q. Li, and Y. Sheng, “Effect of multiquantum barriers in performance enhancement of GaN-based light-emitting diodes”, Appl. Phys. Lett., vol. 102, no. 01, p. 013507, Jan. 2013.

[38] J. Piprek, and Z. M. Simon Li, “Origin of InGaN light-emitting diode efficiency improvements using chirped AlGaN multi-quantum barriers”, Appl. Phys. Lett., vol. 102, no. 02, p. 023510, Jan. 2013.

[39] G. Y. Liu, J. Zhang, C. K. Tan, and N. Tansu, “Efficiency-droop suppression by using large-bandgap AlGaInN thin barrier layers in InGaN quantum-well light-emitting diodes”, IEEE Photonics Journal, vol. 5, no. 2, Apr. 2013.

[40] S. Choi, H. J. Kim, S. S. Kim, J. Liu, J. Kim, J. H. Ryou, R. D. Dupuis, A. M. Fischer, and F. A. Ponce, “Improvement of peak quantum efficiency and efficiency droop in III-Nitride visible light-emitting diodes with an InAlN electron-blocking layer”, Appl. Phys. Lett., vol. 96, no. 22, pp. 221105-1-221105-3, May 2010.

[41] Y. K. Kuo, J. Y. Chang, and M. C. Tsai, “Enhancement in hole-injection efficiency of blue InGaN light-emitting diodes from reduced polarization by some specific designs for the electron blocking layer”, Opt. Lett., vol. 35, no. 19, pp. 3285-3287, Oct. 2010.

[42] J. Hader, J. V. Moloney, B. Pasenow, S. W. Koch, M. Sabathil, N. Linder, and S. Lutgen, “On the importance of radiative and Auger losses in GaN-based quantum wells”, Appl. Phys. Lett., vol. 92, no. 26, p. 261103, Jul. 2008.

[43] M. Heinemann, and C. Heiliger, “Auger recombination rates in ZnMgO from first principles”, Appl. Phys. Lett., vol. 110, no. 08, p. 083103, Oct. 2011.

[44] A. Haug, D. Kerkhoff, and W. Lochmann, “Calculation of Auger coefficients for III-V semiconductors with emphasis on GaSb”, Phys. Stat. Sol. (b), vol. 89, pp. 357-365, 1978.

[45] D. B. Laks, G. F. Neumark, and S. T. Pantelides, "Accurate interband-Auger-recombination rates in silicon", Physical Review B, Volume 42, Number 8(1990).

[46] L. A. Coldren, S. W. Corzine, and M. L. Masanovic, “Diode lasers and photonic integrated circuits”, Wiley, New Jersey, 2012, p. 657-659.

[47] A. Haug, “Theoretical solid state physics”, vol. 2, New York: Pergamon, 1972, p. 331.

[48] A. Sugimura, “Band-to-band Auger effect in long wavelength multinary III-V alloy semiconductor lasers”, IEEE J. Quantum Electron., vol. QE-18, no. 3, pp. 352-363, Mar. 1981.

[49] J. Singh, “Electronic and optoelectronic properties of semiconductor structures”, Cambridge University Press, Cambridge, 2003, p. 112.

[50] N. Tansu, L. J. Mawst, “Low-threshold strain-compensated InGaAs(N)/(λ=1.19-1.31 μm) quantum-well lasers”, IEEE Photonic s Tech. Lett., vol. 14, no. 4, pp. 444-446, Apr. 2002.

[51] M. Kondow, K. Uomi, A. Niwa, T. Kitatani, S. Watahiki, and Y. Yazawa, “GaInNAs: A novel material for long-wavelength-range laser diodes with excellent high-temperature performance”, Jpn. J. Appl. Phys., vol. 35, part 1, no. 2B, pp. 1273-1275, Feb. 1996.

[52] W. W. Chow, E. D. Jones, N. A. Modine, A. A. Allerman, and S. R. Kurtz, “Laser gain and threshold properties in compressive-strained and lattice-matched GaInNAs/GaAs quantum wells”, Appl. Phys. Lett., vol. 75, no. 19, pp. 2891-2893, Nov. 1999.

[53] S. R. Bank, L. L. Goddard, M. A. Wistey, H. B. Yuen, J. S. Harris, “On the temperature sensitivity of 1.5-μm GaInNAsSb lasers,” IEEE J. Sel. Top. Quantum Electron., vol. 11, no. 5, pp. 1089-1098, Sep./Oct. 2005.

[54] L. Xu, D. Patel, C. S. Menoni, J. Y. Yeh, L. J. Mawst, and N. Tansu, “Optical determination of the electron effective mass of strain compensated In0.4Ga0.6As0.995N0.005/GaAs single quantum well”, Appl. Phys. Lett., vol. 89, no. 17, pp. 171112-1-171112-3, Oct. 2006.

[55] L. F. Xu, D. Patel, C. S. Menoni, J. Y. Yeh, L. J. Mawst, and N. Tansu, “Experimental evidence of the impact of nitrogen on carrier capture and escape times in InGaAsN/GaAs single quantum well”, IEEE Photonics Journal, vol. 4, no. 6, pp. 2262-2271, Dec. 2012.

[56] S. Tomic, E. P. O’ Reilly, P. J. Klar, H. Gruning, W. Heimbrodt, W. M. Chen and I. A. Buyanova, “Influence of conduction-band nonparabolicity on electron confinement and effective mass in GaNxAs1-x/GaAs quantum wells”, Phys. Rev. B, vol. 69, no. 24, p. 245305, Jun. 2004.

[57] A. Kimura, C. A. Paulson, H. F. Tang, and T. F. Kuech, “Epitaxial GaN1-yAsy layers with high As content grown by metalorganic vapor phase epitaxy and their band gap energy”, Appl. Phys. Lett., vol. 84, no. 9, pp. 1489-1491, Mar. 2004.

[58] R. A. Arif, H. Zhao, and N. Tansu, “Type-II InGaN-GaNAs quantum wells active regions for laser applications”, Appl. Phys. Lett., vol. 92(1), Art. No. 011104, Jan. 2008.

[59] K. M. Yu, S. V. Novikov, R. Broesler, C. R. Staddon, M. Hawkridge, Z. Liliental-Weber, I. Demchenko, J. D. Denlinger, V. M. Kao, F. Luckert, R. W. Martin, W. Walukiewicz, and C. T. Foxon, “Non-equilibrium GaNAs alloys with band gap ranging from 0.8-3.4 eV”, Phys. Status Solidi C, vol. 7, no. 7-8, pp. 1847-1849, May 2010.

[60] C. K. Tan, J. Zhang, X. H. Li, G. Y. Liu, B. O. Tayo, N. Tansu, “First-Principle Electronic Properties of Dilute-As GaNAs Alloy for Visible Light Emitters”, J. Dis. Tech., vol. 9, no. 4, pp. 272-279, Apr. 2013.

[61] E. Yablonovitch and E. O. Kane, “Reduction of lasing threshold current density by the lowering of valence band effective mass”, J. Lightwave Technology, vol. LT-4, no. 5, pp. 504-506, May 1986.

[62] D. Ahn, S. L. Chuang, “Optical gain in a strained-layer quantum-well laser”, IEEE J. Quantum Electronics, vol. 24, no. 12, pp. 2400-2406, Dec. 1988.

[63] J. P. Loehr, and J. Singh, “Theoretical studies of the effect of strain on the performance of strained quantum well lasers based on GaAs and InP technology”, IEEE Journal of Quantum Electron., vol 27, no. 3, pp. 708-716, Mar. 1991.

[64] T. Ishikawa, and J. E. Bowers, “Band lineup and in-plane effective mass of InGaAsP or InGaAlAs on InP strained-layer quantum well”, IEEE Journal of Quantum Electron., vol. 30, no. 2, pp. 562-570, Feb. 1994.

[65] G. C. Osbourn, “Strained-layer superlattices from lattice mismatched materials”, J. Appl. Phys., vol. 53, no. 3, pp. 1586-1589, Mar. 1982.

[66] W. B. Holzapfel, “Physics of solids under strong compression”, Rep. Prog. Phys., vol. 59, no. 1, pp. 29-90, Jan. 1996.

[67] D. Yu, Y. Zhang, F. Liu, “First-Principles study of electronic properties of biaxially strained silicon: Effects on charge carrier mobility”, Phys. Rev. B, vol. 74, no. 24, p. 245204, Dec. 2008.

[68] Y. Duan, L. Qin, L. Shi, G. Tang, H. Shi, “Hybrid density functional theory study of bang gap tuning in AlN and GaN through equibixial strains”, Appl. Phys. Lett., vol. 100, no. 2, p. 022103, Jan. 2012.

[69] L. Dong, S. K. Yadav, R. Ramprasad, and S. P. Alpay, “Band gap tuning in GaN through equibiaxial in-plane strains”, Appl. Phys. Lett., vol. 96, no. 20, p. 202106, May 2010.

[70] D. Schneider, L. Elbrecht, J. Creutzburg, A. Schlachetzki and G. Zwinge, “In-plane effective mass of electrons in InGaAs/InP quantum wells”, Appl. Phys. Lett., vol. 77, no. 5, pp. 2828-2830, Mar. 1995.

[71] U. Ekenberg, “Nonparabolicity effects in a quantum well: sublevel shift, parallel mass, and Landau levels”, Phys. Rev. B, vol. 40, no. 11, pp. 7714-7726, Oct. 1989.

[72] H. Zhu, K. Lai, D. C. Tsui, S. P. Bayrakci, N. P. Ong, M. Manfra, L. Pfeiffer, and K. West, “Density and well width dependences of the effective mass of two-dimensional holes in (100) GaAs quantum wells measured using cyclotron resonance at microwave frequencies”, Solid State Communication, vol. 141, no. 9, pp. 510-513, Mar. 2007.

[73] A. R. Beattie and P. T. Landsberg, "Auger effect in semiconductors", Proceedings of the Royal Society A, 249(1959).

[74] G. G. Zegrya and A. S. Polkovnikov, "Mechanisms of Auger recombination in quantum wells", Journal of Experimental and Theoretical Physics, 86, 4(1998).

[75] R. I. Taylor, R. A. Abram, M. G. Burt, and C. Smith, “A detailed study of Auger recombination in 1.3 um InGaAsP/InP quantum wells and quantum well wires”, Semicond. Sci. Technol., vol. 5, no. 1, pp. 90-104, Jan. 1990.

[76] C. Smith, R. A. Abram, and M. G. Burt, “Auger recombination in a quantum well heterostructure”, J. Phys. C: Solid State Phys., vol. 16, no. 5, pp. L171-L175, Feb. 1983.

[77] N. K. Dutta, “Calculation of Auger rates in a quantum well structure and its application to InGaAsP quantum well lasers”, J. Appl. Phys., vol. 54, no. 3, pp. 1236-1245, Nov. 1982.

[78] A. Haug, “Auger recombination in quantum well semiconductors: calculation with realistic energy bands”, Semicond. Sci. Technol., vol. 7, pp. 1337-1340, 1992.

[79] J. Wang, P. V. Allmen, J. P. Leburton, and K. Linden, “Auger recombination in long-wavelength strained-layer quantum-well structures”, IEEE J. Quant. Electro., vol. 31, no. 5, pp. 864-875, May 1995.

[80] A. D. Andreev, E. P. O’Reilly, “Theoretical study of Auger recombination in a GaInNAs 1.3 um quantum well laser structure”, Appl. Phys. Lett., vol. 84, no. 11, pp. 1826-1828, Mar. 2004.

[81] H. Sakaki, T. Noda, K. Hirakawa, M. Tanaka, and T. Maysusue, “Interface roughness scattering in GaAs/AlAs quantum wells”, Appl. Phys. Lett., vol. 51, no. 23, pp. 1934-1936, Dec. 1987.

[82] I. Yamakawa, R. Oga, Y. Fujiwara, Y. Takeda, and A. Nakamura, “Atomic-scale observation of interfacial roughness and As-P exchange in InGaAs/InP multiple quantum wells”, Appl. Phys. Lett., vol. 84, no. 22, pp. 4436-4438, May 2004.

[83] G. H. Gu, D. H. Jang, K. B. Nam, and C. G. Park, “Composition fluctuation of In and well-width fluctuation in InGaN/GaN multiple quantum wells in light-emitting diode devices”, Microsc. Microanal., vol. 19, no. s5, pp. 99-104, Aug. 2013.

[84] A. B. Yankovich, A. V. Kvit, X. Li, F. Zhang, V. Avrutin, H. Liu, N. Izyumskaya, U. Ozgur, B. V. Leer, H. Morkoc, and P. M. Voyles, “Thickness variations and absence of lateral compositional fluctuations in aberration-corrected STEM images of InGaN LED active regions at low dose”, Microsc. Microanal, Mar. 2014.

[85] N. Nakagawa, H. Y. Hwang, and D. A. Muller, “Why some interfaces cannot be sharp”, Nature Materials, vol. 5, pp. 204-209, Mar. 2006.

[86] J. Singh, and K. K. Bajaj, “Role of interface roughness and alloy disorder in photoluminescence in quantum-well structures”, J. Appl. Phys., vol. 57, no. 12, pp. 5433-5437, Jan. 1985.

[87] J. Singh, K. K. Bajaj, S. Chaudhuri, “Theory of photoluminescence line shape due to interfacial quality in quantum well structures”, Appl. Phys. Lett., vol. 44, no. 8, pp. 805-807, Apr. 1984.

[88] J. Singh, Electronic and optoelectronic properties of semiconductor structures Ch. 1, 23-24 (Cambridge University Press, 2003).

[89] L. A. Coldren, S. W. Corzine, and M. L. Masanovic, “Diode lasers and photonic integrated circuits”, (Wiley, New Jersey, 2012), pp. 211-212, Chap. 4

[90] P. Harrison, “Quantum Wells, Wires and Dots”, (Wiley, Chichester, 2010), pp. 273, Chap. 10.

[91] S. M. Goodnick, and P. Lugli, “Effect of electron-electron scattering on nonequilibrium transport in quantum-well systems”, Phys. Rev. B, vol. 37, no. 5, pp. 2578-2588, Feb. 1988.

[92] I. Vurgaftman and J. R. Meyer, “Nitride Semiconductor Devices”, J. Piprek, Ed., (Wiley, New York, 2007), pp. xx, Chap. 2.

[93] I. Vurgaftman, and J. R. Meyer, “Band parameters for nitrogen-containing semiconductors”, J. Appl. Phys., vol. 94, pp. 3675-3696, Sep. 2003.

[94] H. Shimizu, K. Kumada, S. Uchiyama, and A. Kasukawa, “1.2um range GaInAs SQW lasers using Sb as surfactant”, Electronics Letters, vol. 36, no. 16, pp. 1379-1381, Aug. 2000.

[95] X. Yang, M. J. Jurkovic, J. B. Heroux, and W. I. Wang, “Low threshold InGaAsN/GaAs single quantum well lasers grown by molecular beam epitaxy using Sb surfactant”, Electronics Letters, vol. 35, no. 13, pp. 1082-1083, Jun. 1999.

Chapter 5: Electronic Properties of Dilute-Anion GaN-Based Semiconductor Alloys

Group III-Nitride is regarded as the important semiconductor class in near decades [1-10]. However, the development in the novel dilute-impurity GaN-based semiconductor materials is at the early stage in comparison to that of the conventional III-Nitride semiconductor materials. As discussed in Chapter 2, the electronic properties in the dilute-anion GaN-based semiconductor materials are still not well understood with limited literature in the past decades until most recently [5, 10-30]. The advances in the dilute-nitride GaAs-based semiconductors for low threshold laser devices in the past have been attributed to the understanding of electronic properties, device physics understanding and material epitaxy improvement [31-35]. While the material epitaxial technique has been progressing in the area of dilute-anion GaN-based semiconductor materials [5, 10-11], the motivations behind the implementation of these semiconductors are still unclear attributed to the lack of understanding in the materials. Therefore, due to the technical importance that is potentially inflicted by the dilute-anion GaN-based semiconductor materials, the understanding of the optoelectronic properties of these materials will provide insightful information for the development of the alloys.

In this work, we focus in the dilute-anion GaN semiconductor especially the dilute-As GaNAs and the dilute-P GaNP alloys. We present the analysis of the electronic properties of dilute-As GaNAs and dilute-P GaNP by using First-Principle Density Functional Theory. The Arsenic (As) atoms with different As concentrations varying from 0%up to 12.5% are introduced into the GaN material as impurities in the alloy. The band structure, energy band gap, and electronic properties of the dilute-As GaNAs alloy are presented. Similar study has also been performed for dilute-P GaNP alloys, with the band structures and related electronic properties presented in section 5.3. In addition, the potential of implementing the material into GaN-based system is evaluated by investigating the natural band alignment of dilute-As GaNAs / GaN material system.

5.1. Analysis of Electronic band Structures of Dilute-As GaNAs Alloy

5.1.1. Computational Details for Band Structure Calculations

In our DFT analysis, the supercell approach was used to build appropriate crystal structures for the band calculations. To illustrate the supercell approach, Figure 5-1 shows a constructed GaNAs alloy crystal structure with 4x4x2 supercell consisting of a total of 128 atoms. The 128-atom model of GaNAs crystal consists of 64 Ga atoms, 63 N atoms and 1 substituted As atom, corresponding to 1.56% As in the dilute-As alloy. The band structure calculations were performed by using the projector augmented wave (PAW) method as implemented in the MedeA-VASP software [36]. The use of local density approximation (LDA) exchange-correlation potential was employed in the calculation. The electronic wave functions are described in plane wave basis with a cutoff energy of 400 eV. The structure optimization was performed by relaxing the atom positions with the Hellmann-Feynman force set to 0.02 eV/Å. The external stress was set to 0 GPa, and the energy convergence tolerance was set to 1 10 eV atom. The Gamma centered Monkhorst-Pack grid and high symmetry k-points were used for the band structure calculations. Note that different Monkhorst-Pack k-point meshes were generated in the calculations attributed to the use of different supercell sizes. The spin-orbit coupling was excluded in the calculation, as its effect in the wide band gap III-nitride semiconductor is insignificant.

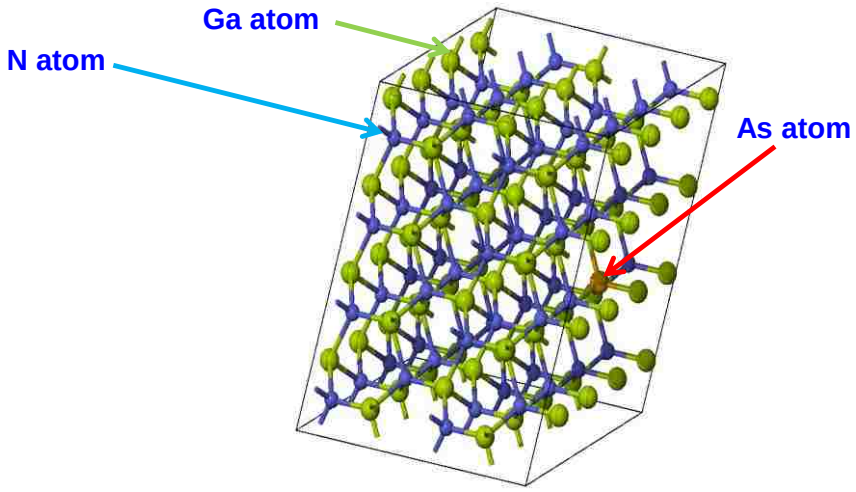

Figure 5-1: *A 4x4x2 supercell built by using MedeA-VASP software. This 128-atom supercell consists of 64 atoms (Ga) atoms, 63 Nitrogen (N) atoms and 1 Arsenic (As) atom, corresponding to 1.56% As-content in GaNAs alloy.*

5.1.2. Electronic Band Structures of Dilute-As GaNAs Alloy

By using the calculations as described in chapter 5.1.1, the electronic band structures of the dilute-As GaNAs alloys can be calculated. Figure 5-2(a) and figure 5-2(b) show the band structures for GaN and GaNAs (6.25% As-content) alloys calculated by using the DFT method respectively. From our analysis, the conduction band minimum (CBM) and valence band maximum (VBM) for dilute As-content GaNAs (up to 12.5% As-content) exhibited direct band gap properties, indicating its suitability for photonics device applications. The energy band gaps for dilute-As GaNAs alloy were obtained from the difference between the CBM and the VBM taking into account the scissor operator [37]. The scissor operator was employed to correct the band gap error originated from the LDA calculation [37]. Scissor operator is a function of dielectric constant, and the scissor operator value for each GaNAs alloy is varied attributed to the changes in the dielectric constant in the material [37]. The dielectric constant is determined through linear interpolation between the GaN and GaAs materials. As shown in figure 5-2, the incorporation of tiny amount of Arsenic impurity into the GaN alloy could lead to the significant reduction in the band gap energy of the alloy. Based on the initial findings in the band structures, further investigation on the dilute-As GaNAs alloy was carried out in order to gain more information on the alloy.

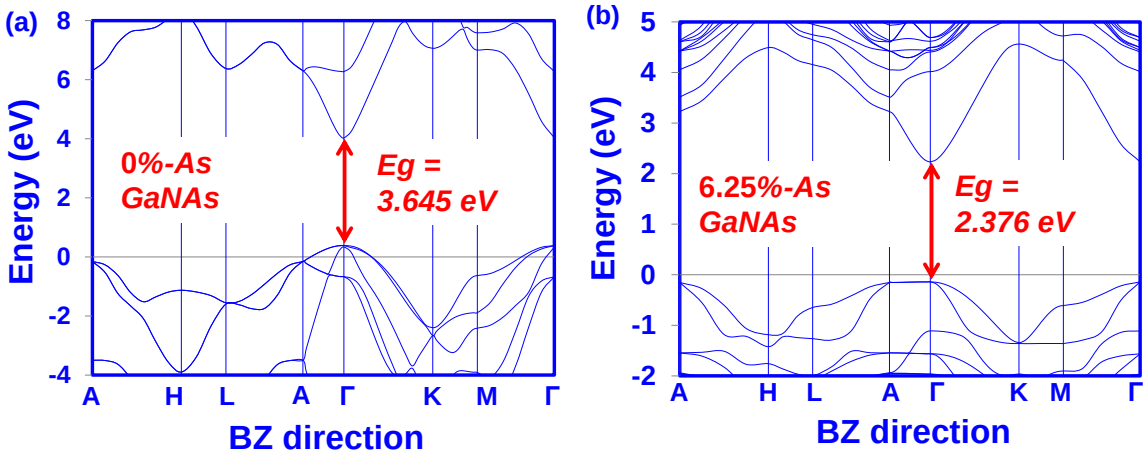

Figure 5-2: *Band structure diagrams for GaNAs alloy with (a) 0% and (b) 6.25% As-content. Energy band gap is the energy difference between the conduction band minimum (CBM) and valence band maximum (VBM).*

5.1.3. Band Gap and Band Bowing Energy of Dilute-As GaNAs Alloy

Figure 5-3 shows the comparison of the DFT-calculated and experimental energy band gaps for dilute-As GaNAs alloy as a function of As-content in the alloy. Kimura and co-workers reported the experimental data for energy band gaps measured from MOCVD-grown dilute-As GaNAs alloy [10], and the numerical results show good agreement with these experimental data. Figure 5-3 shows that when the As-content in the GaNAs alloy increases, the energy band gap of the alloy reduces. The energy band gap covers from 3.645 eV to 2.232 eV for the GaNAs alloy with As-content up to 12.5%.

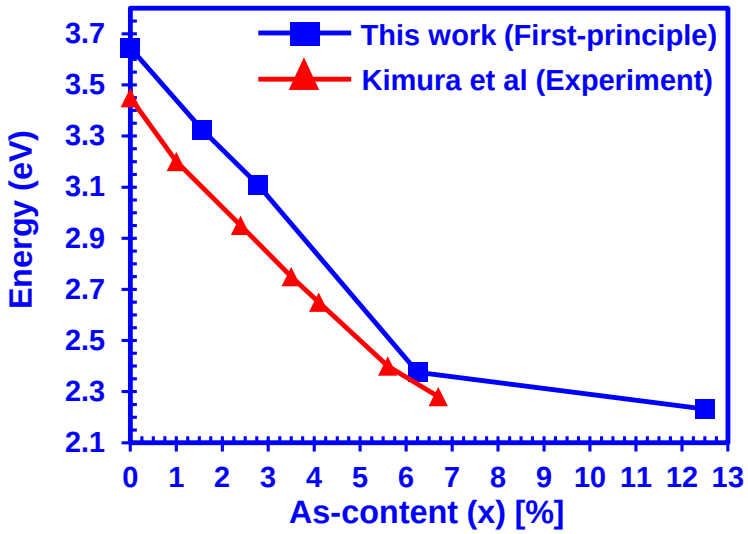

Figure 5-3: *Energy band gap of dilute-As GaNAs alloy from As-content of 0% up to 12.5%, ranging from 3.645 eV to 2.232 eV, with corresponding experimental data [10].*

Slight discrepancies between the calculated and the measured results were observed, even though the trend shows reduction in bandgap as the As-content increases in the dilute-As GaNAs alloy. While these discrepancies potentially arise from the strain effect in the alloy and/or As-clustering effect in the GaNAs alloy grown by MOCVD, another reason is that the band gap information was obtained at two temperature conditions. Our calculation was set for zero-temperature limit, which is commonly used in DFT calculation [38-39]. The optical absorption and reflection measurements by Kimura and co-workers were performed at room temperature. As stated by Shishkin and co-workers [39], the experimental temperature dependence for the band

gap of material is significant and highly dependent on material quality, thus the band gaps of materials will be more accurate for comparison at low temperature whenever possible. However, the available experimental data on dilute-As GaNAs was limited to room-temperature results [10, 11, 18], thus restricting the possibility for comparison at similar temperature. Furthermore, as stated in Section 5.1.2, the band gap problem is well known in DFT calculation. All these conditions would lead to the discrepancies of the result in comparison.

Since the temperature-dependent band gap of semiconductors is known to reduce when the temperature increases [40-42], one could perform molecular dynamics simulation for thermal expansion, with the expense of the computational cost. The Varshni relation [41, 42] can be used for including the temperature dependence of energy band gap. However, it is to be emphasized that this work is aimed to provide the necessary band parameter information of dilute-As GaNAs alloy, as well as its potential application for LEDs/lasers in the visible spectral regimes.

On the other hand, the effect of As impurity in lowering down the energy band gap of dilute-As GaNAs alloy can be attributed primarily to the upward movement of the valence band of the alloy after the As impurity incorporation into the alloy [11, 18]. Moreover, it is also expected to observe similar effect should the As impurity be incorporated into InGaN ternary alloy, resulting in the reduction of energy band gap of the ternary alloy. Nevertheless, this work is focused in the electronic structure of dilute-As GaNAs alloy and its potential use as the optoelectronic devices. Further study on the effect of As impurity on InGaN ternary alloy would be necessary in order to gauge its usefulness for the visible light emitters.

Figure 5-4 shows the emission wavelength as a function of As-content in the dilute-As GaNAs alloy. As shown in figure 5-4, the light emission wavelength is in the region of 400 nm with As-content of 2.78% in the dilute-As GaNAs alloy which can be used for violet LEDs applications. In addition, the light emission wavelength reaches 523 nm with As-content of 6.25% in the GaNAs alloy. This suggests the possibility of the alloy to be implemented as active region for green-emitting LEDs. Further incorporation of As-content up to 12.5% in the GaN alloy leads to the 560 nm light emission wavelength, hinting the possibility of yellow/red light emission should

more As-content be incorporated into the dilute-As GaNAs alloy. Note that the existence of polarization field in the III-Nitride active region will also lead to the conduction and valence bands bending [3, 16-17], which in turn results in red shift of the emission wavelengths [3, 16-17]. Thus, yellow or red light emission might be achieved with low As-content in dilute-As GaNAs QW under the polarization effect.

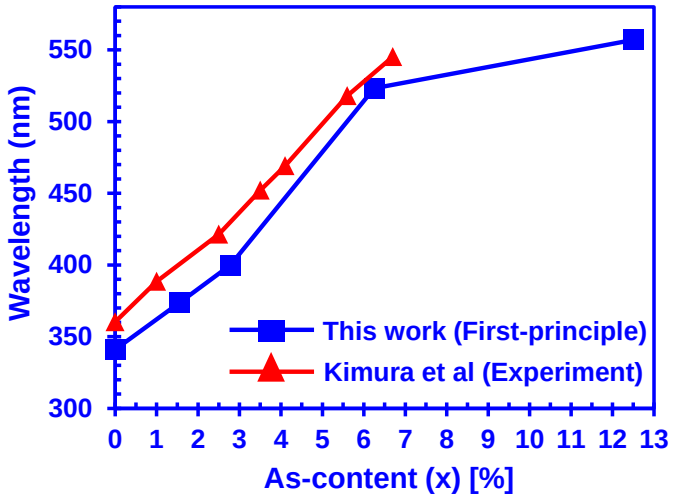

Figure 5-4: *Emission wavelength of dilute-As GaNAs alloy from As-content of 0% up to 12.5%.*

Figure 5-5 displays the energy band gap of GaNAs alloy in the whole composition range. The dotted line in figure 5-5 represents the band gap result by using the virtual crystal approximation (VCA). The overall composition dependence of the alloy band gap is written as

$$E_{g\_GaNAs}(x) = E_{GaN}(1-x) + E_{GaAs}(x) \quad (5.1).$$

The VCA linear interpolation indicates the important effects of the molar fraction of the GaAs or GaN component in the alloy onto the band gap changes. The VCA result without bowing parameter is largely different from the calculated and the experimental data. The linear Vegard relation is thus extended by adding the bowing parameter into the expression. The solid line in the figure shows a line fitting with the DFT-calculated data and the experimental data through the use of the following equation:

$$E_{g\_GaNAs}(x) = E_{GaN}(1-x) + E_{GaAs}(x) - b(1-x)(x) \quad (5.2).$$

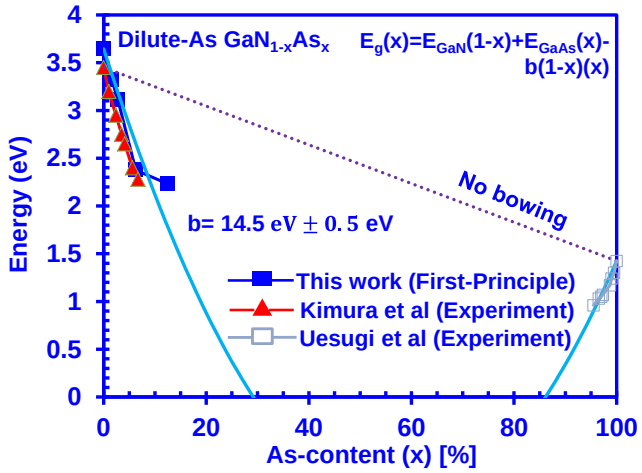

Figure 5-5: *Comparison between our DFT calculations and experimental data, with bowing parameter obtained through line fitting with the data.*

The bowing parameter of 14.5 eV ± 0.5 eV is found to have a reasonable matching with the energy band gap data. Meanwhile, bowing parameter in the 16 eV range were suggested previously [10, 11], but it appears that the line fit in figure 4-5 does not agree very well with our data. Along this quadratic curve, the band gap would rapidly reduce from both ends and become negative within 25% to 85% of As-content of the alloy. This can be understood through the formulated Hamiltonian matrices in the degenerate perturbation theory, explaining that the composition dependency on the N-rich side is more than just a simple quadratic function [11].

5.1.4. Effective Masses and Split-off Band Energy of Dilute-As GaNAs Alloy

The next important band properties that is investigated for the dilute-As GaNAs alloy is the effective mass and split-off band energy. These parameters are essentially important for representing the behaviour of the materials and also for the improvement in the optical properties and carrier transport simulations. Figure 5-6 present the carrier effective masses of the dilute-As GaNAs alloy. The parabolic line fitting method is used in obtaining the effective mass parameter [43]. A parabolic line fit to the conduction band dispersion relation is used to determine the effective mass of electrons. For GaN alloy, the conduction effective mass is 0.2 m_0 in the k_z direction and 0.17 m_0 in the k_xk_y direction. The parabolic line fitting method is also used for the

valence bands consisting of heavy hole, light hole and split-off bands. The effective mass parameters are obtained along the k_z direction, as well as the in plane direction (k_xk_y) near the gamma point. The average effective mass is also obtained for the electrons, heavy hole, light hole and split-off.

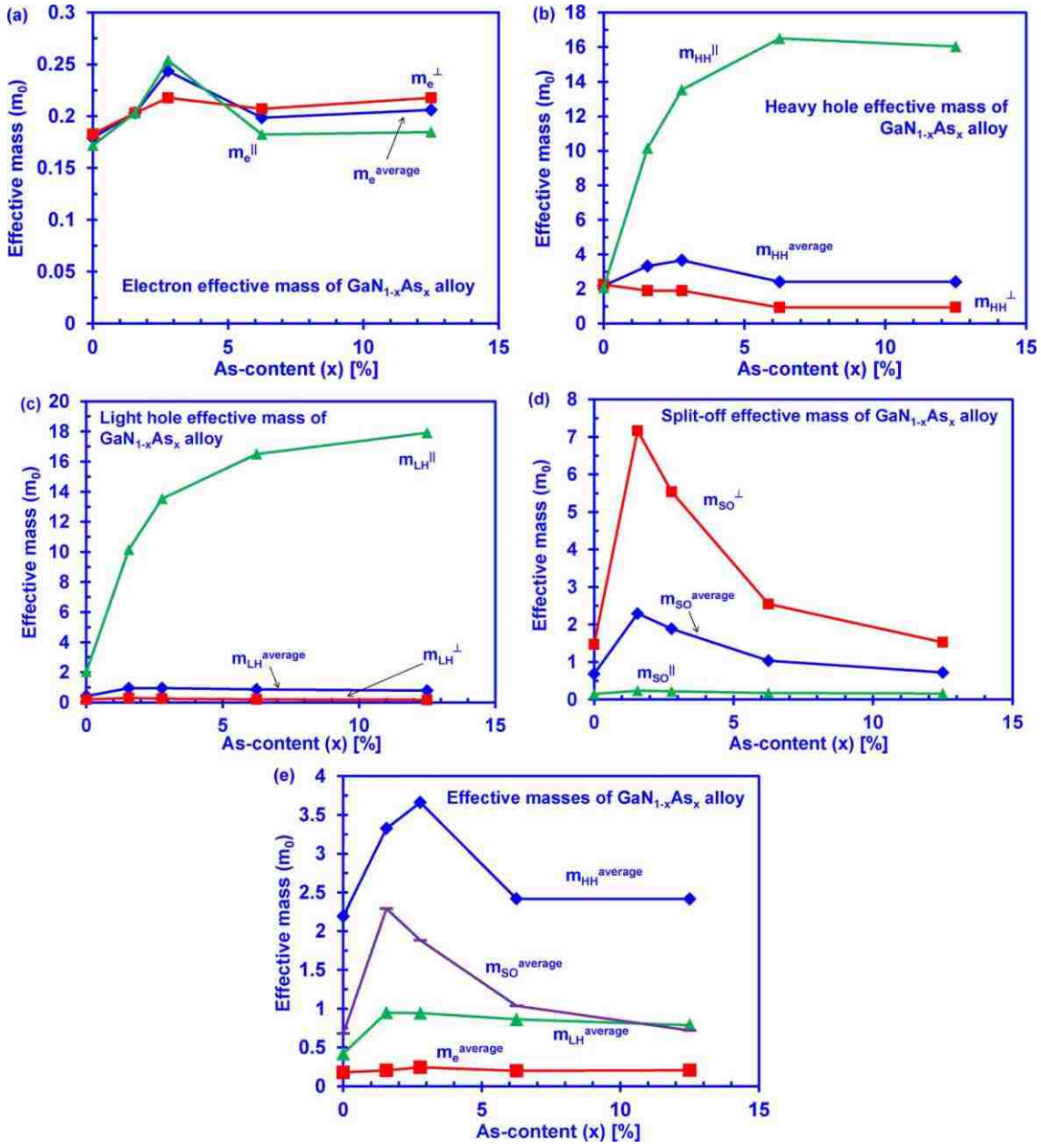

Figure 5-6: *Carrier effective masses obtained through energy dispersion relation and parabolic line fitting with the calculated DFT band for: (a) electron; (b) heavyhole; (c) light hole; (d) split-off bands; and (e) comparison of average carrier effective masses as a function of As-content in GaNAs* alloy.

From figure 5-6, it is shown that the electron effective mass only varies slightly from 0% As-content to 12.5% As-content. Interestingly, the hole effective mass changes rapidly from 0% to 6.25% As-content, but remains constant in a higher percentage of As-content in the GaNAs alloy. From figure 5-6(e), our analysis shows that the electron effective masses for dilute-As GaNAs alloy are relatively unchanged for all compositions studied here, which are very different than the corresponding characteristics observed in dilute-nitride based (In)GaAsN alloy [35]. For dilute-nitride based (In)GaAsN alloy, the electron effective mass have remarkable changes, while the effective masses for hole bands remained unchanged. The reason behind this is that the addition of nitrogen atoms into the dilute-nitride GaAsN alloy plays a key role in the modification of conduction band structure, due to its strong localized resonant energy level close to the conduction band. In contrast, the incorporation of As atoms into the dilute-As GaNAs alloy leads to significant modification in the effective masses for the heavy hole in the material, while the electron effective masses remain largely unperturbed by the impurity addition. Consequently, the possible explanation of the effect shown in the effective masses can be attributed to the impurity level of As-localized states in the bands. The localized As states was theoretically predicted to possess an energy level of 0.4 eV above the uppermost valence band [18], which leads to strong modification of the hole bands in dilute-As GaNAs alloy.

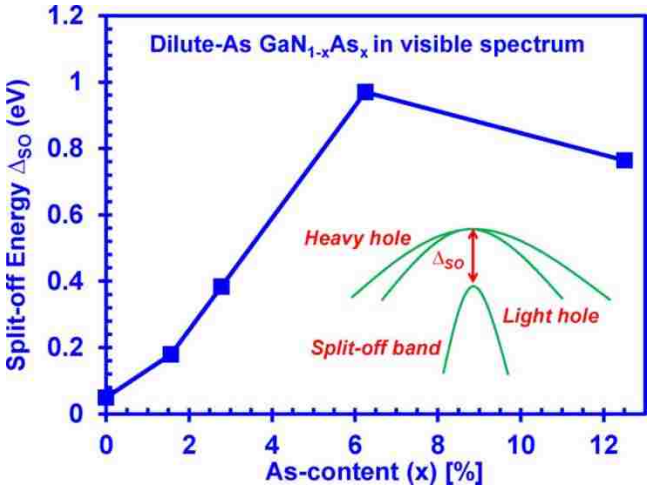

Figure 5-7: *Split-off energy of dilute-As GaNAs alloy from 0% up to 12.5% As-content, obtained through the energy difference between the valence band maximum (VBM) and the split-off band (SO) at Γ–point in Brillouin Zone.*

Figure 5-7 shows the split-off energy of dilute-As GaNAs alloy as a function of As-content. The introduction of As-content in the GaNAs alloy results in the general increase of split-off energy. This characteristic is interesting in the fact that both GaN and GaAs alloys possess split-off energy less than 0.5 eV [44] while the dilute-As GaNAs alloy has significant increase of split-off energy at low As-content.

Based on our finding, for higher As-content dilute-As (> 6.25%) GaNAs alloy, the As clustering effect appears to play significant role resulting in deviation from the trend exhibited in the band parameters for the lower As-content dilute-As GaNAs alloy. In addition, the structural changes had also been reported for high As-content GaNAs alloy [11], which may lead to any deviation. Further investigation on the effect of As clustering in the dilute-As GaNAs alloy with higher As-content is still required.

5.2. Analysis of Band Alignment in Dilute-As GaNAs / GaN Material System

As the electronic properties of the dilute-As GaNAs alloy is studied, the dilute-As GaNAs alloy is shown to exhibit strong potential to be used as an alternative material for the light emitting applications. In order to implement dilute-As GaNAs alloy in devices such as LEDs, semiconductor heterostructures between dilute-As GaNAs alloy and GaN alloy need to be formed. The understanding of the band discontinuities for two different III-V or III-Nitride materials is critical [10, 45-57] for designing nanostructures or heterostructures applicable in device implementation. Up to today, there has been no comprehensive and conclusive study in predicting and determining the natural band alignment between GaN and dilute-As GaNAs alloy. Therefore the understanding of the band discontinuity of GaNAs / GaN will be essential for evaluating the optical and carrier transport properties in devices incorporating this heterostructure.

In this chapter 5.2, a comprehensive quantitative analysis of the relative natural band alignment of dilute-As GaNAs / GaN heterostructures using First-Principle method is carried out. We examine the natural band offsets of the strain-free dilute-As GaNAs alloy relative to the GaN alloy. In addition to that, we also discussed about the source of the drastic reduction of the band

gap from analyzing the band offset between GaN and dilute-As GaNAs alloy, in which the upward movement of the valence band of the dilute-As GaNAs alloy was shown to contribute significantly to this effect. Our finding provides useful understanding of the band parameters important for enabling the implementation of dilute-As GaNAs alloy and heterostructures in GaN-based electronics and optoelectronics device technologies.

5.2.1. Computational Details for Band Alignment Calculations

The determination of band offsets between two materials can be performed through the projected local density of states calculation (LDOS) [47] and also the potential line-up method [48-49]. While both methods are capable of providing insight on how the alignment between two materials should be, the potential line-up method is chosen in this work simply because the LDOS calculation requires higher demand of convergence parameters which were previously identified, resulting in a slower convergence compared to that of the charge density [50]. Note that the natural band alignment of the unstrained system (GaN / dilute-As GaNAs) is focused in our DFT calculation. The advantage of this alignment for a material system is that it can be directly connected to the physical situation of photoelectrode [51-52] and active regions for lasers or LEDs [16, 17]. In the potential line-up method, the calculation of valence band offset (VBO) between two different materials is a combination of two terms which are the band structure term (ΔE_v) and the electrostatic term (ΔV). For the band structure term, it is defined as the difference between the top of the valence bands of two bulk materials with respect to the average electrostatic potential at core. The information of the valence bands of the bulk materials can be obtained from two independent standard bulk band structure calculations. For the electrostatic potential term, it is obtained from the lineup of the macroscopic average electrostatic potential in two material slabs, by aligning it with respect to the vacuum level in the slabs [51].

Consequently, in our DFT analysis, two independent approaches were performed to obtain the valence band maximum (VBM) difference and the macroscopic potential difference between GaN and dilute-As GaNAs materials. The supercell approach was applied to build the appropriate

crystal structure for the electronic properties calculation. The crystal structures of GaN and dilute-As GaNAs alloys were built using the atomistic simulation package MedeA-VASP [36]. Figure 5-8(a) and 5-8(b) show a constructed GaNAs alloy bulk and slab crystal structures consisting of a total of 32 atoms respectively. With one N atom being substituted by one As atom, the composition of the dilute-As GaNAs crystal structure is thus 6.25%-As. Similarly, bulk and slab structures with a total of 48 atoms can also be constructed with one As atom as the impurity in the system, leading to 4.17%-As GaNAs alloy. In addition, the slab structures for the dilute-As GaNAs and GaN in a repeated-slab geometry and nonpolar orientation are chosen in the calculation in order to negate the potential polarization field, which would affect the electrostatic potential in the structures.

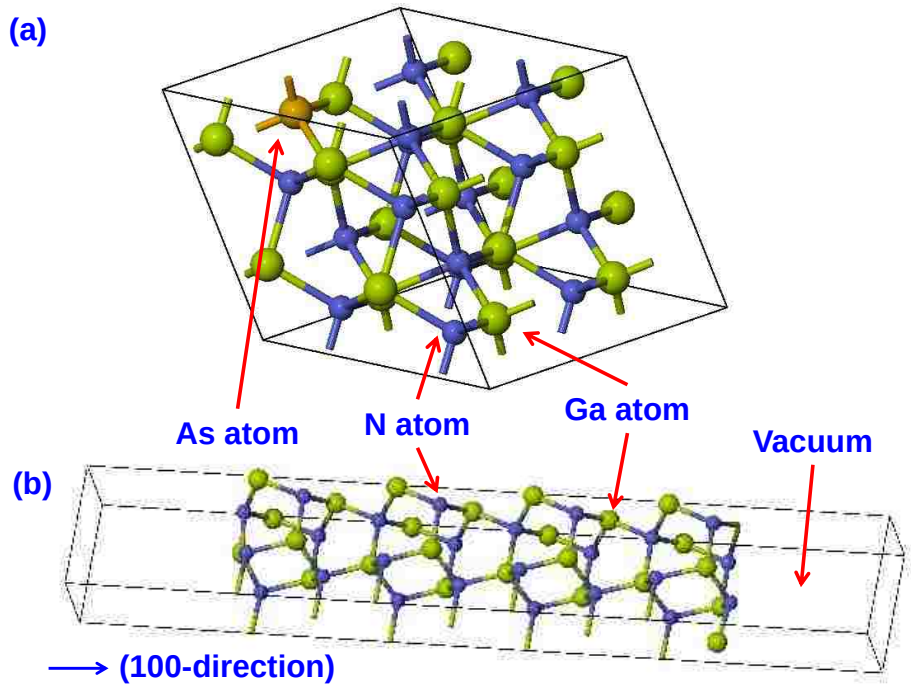

Figure 5-8: *(a) Supercell and (b) Slab of GaNAs alloy built using MedeA-VASP package. These 32-atom supercell consists of 16 Gallium (Ga) atoms, 15 Nitrogen (N) atoms and 1 Arsenic (As) atom, corresponding to 6.25% As-content in GaNAs alloy.*

Based on the constructed crystal structures of dilute-As GaNAs and GaN illustrated in figure 5-8, the calculations of the bulk band structure and the electrostatic potential were then performed using MedeA-VASP with projected augmented wave pseudopotentials (PAW) method

implemented in the code [36]. Local density approximation (LDA) exchange-correlation potential was used in the DFT calculation [36]. The electronic wave functions are described in plane wave basis with the cutoff energy fixed at 400 eV. The structure optimization was performed by relaxing the atom positions with the Hellmann-Feynman force set to 0.02 eV/Å before the calculation takes place. The energy convergence tolerance was set at 1×10^{-5} eV/atom, while the external stress was set to 0 GPa. The Gamma-centered Monkhorst-Pack grid and high symmetry k-points were used for the band structure and the electrostatic potential calculations. Note that different Monkhorst-Pack k-point meshes were generated in the calculations attributed to the use of different supercell and slab sizes. The spin-orbit coupling was excluded in both calculations since the effect in the wide band gap III-nitride semiconductor is negligible. These parameters were consistently used in both supercell and slab approaches.

5.2.2. Conduction and Valence Band Position in Dilute-As GaNAs / GaN System

Figure 5-9 shows the computed planar average and macroscopic average of electrostatic potential energy within slabs consisting of layers of GaN and dilute-As GaNAs, as well as the vacuum region. As shown in figure 5-9, the planar average and macroscopic average electrostatic potential of the GaN and dilute-As GaNAs alloys were aligned by referencing it to the vacuum energy level respectively.

In our study, the vacuum energy level was aligned as 0 eV simply to better represent the result. In addition, due to slight fluctuation of macroscopic average potential, the average of the macroscopic average potential of the GaN and dilute-As GaNAs alloy was obtained which is represented as a solid straight line as shown in figure 5-9. Two key factors need to be taken into consideration for analyzing the planar average and macroscopic average electrostatic potentials in DFT calculation. First, the interface between the GaN alloy or dilute-As GaNAs alloy and the vacuum results in the fluctuation of the planar average electrostatic potential. At some distances away from the interface, the planar average electrostatic potential was stabilized and this could

be represented for the material [51]. Second, the As impurity existence in the dilute-As GaNAs slab results in the fluctuation of planar and macroscopic average around the impurity, due to the different charge density possessed by the different types of atoms.

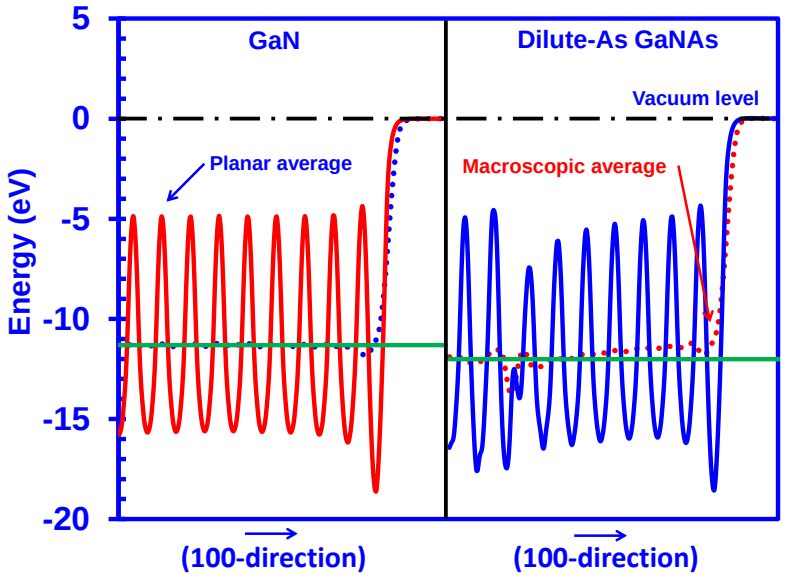

Figure 5-9: *The planar average (solid line) and the macroscopic average (dot line) of the electrostatic potential near the surface for GaN and dilute-As GaNAs alloys computed within the DFT-LDA functional. The vacuum level is aligned as 0 eV(dash line) as shown in the figure.*

Building on the computed result from band structure and macroscopic average electrostatic potential calculations, the VBO of GaN/dilute-As GaNAs material system is determined for various composition ranged from 0% up to 12.5%-As impurity. The conduction band position for GaN / dilute-As GaNAs were obtained by adding the experimental band gaps [11] onto the calculated valence band position, similar to the approaches reported by others [52-54, 57]. This approach is commonly used in DFT calculation to avoid the band gap error originated from the LDA approximation [50-54, 57]. Note that the natural ΔE_v is found as insensitive between semiconductor systems with a common anion or cation and with the same crystal structure [54], thus the use of LDA for the calculation for GaN and dilute-As GaNAs alloys is justified and should provide the necessary insight of how the ΔE_v and ΔE_c evolve with different As impurity composition of dilute-As GaNAs alloy.

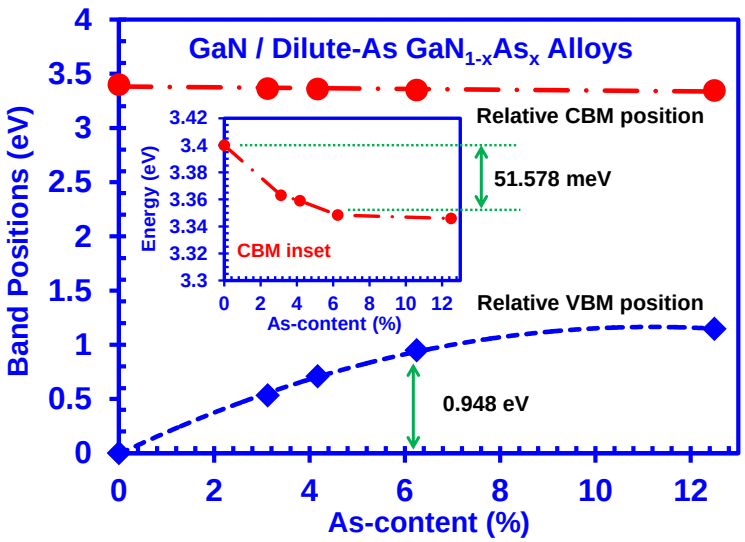

Figure 5-10: *VBM and CBM position of dilute-As GaNAs alloy relative to GaN as a function of arsenic content up to 12.5%. The figure inset shows the CBM position of dilute-As GaNAs alloy in a relatively smaller energy scale.*

Figure 5-10 shows the valence band and conduction band alignment of dilute-As GaNAs alloy with respect to the GaN as a function of As-composition up to 12.5%. As the GaN alloy is taken as a reference, its valence band position is presumed at 0 eV while its conduction band position is set at 3.4 eV, constituting 3.4 eV energy band gap. When As impurity is introduced into GaN, the conduction band position is lowered down from 3.4 eV at 0%-As GaNAs to 3.346 eV at 12.5%-As GaNAs, as shown in figure inset of figure 5-10. In our finding, the conduction band energy of dilute-As GaNAs alloy is reduced by approximately 55 meV over the studied composition range from 0% to 12.5%-As. The corresponding valence band position raises up from 0 eV for 0%-As GaNAs alloy up to 1.15 eV for 12.5%-As GaNAs alloy. Based on the experimental measurement on the MBE-grown GaNAs alloy, Yu and co-workers reported the valence band position for the dilute-As GaNAs alloy relative to GaN as 0.8 eV ± 0.3 eV from 2% to 10% of As-content in the alloy, and 1 eV ± 0.3 eV with roughly 17.5% of As-content in the alloy [11]. Our First-Principle findings are in reasonable agreement with the experimental data available in the literature [11].

The discrepancies between our computed data and experimental results for the GaN / dilute-As GaNAs alloy could mainly be caused by the strain effect existing in the grown alloy due to the much larger atomic size of arsenic atom and also the formation of As-cluster and As-pair in the dilute-As GaNAs alloy. Note that our result is computed based on ideal and relaxed structure, and the polarization field effects as well as charge transfer issue at the interface between GaN and dilute-As GaNAs alloy are not taken into consideration.

As shown in figure 5-10, the valence band offset is significantly larger than the conduction band offset for the GaN / dilute-As GaNAs material system. The results (figure 5-10) for dilute-As GaNAs alloy exhibit very distinct corresponding properties as observed in the dilute-nitride GaAsN / GaAs heterostructures [46]. The incorporation of dilute amount of nitrogen (1-2%) in the GaAs or InGaAs result in large bandgap reduction accompanied by a large conduction band offset ratio (~80%) [46]. The addition of nitrogen atoms in dilute amount into the GaAs or InGaAs alloy introduced the localized energy states near to the conduction band of the GaAs or InGaAs alloy, which in turn result in strong modification of the conduction band properties in the GaAsN or InGaAsN alloys strongly affected by the narrow resonant N energy states.

In dilute-As GaNAs alloy, the addition of As impurity in the GaN alloy results in the formation of localized As states about 0.4 eV above the valence band of GaN alloy [18]. Consequently, there is a strong interaction between the localized As states and the valence band states of GaN resulting in a strong modification in the valence band properties for the dilute-As GaNAs alloy. The conduction states of the dilute-As GaNAs alloy are however much less influenced since the position of the impurity level of the As-states is far away from the conduction band edge. This finding indicates that the valence band of the dilute-As GaNAs alloy is heavily perturbed by the As-impurity while conduction band is relatively less affected.

5.2.3. Natural Band Alignment in Dilute-As GaNAs / GaN MaterialSystem

The understanding of the band offsets provides an intuitive insight into the source of the bandgap bowing [51]. In the case of GaN / dilute-As GaNAs heterojunction, the dominant valence

band offsets strongly indicate the bandgap bowing as attributed to the upward movement of the valence band edge positions. The physical reason behind this finding can be explained due to the strong interactions of the localized As states and the valence band edge in GaN.

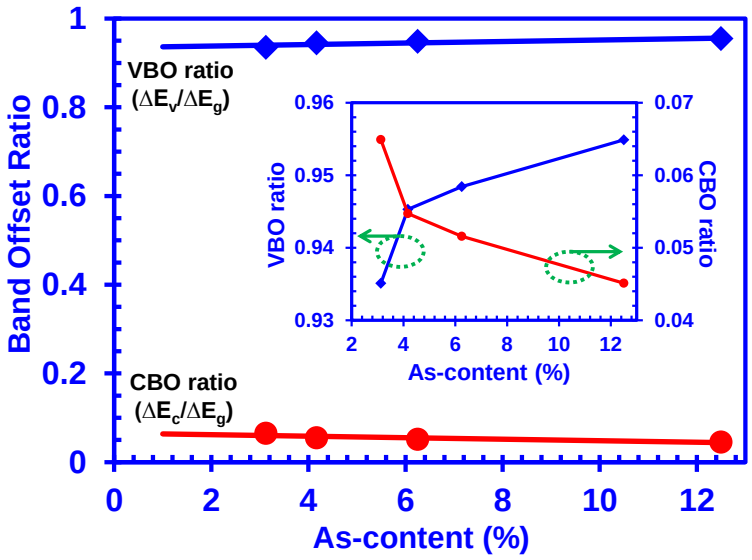

Figure 5-11: *The valence band offset (VBO) ratio and conduction band offset (CBO) ratio of the GaN / dilute-As GaNAs heterojunction as a function of arsenic content up to 12.5%-As.*

Figure 5-11 shows the VBO and CBO ratios as a function of arsenic composition up to 12.5% As-content for the GaN / dilute-As GaNAs material system. The VBO ratio is much higher than that of the CBO ratio in the GaN / dilute-As GaNAs material system. Overall, the VBO ratio can be approximated as 0.95, while the CBO ratio is relatively small at 0.05. The figure inset of the figure 5-11 shows that the VBO ratio has slight increment while CBO ratio has slight reduction over the composition range. This finding can be reasonably explained, as the increment of As percentage in the GaN results in stronger interaction between the localized states and its valence states. Based on this result and judging the trend of the CBO and VBO ratio values with respect to the As composition, the CBO : VBO ratio for dilute-As GaNAs can be taken as 5:95 for As-content up to 12.5 %. The determination of the CBO and VBO ratios is essential for enabling proper design of this heterostructure in nanostructure and device applications [42].

Prior works by MBE epitaxy have shown the challenges in obtaining crystalline form of dilute-As GaNAs for As-content above 25% [11]. Yu and co-workers showed that the XRD

measurement on MBE-grown dilute-As GaNAs retains its crystallinity structure up to As-content of 17.5%, and higher As incorporation into the film results in amorphous structure attributed to the strong clustering of As in the alloy. The crystallinity of the GaNAs alloy was only recovered in the regime of dilute-nitride GaNAs with N-content less than 15% [11]. As a result, the band offset ratio value of GaN / dilute-As GaNAs alloy should only be considered in the crystalline structure for As-content below 17.5%.

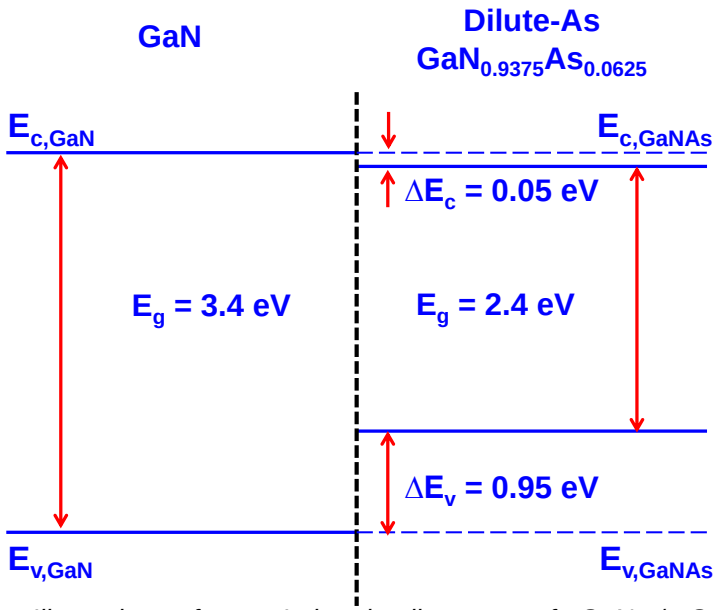

Figure 5-12: *Illustration of type-I band alignment of GaN / $GaN_{0.9375}As_{0.0625}$ heterojunction based on the calculated conduction to valence band offset ratio.*

Our analysis indicates a type-I band alignment for GaN / dilute-As GaNAs heterojunction with As-content ranging from 0% up to 12.5%, as illustrated in figure 5-12. In principle, a single type-I quantum well structure can be formed with dilute-As GaNAs active region and GaN or AlGaN barrier regions. The enhancement of the hole localization by using dilute-As GaNAs QW structure is expected to result in the increment of the exciton binding energy [53, 58]. However, the use of GaN barriers will result in relatively weak electron confinement in the GaNAs QW. The use of AlGaN tensile barriers [59] will potentially result in the strain compensation and improved barrier confinement in type-I GaNAs QW structure. In addition, the use of dilute-As GaNAs alloy had previously been suggested in type-II InGaN / dilute-As GaNAs QWs [16, 17] for addressing the charge separation issue in the QW. The use of dilute-As GaNAs with large valence band offset in

type-II QW structure results in strong hole confinement, which in turn increase the electron-hole wavefunction overlap in polar InGaN-based QWs resulting in improved spontaneous emission rate and optical gain [16, 17].

5.3. Analysis of Electronic Band Properties of Dilute-Anion GaN-based Alloy

As discussed in earlier section in this chapter, in comparison to the progress in the InGaN and AlGaN alloys, the research involving the common-anion nitride-based ternary alloy. This includes the dilute-P GaNP alloy, in which the study is still at its early stage [23-28]. The crystal growth of dilute-P GaNP was first successfully carried out by Igarashi and co-workers with halide vapor phase epitaxy [24]. The pioneering growth of GaNP alloys led to the successful incorporation of P impurity into the GaN alloy by using molecular beam epitaxial (MBE) technique, which resulted in a significant redshift of the photoluminescence peak emission wavelength [25]. Building on the promising features of the dilute-P GaNP alloy, Yoshida and co-workers managed to perform the growth of dilute-P GaNP alloys through metalorganic chemical vapor deposition technique (MOCVD) and fabricated a single quantum well light emitting diode device with the dilute-P GaNP alloy as the medium for the active region [26]. Even though these works demonstrated the possibility of realizing the growth of this alloy, the development on the dilute-P GaNP alloys has not progressed due to the lack of understanding in the physics behind the alloys.

It is important to note that numerous studies have been carried out in the fields of common-anion non-nitride-based semiconductor alloys such as InGaAs(N) alloys [31-36], dilute-N GaPN alloys [60-64] and GaAsP alloys [65-68]. In particular, the mixed PN-based alloys led to the indirect-to-direct band gap transition which opens up the opportunity in developing new light emitting devices [60]. In addition, the incorporation of Phosphorus impurities in the GaAs-based alloys has resulted in improved performance in the telecommunication and infrared device technologies [65].

Up to present, the electronic properties of the dilute-P GaNP alloy have yet to be understood, since the literature on the dilute-P GaNP alloy is severely limited. As there has been a growing interest in the common-anion nitride-based material class, especially for the case of dilute-As GaNAs alloy, where the analyses suggested the alloy as a potential novel material for light emitting devices, mainly due to the suppression of interband Auger recombination [19, 21], the dilute-P GaNP alloys could be of important for light emitting applications as well. Due to the similarity between the dilute-P GaNP alloys and the dilute-As GaNAs alloys, it is thus critical to conduct the analysis on the electronic properties of dilute-P GaNP alloys and provide the first key insights required for future implementation of the alloys in the light emitting applications.

5.3.1. Electronic Band Structures of Dilute-P GaNP Alloy

Figure 5-13(a) and figure 5-13(b) show the DFT-calculated band structures of GaN and 6.25% P-content dilute-P $GaN_{0.9375}P_{0.0625}$ alloy respectively. As shown in figure 5-13(b), the conduction band minimum (CBM) and valence band maximum (VBM) for dilute-P GaNP are both located at the gamma (Γ) point in Brillouin Zone (BZ), indicating the direct band gap property of the alloys, an essential attribute for light emitting applications. Hence, the incorporation of P atoms in the GaN alloy does not lead to the transition from direct band gap to indirect band gap. This is different from the characteristics shown in dilute-N GaPN alloys where the incorporation of N atoms leads to the transition from indirect band gap to direct band gap [63].

The energy band gap values of the dilute-P GaNP alloys were obtained by taking the value of the energy difference between the CBM and the VBM, as well as applying the scissor operator in order to correct the value originating from LDA calculations. As presented in figure 5-13(b), the incorporation of 6.25% Phosphorus impurities into the GaN alloy led to an energy band gap reduction of ~0.81eV compared to GaN. Such findings are analogous to the characteristics shown in dilute-As GaNAs alloys in which the incorporation of Arsenic impurities into the GaN alloy resulted in significant reduction of the band gap energy.

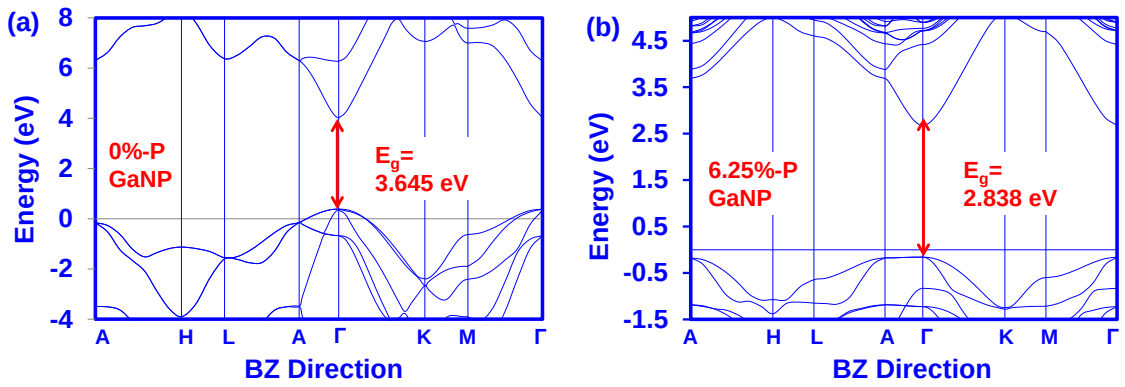

Figure 5-13: *Band structures of GaNP alloy with (a) 0% and (b) 6.25% P-content. Energy band gap (E_g) is the difference in energy between the conduction band minimum (CBM) and valence band maximum (VBM) at the gamma point in the Brillouin Zone.*

5.3.2. Band Gap and Band Bowing Energy of Dilute-P GaNP Alloy

The trend in reduction of the energy band gap with increasing P-content in the GaNP alloy is shown to be consistent at even higher P concentrations as shown in Figure 5-14(a). At P-content of 12.5%, the band gap of dilute-P GaNP alloy is reduced by ~0.95 eV compared to GaN. The experimental data for the energy band gaps obtained by Iwata and co-workers were compared to our results for the dilute-P GaNP alloy [35]. In comparison, the calculated band gap energy data for dilute-As GaNAs alloy is also provided. While the band gap reduction is less significant with the P impurity incorporation in the GaN, the trend of band gap energy reduction in GaNP alloy is similar to that of the dilute-As GaNAs alloy. There are discrepancies observed between the calculated and the measured results, even though the reducing trend of energy band gap is fairly similar. Such discrepancies potentially arise from the strain effect in the alloy and/or P-clustering effect in the experimentally grown GaNP alloy.

In addition, the band gap information of the dilute-P GaNP by Iwata and co-workers is obtained under different temperature conditions than ours. Our DFT calculation was performed for zero-temperature limit which is common in DFT calculations. On the other hand, the band gap measurements by Iwata and co-workers were carried out at higher temperature of 77K. Note that the available experimental data on dilute-P GaNP is severely limited [25] and the possibility for comparison at similar temperature is restricted at the current stage. Besides, the band gap

problem is well known in DFT calculations. The band gap problem is attributed to the discontinuity in the exchange-correlation potential in the calculations, resulting in the underestimation of energy band gap in the material. The underestimated energy band gap from DFT calculations can be corrected by using the scissor operator approach as implemented in this work. Thus, these conditions would contribute to the discrepancies between the band gap results in comparison.

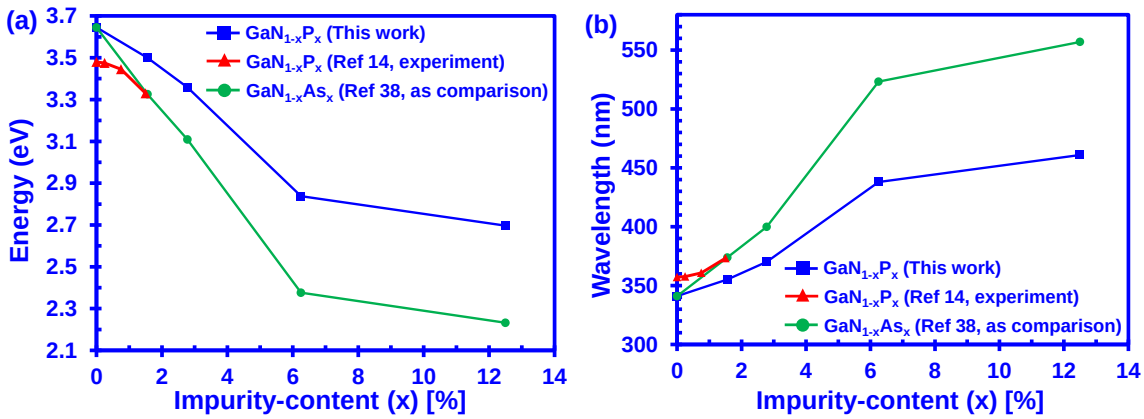

Figure 5-14: *(a) Energy band gap and (b) Emission wavelength of dilute-P GaNP alloy from 0% up to 12.5% P-content. Experimental energy band gap of GaNP by Iwata et al [14] and DFT-calculated energy band gap of dilute-As GaNAs alloy [38] are also plotted in the figure for comparison with the DFT-calculated energy band gap for dilute-P GaNP alloy.*

On the other hand, the band gap narrowing as a result of the incorporation of P impurities into the GaN alloy can be attributed mainly to the upward movement of the valence band of the alloy. It is important to note that the incorporation of Arsenic impurity in the GaN alloy has also been shown to be heavily affecting the valence band structure of the GaN alloy [19]. Similar effect is expected to be observed if the P impurity is incorporated into InGaN ternary alloy. Further study would be necessary to investigate the effect of the P atoms onto the InGaN alloy.

Figure 5-14(b) presents the emission wavelength as a function of P-content in the dilute-P GaNP alloy. As shown in figure 5-14(b), the light emission wavelength of the dilute-P GaNP alloy increases from 340 nm with 0%-P content to ~460 nm with 12.5%-P content in the dilute-P GaNP alloys. Specifically, the incorporation of 6.25%-P and 12.5%-P impurities into the GaN alloys lead to the 450 nm emission wavelength region. This suggests the possibility of the alloys as candidates for blue-light applications. The wavelength of the 12.5%-P GaNP alloy only constitutes

a redshift of 20 nm as compared to the wavelength of the 6.25%-P GaNP alloy. The emission wavelength is expected to increase if more P impurities are incorporated into the dilute-P GaNP alloy. Note that the phase transformation phenomena has been observed and reported in the dilute-As GaNAs alloys when the As-content exceeds roughly 17% [29]. Since dilute-P GaNP alloys are similar to the dilute-As GaNAs alloys in that both P and As atoms are larger than the N atom, structural changes could possibly occur in the dilute-P GaNP alloys, when the percentage of Phosphorus impurities increases in the GaN alloy. Emission wavelength redshift in the dilute-P GaNP alloy could also be achieved by forming a III-Nitride active region heterostructure. Previous findings had shown that the conduction and valence bands will be bent due to the polarization field in the III-Nitride active region [16, 18]. This leads to further reduction of the energy band gap, thus green light emission could possibly be achieved with low P-content in dilute-P GaNP active region.

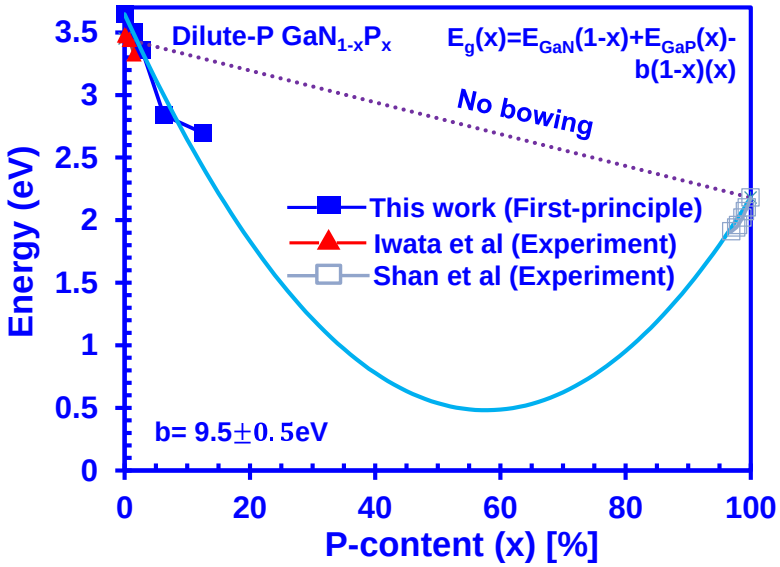

Figure 5-15: *Comparison between our DFT calculations and experimental data, with corresponding bowing parameter of ~9.5 eV obtained through line fitting with the data.*

Figure 5-15 presents the energy band gap of GaNP alloy in the full P-content composition range. The dotted line shown in figure 5-15 represents the energy band gap of GaNP alloys by taking into consideration the virtual crystal approximation model (VCA). On the other hand, the light blue solid line shown in figure 5-15 represents the band gap value of GaNP alloys while

taking into account the bowing effect in the GaNP ternary alloys. As shown in figure 5-15, the VCA result deviates largely from the calculated and experimental energy band gap data, which shows that the bowing effect is significant in the GaNP alloys. By taking into the account the bowing parameter, the overall composition dependence of the alloy band gap is given as $E_g(x)=E_{GaN}(1-x)+E_{GaP}(x)-b(1-x)(x)$. The solid line in figure 5-15 shows a reasonable fitting with the experimental and the calculated energy band gap data for the GaNP alloys. Specifically, the band bowing parameter b is determined to be 9.5 ± 0.5 eV, which agrees well with the reported value of 9.31 eV by Iwata and co-workers [25].

Along the quadratic curve provided by the composition dependent energy band gap equation in figure 5-15, the band gap energy of the GaNP alloys rapidly reduces from both ends, reaching a minimum of only 0.5 eV with 60% of P-impurity in the GaNP alloy. Note also that the formulated Hamiltonian matrices in the degenerate perturbation theory revealed that the composition dependency on the ternary alloy is more than just a simple quadratic function, implying that the minimum energy band gap value in the GaNP ternary alloy requires further investigation. Nevertheless, this work is focused on the electronic properties of dilute-P GaNP alloy and its potential for optoelectronic device applications with a dilute limit of P-content. Further study would be necessary to investigate the effect of high-P-impurity content in the GaN alloy.

5.3.3. Effective Masses and Split-off Band Energy of Dilute-P GaNP Alloy

Figure 5-16 presents the electron and hole effective masses of the dilute-P GaNP alloys from 0% up to 12.5% P-content. Effective mass parameters are obtained through the DFT-calculated band structures of the dilute-P GaNP alloys, in which the parabolic line fitting method is employed to fit the dispersion relation in k-space for the alloys [43]. For the GaN alloy, the electron effective mass is 0.2 m_0 in the k_z direction and 0.17 m_0 in the k_xk_y direction. The effective mass for heavy hole, light hole and split-off have also been obtained via parabolic line fitting method, as shown in figure 5(b), (c) and (d). Further details on the extraction of carrier effective mass from alloy band structures can be found elsewhere [46].

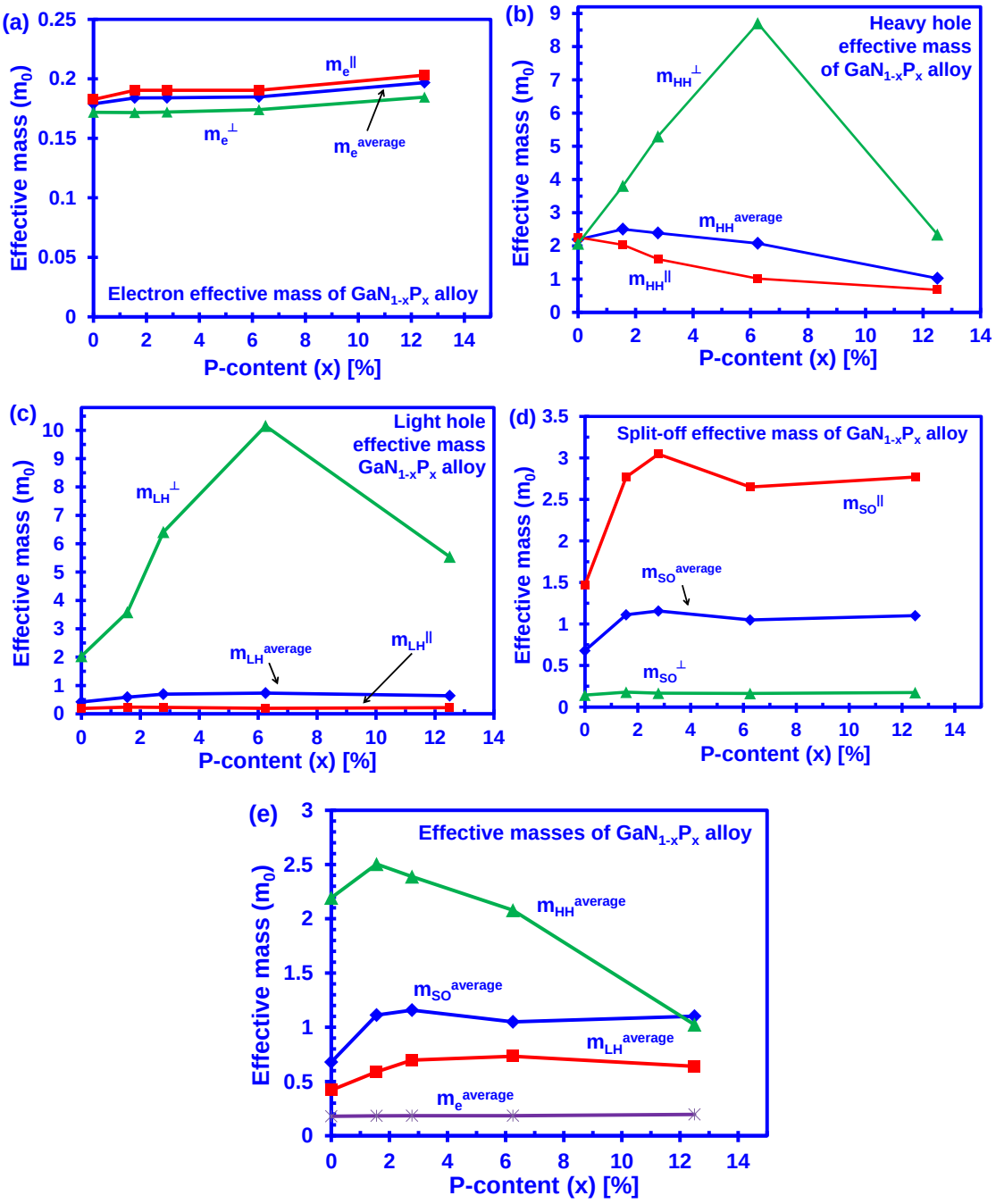

Figure 5-16: *Carrier effective masses of (a) Electron (b) Heavy hole, (c) Light hole, (d) Split-off band and (e) Comparison of carrier effective masses.*

As shown in figure 5-16(e), the average electron effective masses of the dilute-P GaNP alloys show an increasing trend from 0.17 m0 with 0% P-content to 0.18 m0 with 12.5% P-content, corresponding to a 6.67% effective mass increment. On the other hand, the average heavy hole

effective masses of the dilute-P GaNP alloys show a general decreasing trend from 2.15 m_0 with 0% P-content to 1 m0 with 12.5% P-content, leading to an effective mass reduction of 53.5%. The changes of the average electron effective masses are insignificant as compared to that of the average heavy hole effective mass for the dilute-P GaNP alloys, which is not the case in the dilute-nitride based (In)GaAsN and GaPN alloys [35, 64]. It has been shown that there are significant changes occurring in the electron effective mass of the dilute-nitride based (In)GaAsN alloys where the hole bands remain unaffected as compared to the GaAs alloys [35]. The phenomena behind the significant electron effective mass changes is attributed to the addition of nitrogen impurities into the (In)GaAs alloys that leads to significant modification of the alloy conduction band, forming a strongly localized impurity energy band near the conduction band. In contrast to the properties of (In)GaAsN or GaPN alloys, when the Phosphorus atoms are incorporated into the GaN alloy, they form a localized impurity band with an energy level of 0.2eV above the uppermost valence band [13]. Therefore, the hole bands in the dilute-P GaNP alloys are significantly modified, as the reconstruction of the valence bands in the alloys takes place due to the formation of localized P states.

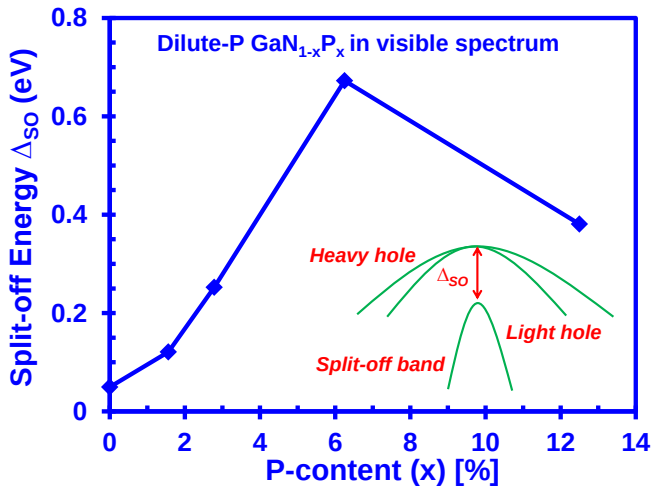

Figure 5-17: *Split-off energy of dilute-P GaNP alloys from 0% up to 12.5% P-content.*

Figure 5-17 presents the split off energy of the dilute-P GaNP alloys as a function of P-content. As shown in figure 5-17, the split-off energy of the dilute-P GaNP alloys has increased from 0.05 eV at 0%-P to 0.4 eV at 12.5%-P. The significant modification of ~0.35 eV in the split-

off energy in the dilute-P GaNP alloys is quite significant as compared to the GaN and GaP alloys where the split-off energy value is only less than 0.1 eV [44].

Based on our findings, the characteristics of the electronic properties shown in the dilute-P GaNP alloys are similar to that of the dilute-As GaNAs alloys [19]. From the MOCVD growth perspective, the GaNP alloy can be grown at temperature of about 850°C-1050°C [26], which is compatible to the growth of GaN layer. The unique features provided by dilute-P GaNP alloys indicate the potential of the alloy as a candidate in the light emitting applications. It is important to note that there is still uncertainty on the electronic and optical properties of the dilute-P GaNP material at this early stage. Specifically, the incorporation of P atoms into the GaN is expected to result in additional defects, which will lower the radiative efficiency from this material system. Future experimental studies will be important to access the potential of the dilute-P GaNP material for the light emitting applications. Further investigations on the design of the GaNP-based heterostructure will be necessary in order to realize and optimize the performance of the GaNP-based devices.

5.3.4. Comparison of Electronic Properties of Dilute-Anion GaN-Based Alloys

The addition of the anion elements into the GaN has resulted in significant changes to the original electronic properties of the GaN. While the analysis have been performed in section 5.3.2 and section 5.3.3 for dilute-As GaNAs and dilute-P GaNP alloys respectively, it is important to also make a comparison between the dilute-anion GaN-based semiconductor alloys to enhance the understanding of the electronic properties. In addition to the P and As atoms, the incorporation of antimony (Sb) element into GaN to form dilute-Sb GaNSb ternary alloy would also result in significant changes to the electronic properties. Similar to the dilute-P GaNP and dilute-As GaNAs alloys, the development in the dilute-Sb GaNSb alloy is extremely limited [29, 30]. Note that the dilute-Sb GaNSb alloys have only been realized using MBE technique in the past five years [29]. Here we provide a comparison of the energy band gaps and band bowing

parameter of the dilute-anion GaN-based semiconductor alloys, with the purpose to provide a better understanding of the effect of different anion element in the GaN material.

Figure 5-18 shows the energy band gap and the corresponding emission wavelength of the dilute-P GaNP, dilute-As GaNAs and dilute-Sb GaNSb ternary alloys. As shown in figure 5-18, the energy band gap of dilute-Sb GaNSb reduces much faster than the dilute-As GaNAs and dilute-P GaNP alloys. At 2.78% anion content, the GaNSb alloy reaches energy band gap of ~2.5 eV, while GaNP and GaNAs reach ~3.35 eV and ~3.1 eV respectively. The strong reduction of energy band gap in dilute-Sb GaNSb is primarily attributed to the significant upward movement of the VBM. Note that scissor operator has been used to correct the energy band gap error originated from the LDA DFT calculations. In addition, higher anion concentration in the dilute-Sb GaNSb is not taken into consideration from current study, which is due to the severe band gap error issue in the calculations. Further study will be required to analyze the electronic properties of dilute-Sb GaNSb with Sb-content of more than 2.78%.

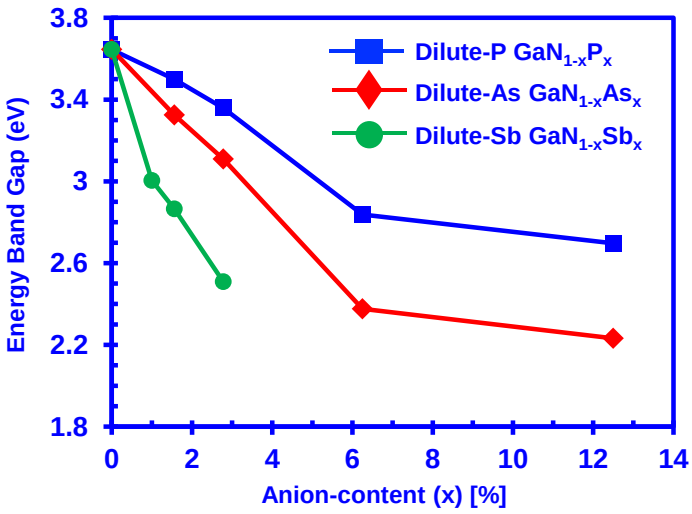

Figure 5-18: *Energy band gap of dilute-anion GaN semiconductor as a function of the anion-content in the GaN alloy.*

Figure 5-19 presents the energy band gap of GaNP, GaNAs and GaNSb ternary alloys in the whole composition range. The dotted lines in figure 5-19 represents the energy band gap of the ternary alloys using the VCA method. As presented in figure 5-19, the bowing of GaNP is the

smallest (9.5 eV) among the three ternary alloys understudied. The bowing parameter of GaNSb reaches ~25 eV, which is significantly large in comparison to that of InGaN alloy (b = ~3 eV). Such large bowing parameter in the GaNSb is primarily due to the large atomic mismatch between the Sb atom and N atom. Besides, it is interesting that there is a very high possibility that the energy band gap will reduce to 0 eV with Sb-content of ~15% in the GaN, leading to zero-gap nitride material. This shows that the GaNSb material can be implemented in various applications in addition to the light emitting application.

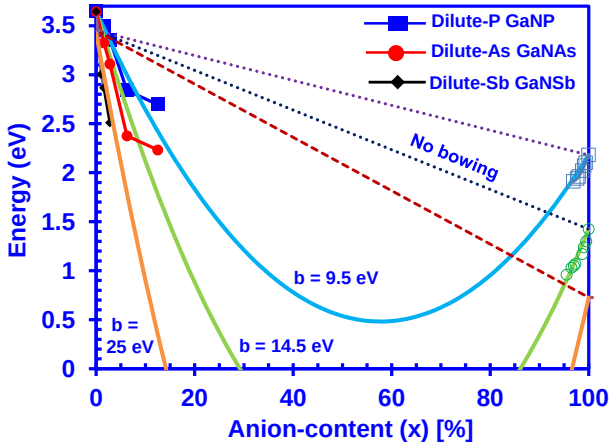

Figure 5-19: *Comparison of the energy band gap of the GaNAs, GaNP and GaNSb semiconductor alloys in the whole composition range.*

5.4. Summary

In summary, First Principle calculations were carried out by using LDA approximation to examine the band structures of dilute-anion GaN-based semiconductor materials. Comprehensive studies have been performed for both dilute-As GaNAs and dilute-P GaNP alloys, with their electronic properties analyzed and presented. For the case of dilute-As GaNAs, with As-content ranging from 0% up to 12.5%, the band structures of the GaNAs alloy remain direct band gaps with band gap covering from 3.645 eV down to 2.232 eV. The electronic band structure parameters for dilute-As GaNAs alloy are also extracted and presented in this work, which are applicable for device physics analysis and simulation for device technologies employing this alloy. In the case of dilute-P GaNP alloy, the electronic properties were found to

be similar to that of dilute-As GaNAs alloys. However, the effect of the P anion in the GaN is less significant in reducing the energy band gap of the GaN, when compared to the effect of the As anion. Brief discussions have also been carried out for the other dilute-anion GaN semiconductor alloy such as dilute-Sb GaNSb alloy. From our analysis the band gap energy will reduce much more significant as compared to that of dilute-P GaNP and dilute-As GaNAs alloys. This shows that there is a high potential to use dilute-Sb GaNSb alloy for light emitting applications.

In addition, the natural band alignment of dilute-As GaNAs / GaN heterostructure is determined via First-Principle method. Our finding shows a type-I natural band alignment of dilute-As GaNAs / GaN heterostructure, with the conduction to valence band offset ratio (CBO : VBO) determined as 5:95 for As-content up to 12.5%. The strong coupling of localized As-states is found as the primary contributing factor in leading to the strong valence band modification resulting in the bandgap reduction observed in the dilute-As GaNAs alloy. Future works on the impacts of the As-clustering in the dilute-As GaNAs with high As-content on its band alignment with respect to that of GaN will be important. The incorporation of dilute-As GaNAs alloy in the type-I or type-II QW structures can result in significantly improved active regions for LEDs and lasers emitting in the visible spectral regimes.

References in Chapter 5

[1] S. Nakamura, “The roles of structural imperfections in InGaN-based blue light-emitting diodes and laser diodes”, Science, vol. 281, no. 5379, pp. 956-961, Aug. 1998.

[2] M. H. Crawford, “LEDs for solid-state lighting: performance chanllenges and recent advances”, IEEE J. Sel. Top. Quantum Electron., vol. **15**, no. 4, pp. 1028–1040, Aug. 2009.

[3] H. Zhao, G. Y. Liu, J. Zhang, J. D. Poplawsky, V. Dierolf, and N. Tansu, “Approaches for high internal quantum efficiency green InGaN light-emitting diodes with large overlap quantum wells”, Optics Express, vol. **19**, no. S4, pp. A991-A1007, Jul. 2011.

[4] H. Zhao, G. Liu, R. A. Arif, and N. Tansu, “Current Injection Efficiency Quenching Leading to Efficiency Droop in InGaN Quantum Well Light-Emitting Diodes,” Solid-State Electronics, vol. 54, pp. 1119–1124, 2010.

[5] X. Li, S. Kim, E. E. Reuter, S. G. Bishop, and J. J. Coleman, “The incorporation of arsenic in GaN by metalorganic chemical vapor deposition”, Appl. Phys. Lett, vol. **72**, no. 16, pp. 1990-1992, Feb. 1998.

[6] X. Li, S. G. Bishop, and J. J. Coleman, “GaN epitaxial lateral overgrowth and optical characterization”, Appl. Phys. Lett., vol.**73**, no. 9, pp. 1179–1181, Jul. 1998.

[7] X. Li, H. Liu, X. Ni, U. Ozgur, H. Morkoc, “Effect of carrier spillover and Auger recombination on the efficiency droop in InGaN-based blue LEDs,” Superlattices and Microstructures, vol. 47, pp. 118-122, 2010.

[8] X. H. Li, R. Song, Y. K. Ee, P. Kumnorkaew, J. F. Gilchrist, and N. Tansu, “Light extraction efficiency and radiation patterns of III-nitride light-emitting diodes with colloidal microlens arrays with various aspect ratios”, IEEE Photon. J., vol. **3**, no. 3, pp. 489–499, Jun. 2011.

[9] I. H. Brown, P. Blood, P. M. Smowton, J. D. Thomson, S. M. Olaizola, A. M. Fox, P. J. Parbrook, and W. W. Chow, “Time evolution of the screening of piezoelectric fields in InGaN quantum wells,” IEEE J. Quantum Electron., vol. 42, no. 12, pp. 1202–1208, Nov-Dec. 2006.

[10] A. Kimura, C.A. Paulson, H. F. Tang and T. F. Kuech, “Epitaxial $GaN_{1-y}As_y$ layers with high As content grown by metalorganic vapor phase epitaxy and their band gap energy”, Appl. Phys. Lett., vol. **84**, no. 9, pp. 1489-1491, Mar. 2004.

[11] K. M. Yu, S. V. Novikov, R. Broesler, C. R. Staddon, M. Hawkridge, Z. Liliental-Weber, I. Demchenko, J. D. Denlinger, V. M. Kao, F. Luckert, R. W. Martin, W. Walukiewicz, and C. T. Foxon, “Non-equilibrium GaNAs alloys with band gap ranging from 0.8-3.4 eV”, Phys. Status Solidi C, vol. **7**, no. 7-8, pp. 1847-1849, May 2010.

[12] X. H. Li, H. Tong, H. P. Zhao, N. Tansu, “Band structure calculation of dilute-As GaNAs by first principle”, Proc. of the SPIE Photonics West 2010, Physics & Simulation of Optoelectronics Devices XVIII, 2010.

[13] T. Mattila, A. Zunger, “P-P and As-As isovalent impurity pairs in GaN: Interaction of deep t2 levels”, Phys. Rev B, vol. **59**, pp.9943-9953, 1999.

[14] C. G. Van de Walle, “Arsenic impurities in GaN”, Appl. Phys. Lett., vol. **76**, no. 8, pp. 1009 – 1011, Feb 2000.

[15] K. Laaksonen, H-P. Komsa, E. Arola, et. al., “Computational study of $GaAs_{1-x}N_x$ and $GaN_{1-y}As_y$ alloys and arsenic impurities in GaN”, J. Phys.: Condens. Matter, vol. **18**, pp. 10097-10114, Oct. 2006.

[16] R. A. Arif, H. Zhao, and N. Tansu, “Type-II InGaN-GaNAs Quantum Wells Active Regions for Lasers Applications,” Appl. Phys. Lett. vol. 92(1), Art. No. 011104, January 2008.

[17] H. Zhao, R. A. Arif, and N. Tansu, “Self Consistent Gain Analysis of Type-II ‘W’ InGaN-GaNAs Quantum Well Lasers,” J. Appl. Phys., vol. 104 (4), Art. 043104, August 2008.

[18] J. Wu, W. Walukiewicz, K.M. Yu, J. D. Denlinger, W. Shan, J. W. Ager III, A. Kimura, H. F. Tang, and T. F. Kuech, “Valence band hybridization in N-rich $GaN_{1-x}As_x$ alloys”, Phys Rev B, vol. **70**, no. 11, pp. 115214-1-115214-7, Sep. 2004.

[19] C. K. Tan, J. Zhang, X. H. Li, G. Y. Liu, B. O. Tayo, and N. Tansu, “First-Principle electronic properties of dilute-As GaNAs alloy for visible light emitters”, J. Disp. Tech., vol. 9, no. 4, pp. 272-279, Apr. 2013.

[20] C. K. Tan, and N. Tansu, “First-Principle natural band alignment of GaN / dilute-As GaNAs alloy”, AIP Advances, vol. 5, no. 1, p. 017129, Jan. 2015.

[21] C. K. Tan, and N. Tansu, “Auger recombination rates in dilute-As GaNAs semiconductor”, AIP Advances, vol. 5, no. 5, p. 057135, May 2015.

[22] C. K. Tan, D. Borovac, W. Sun, and N. Tansu, “InGaN/dilute-As GaNAs interface quantum well for red emitters”, Scientific Reports, vol. 6, p. 19271, Jan. 2016.

[23] C. K. Tan, D. Borovac, W. Sun, and N. Tansu, “First-principle electronic properties of dilute-P GaN1-xPx alloy for visible light emitters”, Scientific Reports, 6, p. 24412, Apr. 2016.

[24] O. Igarashi, “Heteroepitaxial growth of GaN1-xPx (x<0.09) on sapphire substrates, Jpn. J. Appl. Phys., vol. 31, pp. 3791-3793, 1992.

[25] K. Iwata, H. Asahi, K. Asami, and S. Gonda, Gas source MBE growth of GaN rich side of GaN1-xPx using ion-removed ECR radical cell, J. Crystal Growth, vol. 175-176, pp. 150-155, 1997.

[26] S. Yoshida, J. Kikawa, and Y. Itoh, Crystal growth of nitride-rich GaNP by laser-assisted metalorganic chemical-vapor deposition, J. Crystal Growth, vol. 237-239, pp. 1037-1041, 2002.

[27] J. Kikawa, S. Yoshida, and Y. Itoh, Electroluminescence studies under forward and reverse bias conditions of a nitride-rich GaN1-xPx SQW structure LED grown by laser-assisted metal-organic chemical vapor deposition, Solid-State Electronics, vol. 47, pp. 523-527, 2003.

[28] R. Kuroiwa, et al., Optical properties of GaN-rich side of GaNP and GaNAs alloys grown by gas-source molecular beam epitaxy, Appl. Phys. Lett., vol. 73, pp. 2630-2632, 1998.

[29] K. M. Yu, W. L. Sarney, S. V. Novikov, D. Detert, R. Zhao et al, “Highly mismatched N-rich GaN1-xSbx films grown by low temperature molecular beam epitaxy”, Appl. Phys. Lett., vol. 102, p. 102104, Mar. 2013.

[30] R. Sheetz, E. Richter, A. N. Andriotis, S. Lisenkov, C. Pendyala, and M. K. Sunkara, “Visible-light absorption and large band-gap bowing of $GaN_{1-x}Sb_x$ from first principles”, Phys. Rev. B, vol. 84, p. 075304, Aug. 2011.

[31] N. Tansu, J. Y. Yeh, and L. J. Mawst, “High-performance 1200-nm InGaAs and 1300-nm InGaAsN quantum-well lasers by metalorganic chemical vapor deposition”, IEEE J. Sel. Top. Quantum Electron., vol. **9**, no.5, pp. 1220-1227, Sep. 2003.

[32] S. R. Bank, L. L. Goddard, M. A. Wistey, H. B. Yuen, J. S. Harris, “On the temperature sensitivity of 1.5-μm GaInNAsSb lasers,” IEEE J. Sel. Top. Quantum Electron., vol. 11, no. 5, pp. 1089-1098, Sep./Oct. 2005.

[33] A. Lindsay and E. P. O'Reilly, “Unification of the band anticrossing and cluster-state models of dilute nitride semiconductor alloys”, Phys. Rev. Lett., vol. **93**, no. 19, pp. 196402-1-196402-4, Nov. 2004.

[34] K. Uesugi, N. Morooka, and I. Suemune, “Reexamination of N composition dependence of coherently grown GaNAs band gap energy with high-resolution x-ray diffraction mapping measurements”, Appl. Phys. Lett., vol. **74**, no. 9, pp. 1254-1256, Mar. 1999.

[35] L. Xu, D. Patel, C. S. Menoni, J. Y. Yeh, L. J. Mawst, and N. Tansu, “Optical determination of the electron effective mass of strain compensated In0.4Ga0.6As0.995N0.005/GaAs single quantum well”, Appl. Phys. Lett., vol. **89**, no. 17, pp. 171112-1-171112-3, Oct. 2006.

[36] MedeA-VASP, Material Designs Inc.

[37] V. Fiorentini, and A.Baldereschi, “Dielectric scaling of the self-energy scissor operator in semiconductors and insulators”, Phys. Rev. B, vol. **51**, no. 23, pp. 17196-17198, Jun. 1995.

[38] G. Kresse, and J. Furthmuller, “Efficient iterative schemes for ab initio total-energy calculations using a plane-wave basis set”, Phys. Rev. B, vol. 54, no. 16, pp. 11169-11186, Oct. 1996.

[39] M. Shishkin, M. Marsman, and G. Kresse, “Accurate quasiparticle spectra from self-consistent GW calculations with vertex corrections”, Phys. Rev. Lett., vol. 99, no. 24, pp. 246403-1-246403-4, Dec. 2007.

[40] P. D. C. King, T. D. Veal, F. Fuchs, Ch. Y. Wang, D. J. Payne, A. Bourlange, H. Zhang, G. R. Bell, et. al., “Band gap, electronic structure, and surface electron accumulation of cubic and rhombohedral In_2O_3”, Phys. Rev. B, vol. 79, no. 20, pp. 205211-1-205211-10, May. 2009.

[41] Y. P. Varshni, “Temperature dependence of the energy gap in semiconductors”, Physica, vol. 34, no. 1, pp. 149-154, 1967.

[42] I. Vurgaftman, J. R. Meyer, L. R. Ram-Mohan, “Band parameters for III-V compound semiconductors and their alloys”, J. Appl. Phys., vol. 89, no. 11, pp. 5815-5875, Jun. 2001.

[43] M. Suzuki, and T. Uenoyama, “First-principles calculations of effective-mass parameters of AlN and GaN”, Phys. Rev B, vol. **52**, no. 11, pp. 8132-8139, 1995.

[44] S. J. Sweeney, Z. Batool, K. Hild, S. R. Jin, et. al., “The potential role of bismide alloys in future photonic devices”, 13th International Conference on Transparent Optical Networks (ICTON), Jun. 2011.

[45] H. Zhang, E. J. Miller, E. T. Yu, C. Poblez, and J. S. Speck, “Measurement of polarization charge and conduction-band offset at $In_xGa_{1-x}N$/GaN heterojunction interfaces”, Appl. Phys. Lett,. **84**, 4644-4646 (2004).

[46] H-P. Komsa, E. Arola, E. Larkins, and T. T. Rantala, “Band offset determination of the GaAs/GaAsN interface using the density functional theory method”, J. Phys.:Condens. Matter **20**, 315004 (2008).

[47] M. Peressi, N. Binggeli, and A. Baldereschi, “Band engineering at interfaces: theory and numerical experiments”, J. Phys. D: Apply. Phys. **31**, 1273-1299 (1997).

[48] A. Baldereschi, S. Baroni, and R. Resta, “Band offsets in lattice-matched heterojunctions: A model and first-principles calculations for GaAs/AlAs”. Phys. Rev. Lett. **61**, 734-737 (1988).

[49] L. Colombo, R. Resta, and S. Baroni, “Valence-band offsets at strained Si/Ge interfaces”, Phys. Rev. B **44**, 5572-5579 (1991).

[50] N. R. D’Amico, G. Cantele, and D. Ninno, “First principles calculations of the band offset at $SrTiO_3$-TiO_2 interfaces”, Appl. Phys. Lett. **101**, 141606 (2012).

[51] P. G. Moses, M. Miao, Q. Yan, and C. G. Van de Walle, “Hybrid functional investigations of band gaps and band alignments for AlN, GaN, InN, and InGaN”, J. Chem. Phys. **134**, 084703 (2011).

[52] P. G. Moses, and C. G. Van de Walle, “Band bowing and band alignment in InGaN alloys”, Appl. Phys. Lett. **96**, 021908 (2010).

[53] L. Dong, and S. P. Alpay, “Role of heteroepitaxial misfit strains on the band offsets of $Zn_{1-x}Be_xO$/ZnO quantum wells: A first-principles analysis”, J. Appl. Phys. **111**, 113714 (2012).

[54] S. H. Wei, and A. Zunger, “Calculated natural band offsets of all II-VI and III-V semiconductors: Chemical trends and the role of cation d orbitals”, Appl. Phys. Lett. **72**, 2011-2013 (1998).

[55] J. Robertson, “Band offsets of wide-band-gap oxides and implications for future electronic devices”, J. Vac. Sci. Technol. B **18**, 1785-1791 (2000).

[56] B. Hoffling, A. Schleife, C. Rodl, and F. Bechstedt, “Band discontinuities at Si-TCO interfaces from quasiparticle calculations: Comparison of two alignment approaches”, Phys. Rev. B **85**, 035305 (2012).

[57] P. W. Peacock, and J. Robertson, “Bonding, energies, and band offsets of Si-ZrO_2 and HfO_2 gate oxide interfaces”, Phys. Rev. Lett. **92**, 057601 (2004).

[58] D. A. B. Miller, et al, “Electric field dependence of optical absorption near the band gap of quantum-well structures”. Phys. Rev. B **32**, 1043-1060 (1985).

[59] H. P. Zhao, R. A. Arif, Y. K. Ee, and N. Tansu, “Self-consistent analysis of strain-compensated InGaN-AlGaN quantum wells for lasers and light emitting diodes”. IEEE J. Quantum Electron. **45(1-2)**, 66-78 (2009).

[60] J. Chamings, S. Ahmed, S. J. Sweeney, V. A. Odnoblyudov, and C. W. Tu, Physical properties and efficiency of GaNP light emitting diodes, Appl. Phys. Lett., vol. 92, p. 021101, 2008.

[61] W. G. Bi, and C. W. Tu, N incorporation in GaP and band gap bowing of GaNxP1-x, Appl. Phys. Lett., vol. 69, pp. 3710-3712, 1996.

[62] G. Rudko, I. A. Buyanova, W. M. Chen, H. P. Xin, and C. W. Tu, Temperature dependence of the GaNxP1-x band gap and effect of band crossover, Appl. Phys. Lett., vol. 81, pp. 3984-3986, 2002.

[63] W. Shan, et al., Nature of the fundamental band gap in GaNxP1-x alloys, Appl. Phys. Lett., vol. 76, pp. 3251-3253, 2000.

[64] H. P. Xin, C. W. Tu, Y. Zhang, and A. Mascarenhas, Effects of nitrogen on the band structure of GaNxP1-x alloys, Appl. Phys. Lett., vol. 76, pp. 1267-1269, 2000.

[65] N. Tansu, and L. J. Mawst, High-performance, strain compensated InGaAs-GaAsP-GaAs (λ=1.17 μm) quantum well diode lasers, IEEE Photon. Technol. Lett., vol. 13, pp. 179-181, 2001.

[66] Q. H. Hou, K. D. Choquette, K. M. Geib, and B. E. Hammons, High-performance 1.06-μm selectively oxidized vertical-cavity surface-emitting lasers with InGaAs-GaAsP strain-compensated quantum wells, IEEE Photo. Technol. Lett., vol. 9, pp. 1057-1059, 1997.

[67] W. J. Choi, P. D. Dapkus, and J. J. Jewell, 1.2-μm GaAsP/InGaAs strain compensated single-quantum-well diode laser on GaAs using metal organic chemical vapor deposition, IEEE Photonics Technology, vol. 11, pp. 1572-1574, 1999.

[68] N. J. Ekins-Daukes, et al, Strain-balanced GaAsP/InGaAs quantum well solar cells, Appl. Phys. Lett., vol. 75, pp. 4195-4197, 1999.

Chapter 6: Auger Recombination in Dilute-Anion GaN-Based Semiconductor

6.1. Introduction and Motivation – Auger Recombination Issue

As discussed in Chapter 1 and Chapter 2, III-nitride semiconductor alloys have achieved significant progress in the past decade [1-13], in which the key advances in III-Nitride based light emitting diodes (LEDs) were recently awarded by Nobel Prize in Physics in 2014 [14]. Despite the advances in the GaN-based LEDs, LEDs development is hindered by the efficiency-droop phenomena which results in significant reduction in internal quantum efficiency as the operating current density increases. Various reasons have been suggested to contribute to the causes of efficiency droop in the InGaN-based LEDs [15-31]. The origin of the efficiency droop phenomena in the InGaN LEDs is still inconclusive, but research in recent years increasingly focused on the carrier density related mechanisms such as carrier leakage [16-17] and Auger recombination [18-29] in III-nitrides.

Most recently, Iveland and co-workers revealed a linear correlation between the emitted Auger electron and droop current in the InGaN LED, suggesting the existence and important role of Auger processes in leading to the efficiency droop in LEDs [28]. In particular, the interband Auger recombination process has been suggested as a dominant mechanism leading to large Auger coefficient values in the InGaN alloy, which accounts for the efficiency droop phenomena in green LEDs [23]. Previous study indicated the fundamental difficulties in suppressing the interband Auger recombination [23], which is still not solvable by InGaN material up to present.

As discussed in Chapter 5, dilute-As GaNAs alloy was recently shown as an alternative GaN-based material in addition to InGaN alloy that would provide narrow band gap emission, in particular for addressing blue up to yellow emission spectral regime [29]. Our recent studies have also clarified the heterojunction band alignment for dilute-As GaNAs / GaN interface [32], which will be useful for enabling heterostructure-based device implementation. The research on dilute-As GaNAs alloy is however still limited [3, 29, 32-36], in particular no quantification of the Auger recombination coefficients for this alloy had been reported. Note that the Auger coefficient for

dilute-As GaNAs alloy has only been reported very recently [37]. Evaluating the Auger recombination process qualitatively and quantitatively to confirm the suppression of interband Auger recombination using the dilute-As GaNAs alloy are thus critical to advance the technology based on this alloy.

In this chapter, we first discuss about the interband Auger recombination process in a semiconductor material. In particular, there are two materials being investigated which are the dilute-As GaNAs and dilute-P GaNP semiconductor alloys. A preliminary analysis is performed in dilute-As GaNAs material to evaluate the role of interband Auger recombination process qualitatively. Quantitative findings of the Auger recombination coefficients in dilute-As $GaN_{1-x}As_x$ alloy for As-content (*x*) ranging from 0% up to 12.5% are then presented. The effect of the band parameters of the semiconductor on the Auger recombination process is discussed. The temperature dependency of the Auger coefficient for dilute-As GaNAs alloy is also discussed. Similar approach is implemented for the dilute-P GaNP, in order to investigate the potential of the GaNP alloys. Lastly, the Auger recombination coefficients between dilute-anion GaN-based semiconductors (dilute-As GaNAs and dilute-P GaNP) and InGaN alloy taking into consideration of both interband and intraband Auger recombination processes are compared.

6.2. Direct Auger Recombination Mechanisms

For intraband Auger recombination process, the energy released from the recombination between an electron and a hole is transferred to another carrier resulting in excitation of the carrier into a higher-energy state. For the interband Auger recombination process, the carrier receiving the energy is excited to the second conduction band instead of the higher-energy state in the first conduction band. Further details have been discussed in Chapter 4. In both cases, non-radiative recombination processes occurred under the energy and momentum conservation conditions.

In the framework of perturbation theory, a general Auger recombination rate is given by the following relation [38-39]:

$$R_{Auger} = 2\frac{2\pi}{\hbar}\left(\frac{V}{8\pi^3}\right)^3 \int\int\int\int \left|M_{1,1',2,2'}\right|^2 P_{1,1',2,2'} x\delta(E_{sum}) x\delta\left(\vec{k}_{sum}\right) d\vec{k}_1 d\vec{k}_{1'} d\vec{k}_2 d\vec{k}_{2'} \qquad (6.1).$$

In equation (6.1), state 1 and 2 are for electrons in the first conduction band, state 1' is for a heavy hole in the valence band and state 2' is for an electron in the second upper conduction band respectively. E_{sum} and $\vec{k}_{sum}$ stand for $E_{1'} + E_{2'} - E_1 - E_2$ and $\vec{k}_{1'} + \vec{k}_{2'} - \vec{k}_1 - \vec{k}_2$ (k-selection rule) respectively. The probability factor $P_{1,1',2,2'}$ is the term that accounts for the occupation probabilities of the carriers and $M_{1,1',2,2'}$ is the Auger matrix element. The equation (6.1) that involves computationally expensive twelvefold integrations of the momentum vector can be eased with analytical solution. The Auger coefficient (C), defined as $C = R/n^3$, is calculated using the analytical solutions in which the twelvefold integrations are simplified for carrier density up to $n \sim 10^{19}$ cm^{-3} [38].

$GaN_{1-x}As_x$	0%-As	1.56%-As	2.78%-As	6.25%-As	12.5%-As
E_g (eV)	3.645	3.325	3.109	2.376	2.232
Δ (eV)	2.246	2.091	2.107	1.783	1.663
m_e (m_0)	0.179	0.203	0.229	0.198	0.206
m_{hh} (m_0)	2.193	3.326	3.661	2.417	2.415
m_{lh} (m_0)	0.420	0.949	0.942	0.862	0.786
m_{c2} (m_0)	0.675	0.262	0.317	0.447	0.409

Table 6-1: Extracted band parameters from first-principle calculated band structures using LDA formalism for dilute-As GaNAs alloy from 0%-As up to 12.5%-As.

Two specific analytical expressions for the Auger coefficients corresponding to the recombination process can be obtained for the cases of $E_g > \Delta$ and $E_g < \Delta$ [38], where E_g is the energy difference between the conduction band minimum of the first conduction band (CBM) and the valence band maximum (VBM) at the gamma point, or commonly called as the energy band gap. The parameter Δ is the energy difference between the CBM and the conduction band minimum of the second conduction band. Further details are provided in Chapter 4, in which the development of the analytical solution is discussed. Table I provides the required band parameters of the dilute-As GaNAs alloys for the Auger coefficient calculations. The band parameters are extracted from the First-Principle calculated band structures of dilute-As GaNAs

alloy, in which detailed computational descriptions for the band structure calculations can be found in the literature through our recent published work [29].

6.3. Analysis in Dilute-As GaNAs Semiconductor

6.3.1. Effect of Band Parameters on the Auger Recombination Rates

Recently, Delaney and co-workers proposed that the interband Auger recombination contributes considerably to the droop for green-emitting InGaN QWs [23], and the primary factor leading to the interband Auger process can be attributed to the energy difference between the energy gap (E_g) and the interband separation (Δ = 1st and 2nd conduction band separation) that is within the resonance condition ($|E_g - \Delta| < 0.15$ eV) for InGaN alloy emitting at green spectral regime [23].

A simple analytical function as a function of the energy separation ($E_g - \Delta$) is introduced in figure 6-1. The Auger function is proportional to the exponential of energy separation ($E_g - \Delta$). The dominant factor determining the Auger coefficient is due to the energy separation [40], and hence the Auger coefficient is proportional to the Auger function model [40]. There are two conditions (a) $E_g > \Delta$ and (b) $E_g < \Delta$ considered in our study.

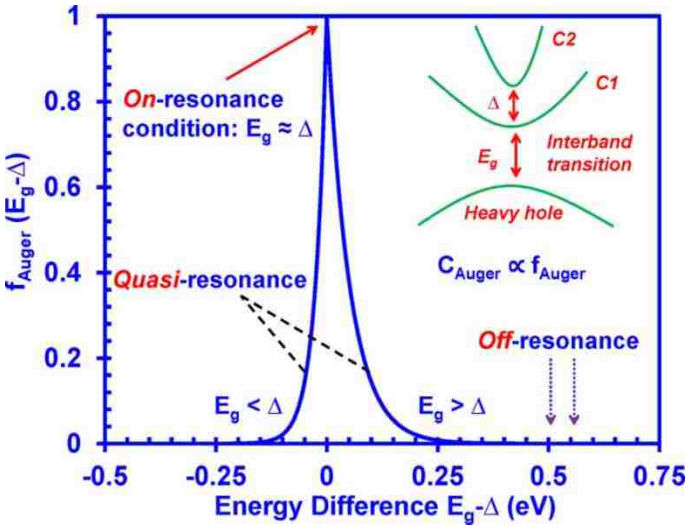

Figure 6-1: *Interband Auger function f_{Auger} as a function for energy difference of dilute-As GaNAs alloy. The f_{Auger} is proportional to the Auger recombination coefficient, resulting in the increased coefficient under resonance condition.*

Under the $E_g > \Delta$ condition, the Auger function is proportional to the exponential term *exp[-(E_g-Δ)/2kT]*. Note that the carrier effective masses are assumed as constant and to possess similar value, resulting in the above simplified expression form. However, under the $E_g < \Delta$ condition, carrier effective masses are excluded from the expression and hence the Auger function is proportional to the exponential term *exp[-(E_g-Δ)/kT]*. In both expressions, the parameter *k* refers to Boltzmann constant, and the parameter *T* corresponds to temperature (T = 300K). It is also important to note that the changes in effective mass would have a secondary effect on the Auger function, and consequently the interband Auger recombination rate. For example, as mentioned earlier in the band parameter sections, the significant increases of heavy hole effective masses in low As-content GaNAs alloy would modify the heavy hole band resulting in flatter band profile. Due to the conservation of energy and momentum, it is expected to give rise to a slightly different exponential decaying function in the Auger function, which would then be inflicted onto the interband Auger recombination rate. Nevertheless, the carrier effective masses in this work are assumed to be constant for the sake of simplicity.

In our simple model, the physical understanding behind the expression can be interpreted as following. When the energy band gap is smaller than the interband separation energy, the Auger process rate will decrease sharply since the energy conservation needs to be satisfied. When the energy band gap is larger than the interband separation energy, there are some possibilities that an electron would be excited to the second lowest conduction band. Yet, due to the restriction of energy and momentum conservation, the Auger process rate will decrease quickly, in a slower rate compared to the former occasion. In both cases, the given exponential term demonstrates that when the energy band gap is similar to the interband separation energy, on-resonance condition is fulfilled and the Auger process could occur easily. Quasi-resonance and off-resonance conditions are introduced to explain the transition from on-resonant energy to off-resonant energy. When the $|E_g-\Delta|$ is less than 0.15 eV [23], the f_{Auger} is no longer in the peak region resulting in quasi-resonance condition.

Figure 6-2(a) shows the comparison between the energy band gap and the Δ interband separation energy of dilute-AsGaNAs alloy from 0% up to 12.5% As-content. Interestingly, the interband separation energy decreases as the As-content increases in the GaNAs alloy while the interband separation energy of the InGaN alloy increases as the In-content increases in the alloy [23].

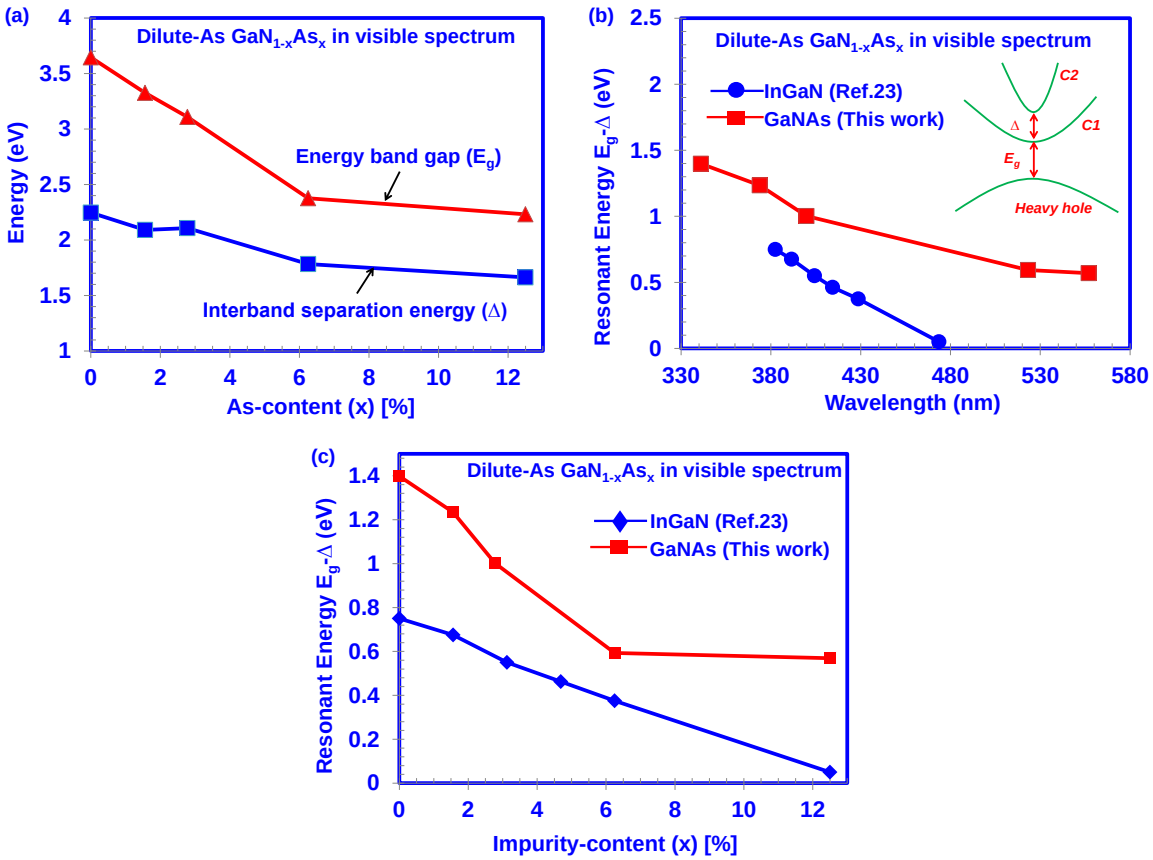

Figure 6-2: (a) Comparison between energy band gap and interband separation energy of GaNAs alloy from 0%up to 12.5% As-content and (b) Comparison between the energy difference E_g-Δ of GaNAs alloy and InGaN alloy as a function of emission wavelength/As content and (c) Comparison of the energy difference E_g-Δ as a function of As-content up to 12.5%.

Figure 6-2(b) and 6-2(c) presents the energy difference (E_g-Δ) as a function of emission wavelengths and impurity contents for dilute-As GaNAs alloys respectively. From these two figures [Figure 6-2(a) and 6-2(b)], it is shown that dilute-As GaNAs alloy has emission wavelength up to 525 nm (green) with only 6.25% As-content. The incorporation of In-content up to 12% in InGaN alloy resulted in emission wavelength of ~480 nm [23]. The comparisons on the energy

differences (E_g-Δ) for the dilute-As GaNAs alloy and InGaN alloy [23] are presented in the Fig. 6-2(b) and 6-2(c). The (E_g-Δ) reduces when the As-concentration is gradually increased in the GaNAs alloy. Similar trend is also observed in the InGaN alloy. It is worth to note that although the (E_g-Δ) of dilute-As GaNAs alloy decreases, the (E_g-Δ) for all the investigated GaNAs alloys are larger than 0.57 eV which correspond to off-resonance Auger process. In contrast, the (E_g-Δ) for InGaN alloy [Fig. 6-2(b) and 6-2(c)] approaches the resonance condition at and In-content of ~12% [23].

This finding strongly indicates that the interband Auger process in dilute-As GaNAs alloy as relatively negligible for serving as active material with emission wavelength in visible spectral regimes, specifically in the green spectral regime. Note that the Auger calculation results from our models were compared with the experimental and other computational values obtained in InGaN and GaN alloys for validation purpose. Our calculated Auger coefficient for InGaN alloy was obtained as $C \sim 3.13 \times 10^{-30}$ cm^6s^{-1}, which agrees well with the experimental data ($C \sim 1.4\text{-}2.7 \times 10^{-30}$ cm^6s^{-1}) [18-22] and with the theoretical results ($C \sim 2.0 \times 10^{-30}$ cm^6s^{-1}) [23, 24]. In addition, our calculated Auger coefficient for GaN alloy at T = 300K is $C = 2 \times 10^{-34}$ cm^6s^{-1}, which agrees considerably with the result by Bertazzi and co-workers [25]. The good agreements of our calculated Auger values for InGaN and GaN alloys with experimental results and computational works by others provide strong validation of the model used here.

Figure 6-3 shows the calculated Auger recombination coefficients of dilute-As $GaN_{1-x}As_x$ alloy with As-contents ranging from 0% up to 12.5%, which corresponds to active materials with emission wavelengths spanning from the ultraviolet up to the yellow spectral regime. The calculated Auger recombination coefficients of dilute-As GaNAs alloy take into account of both intraband and interband Auger recombination processes. The interband Auger recombination process includes the CHCC2 and CLCC2 Auger processes, while the intraband Auger recombination process includes CHCC and CLCC Auger processes. The CHCC2 (CLCC2) process denotes the Auger recombination process involving the C1 band, C2 band and HH (LH)

band. In a similar context, the CHCC (CLCC) processes denote the Auger recombination process involving the C1 band and HH (LH) band.

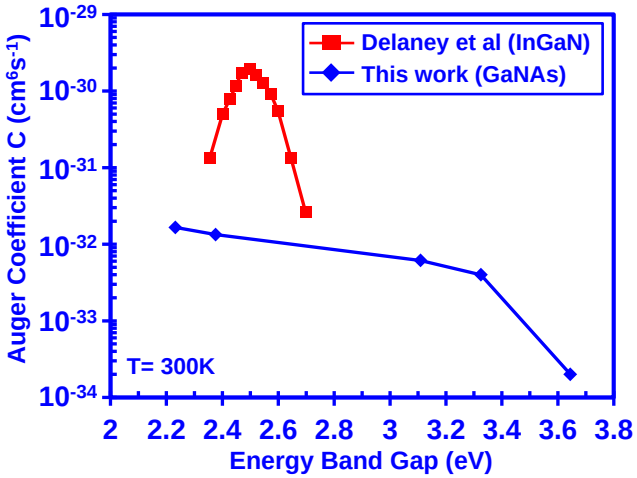

Figure 6-3: *The Auger coefficients for dilute-As GaNAs ternary alloy up to 12.5%-As considering interband and intraband Auger process at 300K. The calculated Auger coefficient of dilute-As GaNAs are compared to that of InGaN alloy from ref. 23.*

As shown in figure 6-3, the calculated Auger recombination coefficients of dilute-As GaNAs alloys are compared to the reported Auger recombination coefficients of InGaN alloys [23]. As can be seen in figure 6-3, the reported Auger recombination coefficients for InGaN alloys constituted a "bell-shaped like" profile as a function of energy band gap value, which centered on the resonant condition of the interband Auger process in this alloy. The Auger recombination coefficient for InGaN alloy increases from 2 x 10^{-32} cm^6s^{-1} at 2.7 eV to 2 x 10^{-30} cm^6s^{-1} at 2.5 eV, then decreases from 2x 10^{-30} cm^6s^{-1} at 2.5 eV to 1 x10^{-31} cm^6s^{-1} at 2.3 eV. Note that without the influence of the interband Auger recombination process, the Auger recombination coefficients for InGaN alloy fall in the range of 1 x 10^{-34} cm^6s^{-1}, which is driven primarily by the intraband Auger process. The "bell-shape like" profile provides strong evidence of dominant interband Auger process in the material, which primarily resulted from the effect of the resonant energy condition ($E_g \approx \Delta$) [23].

Note that the interband Auger process is dominant at the ($E_g \approx \Delta$; also referred as on-resonant condition) as observed in InGaN material with bandgap of ~ 2.5 eV [23]. The resonant condition in the materials achieved for $E_g \approx \Delta$, which results in very large increase in the interband

Auger rate attributed to the simultaneous momentum and energy conservations with large carrier occupation probabilities. This condition was reported for InGaN material [23]. However, in our finding, the dilute-As GaNAs has $E_g - \Delta \sim 0.5$ eV, which results in non-resonant condition for the interband Auger process to be dominant.

The Auger recombination coefficients for dilute-As $GaN_{1-x}As_x$ alloy with x = 0% up to x=12.5% is significantly suppressed over those of the InGaN alloy. The calculated Auger coefficient increases from 2 x 10^{-34} cm^6s^{-1} with 0% As-content of GaNAs alloy at 3.645 eV to 1.66 x 10^{-32} cm^6s^{-1} with 12.5% As-content of GaNAs alloy at 2.232 eV. The maximum Auger recombination coefficient of dilute-As GaNAs alloy is about two orders of magnitude smaller than that of InGaN alloy. In addition, the Auger recombination coefficients of dilute-As GaNAs alloy do not exhibit a bell-shaped profile like InGaN alloy, which can be readily understood from the negligible interband Auger process in this material. The low interband Auger rate in dilute-As GaNAs is attributed primarily to its large E_g-Δ > 0.5 eV, resulting in non-resonant energy condition for such process to be dominant [30].

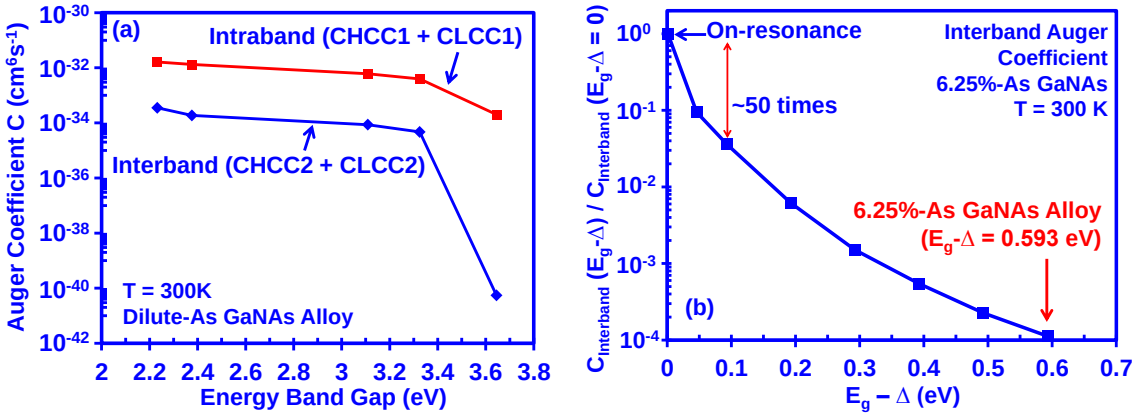

Figure 6-4: *(a) A comparison between interband and intraband Auger coefficient for dilute-As GaNAs ternary alloy up to 12.5%-As at 300K. Note that the interband Auger process consists of CHCC2 and CLCC2 transitions, and the intraband Auger process consists of CHCC1 and CLCC1 transitions. Figure 6-4(b) shows the effect of the parameter E_g-Δ onto the interband Auger recombination rate.*

Further analysis on the impact of interband Auger recombination in dilute-As GaNAs alloy is presented. Figure 6-4(a) shows a comparison between interband and intraband Auger recombination coefficients for dilute-As GaNAs alloys from 0%-As up to 12.5%-As at 300K. As

presented in figure 6-4(a), the interband Auger recombination process yields a maximum Auger coefficient of 3.42 x 10^{-34} cm^6s^{-1} while the intraband Auger recombination process yields a maximum Auger coefficient of 1.62 x 10^{-32} cm^6s^{-1} in GaNAs alloy of 12.5%-As-content at T = 300K. Our finding strongly indicates that the interband Auger rates are at least two orders of magnitude smaller than the corresponding intraband Auger rates for dilute-As GaNAs alloy. The Auger rate in dilute-As GaNAs alloy is dominated by the intraband process, and this rate is approximately two orders of magnitude smaller than those predicted for InGaN alloy.

As previously elaborated [23, 29], the interband Auger process is shown to have exponential dependency to the parameter E_g-Δ for a particular semiconductor. The strong mismatch of E_g-Δ in dilute-As GaNAs results in off-resonance condition, which in turn leads to a significant reduction in the interband Auger rate in the alloy. The effect of the off-resonance condition (E_g-$\Delta \neq 0$) on the interband Auger rates in dilute-As GaNAs can be illustrated in the ratio of the relative comparison on the Auger rate plotted as function of the E_g-Δ, as shown in figure 6-4(b). Figure 6-4(b) shows that the interband Auger process will be significantly suppressed by at least two orders of magnitude attributed directly from the off-resonance condition (E_g-Δ > 100 meV). This implies the important role of the parameter E_g-Δ energy in the interband Auger recombination process, which also suggests the importance of having large E_g-Δ energy to suppress the interband Auger recombination process in a semiconductor alloy.

6.3.2. Effect of Temperature on the Auger Recombination Rates

Figure 6-5(a) and 6-5(b) show the temperature dependency of the Auger recombination coefficients for dilute-As GaNAs ternary alloy from 1.56%-As up to 12.5%-As with a temperature range from 80K to 600K. The Auger coefficients (*C*) for dilute-As GaNAs alloys show an increasing trend for increasing temperature. Our findings show that the Auger coefficients for dilute-As GaNAs are in the range of $C \sim 10^{-31}$ cm^6s^{-1} for temperature T ~ 600 K, and the coefficients are in the range of 10^{-37} - 10^{-38} cm^6s^{-1} for T = 80 K. Specifically, the Auger

recombination coefficient for 6.25%-As GaNAs alloy reaches 1.57 x 10^{-31} cm^6s^{-1} at T = 600K and decreases to only 8.36 x 10^{-39} cm^6s^{-1} at T = 80K.

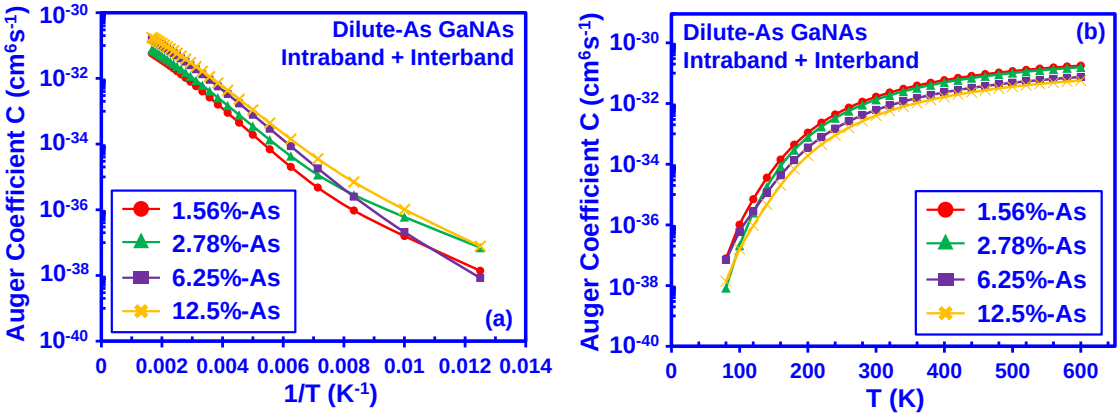

Figure 6-5: *Temperature dependency of Auger coefficients for dilute-As GaNAs ternary alloy from 1.56%-As up to 12.5%-As plotted as a function of (a) 1/ T and (b) T for a temperature range from T = 80 K up to T = 600 K.*

The trends shown in figure 6-5(a) and 6-5(b) are expected for dilute-As GaNAs alloys. The higher temperature results in the Fermi-Dirac function broadening leading to an increase in occupation probability for the carriers, which in turn increases the Auger rate. The Auger rate is shown to have saturation at high temperature primarily limited by restriction from the momentum conservation rule. Note that in this study the effective mass and energy band gap of the dilute-As GaNAs alloys are assumed to be constant over the temperature range. Further studies are required to account for the high temperature characteristics of the Auger rate for dilute-As GaNAs by taking into consideration the temperature variation in its band parameters.

6.4. Auger Recombination Analysis in Dilute-P GaNP Semiconductor

6.4.1. Effect of Interband Separation Energy on the Auger Rates

In the section 6.3, the analysis have shown that dilute-As GaNAs alloy has a much lower Auger recombination rates as compared to the InGaN alloy. This is important as the efficiency droop issue for the LEDs can be potentially alleviated because of the reduction in the Auger recombination rates by using dilute-As GaNAs alloy. Due to the similarities in electronic properties of the dilute-P GaNP alloys and the dilute-As GaNAs alloys [41], it is thus important for

us to determine the role of the interband Auger recombination in the alloys through the investigation on the related band properties of the dilute-P GaNP alloys.

The analytical Auger function model indicated two key conditions which are (a) $E_g > \Delta$ and (b) $E_g < \Delta$; which govern the interband Auger recombination process. Under condition (a), the Auger function is directly proportional to the exponential term of $-(E_g-\Delta)/2kT$, whereas under condition (b), the Auger function is proportional to the exponential term of $-(\Delta-E_g)/kT$. In both expressions the parameter k corresponds to the Boltzmann constant while T corresponds to the room temperature (300K). More importantly, the Auger function model demonstrated the capability of dilute-As GaNAs alloy in suppressing the interband Auger process, as the resonant energy of the alloy does not fulfill the resonance condition ($E_g-\Delta$ <0.25 eV).

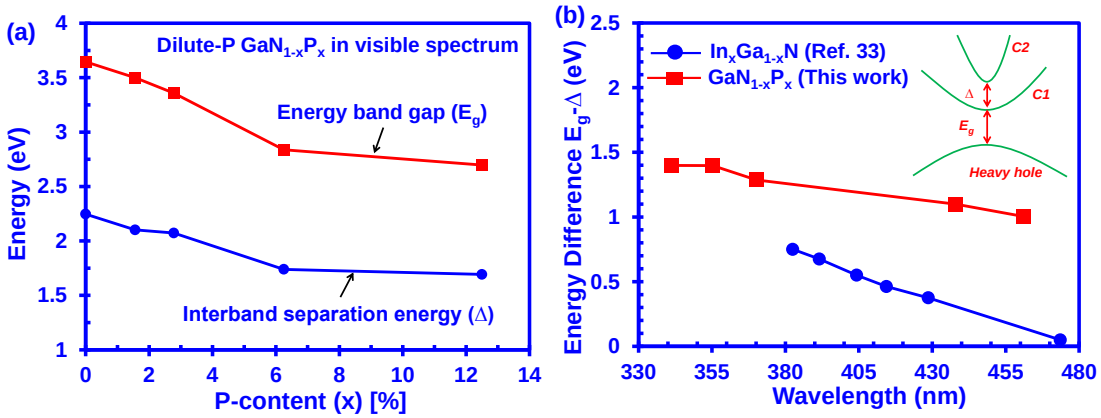

Figure 6-6: *(a) Comparison between energy band gap E_g and interband separation energy Δ of GaNP alloy from 0% up to 12.5% P-content, and (b) Comparison between the resonant energy of GaNP alloy and InGaN alloy as a function of emission wavelength.*

Figure 6-6(a) shows the energy band gap and the interband separation energy of dilute-P GaNP and dilute-As GaNAs alloys from 0% up to 12.5% P and As-content respectively. As shown in figure 6-6(a), the interband separation energy of dilute-P GaNP alloys reduces from 2.25 eV at 0% P-content to 1.75 eV at 12.5% P-content, resulting in an energy reduction of 0.5 eV. Similarly, the energy band gap of the dilute-P GaNP alloys has a decreasing trend from 3.645 eV to 2.697 eV as the P-content increases in the alloy. In contrast, the interband separation energy of the InGaN alloy increases while the energy band gap reduces as the In-content increases in the alloy.

The energy difference (E_g-Δ), or so called the resonant energy, as a function of emission wavelengths for the dilute-P GaNP alloys is shown in figure 6-6(b). As shown in figure 6-6(b), the resonant energy of the dilute-P GaNP alloys reduce slightly from 1.4 eV at wavelength of 340 nm to 1 eV at a wavelength of 460 nm. On the other hand, the resonant energy of the InGaN alloy reduces quicker over a shorter range of wavelengths, spanning from 0.8 eV at a wavelength of 380 nm to ~0 eV at wavelength of 480 nm [23].

As presented in figure 6-6, the resonant energy (E_g-Δ) of all the dilute-P GaNP alloys from 0% to 12.5% P-content remain larger than 1 eV, which is far from satisfying the resonance energy condition (E_g-Δ < 0.25 eV). This corresponds to the off-resonance Auger process [29], indicating minimal interband Auger recombination process in the dilute-P GaNP alloys.

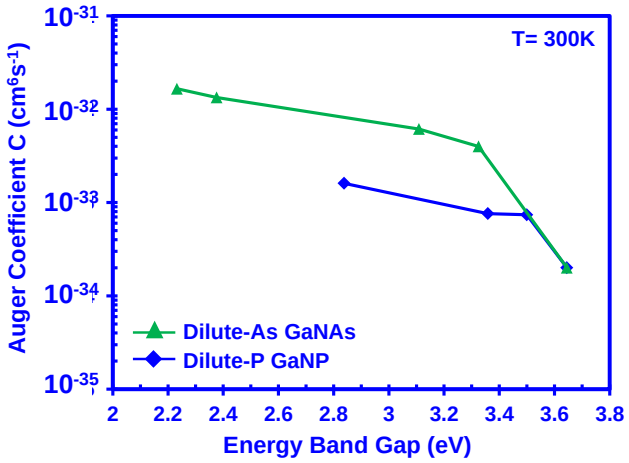

Figure 6-7: *Comparison between the Auger coefficients of dilute-P GaNP and dilute-As GaNAs semiconductor alloys.*

The Auger recombination coefficient can be calculated using the analytical solutions provided in Chapter 4. Figure 6-7 presents a comparison of Auger recombination coefficients between the dilute-P GaNP alloy and the dilute-As GaNAs alloy. As shown in figure 6-7, the Auger coefficients of dilute-P GaNP alloys are lower than that of the dilute-As GaNAs alloys, in which the order of C_{Auger} is ~10^{-33} cm^6s^{-1} around 2.8 eV. The phenomena is largely attributed to the larger interband separation energy in the dilute-P GaNP alloy. In addition, the P-content required in the GaNP alloys to achieve large band gap reduction is small in comparison to that of In-content in InGaN due to larger band gap bowing parameter in the GaNP alloys. Besides, the lattice mismatch

between the GaNP alloy with 6.25%-P and the GaN alloy is ~1.2% which is comparable to that of InGaN alloy. Our findings on the dilute-P GaNP alloy show that the alloys present a new opportunity in the lighting technology due to their potential to serve as the active region material with suppressed interband Auger recombination in the visible spectral regimes.

6.4.2. Effect of Temperature on the Auger Recombination Rates

Figure 6-8(a) and 6-8(b) present the temperature dependency of the Auger recombination coefficients for dilute-P GaNP ternary alloy from 1.56%-P up to 6.25%-P with the temperature ranging from 80K to 600K. Similar to the dilute-As GaNAs alloy, the Auger coefficients for dilute-P GaNP alloys show an increasing trend for increasing temperature. Our findings show that the Auger coefficients for dilute-P GaNP alloys are in the range of $C \sim 10^{-31}$ cm^6s^{-1} for temperature T ~ 600 K, and the coefficients are in the range of 10^{-39} - 10^{-44} cm^6s^{-1} for T = 80 K. Note that the Auger coefficients calculated here include both interband and intraband Auger recombination processes. It is interesting that the Auger coefficients for dilute-P GaNP alloys at low temperature are much smaller than that of dilute-As GaNAs alloys. One possible reason is because of the band gap energy of the dilute-P GaNP. Under the same composition of dilute anion content, the energy band gap of dilute-P GaNP is larger than that of dilute-As GaNAs alloy, leading to a situation where the energy conservation is more difficult to satisfy. However, further analysis will be required to provide the convincing explanation for this phenomena.

The trends shown in figure 5-6(a) and 5-6(b) are however expected for dilute-P GaNP alloys. The reason is similar to that of dilute-As GaNAs alloy. As the temperature goes higher, the occupation probability for the excited carriers increases attributed to the broadening of Fermi-Dirac broadening. As the probability increases, the number of successful Auger recombination transitions also increase, and hence the Auger rates. Further studies are still required to account for the high temperature characteristics of the Auger rate for dilute-P GaNP by taking into consideration the temperature effect in the alloy band parameters.

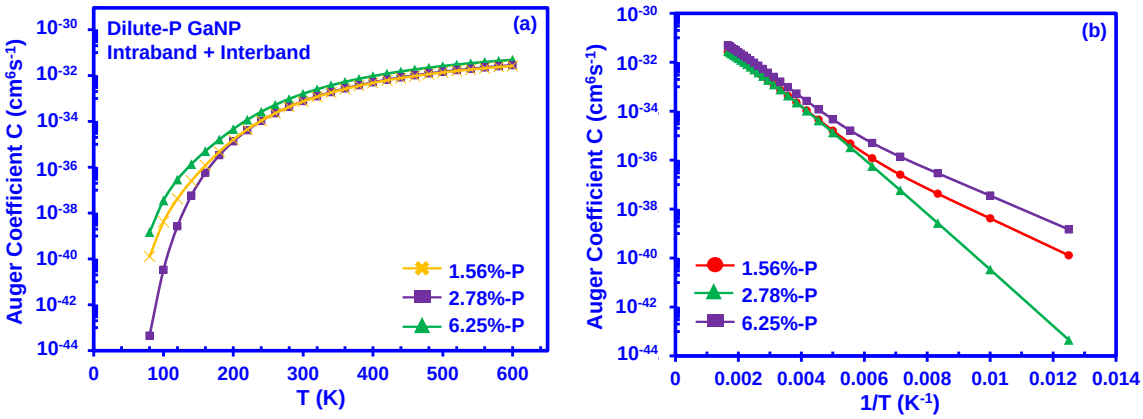

Figure 6-8: *Temperature dependency of Auger coefficients for dilute-P GaNP ternary alloy from 1.56%-P up to 6.25%-P plotted as a function of (a) T and (b) 1/T for a temperature range from T = 80 K up to T = 600 K.*

6.5. Summary

In summary, the analysis of the direct Auger recombination rate for the dilute-As GaNAs and dilute-P GaNP alloys have been performed. The direct Auger recombination rate in the dilute-As GaNAs alloy from 0%-As up to 12.5%-As is quantitatively determined through the First-Principle approach. The maximum Auger recombination coefficient considering intraband and interband Auger recombination processes for dilute-As GaNAs alloy is found as $C \sim 1.66 \times 10^{-32}$ cm^6s^{-1}, which is two orders of magnitude lower than that of InGaN alloy. The interband Auger coefficient is also found to be at least two orders of magnitude smaller than its corresponding intraband Auger coefficient for dilute-As GaNAs alloy. Similarly, the dilute-P GaNP alloy belonged to the dilute-anion GaN-based semiconductor class also shows low direct Auger recombination rates, with the Auger coefficient in the order of 10^{-33} cm^6s^{-1} or less.

The pursuits of experimental synthesis of dilute-As were initiated about two decades ago [2, 3]. However, the lack of a clear motivating factor in the pursuit of dilute-As GaNAs beyond serving as another method to achieve visible light emission in III-Nitride system had resulted in relatively little progress in this area. Similar situation has occurred for the case of dilute-P GaNP material. However, our current findings on the low Auger rates in both dilute-As GaNAs and dilute-P GaNP

alloys provide a strong motivation for the pursuit of these materials as a possible active material for visible LEDs and lasers operating at high operating current density.

References for Chapter 6

[1] S. Nakamura, M. Senoh, N. Iwasa, and S. Nagahama, “High-power InGaN single-quantum-well-structure blue and violet light-emitting diodes”, Appl. Phys. Lett., vol. 67, no. 13, pp. 1868-1870, Sep. 1995.

[2] X. Li, S. G. Bishop, and J. J. Coleman, “GaN epitaxial lateral overgrowth and optical characterization”, Appl. Phys. Lett., vol. 73, no. 9, pp. 1179-1181, Jul. 1998.

[3] X. Li, S. Kim, E.E. Reuter, S. G. Bishop, and J. J. Coleman, “The incorporation of arsenic in GaN by metalorganic chemical vapor deposition”, Appl. Phys. Lett., vol. 72, no. 16, pp. 1990-1992, Feb. 1998.

[4] M. Krames, O. Shchekin, R. Mueller-Mach, G. Mueller, L. Zhou, et.al., “Status and future of high-power light-emitting diodes for solid-state lighting”, J. Disp. Technol., vol. 3, no. 2, pp. 160-175, Jun. 2007.

[5] I. H. Brown, P. Blood, P. M. Smowton, J. D. Thomson, S. M. Olaizola, A. M. Fox, P. J. Parbrook, and W. W. Chow, “Time evolution of the screening of piezoelectric fields in InGaN quantum wells”, IEEE J. Quantum Electron., vol. 42, no. 12, pp. 1202-1208, Nov-Dec. 2006.

[6] M. H. Crawford, “LEDs for solid-state lighting: performance challenges and recent advances”, IEEE. J. Sel. Top. Quantum Electron., vol. 15, no. 4, pp. 1028-1040, Aug. 2009.

[7] M. Zhang, P. Bhattacharya, and W. Guo, “InGaN/GaN self-organized quantum dot green light emitting diodes with reduced efficiency droop”, Appl. Phys. Lett., vol. 97, no. 11, p. 011103, Jul. 2010.

[8] H. Zhao, G. Y. Liu, J. Zhang, J. D. Poplawsky, V. Dierolf, and N. Tansu, “Approaches for high internal quantum efficiency green InGaN light-emitting diodes with large overlap quantum wells”, Optics. Express, vol. 19, no. S4, pp. A991-A1007, Jul. 2011.

[9] A. Laubsch, M. Sabathil, J. Baur, M. Peter, and B. Hahn, IEEE Transactions on Electron Devices, vol. 57, no. 1, pp. 79-87, Jan. 2010.

[10] G. Y. Liu, J. Zhang, C. K. Tan, and N. Tansu, “Efficiency-droop suppression by using large-bandgap AlGaInN thin barrier layers in InGaN quantum well light emitting diodes”, IEEE Photonics Journal, vol. 5, no. 2, p. 2201011, Apr. 2013.

[11] J. Zhang, and N. Tansu, “Optical gain and laser characteristics of InGaN quantum wells on ternary InGaN substrates”, IEEE Photonics Journal, vol. 5, no. 2, Art. 2600111, Apr. 2013.

[12] D. F. Feezell, J. S. Speck, S. P. DenBaars, and S. Nakamura, “Semipolar (2021) InGaN/GaN light-emitting diodes for high-efficiency solid-state lighting”, J. Display Tech., vol. 9, no. 4, pp. 190-198, Apr. 2013.

[13] J. Y. Tsao, M. H. Crawford, M. E. Coltrin, A. J. Fischer, D. D. Koleske, G. S. Subramania, G. T. Wang, J. J. Wierer, and R. F. Karlicek Jr., “Toward smart and ultra-efficient solid-state lighting”, Advanced Optical Materials, vol. 2, no. 9, pp. 809-836, Sep. 2014.

[14] http://www.nobelprize.org/nobel_prizes/physics/laureates/2014/

[15] J. Piprek, “Efficiency droop in nitride-based light-emitting diodes”, Phys. Status Solidi A, vol. 207, no. 10, pp. 2217-2225, Jul. 2010.

[16] M. H. Kim, M. F. Schubert, Q. Dai, J. K. Kim, E. F. Schubert, J. Piprek, and Y. Park, “Origin of efficiency droop in GaN-based light-emitting diodes”, Appl. Phys. Lett., vol. 91, no. 18, p. 183507, Oct. 2007.

[17] H. P. Zhao, G. Y. Liu, J. Zhang, R. A. Arif, and N. Tansu, “Analysis of internal quantum efficiency and current injection efficiency in III-nitride light-emitting diodes”, J. Display Technol., vol. 9, no. 4, pp. 212-225, Apr. 2013.

[18] Y. C. Shen, G. O. Mueller, S. Watanabe, N. F. Gardner, A. Munkholm, and M. R. Krames, Appl. Phys. Lett., vol. 91, no. 14, p. 141101, Oct. 2007.

[19] P. G. Eliseev, M. Osin’ski, H. Li, and I. V. Akimova, “Recombination balance in green-light-emitting GaN/InGaN/AlGaN quantum wells”, Appl. Phys. Lett., vol. 75, pp. 3838-3840, 1999.

[20] M. Zhang, P. Bhattarcharya, J. Singh, and J. Hinckley, “Direct measurement of auger recombination in $In_{0.1}Ga_{0.9}N$/GaN quantum wells and its impact on the efficiency of $In_{0.1}Ga_{0.9}N$/GaN multiple quantum well light emitting diodes”, Appl. Phys. Lett., vol. 95, p. 201108, 2009.

[21] M. Meneghini, N. Triyellin, G. Meneghesso, and E. Zanoni, “A comined electro-optical method for the determination of the recombination parameters in InGaN-based light-emitting diodes”, J. Appl. Phys., vol. 106, p. 114508, 2009.

[22] D. A. Zakheim, A. S. Payluchenko, D. A. Bauman, K. A. Bulashevich, O. V. Khokhlev, and S. Y. Karpov, “Efficiency droop suppression in InGaN-based blue LEDs: Experiment and numerical modeling”, Phys. Status Solidi A, vol. 209, pp. 456-460, 2012.

[23] K. T. Delaney, P. Rinke, and C. G. Van de Walle, “Auger recombination rates in nitrides from first principles”, Appl. Phys. Lett., vol. 94, no. 19, p. 191109, May 2009.

[24] G. Hatakoshi and S. Nunoue, Jap. J. Appl. Phys., “Analysis of Auger recombination in wurtzite InGaN”, vol. 52, no. 8S, p. 08JG17, Aug. 2013.

[25] F. Bertazzi, M. Goano, and E. Bellotti, Appl. Phys. Lett., vol. 97, p. 231118, 2010.

[26] E. Kioupakis, P. Rinke, K. T. Delaney, and C. G. Van de Walle, “Indirect Auger recombination as a cause of efficiency droop in nitride light-emitting diodes”, Appl. Phys. Lett., vol. 98, no. 16, p. 161107, Apr. 2011.

[27] A. David, and M. J. Grundmann, “Droop in InGaN light-emitting diodes: A differential carrier lifetime analysis”, Appl. Phys. Lett., vol. 96, no. 10, p. 103504, Mar. 2010.

[28] J. Iveland, L. Martinelli, J. Peretti, J. S. Speck, and C. Weisbuch, “Direct measurement of Auger electrons emitted from a semiconductor light-emitting diode under electrical injection: Identification of the dominant mechanism for efficiency droop”, Phys. Rev. Lett., vol. 110, no. 17, p. 177406, Apr. 2013.

[29] C. K. Tan, J. Zhang, X. H. Li, G. Y. Liu, B. O. Tayo, N. Tansu, “First-Principle electronic properties of dilute-As GaNAs alloy for visible light emitters”, J. Dis. Tech., vol. 9, no. 4, pp. 272-279, Apr. 2013.

[30] A. A. Efremov, N. I. Bochkareva, R. I. Gorbunov, D. A. Lavrinovich, Y. T. Rebane, D. V. Tarkhin, Y. G. Shreter, “Effect of the joule heating on the quantum efficiency and choice of thermal conditions for high-power blue InGaN/GaN LEDs”, Semiconductors, vol. **40**, pp. 605-610, 2006.

[31] X. Guo, and E. F. Schubert, “Current crowding in GaN/InGaN light emitting diodes on insulating substrates”, J. Appl. Phys., vol. 90, no. 8, pp. 4191-4195, Oct. 2001.

[32] C. K. Tan, and N. Tansu, “First-Principle natural band alignment of GaN / dilute-As GaNAs alloy”, AIP Advances, vol. 5, no. 1, p. 017219, Jan. 2015.

[33] A. Kimura, C. A. Paulson, H. F. Tang, and T. F. Kuech, “Epitaxial GaN1-yAsy layers with high As content grown by metalorganic vapor phase epitaxy and their band gap energy”, Appl. Phys. Lett., vol. 84, no. 9, pp. 1489-1491, Mar. 2004.

[34] R. A. Arif, H. Zhao, and N. Tansu, “Type-II InGaN-GaNAs quantum wells active regions for laser applications”, Appl. Phys. Lett., vol. 92(1), Art. No. 011104, Jan. 2008.

[35] J. Wu, W. Walukiewicz, K. M. Yu, J. D. Denlinger, W. Shan, J. W. Ager III, A. Kimura, H. F. tang, and T. F. Kuech, “Valence band hybridization in N-rich $GaN_{1-x}As_x$ alloys”, Phys. Rev. B, vol. 70, no. 11, p. 115214, Sep. 2004.

[36] K. M. Yu, S. V. Novikov, R. Broesler, C. R. Staddon, M. Hawkridge, Z. Liliental-Weber, I. Demchenko, J. D. Denlinger, V. M. Kao, F. Luckert, R. W. Martin, W. Walukiewicz, and C. T.

Foxon, “Non-equilibrium GaNAs alloys with band gap ranging from 0.8-3.4 eV”, Phys. Status Solidi C, vol. 7, no. 7-8, pp. 1847-1849, May 2010.

[37] C. K. Tan, and N. Tansu, “Auger recombination rates in dilute-As GaNAs semiconductor”, AIP Advances, vol. 5, p. 057135, May 2015.

[38] A. Haug, D. Kerkhoff and W. Lochmann, “Calculation of Auger coefficients for III-V Semiconductors with emphasis on GaSb”, Phys. Status Solidi B, vol. 89, no. 2, pp. 357-365, Oct. 1978.

[39] D. B. Laks, G. F. Neumark, and S. T. Pantelides, “Accurate interband-Auger-recombination rates in silicon”, Phys. Rev. B, vol. 42, no. 8, pp. 5176-5185, Sep. 1990.

[40] A. Sugimura, “Band-to-band Auger effect in long wavelength multinary III-V semiconductor lasers”, IEEE J. Quantum Electron., vol. QE-18, no. 3, pp. 352-363, Mar. 1982.

[41] C. K. Tan, D. Borovac, W. Sun, and N. Tansu, “First principle electronic properties of dilute-P $GaN_{1-x}P_x$ alloy for visible light emitters”, Scientific Reports, vol. 6, p. 24412, Apr. 2016.

Chapter 7: Novel Active Region Design of III-Nitride Semiconductor Alloys for Visible Spectral Regime

The recent development in dilute-As GaNAs semiconductor demonstrate the strong potential of dilute-impurity nitride semiconductor alloys as a novel and unique material class for device applications. Nevertheless, the implementation of dilute-impurity nitride semiconductor alloys into device structure still requires further understanding and investigations. Up to present, there is still no merit in incorporating the dilute-impurity nitride alloys such as dilute-As GaNAs material into device technology since the conventional nitride-based device technology has been well established in the near decades. However, as discussed in Chapter 5 and Chapter 6, the motivations behind the use of dilute-impurity nitride alloys especially the dilute-As GaNAs material have become clear very recently when the materials demonstrate advantages over conventional InGaN material for the light emitting applications. How the humungous potential in the dilute-impurity nitride semiconductor alloys can be fully utilized is currently one of the important question in the related field.

In this chapter, we look into the potential of dilute-As GaNAs alloy as an active material in the GaN-based device technology through a novel quantum well structure design. We first briefly analyze the issue behind conventional quantum well that uses InGaN material in dealing with the long wavelength emission and discuss the latest approaches in enhancing the efficiency of the conventional InGaN QW for long wavelength emission. The concept and the potential of novel active region structure incorporating dilute-As GaNAs alloy will be discussed and evaluated.

7.1. Conventional InGaN Quantum Well in Long Wavelength Emission

As discussed in Chapter 1 and Chapter 2, III-Nitride semiconductor alloys are regarded as an important semiconductor class in solid state lighting technology. The key advances in the development of III-Nitride-based light emitting diodes (LEDs) has since led to practical implementation in various solid-state lighting applications [1-6]. Owing to the capability of InGaN to emit light in the entire visible spectral regime from blue to red, the realization of monolithic

integrated red-green-blue (RGB) GaN-based LEDs will be important towards achieving smart and ultra-efficient solid-state lighting technology [4].

Despite the success in developing high quality blue and green InGaN LEDs, extending the nitride-based QW emission wavelength towards red spectral regime is fundamentally challenging for two primary reasons. Higher In-content in the InGaN QW is always required in order to achieve the emission wavelength in red spectral regime, but phase separation of the InGaN material occurs simultaneously when the In-content becomes higher [7-8]. This leads to crystal degradation in the QW which is detrimental to the optical properties of the InGaN QW LED. Moreover, due to the polarization fields in the InGaN QW, the electron and hole wavefunctions are always spatially separated in the QW [illustrated in Figure 1(a)] which leads to reduction in the electron-hole wavefunction overlap. The detrimental effect from the charge separation issue in the InGaN QW is increasingly worsening as In-content increases in the QW.

Several approaches have been made to address the charge separation issue in blue and green QW LEDs [9-19], including nonpolar / semipolar InGaN QW [9], staggered InGaN QW [10-12] and InGaN QW with AlGaN delta-layer [13-14]. However, the approaches are not entirely applicable to addressing the issues in red QW LEDs since high In-content incorporation needs to be taken into consideration. In the case of nonpolar/semipolar InGaN QW, the compensation of quantum confined stark effect in the quantum well leads to blue-shift of emission wavelength if considering a comparison to the c-plane InGaN QW with same In-content [20]. This implies the requirement of higher In-content in nonpolar/semipolar InGaN QW to extend the emission into longer wavelength regime, which results in additional difficulty for the growth of high quality crystal. On the other hand, in the case of staggered InGaN QWs, the electron-hole wavefunction overlap decreases as the emission wavelength extends into longer wavelength such as red spectral regime [11].

The efforts devoted on extending the nitride-based QW LED emission wavelength towards red spectral regime are still significantly lacking, albeit the research progress is picking up momentum lately. To date a number of approaches have been proposed to address the issues in

red emitting GaN-based QW LEDs which include the InGaN metamorphic buffer layer or InGaN substrate for InGaN QW [18-19], the InGaN-delta-InN QW [21], InGaN with AlGaN interlayer QW [22], Eu-doped GaN QW instead of InGaN QW [23-25], , lattice-relaxed InGaN multiple QW structure [26] and semipolar InGaN QW [27]. Note that most approaches in addressing red nitride QW LED are fairly similar to the approaches in addressing the blue and green nitride QW LEDs. Nonetheless the In-content is more than 30% in the InGaN QW for red emission, and the reported highest external quantum efficiency of the red GaN-based QW LED is 2.9% [22] which is still much lower than that of blue and green GaN-based QW LEDs.

7.2. Novel InGaN / Dilute-As GaNAs Active Region Structure

If a high efficiency red emitting nitride-based QW LED can be realized, the making of a RGB QW nitride LED is prospectively achievable. This will provide an alternative solution for the related community to generate white light emission via nitride-based QW LED. Additionally, from the standpoint of science innovations and engineering, it is of great importance to overcome the barriers in achieving high efficiency red emitting nitride QW LED for further revolution in nitride-based solid state lighting technology.

In this chapter, we present a relatively low In-content nitride-based active region with large electron-hole wavefunction overlap by employing InGaN-GaNAs interface QW concept. The insertion of an interface layer of dilute-As GaNAs alloy adjacent to the InGaN QW layer leads to significantly enhanced electron-hole wavefunction overlap. In contrast to the existing approaches in incorporating high In-content (~35%-50%) in the active region for red emission, the In-content in the InGaN QW layer for the InGaN-GaNAs interface QW is relatively small (20%). The characteristics of InGaN-GaNAs QW are presented and are compared to those of the conventional InGaN QW. Note that dilute-As GaNAs alloy has recently been suggested as a potential candidate to be used for LED applications and to suppress interband Auger recombination process which could be important to reduce the efficiency droop issue in the InGaN-based LED devices [28-31].

7.2.1. Interface Quantum Well Concept

The utilization of interface quantum well concept originated from the development in GaAs-based and GaSb-based QW systems [35-39]. In conventional GaAs-based QW systems as shown in figure 7-1, which lacks the spontaneous polarization field, a type-I confinement of the electrons and holes in the QW results in close-to-unity overlap of the electron and hole wavefunctions. In order to elongate the transition wavelength towards mid-infrared spectral regime using GaAs-based and GaSb-based material system, interface quantum well was proposed which then lead to the state-of-the-art laser devices in the infrared regime [35-39]. The penalty of interface QW in the GaAs-based or GaSb-based material systems is the reduction of electron-hole wavefunction overlap in the active region, due to the separate confinement of electron and hole wave function in the adjacent layers respectively.

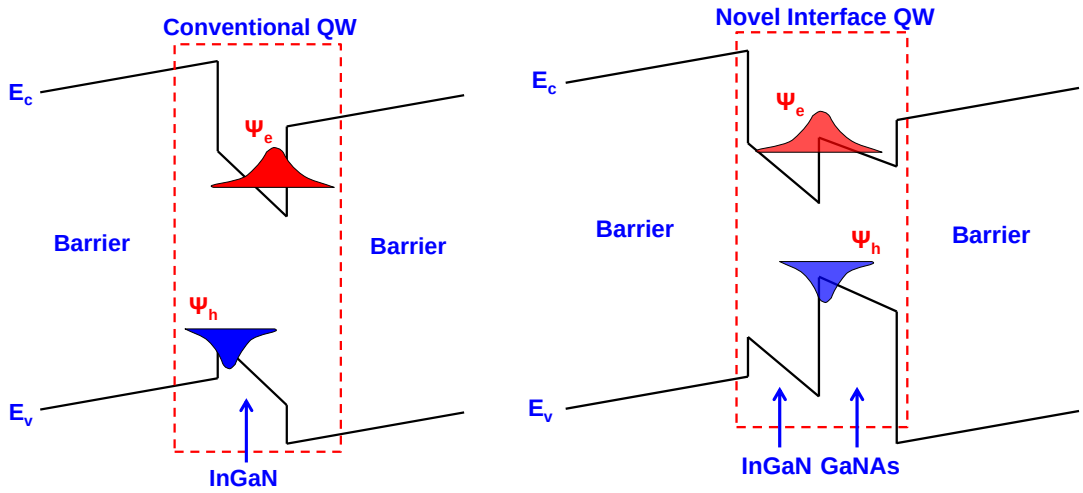

Figure 7-1: *Illustration of (a) Conventional nitride-based QW band lineup where the hole and the electron wavefunction are spatially separated in the opposite direction, and (b) Novel nitride-based interface QW where the holes and electrons are confined at the interface of two quantum well layers.*

On the other hand, as illustrated in figure 7-1(b), the electron and hole wavefunctions are trapped near the hetero-interface in the interface QW structure driven by the large heterojunction discontinuity and the large polarization field mismatch between the InGaN and dilute-As GaNAs layers. As such, the electron wave function and hole wave function will be confined in the first and second layers, respectively, so that the confinement of the wave functions occurs close to the

interface of the two material layers. Such carrier localization at the interface would thus dramatically enhance the electron-hole wavefunction overlap in the active region as compared to that of the conventional InGaN QW. Note that a similar concept using type-II "W" QW structure has previously been suggested to suppress the charge separation issue in InGaN QWs [15-16]. However, to our knowledge, the interface QW concept is yet to be applied and studied in nitride-based material systems. The type-II "W" QW [15, 16] used three layer structures (InGaN / dilute-As GaNAs / InGaN) for achieving improved overlap design, which provided an additional challenge attributed to the need for having three layers grown to form the active region. In this present work, by taking advantage of the large heterojunction discontinuity and the existence of the large polarization field mismatch between the InGaN and dilute-As GaNAs layer, the electron and hole wavefunctions are trapped near the hetero-interface in the interface QW structure.

7.2.2. Band Diagram and Characteristics of Interface Quantum Well

Our analysis and calculations are carried out based on self-consistent 6-band ***k·p*** formalism for wurtzite semiconductors, in which the valence band mixing, carrier screening effects, polarization fields and strain effect are taken into consideration [17, 32-33]. III-Nitride band parameters are obtained from Ref. 34 and conduction to valence band offset ratio (ΔE_c:ΔE_v=70:30) is set constant for all layers except for dilute-As GaNAs layer. The material parameters of dilute-As GaNAs layer used in our calculations were obtained through our previous First-Principle Density Functional Theory calculations, including the band properties [28] and the conduction to valence band offset ratio of GaN / dilute-As GaNAs (ΔE_c:ΔE_v=5:95) [29]. In our present study, the focus of the structure employed the GaNAs layer with 5% As-content for aiming at the red emitting active region. The use of 5% As-content in the dilute-As GaNAs layer significantly shifts the valence band edge energy upwards, leading to a reduction of the energy band gap.

Figure 7-2(a) and figure 7-2(b) show the energy band lineup of conventional 30Å $In_{0.35}Ga_{0.65}N$ QW and 30Å $In_{0.2}Ga_{0.8}N$ QW coupled with 10Å $GaN_{0.95}As_{0.05}$ interface-layer respectively, along

with the plotted wavefunctions of first conduction subband and first valence subband in both QW structures. Both structures are designed for transition wavelength of 620-630 nm for red spectral regime. As can be seen in figure 7-2(a), the existence of an internal electric field leads to the tilted band lineup across the structure, causing the charge separation such that the hole wavefunction is pulled towards the left side while the electron wavefunction is pulled towards the right side. The spatially separated electron and hole wavefunctions accordingly lead to significantly reduced overlap of 10.9% between the wavefunctions for conventional 30 Å $In_{0.35}Ga_{0.65}N$ QWs.

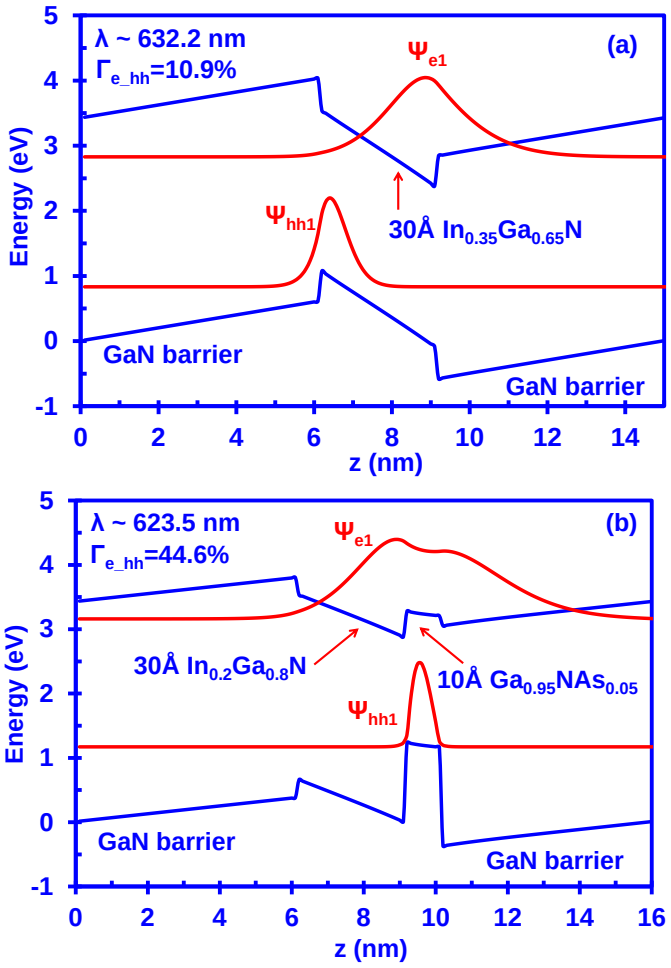

Figure 7-2: *Energy band lineups of (a) conventional 30 Å $In_{0.2}Ga_{0.8}N$ QW, and (b) 30 Å $In_{0.2}Ga_{0.8}N$ / 10 Å $GaN_{0.95}As_{0.05}$ QW with electron wave function (Ψ_{e1}) and hole wave function (Ψ_{hh1}).*

On the other hand, as shown in figure 7-2(b), by using a lower In-content (20%-In) for the InGaN QW layer and by coupling the InGaN QW layer with 10 Å $GaN_{0.95}As_{0.05}$ interface layer in

the active region, the large electron-hole wavefunction overlap could be achieved for the QW structure. The large valence band offset between InGaN and GaNAs layers leads to strong hole localizations towards the GaNAs layer, while the electron wavefunction is extended beyond the active region for structure employing GaN as the barrier layers. The wavefunction overlap in the interface QW structure therefore results in the enhanced electron-hole wavefunction overlap of 44.6%. The natural band alignment for dilute-As GaNAs / GaN results in $\Delta E_c : \Delta E_v = 5 : 95$ [29]. It is important to note that the inclusion of strain effect in the dilute-As GaNAs resulted in the "weak" type-II band alignment in dilute-As GaNAs / GaN interface attributed to its upward shift of the conduction band edge.

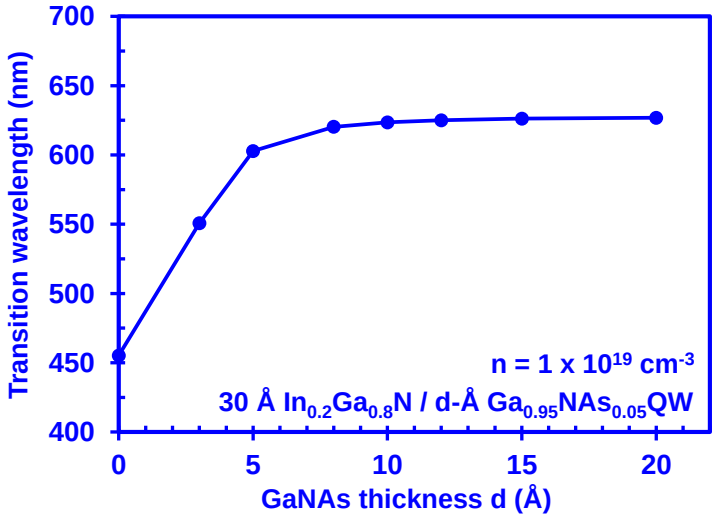

Figure 7-3: *Interband transition wavelength as a function of GaNAs layer thickness for 30 Å $In_{0.2}Ga_{0.8}N$ / d-Å $GaN_{0.95}As_{0.05}$ QW at carrier density of 1 x 10^{19} cm^{-3}.*

Figure 7-3 shows the interband transition wavelength as a function of the GaNAs layer thickness (d) for 30Å $In_{0.2}Ga_{0.8}N$ / d-Å $GaN_{0.95}As_{0.05}$ QW structure at carrier density of 1 x 10^{19} cm^{-3}. As shown in figure 7-3, the transition wavelength of the QW structure increases rapidly from 455.2 nm to 623.52 nm as the thickness of the GaNAs layer increases. The interband transition wavelength remains relatively unchanged in the ~625 nm spectral regime when the thickness of the GaNAs layer increases from 10 Å to 20Å, which is attributed to the deep hole localization in the GaNAs layer.

Figure 7-4 shows the electron-hole wavefunction overlap as a function of the GaNAs layer thickness for the 30Å InGaN / d-Å GaNAs QW structure at carrier density of 1 x 10^{19} cm^{-3}. In general, the electron-hole wavefunction overlap increases as the GaNAs layer thickness increases due to the shifting of the electron and hole wavefunction towards the interface of the two-layer QW. However, the electron-hole wavefunction overlap of the InGaN-GaNAs QW decreases slightly from 45% to 42.5% when the thickness of the GaNAs layer increases from 15Å to 20Å. Note that the 30Å $In_{0.2}Ga_{0.8}N$ QW without the GaNAs layer will yield a transition wavelength of 455 nm and wavefunction overlap of 22.9% which is considerably low as compared to that of the 30Å $In_{0.2}Ga_{0.8}N$ / d-Å $GaN_{0.95}As_{0.05}$ QW structure. As a comparison, even though 30Å $In_{0.35}Ga_{0.65}N$ QW yields a transition wavelength of 632 nm, the wavefunction overlap is small (10.9%), which is 4 times smaller than that of 30Å $In_{0.2}Ga_{0.8}N$ / d-Å $GaN_{0.95}As_{0.05}$ QW structure.

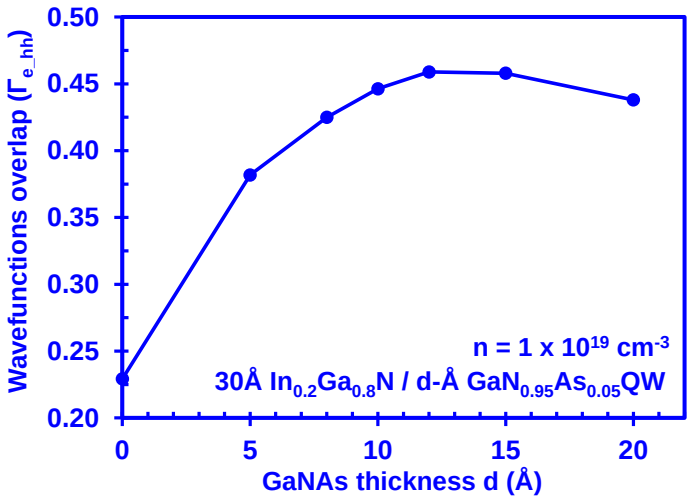

Figure 7-4: *Electron-hole wavefunction overlap as a function of GaNAs layer thickness for 30 Å $In_{0.2}Ga_{0.8}N$ / d-Å $GaN_{0.95}As_{0.05}$ QW at carrier density of 1 x 10^{19} cm^{-3}.*

Note that the designed structure of the InGaN QW with the coupling of the dilute-As GaNAs layer allows one to have transition wavelength redshift from blue spectral regime to red spectral regime and significantly enhanced electron-hole wavefunction overlap in the QW as compared to the conventional InGaN QW with same Indium composition and same InGaN QW thickness. In addition, the interband transition wavelength of the interface QW structure is relatively insensitive to the thickness of GaNAs layers beyond 10 Å as can be seen in figure 7-3, which is different

from the InGaN-delta-InN QW structure [21] where the resulting interband transition wavelength is highly dependent on the InN QW thickness. Accordingly, the similar redshifted transition wavelength (in this case blue to red spectral regime) independent of the varying interface layer thickness indicates the high potential of using interface QW concept in realizing highly controllable transition wavelength with large electron-hole wavefunction overlap under state-of-the-art growth technology.

7.3. Spontaneous Emission and Optical Gain Characteristics of InGaN-GaNAs QW in Red Emission

The characteristics shown by InGaN-GaNAs interface QW structure indicates the advantages over that of the conventional InGaN QW. As such, it is important to further investigate the spontaneous emission characteristics in the InGaN-GaNAs QW structure. The spontaneous emission rates are regarded as an important criteria in evaluating the potential of the active region for the light emitting diode applications. The calculation of the spontaneous emission rates for the interface QW structure are based on the calculated band diagrams in the section 7.2.2. The calculation details can be found in Chapter 3.

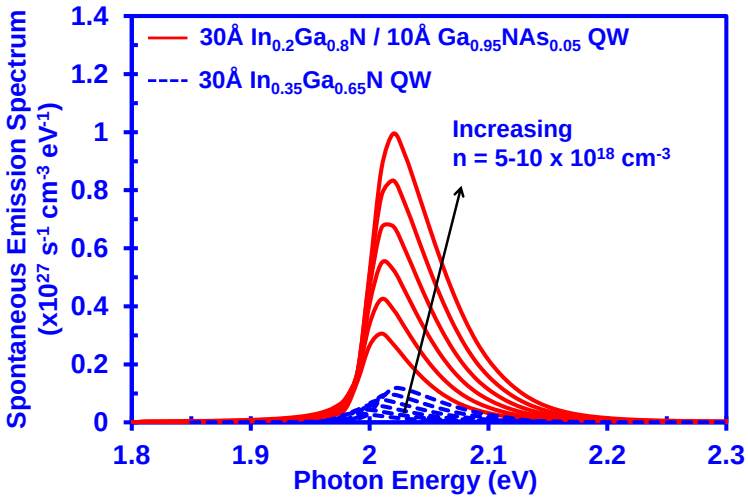

Figure 7-5: *Spontaneous emission spectra as a function of photon energy with carrier density from 5 x 10^{18} cm^{-3} to 1 x 10^{19} cm^{-3} for conventional 30 Å $In_{0.35}Ga_{0.65}N$ QW and 30 Å $In_{0.2}Ga_{0.8}N$ / 10 Å $GaN_{0.95}As_{0.05}$ QW.*

Figure 7-5 shows a comparison of spontaneous emission spectra for conventional 30Å $In_{0.35}Ga_{0.65}N$ QW (dash line) and 30Å $In_{0.2}Ga_{0.8}N$ / 10Å $GaN_{0.95}As_{0.05}$ QW (solid line) at carrier densities from 5 x 10^{18} cm^{-3} to 1 x 10^{19} cm^{-3} at T=300K. As shown in figure 7-5, the spontaneous emission rates for the conventional 30Å $In_{0.35}Ga_{0.65}N$ QW is much smaller than that of the 30Å $In_{0.2}Ga_{0.8}N$ / 10Å $GaN_{0.95}As_{0.05}$ QW. The spontaneous emission rate of 30Å $In_{0.2}Ga_{0.8}N$ / 10Å $GaN_{0.95}As_{0.05}$ QW is enhanced by 8.5 times as compared to that of conventional 30Å $In_{0.35}Ga_{0.65}N$ QW. Specifically, at n=1 x 10^{19} cm^{-3}, the peak spontaneous emission rate of conventional 30Å $In_{0.35}Ga_{0.65}N$ QW reaches 1.17 x 10^{26} s^{-1} cm^{-3} eV^{-1} whereas the peak spontaneous emission rate of 30Å $In_{0.2}Ga_{0.8}N$ / 10Å $GaN_{0.95}As_{0.05}$ QW reaches 9.95 x 10^{26} s^{-1} cm^{-3} eV^{-1}.

The improvement in the spontaneous emission recombination rates for the 30Å $In_{0.2}Ga_{0.8}N$ / 10Å $GaN_{0.95}As_{0.05}$ interface QW could be attributed to the improved hole wavefunction confinement in the GaNAs layer, resulting in the improvement in the electron-hole wavefunction overlap. As a side note, our findings indicate blueshift of transition wavelength for both structures when the carrier density increases. Nevertheless the wavelength blueshift of 30Å $In_{0.2}Ga_{0.8}N$ / 10Å $GaN_{0.95}As_{0.05}$ QW is considerably smaller than that of the conventional 30Å $In_{0.35}Ga_{0.65}N$ QW when the carrier density increases from 5 x 10^{18} cm^{-3} to 1 x 10^{19} cm^{-3}. The improvement in the wavelength blueshift for 30Å $In_{0.2}Ga_{0.8}N$ / 10Å $GaN_{0.95}As_{0.05}$ QW could be attributed to the reduction of the quantum confined stark effect in the active region.

Figure 7-6 shows the spontaneous emission radiative recombination rate per unit volume (R_{sp}) for conventional 30Å $In_{0.35}Ga_{0.65}N$ QW (dash-dot), 30Å $In_{0.2}Ga_{0.8}N$ / 10Å $GaN_{0.95}As_{0.05}$ QW (solid), 30Å $In_{0.2}Ga_{0.8}N$ / 15Å $GaN_{0.95}As_{0.05}$ QW (dot) and 30Å $In_{0.2}Ga_{0.8}N$ / 20Å $GaN_{0.95}As_{0.05}$ QW (dash) as a function of carrier density up to 10 x 10^{18} cm^{-3}. As shown in figure 7-6, the R_{sp} of 30Å $In_{0.2}Ga_{0.8}N$ / d-Å $GaN_{0.95}As_{0.05}$ QW is enhanced at each carrier density as compared to that of conventional 30Å $In_{0.35}Ga_{0.65}N$. Specifically, the enhancement of R_{sp} for the 30Å $In_{0.2}Ga_{0.8}N$ / 10Å $GaN_{0.95}As_{0.05}$ QW ranges from 8.8-11.3 times.

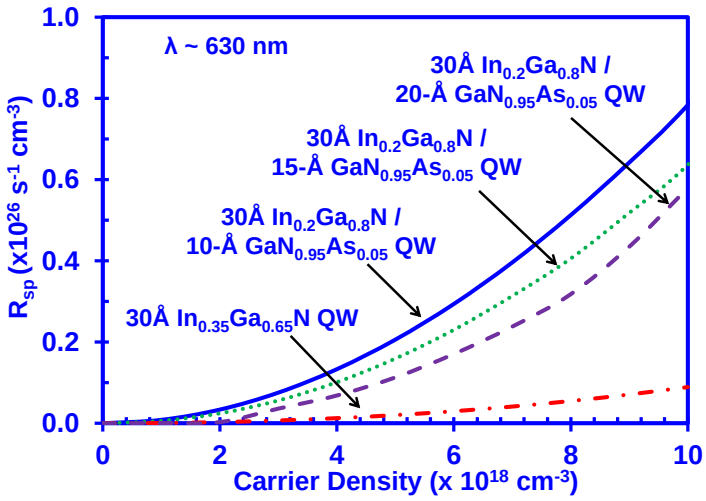

Figure 7-6: *Spontaneous emission rate R_{sp} as a function of carrier density for conventional 30 Å $In_{0.35}Ga_{0.65}N$ QW, 30 Å $In_{0.2}Ga_{0.8}N$ / 10 Å $GaN_{0.95}As_{0.05}$ QW, 30 Å $In_{0.2}Ga_{0.8}N$ / 15 Å $GaN_{0.95}As_{0.05}$ QW, and 30 Å $In_{0.2}Ga_{0.8}N$ / 20 Å $GaN_{0.95}As_{0.05}$ QW at T=300K.*

For further investigations of the potential of the interface QW for the laser applications in red spectral regime, optical gain characteristics have been analyzed. Figure 7-7(a) and 7-7(b) shows the optical gain spectra for conventional 30Å $In_{0.35}Ga_{0.65}N$ QW and 30Å $In_{0.2}Ga_{0.8}N$ / 10Å $GaN_{0.95}As_{0.05}$ QW with GaN barriers at *n* ranging from 3 x 10^{19} cm^{-3} to 5 x 10^{19} cm^{-3} and at *n* ranging from 2 x 10^{19} cm^{-3} to 5 x 10^{19} cm^{-3} respectively. As shown in figure 7-7, the optical gain of 30Å $In_{0.2}Ga_{0.8}N$ / 10Å $GaN_{0.95}As_{0.05}$ QW is at least10 times higher. Besides, as the carrier density increases, the peak wavelength blueshift in the InGaN / GaNAs QW is minimal (less than 0.1 eV) as compared to the conventional 30Å $In_{0.35}Ga_{0.65}N$ QW (shifted > 0.1 eV).

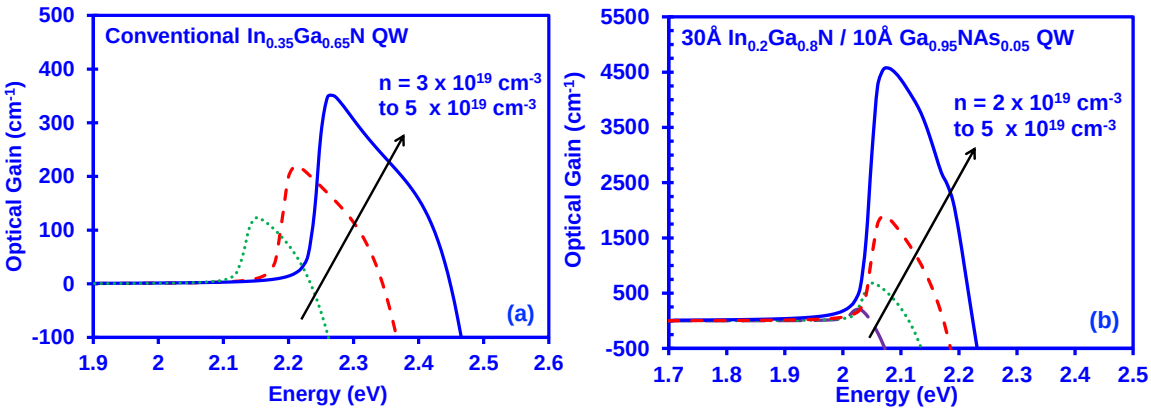

Figure 7-7: *Optical gain spectra for (a) conventional 30 Å $In_{0.35}Ga_{0.65}N$ QW and (b) 30 Å $In_{0.2}Ga_{0.8}N$ / 10 Å $GaN_{0.95}As_{0.05}$ QW with n from 2x10^{19} cm^{-3} to 5 x 10^{19} cm^{-3}.*

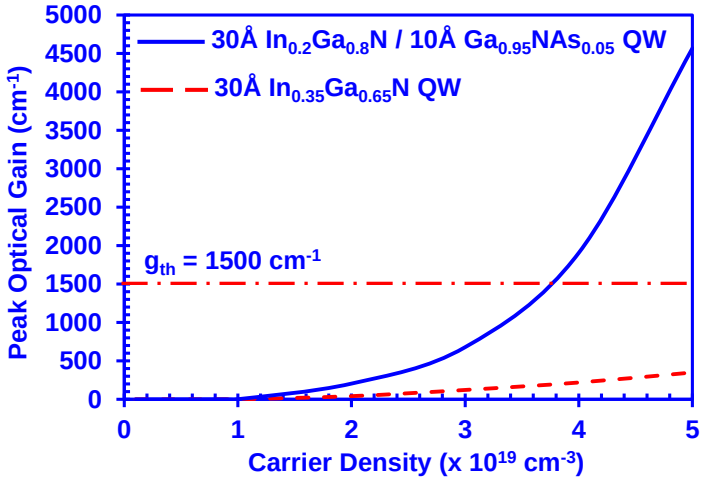

Figure 7-8: *Peak optical gain as a function of carrier density from n = 1x10^{18} cm^{-3} to 5 x 10^{19} cm^{-3} for conventional 30 Å $In_{0.35}Ga_{0.65}N$ QW and 30 Å $In_{0.2}Ga_{0.8}N$ / 10 Å $GaN_{0.95}As_{0.05}$ QW at T=300K.*

Figure 7-8 shows the peak optical gain as a function of carrier density from *n* ranging from 1 x 10^{18} cm^{-3} to 5 x 10^{19} cm^{-3} for conventional 30Å $In_{0.35}Ga_{0.65}N$ QW and 30Å $In_{0.2}Ga_{0.8}N$ / 10Å $GaN_{0.95}As_{0.05}$ QW. From figure 7-8, it can be seen that threshold carrier density to achieve gain of 1500 cm^{-1} for InGaN / GaNAs QW is roughly 3.8 x 10^{19} cm^{-3}. On the other hand, for conventional InGaN QW, the threshold carrier density to reach excited lasing condition is ~1020 cm-3. Note that ground state lasing condition could not be reached if the threshold gain is 1500 cm-1. As a result, the optical gain threshold analysis show that the carrier density can be reduced significantly by using InGaN / GaNAs QW, which is important for laser applications.

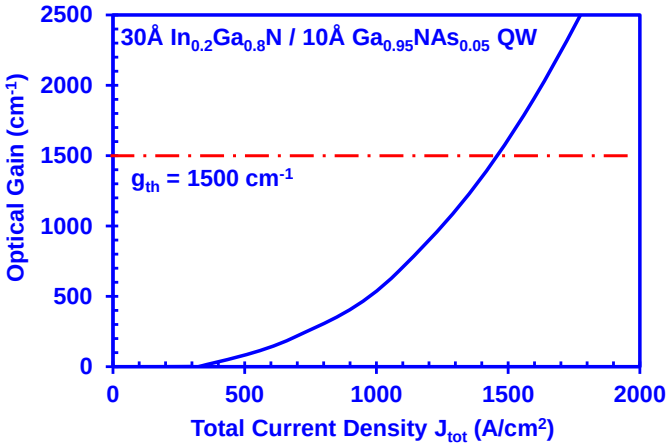

Figure 7-9: *Peak optical gain as a function of total current density for 30 Å $In_{0.2}Ga_{0.8}N$ / 10 Å $GaN_{0.95}As_{0.05}$ QW.*

One of the reason why low carrier density is important for laser applications is attributed to the non-radiative current density. Note that the Auger current density is proportional to the carrier density ($J_{Auger} \sim Cn_{th}^3$) in which C is the Auger coefficient parameter. Thus, by reducing the threshold carrier density 3 times, the Auger current density of the InGaN / GaNAs QW can be reduced by ~ 20 times as compared to that of conventional InGaN QW. Figure 7-9 presents the peak optical gain as a function of total current density for 30Å $In_{0.2}Ga_{0.8}N$ / 10Å $GaN_{0.95}As_{0.05}$ QW. Here the total current density implies the radiative recombination current density and non-radiative recombination current density. Taking C = 1 x 10^{-32} cm^6s^{-1} for the non-radiative current density, it can be seen from figure 7-9 that the total current density required to achieve optical gain of 1500 cm^{-1} is ~1400 A/cm^2. This finding indicates the importance of having low Auger recombination rates in the III-Nitride semiconductor device for practical lasing applications, and the strong potential of dilute-As GaNAs alloy in LEDs and laser applications.

Note that dilute-As GaNAs alloy has been reported for material growth using metal organic chemical vapor deposition (MOCVD) [40-41] and molecular beam epitaxy (MBE) [42]. In the perspective of MOCVD growth, the growth of dilute-As GaNAs thin film was operated at 700 – 750°C [41] which is comparable to the growth temperature of InGaN QW. Recent experimental studies by MBE have also demonstrated the capability to grow full As composition GaNAs alloy [42]. However, the implementation of GaNAs material in the active region for emitters is yet to be realized up to present. The field of dilute-As GaNAs is still in the early stage due to the lack of clear motivation on the importance of this material system for development of visible emitters. The identification of the dilute-As GaNAs alloy as a promising active material for red emitters with large spontaneous emission rate, as well as our recent work on identifying the non-resonant Auger process in this alloy, will provide a clear and strong motivation on the importance of the experimental pursuit of this material system. Future experimental studies are required to evaluate the performance and advantages presented in the InGaN / dilute-As GaNAs interface QW LEDs.

It is important to also mention that the main idea of this work is to illustrate the advantage of using an interface layer to extend the emission wavelength, while enhancing the matrix element

and radiative recombination rates in the QW as compared to the conventional InGaN QW. By controlling the As-content in the dilute-As GaNAs interface layer, it could be expected that the proposed structure of InGaN / GaNAs QW in this study has a high potential for control of the emission wavelength in green and red spectral regime with enhanced matrix element and radiative recombination rates in the QW. Further study have been carried out in section 7.4 to investigate the impact of the proposed interface QW on green and yellow spectral regime.

7.4. Spontaneous Emission and Optical Gain Characteristics of InGaN-GaNAs QW in Visible Spectrum

As discussed in section 7.3, there are numerous advantages to implement dilute-As GaNAs semiconductor in the III-Nitride LEDs and laser for red emission. However, the potential of dilute-As GaNAs in the LEDs for the whole visible spectrum is yet to be evaluated. It is expected that the addition of dilute-As GaNAs layer in the InGaN QW would lead to improvement in spontaneous emission rates as well as optical gain for various emission wavelength. The study is required to provide the clarification on whether dilute-As GaNAs is useful for emission other than red spectral regime. Here before the evaluation of InGaN / dilute-As GaNAs QW in the visible spectrum, it is important to evaluate the challenging issue of applying conventional InGaN QW for longer wavelength visible emission.

The spontaneous emission spectra of 30 Å conventional $In_xGa_{1-x}N$ QW with varying In-content (x) were calculated and presented in figure 7-10(a). As shown in this figure, the 30 Å conventional $In_{0.2}Ga_{0.8}N$ QW structure yields relatively large peak spontaneous emission rate at ~ 0.8 x 10^{27} s^{-1} cm^{-3} eV^{-1} with blue color emission (~ 451 nm). However, when the Indium composition of the InGaN QW is increased to cover longer emission wavelength (visible spectrum up to near infrared), the peak spontaneous emission rate starts to drop significantly. Figure 7-10(a) shows that the 30 Å conventional $In_{0.28}Ga_{0.72}N$ QW produces green light emission (~520 nm) with ~ 0.3 x 10^{27} s^{-1} cm^{-3} eV^{-1} peak spontaneous emission rate which is less than 40% of the spontaneous emission rate at blue regime. Further increase in In-content to 35% and beyond

redshifts the emission wavelength to red color regime with less than 0.1 x 10^{27} s^{-1} cm^{-3} eV^{-1} peak spontaneous emission rate. Such huge reduction (~ 8 times reduction) in the peak spontaneous emission rate of the conventional InGaN QW leads to the detrimental issue that prevents the conventional InGaN QW being applied as a high efficiency active region for longer wavelength visible light emission applications.

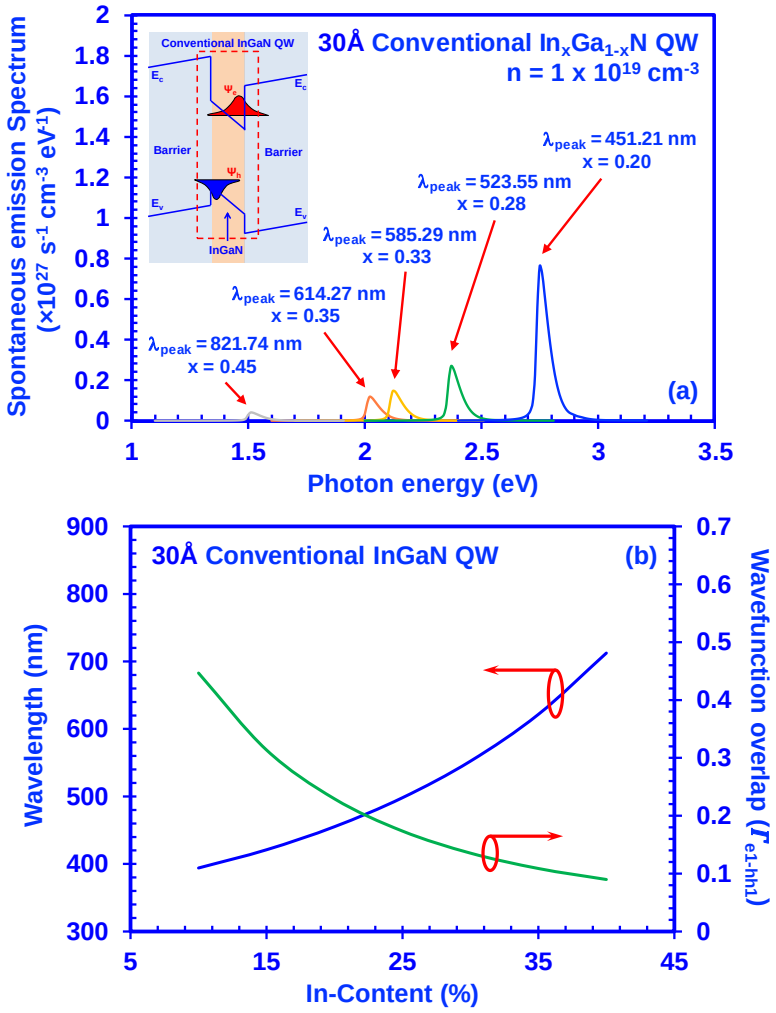

Figure 7-10: *(a)Spontaneous emission spectra and (b)Transition wavelength and ground-state carrier wavefunction for conventional 30 Å $In_{0.35}Ga_{0.65}N$ QW with varying In-content respectively.*

The large reduction of the peak spontaneous emission rate of conventional InGaN QW is mainly attributed to the fierce decrement of the carrier wavefunction overlap in such active region when the In-content increases. Figure 7-10(b) illustrates the change of the wavefunction overlap

in a 30 Å conventional $In_xGa_{1-x}N$ QW with respect to the In-content. The corresponding emission wavelength is also plotted as a function of the In-content in this figure. When the In-content increases from 10% to 40%, the transition wavelength of the InGaN QW can be extended from ~ 400 nm to ~ 700 nm. Such phenomenon indeed provides a great opportunity to achieve active regions covering entire visible emission spectrum regime. However, as shown in figure 7-10(b), the carrier wavefunction overlap of the 30 Å conventional $In_xGa_{1-x}N$ QW drops quickly from ~ 45% to ~ 10% when the In-content increase from 10% to 40%. This dramatic reduction of the carrier wavefunction overlap is attributed to the enlarged charge separation issue caused by the increased built-in polarization field within the QW region when the In-content is increased. The results presented in figure 7-10 clearly illustrate the critical issue associated with conventional InGaN QW, in which the dramatic reduction of carrier wavefunction overlap will result in the tremendous drop of peak spontaneous emission rate when the high In-content InGaN QW is applied for visible emission covering from green to red spectrum regime. Therefore, a novel solution is desired to provide access to a high efficiency visible emitting active region.

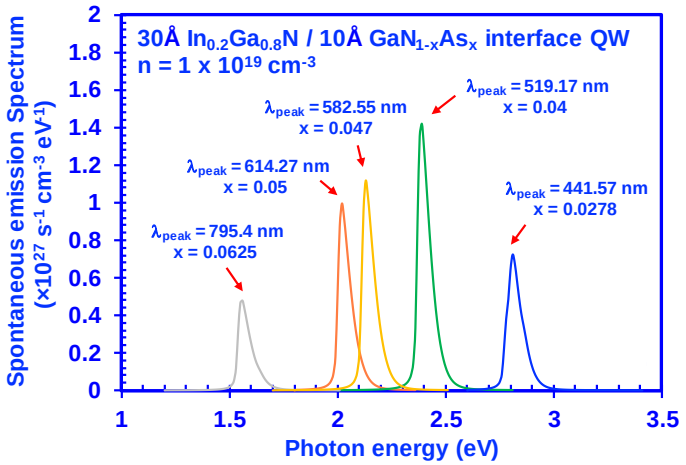

Figure 7-11: *Spontaneous emission spectra as a function of photon energy for for 30 Å $In_{0.2}Ga_{0.8}N$ / 10 Å $GaN_{1-x}As_x$ interface QW with n = 1 x 10^{19} cm^{-3} at T=300K.*

Figure 7-11 shows the spontaneous emission spectrum of the 30 Å $In_{0.2}Ga_{0.8}N$ / 10 Å $GaN_{1-x}As_x$ interface QW with various As-content. As shown in the figure, a 30 Å $In_{0.2}Ga_{0.8}N$ / 10 Å $GaN_{1-x}As_x$ interface QW with 2.78% As-content yields peak spontaneous emission rate around 0.72 x 10^{27} s^{-1} cm^{-3} eV^{-1} at blue emission regime, which is comparable to the conventional InGaN QW.

When As-content increases to 4% to shift the emission spectrum towards the green regime (~520 nm), the peak spontaneous emission of the interface QW increases to ~1.42 x 10^{27} s^{-1} cm^{-3} eV^{-1} which is almost 5 times larger than that of the conventional InGaN QW. Even though the peak spontaneous emission rates of the interface QW at yellow (~580 nm) and red (~610 nm) regime decrease slightly to ~1.12 x 10^{27} s^{-1} cm^{-3} eV^{-1} and ~1 x 10^{27} s^{-1} cm^{-3} eV^{-1} respectively due to the reduction of the wavefunction overlap, the values are still ~10 times larger in comparison to those of conventional InGaN QWs. Our analysis indicates that the InGaN / dilute-As GaNAs interface QW experiences no fierce degradation of the spontaneous emission rate when the emission wavelength redshifts to longer wavelength, which is in contrast to the conventional InGaN QW. Such stable and significantly large peak spontaneous emission rates of InGaN / dilute-As GaNAs interface QW across longer wavelength regime of the visible emission spectrum points out the potential of applying the InGaN / dilute-As GaNAs interface QW as high efficiency active regions for light emitters with emission wavelength across the entire visible spectrum regime.

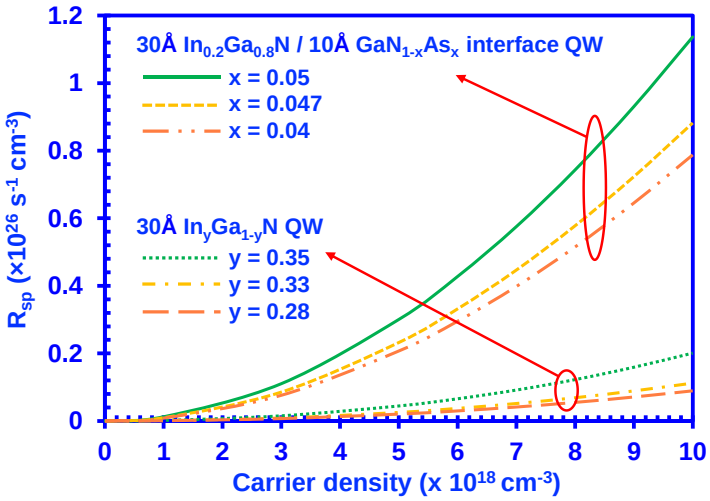

Figure 7-12: *Spontaneous emission rate R_{sp} as a function of carrier density for 30 Å $In_{0.2}Ga_{0.8}N$ / 10 Å $GaN_{1-x}As_x$ interface QW and 30Å conventional $In_yGa_{1-y}N$ QW.*

Figure 7-12 illustrates the comparison of the spontaneous emission rate per unit volume (R_{sp}) with respect to the carrier density between the 30Å $In_{0.2}Ga_{0.8}N$ / 10Å $GaN_{1-x}As_x$ interface QW and the conventional 30Å $In_yGa_{1-y}N$ QW. As shown in figure 7-12, the R_{sp} for the 30Å $In_{0.2}Ga_{0.8}N$ / 10Å $GaN_{1-x}As_x$ interface QW is significantly improved than that of the conventional 30Å $In_yGa_{1-y}N$ QW

across the carrier density (*n*) ranging from 1 x 10^{18} cm^{-3} to 1 x 10^{19} cm^{-3}. The remarkable enhancement of R_{sp} yielded by the 30Å $In_{0.2}Ga_{0.8}N$ / 10Å $GaN_{1-x}As_x$ interface QW is attributed to the large carrier wave function overlap in comparison to the conventional InGaN QW active region.

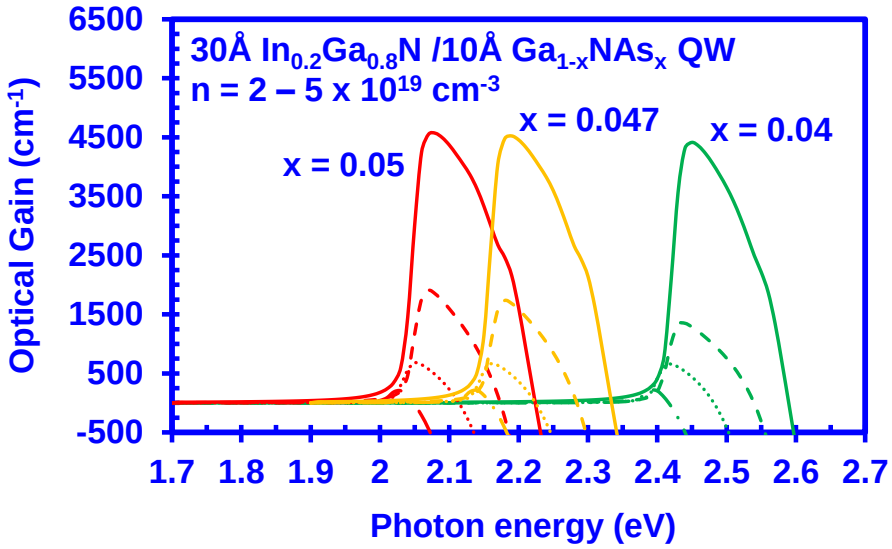

Figure 7-13: *Spontaneous spectra as a function of photon energy for 30 Å $In_{0.2}Ga_{0.8}N$ / 10 Å $GaN_{1-x}As_x$ interface QW with n = 1 x 10^{19} cm^{-3} at T=300K.*

Figure 7-13 presents the optical gain spectra as function of photon energy for the 30 Å $In_{0.2}Ga_{0.8}N$ / 10 Å $GaN_{1-x}As_x$ interface QW with various As-content. As shown in figure 7-13, the optical gain of the InGaN / dilute-As GaNAs QW reaches ~4500 cm-1 for green, amber, and red spectral regime. Considering that the threshold optical gain is ~1500 cm-1, the use of InGaN / dilute-As GaNAs QW will allow practical ground state lasing condition with considerably low carrier density (~4 x 10^{19} cm^{-3}). Besides, it can be seen from figure 7-13 that the peak optical gain is relatively similar across the spectrum, which is extremely useful to achieve uniform optical power when the injected current density is the same for each InGaN / GaNAs QW with different As-content in the active layer. Our analysis strongly indicate the importance of implementing InGaN / dilute-As GaNAs interface QW for the next-generation visible light LEDs and laser device applications.

7.5. Summary

In summary, the design of interface QW consisting of InGaN layer and dilute-As GaNAs layer leads to the emission wavelength in red spectral regime, along with enhanced electron-hole wavefunction overlap and spontaneous emission rate. Specifically, the design of the 30Å $In_{0.2}Ga_{0.8}N$ with 10Å $GaN_{0.95}As_{0.05}$ interface QW results in significant emission wavelength redshift from 455.2 nm to 623.52 nm. Moreover, the spontaneous emission rate of 30Å $In_{0.2}Ga_{0.8}N$ / 10Å $GaN_{0.95}As_{0.05}$ interface QW is greatly enhanced by 8.5 times as compared to that of the conventional 30Å $In_{0.35}Ga_{0.65}N$ QW for red emission. In addition, the emission wavelength of the InGaN / GaNAs interface QW is relatively insensitive to the variation of dilute-As GaNAs interface layer thickness beyond 10Å, indicating the potential of easing the difficulty for precise control of layer thickness during the epitaxial growth. Therefore the design of interface QW such as InGaN / dilute-As GaNAs QW has the high potential to be used for achieving high-efficiency nitride-based LEDs in red spectral regime.

In addition, the spontaneous emission and optical gain characteristics of the InGaN / dilute-As GaNAs QW have been analyzed for the emission in whole visible spectral regime. Similar to the performance in red regime, the use of dilute-As GaNAs as the interface layer next to InGaN layer in the QW leads to significant improvement in the spontaneous emission rate and optical gain from blue to red emission wavelength. Our analysis indicate the strong motivation to realize the development of dilute-As GaNAs alloy and implement the alloy in the III-Nitride based LEDs and laser devices.

References for Chapter 7

[1] M. Krames, O. Shchekin, R. Mueller-Mach, G. Mueller, L. Zhou, et.al., “Status and future of high-power light-emitting diodes for solid-state lighting”, J. Disp. Technol., vol. 3, no. 2, pp. 160-175, Jun. 2007.

[2] M. H. Crawford, “LEDs for solid-state lighting: performance challenges and recent advances”, IEEE. J. Sel. Top. Quantum Electron., vol. 15, no. 4, pp. 1028-1040, Aug. 2009.

[3] N. Tansu, H. P. Zhao, G. Y. Liu, X. H. Li, J. Zhang, H. Tong, and Y. K. Ee, “III-Nitride Photonics”, IEEE Photonics Journal, vol. 2, no. 2, pp. 241-248, Apr. 2010.

[4] J. Y. Tsao, M. H. Crawford, M. E. Coltrin, A. J. Fischer, D. D. Koleske, G. S. Subramania, G. T. Wang, J. J. Wierer, and R. F. Karlicek Jr., “Toward smart and ultra-efficient solid-state lighting”, Adv. Opt. Mat., vol. 2, pp. 809-836, 2014.

[5] C. K. Tan, and N. Tansu, “Nanostructured lasers: Electrons and holes get closer”, Nature Nanotech., vol. 10, pp. 107-109, Jan. 2015.

[6] P. Pust, P. J. Schmidt, and W. Schnick, “A revolution in lighting”, Nature Mater., vol. 14, pp. 454-458, Apr. 2015.

[7] K. G. Belyaev, M. V. Rakhlin, V. N. Jmerik, A. M. Mizerov, Ya. V. Kuznetsova, M. V. Zamoryanskaya, S. V. Ivanov, and A. A. Toropov, “Phase separation in InxGa1-xN (0.10 < x< 0.40), Phys. Status Solidi C, vol. 10, no. 3, pp. 527-531, Feb. 2013.

[8] M. D. McCluskey, L. T. Romano, B. S. Krusor, D. P. Bour, N. M. Johnson, and S. Brennan, “Phase separation in InGaN multiple quantum wells”, Appl. Phys. Lett., vol. 72, no. 14, pp. 1730-1732, Apr. 1998.

[9] D. F. Feezell, J. S. Speck, S. P. DenBaars, and S. Nakamura, “Semipolar ($20\bar{2}1$) InGaN/GaN light emitting diodes for high-efficiency solid-state lighting”, J. Disp. Tech., vol. 9, no. 4, pp. 190-198, Apr. 2013.

[10] R. A. Arif, Y. K. Ee, and N. Tansu, “Polarization engineering via staggered InGaN quantum wells for radiative efficiency enhancement of light emitting diodes”, Appl. Phys. Lett., vol. 91, no. 9, p. 091110, Aug. 2007.

[11] R. A. Arif, H. P. Zhao, Y. K. Ee, and N. Tansu, “Spontaneous emission and characteristics of staggered InGaN quantum-well light-emitting diodes”, IEEE J. Quantum Electron., vol. 44, no. 6, pp. 573-580, Jun. 2008.

[12] H. Zhao, G. Y. Liu, J. Zhang, J. D. Poplawsky, V. Dierolf, and N. Tansu, “Approaches for high internal quantum efficiency green InGaN light-emitting diodes with large overlap quantum wells”, Optics. Express, vol. 19, no. S4, pp. A991-A1007, Jul. 2011.

[13] J. Park, and Y. Kawakami, “Photoluminescence property of InGaN single quantum well with embedded AlGaN delta layer”, Appl. Phys. Lett., vol. 88, no. 20, p. 202107, May 2006.

[14] S. H. Park, J. Park, and E. Yoon, “Optical gain in InGaN/GaN quantum well structures with embedded AlGaN delta layer”, Appl. Phys. Lett., vol. 90, no. 2, p. 023508, Jan. 2007.

[15] R. A. Arif, H. Zhao, and N. Tansu, “Type-II InGaN-GaNAs quantum wells for lasers applications”, Appl. Phys. Lett., vol. 92, no. 1, p. 011104, Jan. 2008.

[16] H. Zhao, R. A. Arif, and N. Tansu, “Self-consistent gain analysis of type-II ‘W’ InGaN-GaNAs quantum well lasers”, J. Appl. Phys., vol. 104, no. 4, p. 043104, Aug. 2008.

[17] H. P. Zhao, R. A. Arif, Y. K. Ee, and N. Tansu, “Self-consistent analysis of strain-compensated InGaN-AlGaN quantum wells for lasers and light emitting diodes”, IEEE J. Quantum Electron., vol. 45, no. 1-2, pp. 66-78, Jan. 2009.

[18] J. Zhang, and N. Tansu, “Improvement in spontaneous emission rates for InGaN quantum wells on ternary InGaN substrate for light-emitting diodes”, J. Appl. Phys., vol. 110, no. 11, p. 113110, Dec. 2011.

[19] J. Daubler, T. Passow, R. Aidam, K. Kohler, L. Kirste, M. Kunzer, and J. Wagner, “Long wavelength emitting GaInN quantum wells on metamorphic GaInN buffer layers with enlarged in-plane lattice parameter”, Appl. Phys. Lett., vol. 105, no. 11, p. 111111, Sep. 2014.

[20] A. Avramescu, T. Lermer, J. Muller, C. Eichler, G. Bruederl, M. Sabathil, S. Lutgen, and U. Strauss, “True green laser diodes at 524 nm with 50mW continuous wave output power on c-plane GaN”, Appl. Phys. Express, vol. 3, no. 6, p. 061003, Jun. 2010.

[21] H. P. Zhao, G. Y. Liu, and N. Tansu, “Analysis of InGaN-delta-InN quantum wells for light-emitting diodes”, Appl. Phys. Lett., vol. 97, no. 13, p. 131114, Oct. 2010.

[22] J. Hwang, R. Hashimoto, S. Saito, and S. Nunoue, “Development of InGaN-based red LED grown on (0001) polar surface”, Appl. Phys. Express, vol. 7, no. 7, p. 071003, Jun. 2014.

[23] J. Heikenfeld, M. Garter, D. S. Lee, R. Birkhahn, and A. J. Steckl, “Red light emission by photoluminescence and electroluminescence from Eu-doped GaN”, Appl. Phys. Lett.,vol. 75, no. 9, pp. 1189-1191, Aug. 1999.

[24] A. Nishikawa, N. Furukawa, T. Kawasaki, Y. Terai, and Y. Fujiwara, “Room-temperature red emission from light-emitting diodes with Eu-doped GaN grown by organometallic vapor phase epitaxy”, Optical Materials, vol. 33, no. 7, pp. 1071-1074, May 2011.

[25] A. Nishikawa, T. Kawasaki, N. Furukawa, Y. Terai, and Y. Fujiwara, “Room-temperature red emission from a p-type/Europium-doped/n-type gallium nitride light-emitting diode under current injection”, Appl. Phys. Express, vol. 2, no. 07, p. 071004, Jun. 2009.

[26] K. Ohkawa, T. Watanabe, M. Sakamoto, A. Hirako, and M. Deura, “740-nm emission from InGaN-based LEDs on c-plane sapphire substrates by MOVPE”, J. Crys. Growth, vol. 343, no. 1, pp. 13-16, Mar. 2012.

[27] Y. Kawaguchi, C. Y. Huang, Y. R. Wu, Y. Zhao, S. P. DenBaars, and S. Nakamura, “Semipolar (2021) single-quantum-well red light-emitting diodes with a low forward voltage”, Jap. J. Appl. Phys., vol. 52, no. 8S, p. 08JC08, Jun. 2013.

[28] C. K. Tan, J. Zhang, X. H. Li, G. Y. Liu, B. O. Tayo, N. Tansu, “First-Principle electronic properties of dilute-As GaNAs alloy for visible light emitters”, J. Disp. Tech., vol. 9, no. 4, pp. 272-279, Apr. 2013.

[29] C. K. Tan, and N. Tansu, “First-Principle natural band alignment of GaN / dilute-As GaNAs alloy”, AIP Advances, vol. 5, no. 1, p. 071129, Jan. 2015.

[30] C. K. Tan, and N. Tansu, “Auger recombination rates in dilute-As GaNAs semiconductor”, AIP Advances, vol. 5, p. 057135, May 2015.

[31] C. K. Tan, D. Borovac, W. Sun and N. Tansu, “InGaN / Dilute-As GaNAs interface quantum well for red emitters”, Scientific Reports, vol. 6, p. 19271, Jan. 2016.

[32] S. L. Chuang, and C. S. Chang, “k.p method for strained wurtzite semiconductors”, Phys. Rev. B, vol. 54, pp. 2491-2504, Jul. 1996.

[33] S. L. Chuang, “Optical gain of strained wurtzite GaN quantum –well lasers”, IEEE J. Quantum Electron., vol. 32, no. 10, pp. 1791-1800, Oct. 1996.

[34] I. Vurgaftman and J. R. Meyer, Nitride semiconductor Devices, J. Piprek, Ed. New York: Wiley, 2007, ch. 2.

[35] J. R. Meyer, C. A. Hoffman, F. J. Bartoli, and L. R. Ram-Mohan, “Type-II quantum-well lasers for mid-wavelength infrared”, Appl. Phys. Lett., vol. 67, no. 6, pp. 757-759 , Aug. 1995.

[36] I. Vurgaftman, W. W. Bewley, C. L. Canedy, C. S. Kim, M. Kim, J. R. Lindle, C. D. Merritt, J. Abell, and J. R. Meyer, “Mid-IR type-II interband cascade lasers”, IEEE J. Selected Topics in Quantum Electronics, vol. 17, no. 5, pp. 1435-1444, Sep. 2011.

[37] R. Q. Yang, B. H. Yang, D. Zhang, C. H. Lin, S. J. Murry, H. Wu, and S. S. Pei, “High power mid-infrared interband cascade lasers based on type-II quantum wells”, Appl. Phys. Lett., vol. 71, no. 17, pp. 2409-2411, Oct. 1997.

[38] I. Vurgaftman, J. R. Meyer, N. Tansu, and L. J. Mawst, “(In)GaAsN-based type-II “W” quantum-well lasers for emission at λ = 1.55 μm”, vol. 83, no. 14, pp. 2742-2744, Oct. 2003.

[39] S. R. Bank, L. L. Goddard, M. A. Wistey, H. B. Yuen, and J. S. Harris, “On the temperature sensitivity of 1.5 μm GaInNAsSb lasers”, IEEE J. Sel. Topics Quantum Electron., vo. 11, no. 5, pp. 1089-1098, Sep./Oct. 2005.

[40] X. Li, S. Kim, E.E. Reuter, S. G. Bishop, and J. J. Coleman, “The incorporation of arsenic in GaN by metalorganic chemical vapor deposition”, Appl. Phys. Lett., vol. 72, no. 16, pp. 1990-1992, Feb. 1998.

[41] A. Kimura, C. A. Paulson, H. F. Tang, and T. F. Kuech, “Epitaxial GaN1-yAsy layers with high As content grown by metalorganic vapor phase epitaxy and their band gap energy”, Appl. Phys. Lett., vol. 84, no. 9, pp. 1489-1491, Mar. 2004.

[42] K. M. Yu, S. V. Novikov, R. Broesler, C. R. Staddon, M. Hawkridge, Z. Liliental-Weber, I. Demchenko, J. D. Denlinger, V. M. Kao, F. Luckert, R. W. Martin, W. Walukiewicz, and C. T. Foxon, “Non-equilibrium GaNAs alloys with band gap ranging from 0.8-3.4 eV”, Phys. Status Solidi C, vol. 7, no. 7-8, pp. 1847-1849, May 2010.

Chapter 8: Novel Deep-Ultraviolet III-Nitride Materials and Nanostructures

In Chapter 1, the importance of the deep UV applications and the potential of using III-Nitrides to achieve ultraviolet emission has been reviewed. In this chapter, the challenges and limitations to achieve high-efficiency UV light emitters, and the approaches implemented in recent years to improve the efficiency of AlGaN QW deep UV devices will be discussed. Furthermore, in this dissertation we look into the alternative material solutions in seeking the resolution of a fundamental issue existing in the AlGaN material. Comprehensive discussions are presented in this chapter to evaluate the potential of the alternative III-Nitride-based materials in the deep UV emitting applications.

8.1. Challenges and Limitations for III-Nitride Deep UV Light Emitters

III-Nitride semiconductor alloys have been widely implemented for solid state lighting applications over the past decade [1-5]. The progress in material epitaxy and device innovations of GaN-based semiconductor alloys have led to a revolution in lighting technology [6], in which the advances in the GaN-based light emitting diodes (LEDs) were recently recognized by the Nobel Prize in Physics in 2014 [7]. In recent years, III-Nitride deep ultraviolet (UV) LEDs and laser diodes have attracted much interests due to the prospective applications in sterilization, water purification and waste water treatment [8-33]. Extensive studies have been focused in the use of AlGaN-based quantum well (QW) active region for the UV emitters, attributed to the direct band gap property of the AlGaN alloy and the band gap coverage in the UV spectral regime from 210 nm up to 370 nm.

In comparison to the advances in the InGaN-based LEDs in the blue and green emitting regime, the AlGaN-based QW deep UV-LEDs still suffer from the low external quantum efficiency (EQE) issue [8-11]. Figure 8-1 shows the external quantum efficiency of the AlGaN UV devices across the UV spectral regime from 220 nm to 400 nm [9]. By carefully looking into the external quantum efficiency (EQE) of the AlGaN UV devices as a function of peak emission wavelength as

shown in figure 8-1, it can be seen that the EQE drops rapidly from ~30% at 400 nm to ~0.1% at 220 nm. As discussed in Chapter 1, deep UV emission from 220 nm – 280 nm is critical for various applications and such low efficiency from AlGaN devices render it useless for practical implementation. Thus, finding the causes behind the low efficiency issue in the deep UV AlGaN devices and improving the efficiency by eliminating the efficiency limiting factors have been one major research direction in the field of deep UV AlGaN devices.

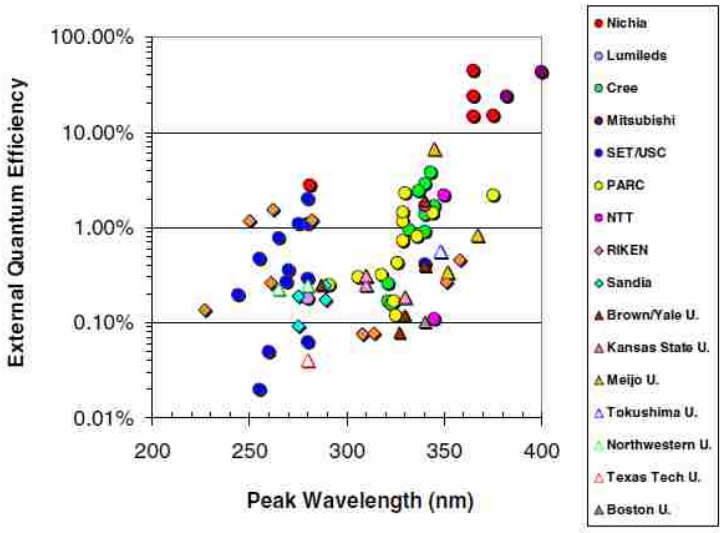

Figure 8-1: *The external quantum efficiency of AlGaN devices in the UV spectral regime from 220 nm to 400 nm [9].*

Throughout the research effort in the past decade, the conclusion has reached that the low EQE in the AlGaN LEDs is attributed to several factors including the low material growth quality due to high threading dislocation density [12], poor hole concentration [13], poor light extraction efficiency [14], fundamental valence bands crossover issue [15-17] and the charge separation issue due to the polarization effect [5, 18]. In the past few years, tremendous efforts have been devoted to enhancing the efficiency of the AlGaN deep UV (DUV) LED by looking into each of the causes mentioned above [11]. Thus, the efficiency of the AlGaN DUV devices has been improved since. However, it is shown that the EQE is still in the low (~10%) despite the tremendous efforts [11]. Most of the issues encountered in the AlGaN DUV LED are nonetheless similar to those of

InGaN LEDs, except the fundamental valence bands crossover issue present in the AlGaN active region material.

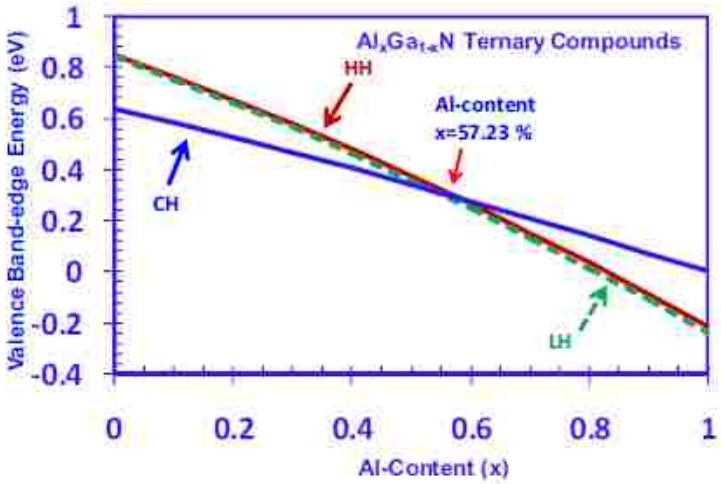

Figure 8-2: *Energy band edges of the heavy hole (HH), light hole (LH) and crystal-field split off (CH) bands as a function of Al-content (x) for $Al_xGa_{1-x}N$ ternary alloys [16].*

Figure 8-2 presents the energy band edges of the HH, LH and CH bands as a function of Al-content for the AlGaN ternary alloys. As shown in figure 8-2, the increase of the Al-content in the AlGaN alloy will result in the lowering of both HH / LH and CH bands. However, the rate of band edge lowering differs for HH / LH and CH band. As a result, when the Al-content reaches ~57% in the AlGaN alloy, the CH band will crossover with the HH / LH band. Similar situation is showcased for the AlGaN QW. In the low Al-content AlGaN QW, the heavy hole (HH) / light hole (LH) band edge is located above the crystal field split-off hole (CH) band edge. The increase of the Al-content in the AlGaN QW will result in the reduction of band-edge energy separation between the CH band and HH / LH band, eventually leading to the crossover between CH band and HH / LH band. Thus, for high Al-content AlGaN QW that is needed for deep UV emission, the CH band edge is located above the HH / LH band.

Recent works on valence bands crossover issue showed that the use of high Al-content AlGaN quantum well (QW) for deep UV emitter led to large transverse-magnetic (TM)-polarized gain but small transverse-electric (TE)-polarized gain, as shown in figure 8-3. This phenomenon

is primarily driven by the dominant conduction (C) – crystal field split-off hole (CH) transition in the AlGaN QW, due to the arrangement of the CH band as the uppermost valence band [16].

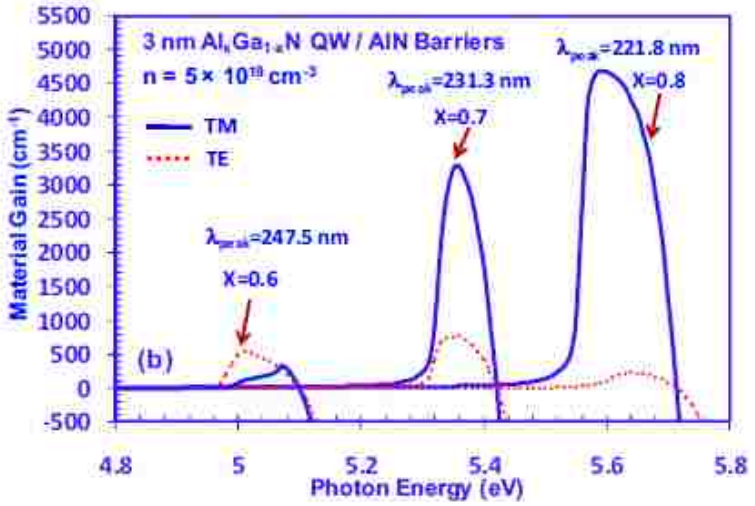

Figure 8-3: *Material gain of TE and TM polarization for 3 nm $Al_xGa_{1-x}N$ QW of x =0.6, 0.7 and 0.8 with AlN barriers at n=5 x 10^{19} cm^{-3} [16].*

Note that the TE-polarized emission refers to the light propagating perpendicular to the QW plane, while the TM-polarized emission refers to the in-plane light propagating parallel to the QW plane. However, the TM-polarized emission of the AlGaN QW is undesirable for the deep UV top emitting devices due to the difficulty of extracting the TM-polarized light from the top surface of the device, resulting in low light extraction efficiency [19]. The inefficient light extraction in combination with the weak TE polarized emission from valence band crossover issue therefore leads to low quantum efficiency in the high Al-content AlGaN QWs.

8.2. Approaches in Efficiency Enhancement of AlGaN Deep UV Emitters

As discussed in section 8.2, there are various approaches implemented to improve the efficiency by alleviating the various factors behind the low efficiency issue. One of the key problems that is threading dislocation density can be reduced by using special growth condition for the AlN template on sapphire [11]. Figure 8-4 shows the schematic view of the growth control method used for growing the multilayer AlN on sapphire. It is found that the edge and screw-type dislocation densities of the AlN multilayer were in the order of 10^8 and 10^7 cm^{-2} respectively.

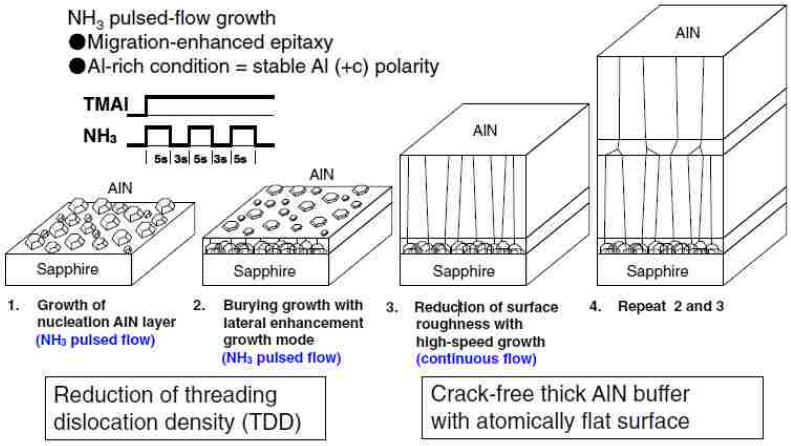

Figure 8-4: *Schematic diagram of the growth method to reduce the threading dislocation density on the AlN buffer layer on sapphire [11].*

In addition, there has been approach in trying to increase the transmission of the deep UV light. It is known that p-type AlN layer has significantly large activation energy, rendering it inefficient for p-type conduction. Most deep UV AlGaN QW emitters studied by various groups need to employ p-type GaN layer for the p-type conductivity. However, there is a tradeoff in that p-GaN layer would have strong absorption of the UV light, leading to low light transmission of ~10% in the regime of 250 nm – 300 nm. Recent work showed that the transmission can be significantly improved by switching from p-GaN layer to p-type AlGaN/AlGaN short-period superlattices [10]. As a result, the UV light transmission is improved by at least 6 times in the spectral regime of 250 nm – 300 nm.

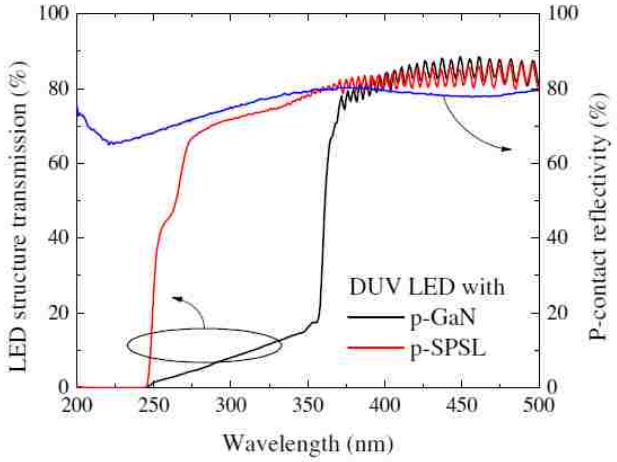

Figure 8-5: *Transmission spectra of DUV LED structures with p-GaN layer and p-type AlGaN/AlGaN short-period superlattices [10].*

Besides, various studies targeting the polarization switching in the AlGaN QW for dominant TE-polarized emission have been carried out by investigating the effect of variables such as Al composition of the QW, the QW thickness and the strain in the QW [19, 22]. A different approach has also been suggested by employing AlGaN-delta-GaN QW structure, in which the valence bands are rearranged, leading to dominant TE-polarized emission [23-24]. Figure 8-6 shows that the TE-polarized gain is much higher than the TM-polarized gain for the AlGaN-delta-GaN QW structure when the delta-GaN layer is inserted into the AlGaN QW. Note that the valence band crossover issue can be alleviated by using such approach. However, it is also important to note that the Al-content required in the AlGaN layer is quite high, which could be complicated for realistic growth.

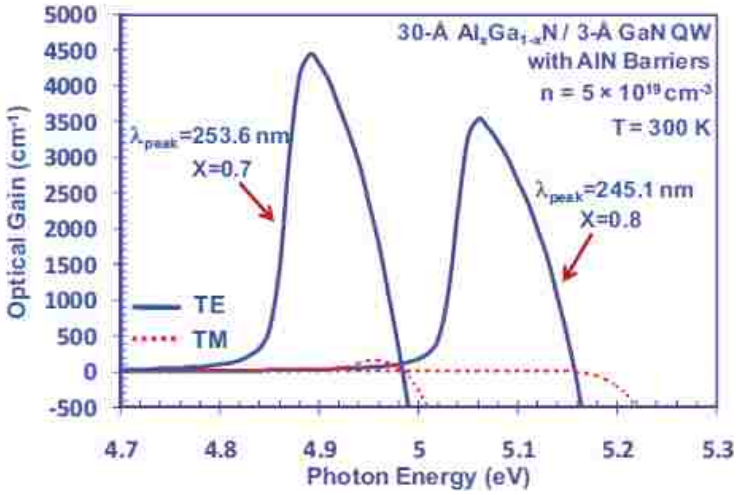

Figure 8-6: *Material gain of TE and TM polarization for 3 nm $Al_xGa_{1-x}N$ / 0.3 nm GaN QW of x = 0.7 and 0.8 with AlN barriers at n=5 x 10^{19} cm^{-3} [23].*

While the discussions only cover a few approaches, there are numerous different approaches being implemented to improve the device performance for deep UV emission. These approaches nonetheless focused in the use of AlGaN alloy in the active region, while the approach on using different III-Nitride UV materials is relatively unexplored. Identifying and developing the potential of alternative UV materials will be critical towards the progress in deep UV emitters. Here we have looked into two possibilities of materials which are AlInN alloy and dilute-As AlNAs alloys.

8.3. Conventional AlInN Quantum Well Structure for Deep UV Emission

8.3.1. Current Status of AlInN Alloy in Applications

In recent years, there has been proposal suggesting that AlInN alloy can be used as the electron blocking layer for the InGaN QW LEDs. The study shows that a thin AlInN layer can be used to block the electrons effectively and result in improved performance of the LED devices [34]. Besides, AlInN material has been suggested as a thermoelectric material, in which the thermoelectric figure of merit is as high as ~0.52 [35]. AlInN alloy has also been suggested as a possible material for power electronic applications due to its lattice-matching to GaN [36-37]. The growth of AlInN alloy has also been realized by using MOCVD technique [21], indicating the strong potential of AlInN alloy as a promising material for various device applications.

Nevertheless, the literature on AlInN QW as the active region for deep UV emitters is still highly limited up to present [28, 29, 32], despite that the AlInN alloy has been extensively studied for employing in the visible light emitting and power electronics applications. Very recently, there has been an emerging interest in using the AlInN alloy as the active region for deep UV laser diodes (λ ~ 250 nm) [28], attributed to the full band gap coverage of the material in the UV spectrum. However, the understanding of the optical characteristics of the AlInN QW is still lacking, and it is important to investigate the AlInN QW to evaluate its potential as the deep UV active region material.

8.3.2. AlInN Quantum Well Structure with AlN Barriers

Figure 1 shows the energy band lineup of single 20Å $Al_{0.85}In_{0.15}N$ QW with AlN barriers, along with the plotted wavefunctions of the first conduction and valence subbands. The existence of the spontaneous and piezoelectric polarization fields in the active region leads to the tilting of the energy band lineup, resulting in the spatial separation of electron and hole wavefunctions in the QW. The pulling of the electron and hole wavefunctions away from one another thus results in the low electron-hole wavefunction overlap of 35.8% as shown in figure 1.

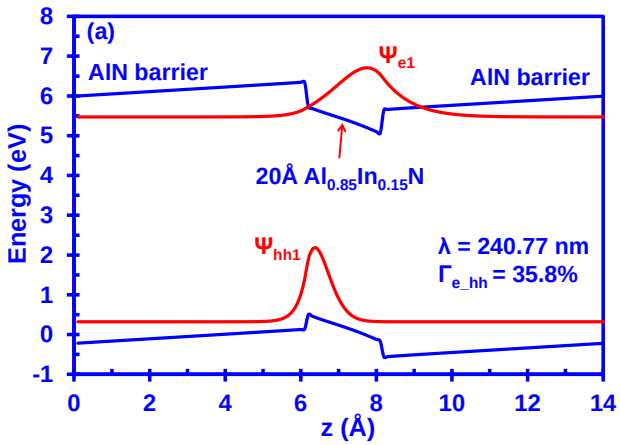

Figure 8-7: *Energy band lineup of conventional 20Å $Al_{0.85}In_{0.15}N$ QW with emission wavelength of 240.77 nm and electron-hole wavefunction overlap of 35.8%.*

Figure 8-8 presents the transition wavelength and the electron-hole wavefunction overlap of the conventional 20Å $Al_{1-x}In_xN$ QW as a function of the In-content (x). As shown in figure 8-8, the transition wavelength of the AlInN QW will reduce as the In-content increases in the QW. This is expected since the conduction and valence band edges will move down and up respectively with the increase of In-content. As such, the corresponding energy levels will be shifted. However, when the In-content increases, the electron-hole wavefunction overlap reduces accordingly in the AlInN QW. The reason is that the piezoelectric polarization field increases in the QW as the In-content increases due to the increased strain, and consequently the electron and hole are spatially separated even more significantly.

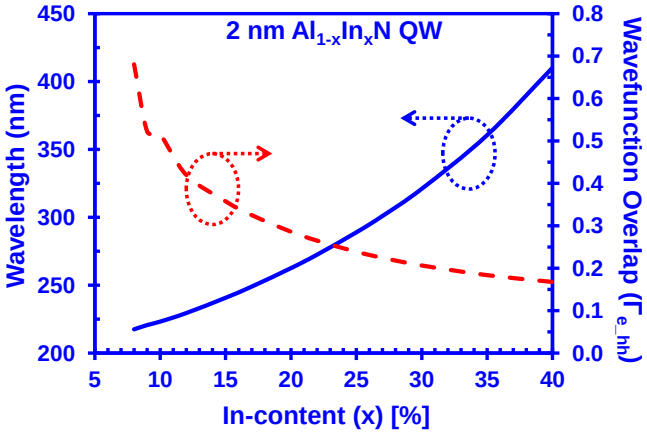

Figure 8-8: *Transition wavelength and electron-hole wavefunction overlap as a function of In-content (x) of conventional 20Å $Al_{1-x}In_xN$ QW.*

Besides, an increase of the QW thickness is expected to reduce the electron-hole wavefunction overlap even further in the QW which is not an ideal case for light emitting diodes. Note that the charge separation effect in a nitride-based QW due to the polarization charge induced built-in electric fields has been well documented [41-44]. Several approaches have been successfully applied in suppressing the charge separation effect in the QW, especially with the invention of staggered QW [42, 43] and semipolar / nonpolar QW concepts [41]. Similar approaches are expected to improve the electron-hole wavefunction overlap in the AlInN QW.

8.3.3. Spontaneous Emission and Optical Gain Characteristics of AlInN QW

Figure 8-9 shows the spontaneous emission spectra as a function of photon energy for conventional 20Å $Al_{0.92}In_{0.08}N$ QW, 20Å $Al_{0.88}In_{0.12}N$ QW, 20Å $Al_{0.85}In_{0.15}N$ QW, and 20Å $Al_{0.83}In_{0.17}N$ QW at a carrier density (*n*) of 5 x 10^{19} cm^{-3} at T = 300K. The peak spontaneous emission rate shows the redshift of emission wavelength from 217.5 nm to 249 nm when the In-content increases from 8% to 17% in the AlInN QW. As shown in figure 8-9, the TM-polarized spontaneous emission is dominant as compared to the TE-polarized emission when the In-content is 8% in the AlInN QW. When the In-content increases, the TM-polarized spontaneous emission rate reduces rapidly and TE-polarized emission begins to dominate in the $Al_{1-x}In_xN$ QW.

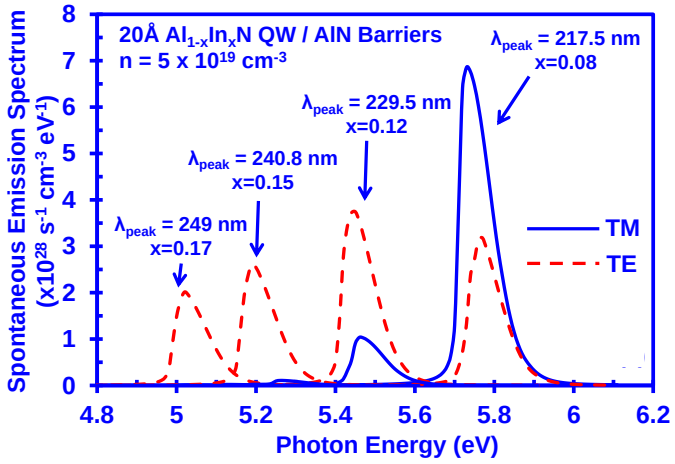

Figure 8-9: *Spontaneous emission spectrum as a function of photon energy at carrier density of 5 x 10^{19} cm^{-3} at T=300K for conventional 20Å $Al_{0.92}In_{0.08}N$ QW, 20Å $Al_{0.88}In_{0.12}N$ QW, 20Å $Al_{0.85}In_{0.15}N$ QW and 20Å $Al_{0.83}In_{0.17}N$ QW.*

The phenomenon shown in figure 8-9 is attributed to the CH-HH bands crossover in which the HH / LH bands have moved to the uppermost level when the In-content increased from 8% to 17%. Note that the peak TE-polarized spontaneous emission rate gradually reduces when the In-content increases from 12% to 17%. Specifically, the peak TE spontaneous emission rate of 3.74 x 10^{28} $s^{-1}cm^{-3}eV^{-1}$ for 20Å $Al_{0.88}In_{0.12}N$ QW reduces to TE spontaneous emission rate of 2.01 x 10^{28} $s^{-1}cm^{-3}eV^{-1}$ for 20Å $Al_{0.83}In_{0.17}N$ QW. Our analysis indicates that the reduction of the TE-polarized spontaneous emission rate is caused by the reduction of the electron-hole wavefunction overlap in the QW, as the charge separation effect is worsened due to the increasing compressive strain in the well when the In-content increases.

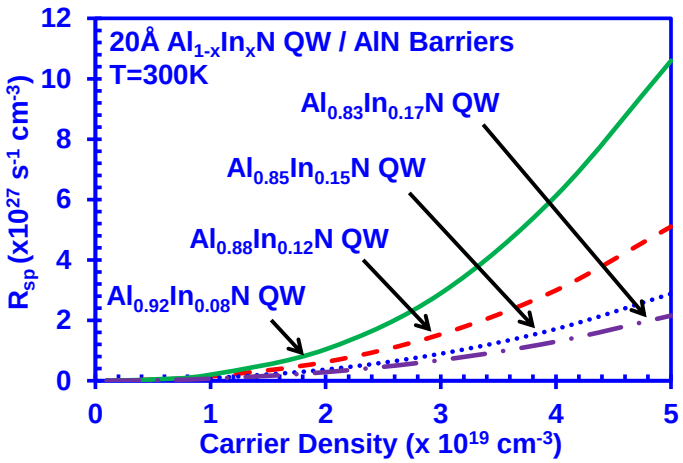

Figure 8-10: *Spontaneous emission rate per unit volume as a function of carrier density from 1 x 10^{18} cm^{-3} to 5 x 10^{19} cm^{-3} for conventional 20Å $Al_{0.92}In_{0.08}N$ QW, 20Å $Al_{0.88}In_{0.12}N$ QW, 20Å $Al_{0.85}In_{0.15}N$ QW and 20Å $Al_{0.83}In_{0.17}N$ QW.*

Figure 8-10 shows the spontaneous emission rate per unit volume (R_{sp}) for 20Å $Al_{0.92}In_{0.08}N$ QW, 20Å $Al_{0.88}In_{0.12}N$ QW, 20Å $Al_{0.85}In_{0.15}N$ QW, and 20Å $Al_{0.83}In_{0.17}N$ QW with n ranging from 1 x 10^{18} cm^{-3} up to 5 x 10^{19} cm^{-3}. As shown in figure 8-10, the R_{sp} for $Al_{0.92}In_{0.08}N$ QW is 4.7 times higher than that of $Al_{0.83}In_{0.17}N$ QW at a carrier density of n = 5 x 10^{19} cm^{-3} respectively. The larger R_{sp} shown in the low In-content (x = 8%) AlInN QW is attributed to the large and dominant TM-polarized spontaneous emission rate in the QW. As a result, it is interesting that the valence band crossover issue can also be resolved using AlInN QW through our inspection in the spontaneous emission rates.

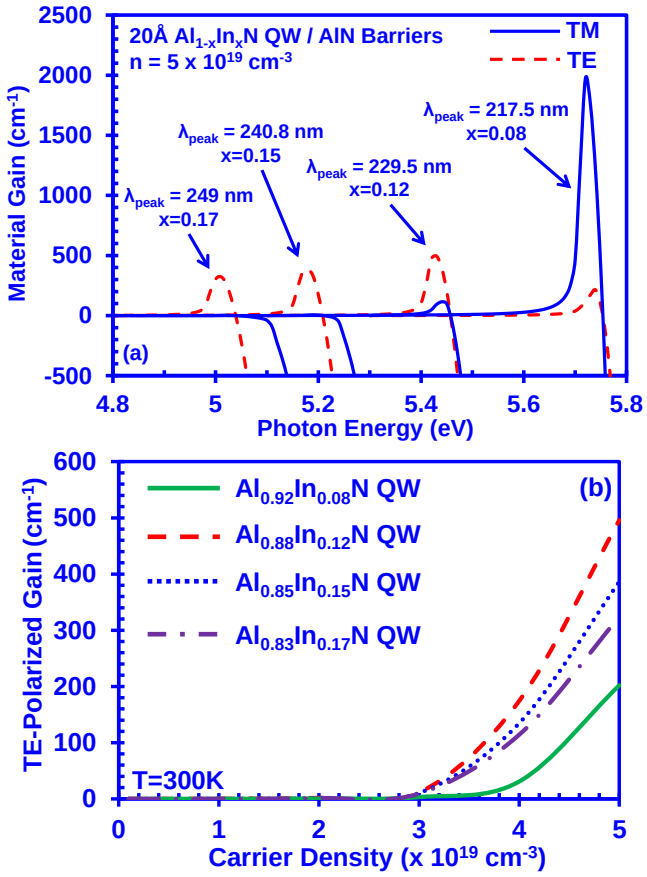

Figure 8-11: *(a) TE and TM optical gain spectra for conventional 20Å $Al_{0.92}In_{0.08}N$ QW, 20Å $Al_{0.88}In_{0.12}N$ QW, 20Å $Al_{0.85}In_{0.15}N$ QW and 20Å $Al_{0.83}In_{0.17}N$ QW with AlN barriers at n = 5 x 10^{19} cm^{-3} and (b) TE-polarized gain as a function of carrier density for conventional 20Å $Al_{0.92}In_{0.08}N$ QW, 20Å $Al_{0.88}In_{0.12}N$ QW, 20Å $Al_{0.85}In_{0.15}N$ QW and 20Å $Al_{0.83}In_{0.17}N$ QW.*

Figure 8-11(a) shows the TE and TM optical gain spectra for 20Å $Al_{0.92}In_{0.08}N$ QW, 20Å $Al_{0.88}In_{0.12}N$ QW, 20Å $Al_{0.85}In_{0.15}N$ QW and 20Å $Al_{0.83}In_{0.17}N$ QW with AlN barriers at *n* of 5 x 10^{19} cm^{-3}. As shown in figure 8-11(a), the peak TM optical gain for 20Å $Al_{0.92}In_{0.08}N$ QW reaches 1972.9 cm^{-1}, which is much larger than the peak TE optical gain of 202.1 cm^{-1}. While the TM optical gain dominates at low In-content AlInN QW, the TM optical gain diminish as the In-content increases in the QW. As such, the TM optical gain is negligible for both 20Å $Al_{0.85}In_{0.15}N$ QW and 20Å $Al_{0.83}In_{0.17}N$ QW. On the other hand, TE optical gain is dominant in $Al_{1-x}In_xN$ QW with x > 12%. The peak TE optical gains are in the range of 320-500 cm^{-1} for AlInN QWs with x up to 17%, which is attributed to the small momentum matrix element.

In figure 8-11(b), the TE peak material gains (g^{TE}_{peak}) for the 20Å $Al_{0.92}In_{0.08}N$ QW, 20Å $Al_{0.88}In_{0.12}N$ QW, 20Å $Al_{0.85}In_{0.15}N$ QW and 20Å $Al_{0.83}In_{0.17}N$ QW is plotted as a function of carrier density ranging from $n = 1 \times 10^{18}$ cm^{-3} to $n = 5 \times 10^{19}$ cm^{-3}. It shows that the TE-polarized gain for the 8% In-content AlInN QW is much lower compared to the higher In-content QWs. The highest value for the TE-polarized gain is observed in the $Al_{0.88}In_{0.12}N$ QW, where the gain reaches ~500 cm^{-1} at a carrier density of $n = 5 \times 10^{19}$ cm^{-3}. However, as the Indium content is further increased, the TE–polarized gain reduces, resulting in values of ~ 380 cm^{-1} and ~ 300 cm^{-1} for the $Al_{0.85}In_{0.15}N$ QW and $Al_{0.83}In_{0.17}N$ QW respectively, at n of 5×10^{19} cm^{-3}.

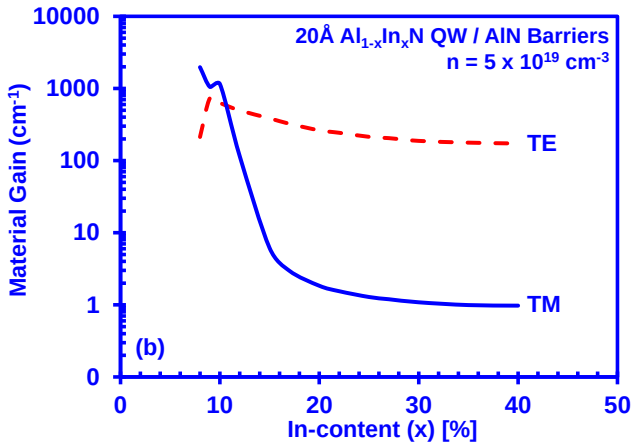

Figure 8-12: *TM peak material gains (g^{TM}_{peak}) and TE peak material gains (g^{TE}_{peak}) as a function of In-content (x) for 20Å AlInN QW with AlN barriers for n = 5 x 10^{19} cm^{-3}.*

For further clarification on the effect of In-content onto the material gain in the AlInN QW, figure 8-12 presents both the TM peak material gains (g^{TM}_{peak}) and TE peak material gains (g^{TE}_{peak}) as a function of In-content up to 40% for the 2 nm $Al_{1-x}In_xN$ QW with AlN barriers at n of 5 x 10^{19} cm^{-3}. Both the TE- and TM-polarized g_{peak} show a reducing trend for increasing In-content, which is caused by the lower momentum matrix element at higher In-content of $Al_{1-x}In_xN$ QWs. Both the TE- and TM-polarized g_{peak} for high In-content AlInN QW are relatively low (< 500 cm^{-1}), but the g^{TE}_{peak} is much larger than the g^{TM}_{peak}, as illustrated in figure 8-12.

Our analysis shows that the carriers are dominantly confined in the HH / LH bands instead of CH band in higher In-content $Al_{1-x}In_xN$ QW (x > 12%), leading to high $g^{TE}_{peak}/g^{TM}_{peak}$ ratio of more than one order of magnitude. Note that the g^{TE}_{peak} is still low, which is attributed by low electron-

hole wavefunction overlap in the AlInN QW. Thus the active region innovations are required to enhance the electron-hole wavefunction overlap for the AlInN QW based light emitting devices.

High quality AlInN alloys with various In-content have been reported for material grown with Metal-Organic Chemical Vapor Deposition (MOCVD) technique [21]. The feasibility of AlInN material growth implies the strong potential of implementing the alloy in the deep UV device applications. It is also important to note that the key idea of this work is to illustrate the potential of using AlInN alloy as the active region material, which enables the potential solution to overcome the valence bands crossover issue in the AlN-based devices by applying relatively low In-composition AlInN alloy.

As a summary for the investigation of single AlInN QW with AlN barriers, the analysis of the gain and spontaneous emission characteristics of the AlInN QWs for deep UV light emitters are provided. Our analysis shows that the switch between TE-polarized and TM-polarized dominant emission occurs when the In-content increases from 8% to 12% in the 2 nm $Al_{1-x}In_xN$ QW, attributed to the CH and HH bands crossover for the AlInN QWs. Specifically, the TE-polarized emission is dominant in the $Al_{1-x}In_xN$ QW with $x > 12\%$ whereas TM-polarized emission is dominant for $Al_{1-x}In_xN$ QW with $x < 12\%$. The gain analysis shows that even though high $g^{TE}_{peak}/g^{TM}_{peak}$ ratio can be achieved when In-content is larger than 12% in the AlInN QW, the TE-polarized material gain is relatively low (~500 cm^{-1}). It is important to note that the realization of AlInN QWs light emitters will require further active region optimization to improve the performance for emission at ~230-280 nm. Nonetheless, the current study presents a potential solution of overcoming the valence bands crossover issue in the AlN-based UV devices by implementing the AlInN alloys with relatively low In-content, which provide an alternative direction in the pursuit of high-efficiency UV emitting devices. In the next section, an active region innovation based on AlInN alloy is suggested and evaluated, with the purpose to improve the AlInN QW performance.

8.4. Characteristics of AlInN-delta-GaN QW Structure for Deep UV Emission

8.4.1. Concept and Valence Band Structures for AlInN-delta-GaN QW

In this section, we discuss about an innovative active region design by using AlInN-delta-GaN QW for improving the deep UV performance [33]. Figure 8-13 presents the energy band lineup of the 20Å $Al_{0.92}In_{0.08}N$ / 5Å delta-GaN QW with AlN barriers along with the carrier wavefunctions of the first conduction and valence sub-bands at sheet carrier density n_{2D} of 1 x 10^{13} cm^{-2}. The band lineups for all the AlInN-based QW structures are calculated self-consistently taking into account the carrier screening effect. Note that the gain and spontaneous emission rates were also calculated self-consistently for all the conventional AlInN QW and AlInN-delta-GaN QW structures at different carrier densities, which is similar to the treatment shown in previous work [41]. The charge neutrality requirement is applied to the structure including the well and barriers.

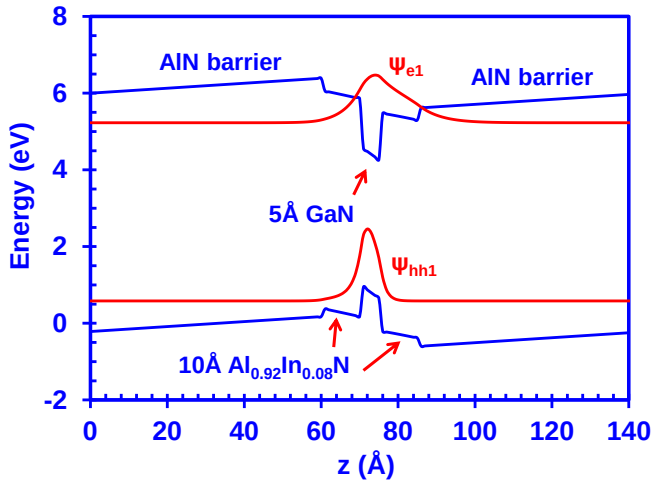

Figure 8-13: *Energy band lineup of AlInN-delta-GaN QW along with the carrier wavefunctions for both the electron and heavy hole in the conduction and valence band, respectively, with the calculation performed self-consistently at sheet carrier density (n_{2D}) = 1 x 10^{13} cm^{-2}.*

As shown in figure 8-13, the insertion of a delta-GaN layer traps the electron and hole wavefunctions in the center of the active region, resulting in large electron-hole wavefunction overlap. The change of In-content for the AlInN layers will result in the change of electron-hole wavefunction overlap accordingly. As an example, the electron-hole wavefunction overlap in $Al_{0.83}In_{0.17}N$-delta-GaN QW exhibits ~69%, while the electron-hole wavefunction overlap in

$Al_{0.92}In_{0.08}N$-delta-GaN QW exhibits ~82%. Note that in the conventional AlInN QW, due to the built-in polarization field the electron and hole wavefunctions being spatially separated, a lower electron-hole wavefunction overlap is observed.

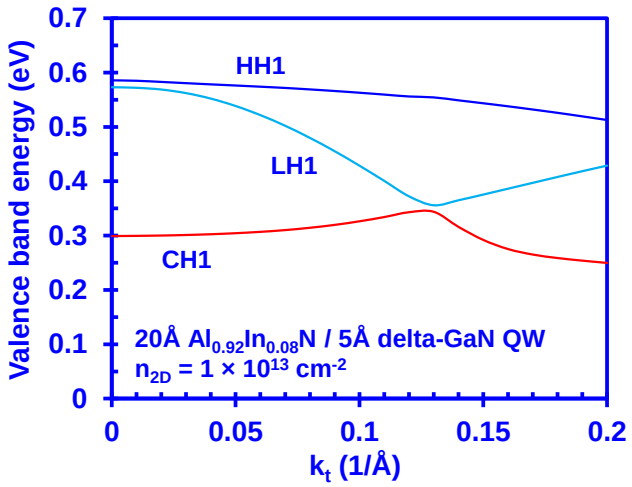

Figure 8-14: *Valence band structure of the 20Å $Al_{0.92}In_{0.08}N$ / 5Å delta-GaN QW with AlN barriers.*

Figure 8-14 provides the valence band structure of 20Å $Al_{0.88}In_{0.12}N$ / 5Å delta-GaN QW with AlN barriers. By employing the AlGaN-delta-GaN QW, the strong valence band mixing effect introduced by the delta-GaN layer results in valence band rearrangement, leading to higher heavy hole (HH1) band and light hole (LH1) band in comparison to that of the crystal-field split-off hole (CH1) band. The large energy separation of 0.27 eV at the gamma-point between the HH1 and CH1 subbands thus results in dominant TE-polarized emission in the AlInN-delta-GaN QW structure.

8.4.2. Enhanced Optical Properties of AlInN-delta-GaN QW Structure

Figure 8-15 illustrates the TE-polarized spontaneous emission spectra as a function of photon energy for the 20Å $Al_{1-x}In_xN$ / 5Å delta-GaN QWs and the conventional $Al_{1-x}In_xN$ QWs at a sheet carrier density (n_{2D}) of 1 x 10^{13} cm^{-2} at T = 300K. The peak TE-polarized spontaneous emission rates of the 20Å $Al_{1-x}In_xN$ / 5Å delta-GaN QW range from 1.25 x 10^{29} $s^{-1}cm^{-3}eV^{-1}$ for 20Å $Al_{0.92}In_{0.08}N$ / 5Å delta-GaN QW to 0.54 x 10^{29} $s^{-1}cm^{-3}eV^{-1}$ for 20Å $Al_{0.83}In_{0.17}N$ / 5Å delta-GaN QW, which are nearly 4 times larger than those of 20Å $Al_xIn_{1-x}N$ conventional QWs. Our analysis

indicates that the dominant TE-polarized spontaneous emission rate is significantly enhanced by applying the delta-GaN layer into the $Al_xIn_{1-x}N$ QW structure. In comparison to the redshift from 215 nm to 247 nm in 20Å conventional $Al_xIn_{1-x}N$ QWs, the spontaneous emission spectra show the relatively smaller redshift of emission wavelength from 265 nm to 280 nm when the In-content increases from 8% to 17% in the 20Å $Al_xIn_{1-x}N$ / 5Å delta-GaN QWs. Note that the peak spontaneous emission rate increases with respect to the reduction of In-content in AlInN-delta-GaN QW. This phenomenon is attributed to the increase of electron-hole wavefunction overlap in the active region, as a result of the decreased compressive strain when the In-composition of AlInN layer reduces. Our study shows the potential of applying AlInN-delta-GaN QW with low In-content to achieve sufficient spontaneous emission rates for high performance UV LEDs.

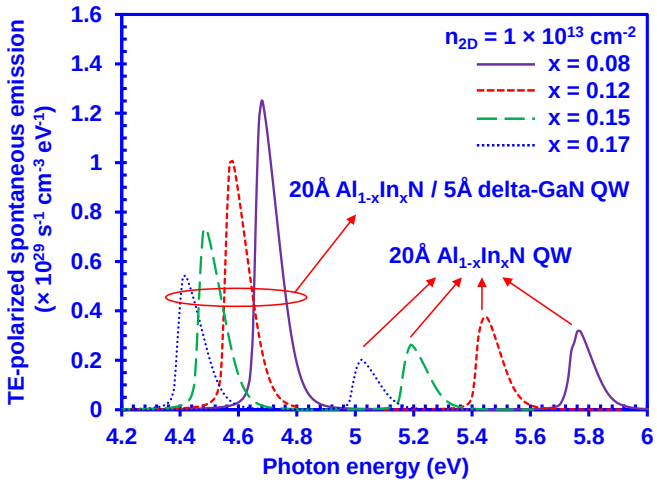

Figure 8-15: *TE-polarized spontaneous emission spectra as a function of photon energy at sheet carrier density of 1 x 10^{13} cm^{-2} at T=300K for 20Å $Al_{1-x}In_xN$ / 5Å delta-GaN QW and 20Å $Al_{1-x}In_xN$ QW.*

Figure 8-16 shows the comparison of the spontaneous emission rate per unit volume (R_{sp}) with respect to the sheet carrier density between the 20Å $Al_{1-x}In_xN$ / 5Å delta-GaN QW and the conventional 20Å $Al_{1-x}In_xN$ QW. As shown in figure 8-16, the R_{sp} for the 20Å $Al_xIn_{1-x}N$ / 5Å delta-GaN QW is significantly larger than that of the conventional $Al_{1-x}In_xN$ QW, as sheet carrier density (n_{2D}) increases from 2.5 x 10^{11} cm^{-2} to 1 x 10^{13} cm^{-2}. The larger R_{sp} shown in the 20Å $Al_{1-x}In_xN$ / 5Å delta-GaN QW is attributed to the large and dominant TE-polarized spontaneous emission in the active region.

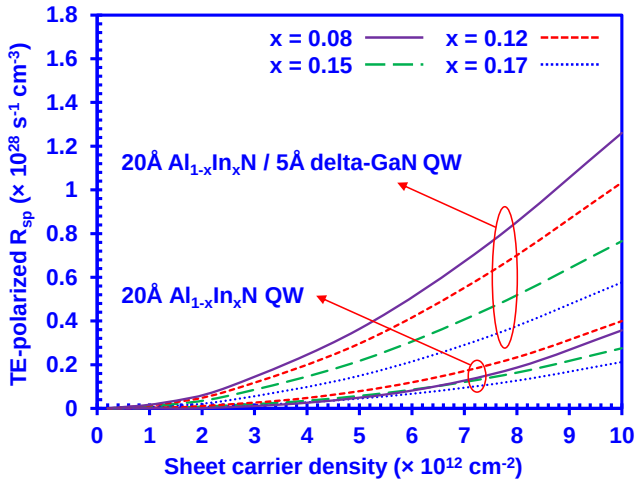

Figure 8-16: *TE-polarized spontaneous emission rate per unit volume as a function of sheet carrier density from 2.5 x 10^{11} cm^{-2} to 1 x 10^{13} cm^{-2}, for 20Å $Al_{1-x}In_xN$ / 5Å delta-GaN QW and 20Å $Al_{1-x}In_xN$ QW.*

Figure 8-17(a) shows the TE-polarized optical gain spectra for the 20Å $Al_{1-x}In_xN$ / 5Å delta-GaN QWs as well as the conventional 20Å $Al_{1-x}In_xN$ QWs at an n of 1 x 10^{13} cm^{-2}. As shown in figure 8-17(a), the peak TE-polarized optical gain of the 20Å $Al_{1-x}In_xN$ / 5Å delta-GaN QW yields an increasing trend with the reduction of In-composition (x). The peak TE-polarized optical gain reaches ~ 2750 cm^{-1} for the 20Å $Al_{1-x}In_xN$ / 5Å delta-GaN QW with 8% In-content, whereas the 20Å $Al_{1-x}In_xN$ / 5Å delta-GaN QWs with x = 12%, 15% and 17% have a lower TE optical gain corresponding to around 2400 cm^{-1}, 1700 cm^{-1} and 1230 cm^{-1}, respectively. In comparison to the conventional 20Å $Al_{1-x}In_xN$ QWs, the 20Å $Al_{1-x}In_xN$ / 5Å delta-GaN QW yields around 6 times the increase in its peak TE-polarized optical gain. The enhancement of the TE-polarized optical gain can be attributed to a significant increase in the optical transition matrix element in the 20Å $Al_{1-x}In_xN$ / 5Å delta-GaN QW structure. Similar to the phenomena shown in the spontaneous emission spectra for the AlInN-delta-GaN QW, the larger enhancement of the optical gain as In-content reduces in the AlInN-delta-GaN QWs is attributed to the larger optical matrix element. Note that in contrast to the the AlInN-delta-GaN QW, the TE-polarized optical gain is smaller in the conventional AlInN QW with In-content of 8% in comparison to that of AlInN QW with In-content of 12%. This is attributed to the fact that the conventional AlInN QWs with In-content of

8% suffers from the valence band crossover issue, which leads to a small value of TE-polarized optical gain.

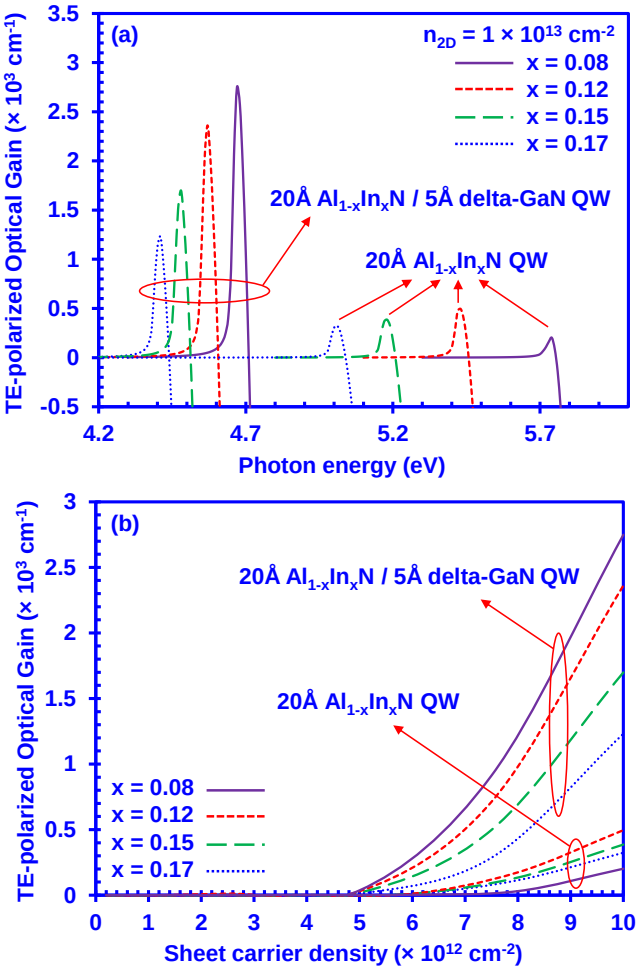

Figure 8-17: *(a) TE-polarized optical gain spectra at n_{2D} = 1 x 10^{13} cm^{-2}, and (b) TE-polarized peak optical gain as a function of sheet carrier density for 20Å $Al_{1-x}In_xN$ / 5Å delta-GaN QW and for 20Å $Al_{1-x}In_xN$ QW.*

In figure 8-17(b), the peak TE-polarized optical gain of the 20Å $Al_{1-x}In_xN$ / 5Å delta-GaN QW and the conventional 20Å $Al_{1-x}In_xN$ QWs is plotted as a function of sheet carrier density ranging from n_{2D} = 2.5 x 10^{11} cm^{-2} to n_{2D} = 1 x 10^{13} cm^{-2}. The figure shows that the TE-polarized optical gain of the 20Å $Al_{1-x}In_xN$ / 5Å delta-GaN QWs structure has a significant increase over that of the conventional 20Å $Al_{1-x}In_xN$ QWs at various sheet carrier densities ranging from 2.5 x 10^{11} cm^{-2} to 1 x 10^{13} cm^{-2}. Our analysis demonstrates the importance of applying the delta-GaN layer in the

conventional AlInN QW, in order to enhance the dominant TE-polarized optical gain for high performance deep UV lasers.

8.4.3. Threshold Analysis of AlInN-delta-GaN QW Deep UV Lasers

The potential of the AlInN-delta-GaN QW as the active region for laser diode applications can be assessed through the investigation of the threshold properties of the QW. In our analysis, an optical confinement factor (Γ_{opt}) of 0.02 [24, 31] is used for the AlInN-delta-GaN QW lasers. The internal loss is assumed to be 14 cm^{-1} for the AlInN-delta-GaN QW laser, while the laser cavity length is assumed as 500 μm with a mirror loss of 11 cm^{-1} [24]. The resulting threshold gain (g_{th}) for the AlInN-delta-GaN laser is ~1250 cm^{-1}, with corresponding modal gain of 25 cm^{-1}. As an example, as shown in figure 8-17(b), the threshold sheet carrier density (n_{2D_th}) is 8.4 x 10^{12} cm^{-2} for $Al_{0.88}In_{0.12}N$-delta-GaN QWs. On the other hand, the TE-polarized gain obtained at similar carrier density in conventional AlInN QW is only ~220 cm^{-1}. This indicates that significantly higher carrier density will be required for the conventional QW to achieve g_{th} of ~1250 cm^{-1}. The reduction in threshold carrier density via the use of delta-based QW is essential for suppressing the non-radiative recombination current, namely monomolecular (~ $A \cdot n_{th}$) and Auger (~ $C \cdot n_{th}^3$) current densities.

In order to analyze the impact on devices, our study then takes into account the radiative recombination current density (J_{rad}) and non-radiative recombination current density ($J_{non\text{-}rad}$) in the QW active region. Note that the total injected current density (J_{total}) in the devices will depend on the injection efficiency (η_{inj}) [42], which represents the fraction of the injected current density that recombines in the QW [$\eta_{inj} = (J_{rad} + J_{non\text{-}rad}) / J_{total}$]. Figure 8-18 shows the peak TE modal gain as a function of total recombination current density in the QW ($J_{QW} = J_{rad} + J_{non\text{-}rad}$) for the AlInN-delta-GaN QWs. The reported values for the Auger coefficient C range from ~10^{-30} cm^6s^{-1} up to ~ 10^{-31} cm^6s^{-1} [28]. In our analysis of the $J_{non\text{-}rad}$ term, we have employed C = 10^{-31} cm^6s^{-1}. The monomolecular recombination rate of A = 1 x 10^9 s^{-1} was used [31]. As shown in figure 8-18, to achieve the modal threshold gain of 25 cm^{-1}, the threshold current densities (J_{QW_th}) of in the

AlInN-delta-GaN QW are estimated as ranging from ~ 1750 A/cm^2 up to ~2100 A/cm^2, which represent practical lasing threshold current densities in devices.

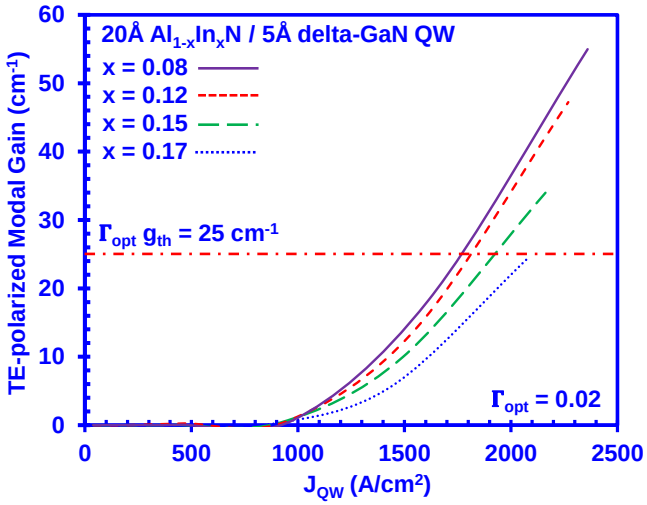

Figure 8-18: *Peak TE-polarized modal gain as a function of current density in the active region ($J_{QW} = J_{rad}+J_{non\text{-}rad}$) for 20Å $Al_{1-x}In_xN$ / 5Å delta-GaN QW.*

On the other hand, the total threshold sheet carrier density for the corresponding conventional AlInN QW to overcome the threshold modal gain of 25 cm^{-1} exceeds n_{2D_th} ~ 1.6 x 10^{13} cm^{-2}, which is more than twice of that for the delta-based QW. This significantly higher n_{2D_th} in the conventional QW active regions results in an order of magnitude higher non-radiative recombination current in the active region ($J_{non\text{-}rad} \sim A \cdot n_{th} + C \cdot n_{th}^3$), which will be impractical for implementation. This work shows the applicability of the AlInN-delta-GaN QW as active region for laser diodes strongly attributed from the reduction in its threshold carrier densities.

8.4.4. Effect of Delta-GaN Layer Thickness on the Emission Characteristics

Our analysis has shown that the AlInN-delta-GaN QW yields remarkable advantages with sufficiently high TE-polarized spontaneous emission and optical gain for UV application. However, the TE-polarized spontaneous emission and optical gain spectra of the AlInN-delta-GaN QWs suffer undesirable redshift with increased In-content which should be carefully treated. Previous studies show the possibility of engineering the delta-GaN layer in the QW structure for achieving various emission wavelengths [23]. In our study, the TE-polarized optical gain spectra

were calculated for 20Å $Al_{0.88}In_{0.12}N$ / delta-GaN QWs with various delta-GaN layer thickness (d). Figure 8-18 presents the plot of the TE-polarized optical gain spectra of the 20Å $Al_{0.88}In_{0.12}N$ / d-Å delta-GaN QW with d varying from 3Å up to 15Å, at a sheet carrier density of n_{2D} = 1 x 10^{13} cm^{-2}. As seen from figure 8-19, the thickness of the delta-GaN layer can be engineered so that the peak TE optical gain can be shifted correspondingly, as well as the emission wavelength. Specifically, reducing the delta-GaN layer thickness to 3 Å shifts the emission wavelength down to ~250 nm with a TE optical gain peak of ~2000 cm^{-1}. Although the TE-polarized peak optical gain is reduced as the thickness of delta-GaN layer decreases, it is still much larger than that of the conventional AlInN QW structure. Note that the results for AlInN-delta-GaN QW shown in figure 8-18 correspond to a 12% Indium composition, which could be further reduced if lower emission wavelength is desired. Hence, the optimization of the delta-GaN layer thickness is instrumental for achieving the desired emission wavelength along with high TE-polarized optical gain in the AlInN-delta-GaN QW structure.

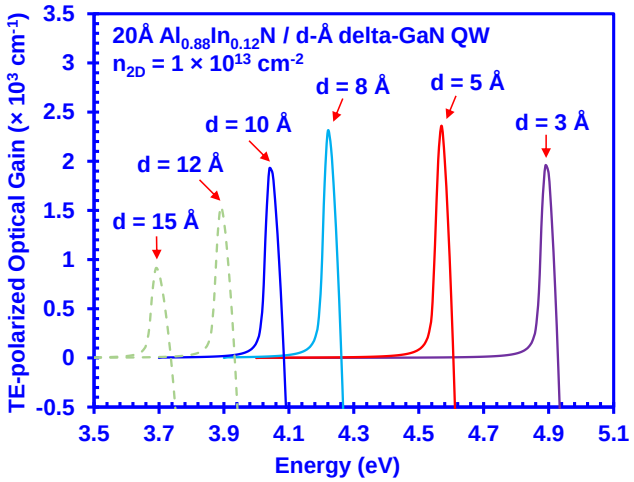

Figure 8-19: *TE peak material gains (g^{TE}_{peak}) spectra for 20Å AlInN / d-Å delta-GaN QW with AlN barriers at n_{2D} = 1 x 10^{13} cm^{-2}.*

It is also important to point out that AlInN alloys with various In-content have been grown on GaN template with metalorganic chemical vapor deposition (MOCVD) technique [21]. The growth of AlInN layer can be carried out at temperatures in the range from 750°C to 860°C, which is compatible with the growth of the GaN layer [21]. In addition, recent MOCVD work demonstrated the growth of AlN/GaN superlattice structures with thin GaN layer (~0.9-2.5 monolayers) [30],

indicating that the growth of delta-GaN layer can be practically implemented in the AlInN-delta-GaN structure. However, it is also important to note that the growth of AlInN layer is still in the early stage where technical challenges remain to synthesize AlInN alloy with more than 20% In-content [21]. While further optimizations of the growth conditions will still be required to realize the AlInN-delta-GaN structure, the feasibility of the AlInN material growth implies the strong potential of implementing the alloy in the deep UV device applications. The key idea of this work is to illustrate the potential of using the AlInN / delta-GaN QW structure as the active region material, which enables the potential solution to overcome the valence bands crossover issue in the AlN-based devices by applying a relatively low In-composition AlInN alloy.

8.5. Dilute-As AlNAs Semiconductor for Deep UV Light Emitter

Extensive studies carried out in the past decade in III-Nitride emitters are based on InGaN, AlGaN and AlInN alloys for visible and deep UV light emissions. In contrast, the progress of developing mixed-anion III-Nitride alloys is relatively slow and the development is still in the early stage. There are significant studies in other mixed anion material systems [43-49]. Specifically, the incorporation of N impurity in the GaAs material has led to the advances in the field of dilute-N InGaAs(N)-based alloy, resulting in the state-of-the-art and low threshold laser devices for telecommunication applications [43-45]. These advances can only be realized through significant understanding in the electronic properties and the device physics, as well as the improvement in material epitaxy [43-49].

Our recent work has shown the promising potential of the dilute-As GaNAs alloy as an alternative light emitting active material for high efficiency visible light applications [50-53]. Specifically, the understanding of the electronic properties of the dilute-As GaNAs alloys revealed the ability of the alloy in suppressing the detrimental interband Auger recombination effect [50, 52]. While dilute-As GaNAs alloy shows promising progress from the experimental and theoretical aspects for visible spectral regime [53-58], the effect of arsenic (As) incorporation in other nitride-based materials such as AlN alloy for deep UV light emitters is still unexplored. Deep UV light

emitters have become increasingly important in recent years [8-33], and the pursuit of novel materials, such as dilute-As AlNAs alloy, can further stimulate the development of the UV light-based technology. Up to date the literature on AlNAs alloy is extremely limited [59]. Hence the understanding of the electronic properties of dilute-As AlNAs alloy is an important first step towards developing the alloy for deep UV applications.

In this work, we present the electronic properties of dilute-As AlNAs alloy by using First-Principle Density Functional Theory (DFT). The arsenic (As) atoms are introduced into the AlN bulk material to form the AlNAs ternary alloy with As-content ranging from 0% up to 6.25%. The DFT-calculated band structures and the related electronic properties including energy band gap and effective masses of dilute-As AlNAs alloy are presented. In addition, the valence band structures of dilute-As AlNAs alloys are further investigated, in which the effect of As impurity onto the issue of band crossover between the crystal-field split-off (CH) and heavy hole (HH) bands is briefly discussed.

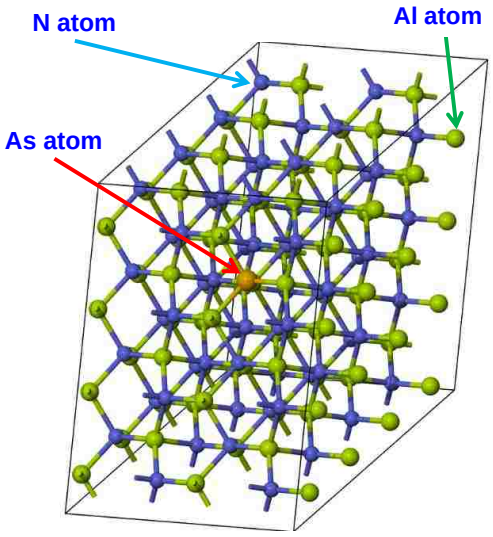

Figure 8-20**:** *Illustration of 4x4x2 supercell with 128 atoms using MedeA-VASP software.*

In our DFT analysis, the supercell approach has been employed to build the corresponding crystal structures for AlNAs alloy for the band calculations. Similar technique used for dilute-As GaNAs and dilute-P GaNP alloy as discussed in Chapter 5 is used for AlNAs alloy. For completeness, here the computational details are discussed briefly for the AlNAs alloy. Figure 8-

20 illustrates a constructed 4x4x2 AlNAs supercell with a total of 128 atoms, which consists of 64 Al atoms, 63 N atoms and 1 substituted As atom. The illustrated 128-atom supercell corresponds to 1.56%-As in the dilute-As AlNAs alloy. The supercell size was varied in our calculations to provide different As percentage for the AlNAs alloy, which is similar to previous work [25]. Note that in each AlNAs supercell only one N atom is replaced by the As atom. The band structure calculations for AlNAs alloy were performed using the projector augmented wave (PAW) method as implemented in the MedeA-VASP software [60]. Local density approximation (LDA) exchange-correlation potential was employed in our calculations, and the electronic wave functions are described in plane wave basis with a cutoff energy of 400eV. The structure optimization was performed for the supercell by relaxing the atom positions with the Hellmann-Feynman force set to 0.02eV/Å. The external stress in the supercell was set to 0 GPa, and the energy convergence tolerance was set to $1x10^{-5}$ eV/atom. Different Monkhorst-Pack k-point meshes were generated in the calculations attributed to the use of different supercell sizes. In addition, the spin-orbit coupling effect is not considered in the DFT calculation due to its insignificant effect in the wide band gap III-Nitride semiconductor alloy.

8.5.1. Electronic Band Structures of Dilute-As AlNAs Alloy

Figure 8-21(a) and 8-21(b) present the DFT-calculated band structures for AlN and $AlN_{0.9375}As_{0.0625}$ alloys respectively. As shown in figure 8-21, the incorporation of As atoms in the AlN alloy has shown to affect both the conduction and valence bands, leading to significant difference in the band dispersions between the AlN and AlNAs alloys. The effect of the As-related defect in the band structures of AlN alloy is similar to that of the dilute-As GaNAs alloy [50], in which the defect states are introduced in the energy gap resulting in the band structure modifications. Therefore, the incorporation of As impurity in the AlN alloy to form the AlNAs alloy is expected to lead to significant changes in the optoelectronic properties of the alloy. Meanwhile, as shown in figure 8-21, the conduction band minimum (CBM) and the valence band maximum (VBM) for dilute-As AlNAs alloys are located at the gamma point (Γ) in the Brillouin Zone. The

direct band gap property of dilute-As AlNAs alloys indicates the potential of the alloys to achieve high efficiency electron-hole recombination, a key ingredient for photonics device applications.

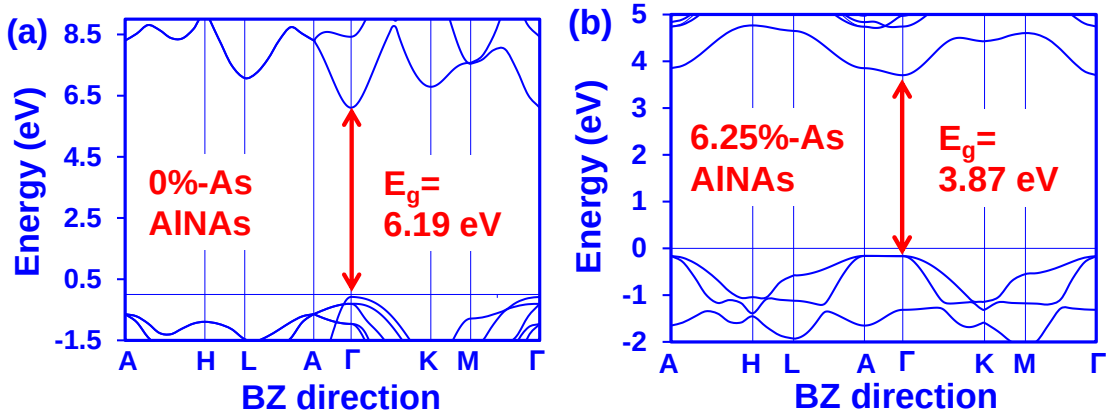

Figure 8-21**:** *DFT-calculated band structures of AlNAs alloys with (a) 0% and (b) 6.25% As-content, with the energy band gap (E_g) taken as the energy difference between the CBM and VBM.*

The energy band gap value for the dilute-As AlNAs alloy has been taken as the energy difference between the CBM and VBM of the band structures. Note that the scissor operator has been applied in our analysis for the dilute-As AlNAs alloys in order to correct the energy band gap error originated from the LDA calculations [61]. As the scissor operator is inversely proportional to the dielectric constant, the energy correction from scissor operator ranges from 1.8 eV for AlNAs alloy with 6.25% As-content to 1.98 eV for AlN alloy, attributed to the linear interpolation of dielectric constant between AlN and AlAs alloy. As shown in figure 8-21, the energy band gap reduces significantly from 6.19 eV to 3.87 eV with the incorporation of 6.25% As concentrations into the AlN alloy. The large reduction of 2.32 eV in the energy band gap with dilute amount of As impurity (6.25%-As) in the AlN alloy indicates the significant band gap narrowing effect. Similar band gap narrowing effect has also been reported in other dilute-anion III-Nitride material system [50, 62]. Specifically, dramatic reduction of the band gap energy of the host material has been observed in the dilute-As GaNAs material, which provides the possibility of accessing the entire visible spectral range from blue to red emission. Note that the replacement of a single N atom with As atom in the GaN results in the introduction of defect states in the GaN energy gap [47]. Similar behaviour is expected in the AlN alloy when an N atom is replaced with an As atom, in

which the defect states introduced in the energy gap lead to strong modification of the AlN band structure. Thus, the optoelectronic properties of the AlN alloy are heavily affected, leading to unusual behaviour in the AlNAs alloy. Interestingly, the alloys of AlN such as the AlInN alloy also display unusual behaviour attributed to the formation of In-related localized states [63].

8.5.2. Band Gap, Band Bowing Energy and Effective Masses

Figure 8-22 presents the DFT-calculated energy band gaps and the corresponding emission wavelength for dilute-As AlNAs alloys with As-content from 0% up to 6.25%. The solid line in figure 8-22 is to show a general trend of energy band gap reduction for the dilute-As AlNAs alloy. As shown in figure 8-22, the energy band gap reduces as the As-content increases from 0% to 6.25% in the AlN alloy, while the emission wavelength of the dilute-As AlNAs alloy covers the regime from 200 nm up to 320 nm. The broad wavelength coverage indicates the accessibility of the dilute-As AlNAs alloy to the entire deep UV spectral regime, which shows the potential of the alloy as a candidate for the deep UV optoelectronic device applications.

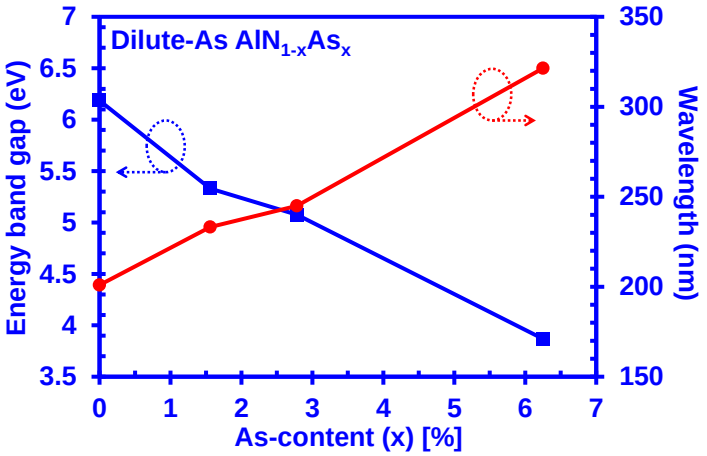

Figure 8-22: *DFT-calculated energy band gap and corresponding emission wavelength of dilute-As AlNAs alloys with As-content varying from 0% up to 6.25%.*

Previous DFT work in the dilute-As GaNAs alloy has shown a trend of energy band gap reduction similar to the experimental data [50], The trend of energy band gap reduction in the dilute-As AlNAs alloy is expected to be similar to that of dilute-As GaNAs alloy, albeit the current

analysis in this work is still in the early stage. Note that there is no comparison available for the experimental data since the dilute-As AlNAs alloy is yet to be understood prior to this study.

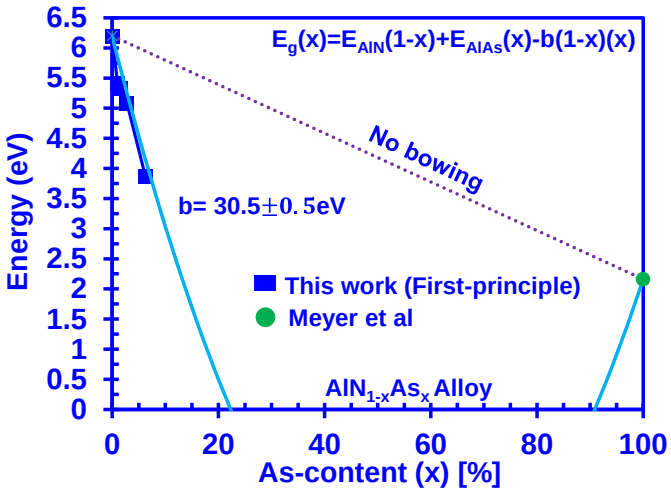

Figure 8-23: *Energy band gap of AlNAs alloy with full composition range with corresponding bowing parameter obtained through line fitting with the data.*

Figure 8-23 shows the energy band gap of AlNAs alloy with full composition range. The energy band gap for AlNAs alloys can be described using the following equation $E_g(x) = E_{AlN}(1-x) + E_{AlAs}(x) – b(1-x)(x)$, where b is the bowing parameter. By line fitting the equation with the DFT-calculated band gap data for dilute-As AlNAs alloy, our analysis reveals a giant bowing parameter of 30.5 eV ± 0.5 eV, as shown in figure 8-23. The findings of large bowing parameters have also been reported in other mixed-anion material systems including dilute-nitride-based materials [21-23] and dilute-As GaNAs alloy [50]. The unusually large bowing parameter in AlNAs alloy can be attributed to the large atomic size difference between N atom and As atom. It is important to note that the bowing parameter is strongly composition dependent in highly-mismatched alloy such as the GaAsN alloy [46-48], and similar behaviour is also expected in AlNAs alloy when the As-content becomes higher than 10%. The single bowing parameter provided in this work provides a suitable fit to the corresponding band gap energy of dilute-As AlNAs alloy with As-content less than 6.25%. The literature on AlNAs alloy is still extremely limited up to present. Thus additional studies are still required to provide further understanding of this AlNAs alloy, as well as the composition dependency of the bowing parameter in the alloy.

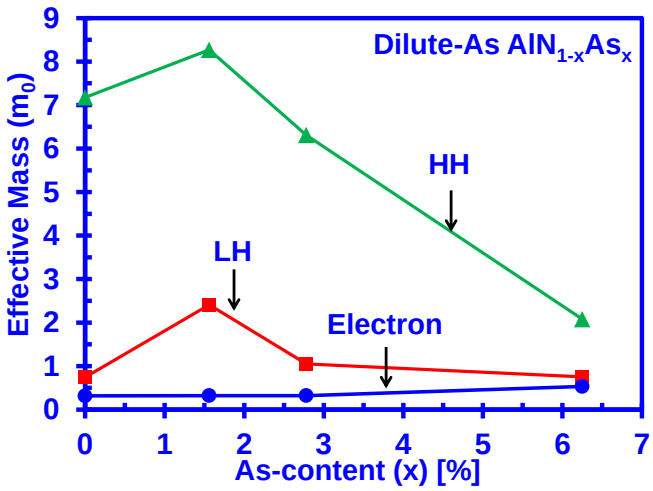

Figure 8-24**:** *Comparison of effective masses for electron, heavy hole (HH) and light hole (LH) that are obtained through energy dispersion relation and parabolic line fitting with the DFT-calculated band structures for dilute-As AlNAs alloy.*

Figure 8-24 shows the carrier effective masses of dilute-As AlNAs alloy for As-content from 0% up to 6.25%. The effective mass values for the dilute-As AlNAs alloys are obtained by employing parabolic line fitting method to fit the DFT-calculated band structures [64]. The average effective masses are calculated taking into account the effective masses in parallel and perpendicular directions near the gamma (Γ) point. The effective masses are calculated by fitting the calculated energy band dispersions, in which the effective masses calculated for AlN alloy are in agreement with previous literature [45]. For the AlNAs alloy, the electron effective mass is presented in figure 8-24 and it can be observed that the average effective mass of the electron increases slightly, with increasing As-content. On the other hand, the incorporation of As concentrations into the AlN alloy leads to significant changes in the average effective masses for both heavy holes and light holes. The phenomena observed in our findings are similar with the corresponding characteristics shown in dilute-As GaNAs alloy, in which there are significant changes in the average effective masses for both heavy holes and light holes in the GaNAs material. The phenomena behind this significant hole effective mass changes is attributed to the strong valence bands modifications with the As impurity incorporation into the AlN alloy [50].

8.5.3. Valence Band Crossover with Dilute-As AlNAs Alloy

The band gap coverage provided by dilute-As AlNAs alloy is attractive for deep UV emitting applications. As discussed previously, one of the challenging issues in the AlGaN-based deep-UV light emitter is the fundamental valence band crossover issue, in which the crystal-field split-off band (CH) is on top of the heavy hole (HH) band and light hole (LH) band in the high Al-content AlGaN material [16]. This leads to dominant transverse-magnetic (TM) polarized emission which is attributed to the transition between the conduction band and the CH band in the AlGaN quantum well [16]. TM-polarized emission is undesirable for the deep UV light emitter as the light propagation parallel to the quantum well plane is difficult for light extraction [19]. The crossover of CH and HH/LH band will only occur when the Al-content becomes sufficiently small (< 60%) for the AlGaN material, resulting in dominant TE-polarized emission that is attributed to the C-HH transition [16]. Overcoming the valence band crossover issue is thus critical to achieve dominant TE-polarized emission for the deep UV emitters.

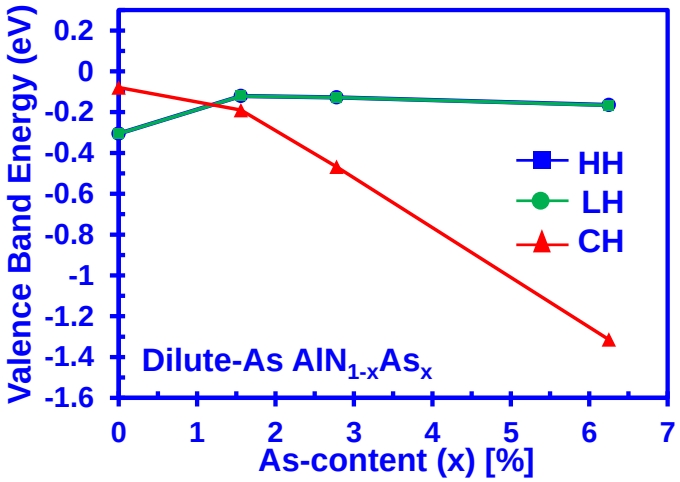

Figure 8-25: *Valence band edges of the HH, LH and CH bands for the dilute-As AlNAs alloys with As-content varying from 0% up to 6.25%. Note that the lines in the figure are provided only as guides to represent the trend of how the energy splitting between CH and HH band varies as a function of As-content in the alloy.*

Figure 8-25 presents the valence energy band edges (HH, LH, and CH) as a function of As-content for dilute-As AlNAs alloys with As-content varying from 0% up to 6.25%. Note that the lines in figure 8-25 are provided only as guides to represent the trend of how the energy splitting

between CH and HH band varies as a function of As-content in the dilute-As AlNAs alloy. As shown in figure 8-25, the CH band is on top of the HH/LH bands in the AlN alloy as expected. On the other hand, the HH/LH bands sit above CH band for the dilute-As AlNAs alloy with 1.56% As-content. Thus the crossover between the HH/LH and CH bands is estimated to occur with As-content of ~1.5% in the AlNAs alloy. Further studies will be required to predict a more accurate band crossover composition for the AlNAs alloy. Following the increase in the As-content of the dilute-As AlNAs alloy, the energy separation between HH/LH bands and CH band further increases. The phenomenon of the increasing energy splitting between HH/LH bands and CH band with the increasing anion impurity composition has also been observed in other highly-mismatched alloy such as the GaAsBi alloy [49]. This phenomenon in the AlNAs alloy is partially caused by the increase in the anion atomic number [65]. On the other hand, this phenomenon might be affected by the clustering of atoms which in turn has strong effects on the band structure as observed in the InGaN alloy [66, 67]. However, the clustering effect is not taken into consideration in this work since only one N atom is replaced in each AlNAs supercell. Further investigations will be needed to provide a more thorough discussion for the phenomenon of the increasing energy splitting in the AlNAs alloy. In addition, the large energy separation between CH band energy and HH/LH band energy for the dilute-As AlNAs alloy is important to avoid the valence bands cluttering effect shown in AlGaN material [16].

Our findings indicate the possibility of using dilute-As AlNAs alloy to achieve dominant transition between conduction band and HH/LH bands instead of conduction and CH bands. The possibility of using only dilute amount of As impurity in the AlN alloy to overcome the valence band crossover issue shows the strong potential of dilute-As AlNAs alloy to achieve dominant TE-polarized emission. The field of dilute-As AlNAs is still in the extremely early stage due to the novelty of this material. Our goal in this work is to open up a new direction and enhance the understanding in the dilute-As AlNAs material for the UV emission. The identification of the dilute-As AlNAs alloy as a promising active material for deep UV emitters, as well as the identification of overcoming valence band crossover issue using this alloy, will provide a clear and strong

motivation on the importance of the pursuit of this material system. Future studies in both the experimental and theoretical aspects are required to provide further understanding in the dilute-As AlNAs material.

8.6. Summary

In summary, the motivations and limitations in the AlGaN-based deep UV emitters were reviewed. Some of the approaches in improving the deep UV emitter performance were also discussed. The analysis on the gain and spontaneous emission characteristics of AlInN QWs were provided for deep UV light emitters. Our analysis shows that the switch between TE-polarized and TM-polarized dominant emission occurs when the In-content increases from 8% to 12% in the 2 nm $Al_{1-x}In_xN$ QW, attributed to the CH and HH bands crossover for the AlInN QWs. Specifically, the TE-polarized emission is dominant in the $Al_{1-x}In_xN$ QW with $x > 12\%$ whereas TM-polarized emission is dominant for $Al_{1-x}In_xN$ QW with $x < 12\%$. The gain analysis shows that even though high $g^{TE}_{peak}/g^{TM}_{peak}$ ratio can be achieved when In-content is larger than 12% in the AlInN QW, the TE-polarized material gain is relatively low (~500 cm^{-1}). The realization of AlInN QWs light emitters will require further active region optimization to improve the performance for emission at ~230-280 nm.

For further optimization, the AlInN-delta-GaN QWs were proposed for deep UV emission. The spontaneous emission and gain characteristics of the AlInN-delta-GaN QWs are analyzed for high performance deep UV light emitters. Our analysis shows that the AlInN-delta-GaN QWs yields ~4 and ~6 times enhancement of the dominant TE-polarized spontaneous emission rate and optical gain, respectively. These significant improvements are attributed to the valance band rearrangement and larger optical transition matrix elements in the AlInN-delta-GaN QWs compared with the conventional AlInN QWs. In addition, our analysis suggests that further optimizations of the delta-GaN layer in the AlInN-delta-GaN are crucial to realize the high performance AlInN-based deep UV emitter devices with the desired emission wavelength. These analyses show a potential solution of using the low In-content AlInN-delta-GaN QW structure to

achieve sufficiently high dominant TE-polarized spontaneous emission rates and optical gains for the high performance AlN-based UV devices

In addition to AlInN ternary alloy, evaluations were performed for dilute-As AlNAs alloy. Dilute-As AlNAs alloy is a new material being studied recently, with no information available up to present. In this dissertation, the band structures of dilute-As AlNAs alloys from 0%-As up to 6.25%-As were calculated using First-Principle Density Functional Theory calculation. The band structures of the dilute-As AlNAs alloys are presented, which shows the significant reduction of the energy band gap with the incorporation of As-content into the AlN alloy. Specifically, the band gap energy of dilute-As AlNAs alloy ranges from 6.19 eV to 3.87 eV with As-content varying from 0% to 6.25% respectively. The broad band gap energy coverage of the dilute-As AlNAs material with dilute amount of As concentrations implies the accessibility of emission wavelength range from 200 nm to 320 nm, which is the entire deep UV spectral regime. The band gap bowing and carrier effective masses parameters for the dilute-As AlNAs alloy are obtained through line fitting with the DFT-calculated band structures of the alloys. The band properties show similar characteristics as observed in the dilute-As GaNAs alloys, specifically on the remarkable band gap narrowing effect provided by the As incorporation into the host material. In addition, our findings show that the HH and LH bands crossover with the CH band in the dilute-As AlNAs alloy with As-content of ~1.5%, which indicate the possibility of achieving dominant TE-polarized emission with the alloy. The understanding of the electronic properties of the dilute-As AlNAs semiconductor as presented in this work will provide a clear motivation to pursue this alloy for deep UV III-Nitride optoelectronic applications. Our finding shows that the addition of a minute amount of As into AlN to form dilute-As AlNAs results in a dramatic change in its corresponding electronic band structure property, which opens a new avenue of using this alloy to form heterostructure serving as active regions for photonics devices in the deep UV and mid UV spectral regime.

References for Chapter 8

[1] M. Krames, O. Shchekin, R. Mueller-Mach, G. Mueller, L. Zhou, et.al., “Status and future of high-power light-emitting diodes for solid-state lighting”, J. Disp. Technol., vol. 3, no. 2, pp. 160-175, Jun. 2007.

[2] M. H. Crawford, “LEDs for solid-state lighting: performance challenges and recent advances”, IEEE. J. Sel. Top. Quantum Electron., vol. 15, no. 4, pp. 1028-1040, Aug. 2009.

[3] N. Tansu, H. P. Zhao, G. Y. Liu, X. H. Li, J. Zhang, H. Tong, and Y. K. Ee, “III-Nitride Photonics”, IEEE Photonics Journal, vol. 2, no. 2, pp. 241-248, Apr. 2010.

[4] J. Y. Tsao, M. H. Crawford, M. E. Coltrin, A. J. Fischer, D. D. Koleske, G. S. Subramania, G. T. Wang, J. J. Wierer, and R. F. Karlicek Jr., “Toward smart and ultra-efficient solid-state lighting”, Adv. Opt. Mat., vol. 2, pp. 809-836, 2014.

[5] C. K. Tan, and N. Tansu, “Nanostructured lasers: Electrons and holes get closer”, Nature Nanotech., vol. 10, pp. 107-109, Jan. 2015.

[6] P. Pust, P. J. Schmidt, and W. Schnick, “A revolution in lighting”, Nature Mater., vol. 14, pp. 454-458, Apr. 2015.

[7] The Nobel Prize in Physics 2014. Nobelprize.org. Nobel Media AB (2014). Available at: http://www.nobelprize.org/nobel_prizes/physics/laureates/2014/ (Accessed. 4th December 2015).

[8] M. Shur, and R. Gaska, “Deep-ultraviolet light-emitting diodes”, *IEEE Trans. Electron. Devices*, vol. **57**, pp. 12-25, 2010.

[9] M. Kneissl, et al. “Advances in group III-nitride-based deep UV light-emitting diode technology”. *Semicond. Sci. Technol*., vol. **26**, p. 014306, 2011.

[10] M. Shatalov, et al. “High power AlGaN ultraviolet light emitters”, *Semicond. Sci. Technol.*, vol. **29**, p. 084007, 2014.

[11] H. Hirayama, N. Maeda, S. Fujikawa, S. Toyoda, and N. Kamata, “Recent progress and future prospects of AlGaN-based high-efficiency deep-ultraviolet light-emitting diodes”, *Jap. J. Appl. Phys.*, vol. **53**, p. 100209, 2014.

[12] T. Takano, Y. Ohtaki, Y. Narita, and H. Kawanishi, “Improvement of crystal quality of AlGaN multi quantum well structure by combination of flow-rate modulation epitaxy and AlN/GaN multi-buffer and resultant lasing at deep ultra-violet region”, *Jap. J. Appl. Phys.*, vol. **43**, pp. L1258-1260, 2004.

[13] K. B. Nam, M. L. Nakarmi, J. Li, J. Y. Lin, and H. X. Jiang, “Mg acceptor level in AlN probed by deep ultraviolet photoluminescence”,*Appl. Phys. Lett.*, vol. **83**, pp. 878-880, 2003.

[14] H. Y. Ryu, I. G. Choi, H. S. Choi, and J. I. Shim, “Investigation of light extraction efficiency in AlGaN deep-ultraviolet light-emitting diodes”, *Appl. Phys. Exp.*, vol. **6**, p. 062101, 2013.

[15] K. B. Nam, J. Li, M. L. Nakarmi, J. Y. Lin, and H. X. Jiang, “Unique optical properties of AlGaN alloys and related ultraviolet emitters”, *Appl. Phys. Lett.*, vol. **84**, pp. 5264-5266, 2004.

[16] J. Zhang, H. P. Zhao, and N. Tansu, “Effect of crystal-field split-off hole and heavy-hole bands crossover on gain characteristics of high Al-content AlGaN quantum well lasers”, *Appl. Phys. Lett.*, vol. **97**, p. 111105, 2010.

[17] T. Kolbe, et al. “Optical polarization characteristics of ultraviolet (In)(Al)GaN multiple quantum well light emitting diodes”, *Appl. Phys. Lett.*, vol. **97**, p. 171105, 2010.

[18] E. Kuokstis, et al. “Polarization effects in photoluminescence of C- and M-plane GaN/AlGaN multiple quantum wells”, *Appl. Phys. Lett.*, vol. **81**, pp. 4130-4132, 2002.

[19] J. J. Wierer, I. Montano, M .H. Crawford, and A. A. Allerman, “Effect of thickness and carrier density on the optical polarization of $Al_{0.44}Ga_{0.56}N/Al_{0.55}Ga_{0.45}N$ quantum well layers”, *J. Appl. Phys.*, vol. **115**, p. 174501, 2014.

[20] T. M. Al Tahtamouni, N. Nepal, J. Y. Lin, H. X. Jiang, and W. W. Chow, “Growth and photoluminescence studies of Al-rich $AlN/Al_xGa_{1-x}N$ quantum wells”, *Appl. Phys. Lett.*, vol. **89**, p. 131922, 2006.

[21] G. Y. Liu, et al. “Metalorganic vapor phase epitaxy and characterizations of nearly-lattice-matched AlInN alloys on GaN/sapphire templates and free-standing GaN substrates”. *J. Crys. Growth*, vol. **340**, pp. 66-73, 2012.

[22] J. E. Northrup, “Effect of strain and barrier composition on the polarization of light emission from AlGaN/AlN quantum wells”, *Appl. Phys. Lett.*, vol. **100**, p. 021101, 2012.

[23] J. Zhang, H. P. Zhao, and N. Tansu, “Large optical gain AlGaN-delta-GaN quantum wells laser active regions in mid- and deep-ultraviolet spectral regimes”, *Appl. Phys. Lett.*, vol. **98**, p. 171111, 2011.

[24] J. Zhang, and N. Tansu, “Engineering of AlGaN-Delta-GaN quantum wells gain media for mid- and deep-ultraviolet lasers”, *IEEE Photonics Journal*, vol. **5**, p. 2600209, 2013.

[25] Y. Taniyasu, M. Kasu, and T. Makimoto, “An aluminium nitride light-emitting diode with a wavelength of 210 nanometres”, *Nature*, vol. **441**, pp. 325-328, 2006.

[26] X. H. Li, et al. “Low-threshold stimulated emission at 249 nm and 256 nm from AlGaN-based multiple-quantum-well lasers grown on sapphire substrates”, *Appl. Phys. Lett.*, vol. **105**, p. 141106, 2014.

[27] K. H. Li, X. Liu, Q. Wang, S. Zhao, and Z. Mi, “Ultralow-threshold electrically injected AlGaN nanowire ultraviolet lasers on Si operating at low temperature”. *Nat. Nanotech.*, vol. **10**, pp. 140-144, 2015.

[28] M. M. Satter, et al. “Design and analysis of 250-nm AlInN laser diodes on AlN substrates using tapered electron blocking layers”, *IEEE J. Quantum Electron.*, vol. **48**, pp. 703-711, 2012.

[29] C. K. Tan, and N. Tansu, “Gain and spontaneous emission characteristics of AlInN quantum well for deep ultraviolet emitters”. Proc. of the IEEE Photonics Conference, pp. 577-578, 2015.

[30] Y. Taniyasu, and M. Kasu, “Polarization property of deep-ultraviolet light emission from C-plane AlN/GaN short-period superlattices”, *Appl. Phys. Lett.*, vol. **99**, p. 251112, 2011.

[31] W. W. Chow, and M. Kneissl, “Laser gain properties of AlGaN quantum wells”, *J. Appl. Phys.*, vol. **98**, p. 114502, 2005.

[32] C. K. Tan, D. Borovac, W. Sun, and N. Tansu, “Dilute-As AlNAs alloy for deep-ultraviolet emitter”, Scientific Reports, vol. 6, p. 22215, Feb. 2016.

[33] C. K. Tan, W. Sun, D. Borovac, and N. Tansu, “Large optical gain AlInN-delta-GaN quantum well for deep ultraviolet emitters”, Scientific Reports, vol. 6, p. 22983, Mar. 2016.

[34] G. Y. Liu, J. Zhang, C. K. Tan, and N. Tansu, “Efficiency-droop suppression by using large-bandgap AlGaInN thin barrier layers in InGaN quantum wells light-emitting diodes”, *IEEE Photonics Journal*, vol. **5**, p. 2201011, 2013.

[35] H. Tong, J. Zhang, G. Y. Liu, J. Herbsommer, G. S. Huang, and N. Tansu, “Thermoelectric properties of lattice-matched AlInN alloy grown by metalorganic chemical vapor deposition”, Appl. Phys. Lett., vol. 97, p. 112105, Sep. 2010.

[36] R. Butte, et al. “Current status of AlInN layers lattice-matched to GaN for photonics and electronics”, *J. Phys. D: Appl. Phys.*, vol. **40**, pp. 6328-6344, 2007.

[37] M. Gonschorek, J. F. Carlin, E. Feltin, M. A. Py, and N. Grandjean, “High electron mobility lattice-matched AlInN/GaN field-effect transistor heterostructures”. *Appl. Phys. Lett.*, vol. **89**, p. 062106, 2006.

[38] D. F. Feezell, J. S. Speck, S. P. DenBaars, and S. Nakamura, “Semipolar (20$\bar{2}\bar{1}$) InGaN/GaN light emitting diodes for high-efficiency solid-state lighting”, J. Disp. Tech., vol. 9, no. 4, pp. 190-198, Apr. 2013.

[39] R. A. Arif, Y. K. Ee, and N. Tansu, “Polarization engineering via staggered InGaN quantum wells for radiative efficiency enhancement of light emitting diodes”, Appl. Phys. Lett., vol. 91, no. 9, p. 091110, Aug. 2007.

[40] R. A. Arif, H. P. Zhao, Y. K. Ee, and N. Tansu, “Spontaneous emission and characteristics of staggered InGaN quantum-well light-emitting diodes”, IEEE J. Quantum Electron., vol. 44, no. 6, pp. 573-580, Jun. 2008.

[41] H. P. Zhao, R. A. Arif, Y. K. Ee, and N. Tansu, “Self-consistent analysis of strain-compensated InGaN-AlGaN quantum wells for lasers and light emitting diodes”, IEEE J. Quantum Electron., vol. 45, no. 1-2, pp. 66-78, Jan. 2009.

[42] H. Zhao, G. Y. Liu, J. Zhang, R. A. Arif, and N. Tansu, “Analysis of internal quantum efficiency and current injection efficiency in III-Nitride light-emitting diodes”, *J. Disp. Tech.*, vol. **9**, pp. 212-225, 2013.

[43] N. Tansu, J. Y. Yeh, and L. J. Mawst, “High-performance 1200-nm InGaAs and 1300-nm InGaAsN quantum-well lasers by metalorganic chemical vapor deposition”, *IEEE J. Sel. Top. Quantum Electron*., vol. **9**, pp. 1220-1227, 2003.

[44] S. R. Bank, L. L. Goddard, M. A. Wistey, H. B. Yuen, and J. S. Harris, “On the temperature sensitivity of 1.5-um GaInNAsSb lasers”, *IEEE J. Sel. Top. Quantum Electron.*, vol. **11**, pp. 1089-1098, 2005.

[45] A. Lindsay, and E. P. O’Reilly, “Unification of the band anticrossing and cluster-state models of dilute nitride semiconductor alloys”, *Phys. Rev. Lett*., vol. **93**, p. 196402, 2004.

[46] S. H. Wei, and A. Zunger, “Giant and composition-dependent optical bowing coefficient in GaAsN alloys”, *Phys. Rev. Lett.,* vol. **76**, pp. 664-667, 1996.

[47] L. Bellaiche, S. H. Wei, and A. Zunger, “Localization and percolation in semiconductor alloys: GaAsN vs GaAsP”, *Phys. Rev. B*, vol. **54**, pp. 17568-17576, 1996.

[48] W. G. Bi, and C. W. Tu, “Bowing parameter of the band-gap energy of GaNxAs1-x”, *Appl. Phys. Lett.*, vol. **70**, pp. 1608-1610, 1997.

[49] S. J. Sweeney, and S. R. Jin, “Bismide-nitride alloys: Promising for efficient light emitting devices in the near- and mid-infrared”, *J. Appl. Phys.*, vol. **113**, p. 043110, 2013.

[50] C. K. Tan, J. Zhang, X. H. Li, G. Y. Liu, B. O. Tayo, N. Tansu, “First-Principle electronic properties of dilute-As GaNAs alloy for visible light emitters”, J. Disp. Tech., vol. 9, no. 4, pp. 272-279, Apr. 2013.

[51] C. K. Tan, and N. Tansu, “First-Principle natural band alignment of GaN / dilute-As GaNAs alloy”, AIP Advances, vol. 5, no. 1, p. 071129, Jan. 2015.

[52] C. K. Tan, and N. Tansu, “Auger recombination rates in dilute-As GaNAs semiconductor”, AIP Advances, vol. 5, p. 057135, May 2015.

[53] C. K. Tan, D. Borovac, W. Sun and N. Tansu, “InGaN / Dilute-As GaNAs interface quantum well for red emitters”, Scientific Reports, vol. 6, p. 19271, Jan. 2016.

[54] X. Li, S. Kim, E.E. Reuter, S. G. Bishop, and J. J. Coleman, “The incorporation of arsenic in GaN by metalorganic chemical vapor deposition”, Appl. Phys. Lett., vol. 72, no. 16, pp. 1990-1992, Feb. 1998.

[55] A. Kimura, C. A. Paulson, H. F. Tang, and T. F. Kuech, “Epitaxial GaN1-yAsy layers with high As content grown by metalorganic vapor phase epitaxy and their band gap energy”, Appl. Phys. Lett., vol. 84, no. 9, pp. 1489-1491, Mar. 2004.

[56] K. M. Yu, S. V. Novikov, R. Broesler, C. R. Staddon, M. Hawkridge, Z. Liliental-Weber, I. Demchenko, J. D. Denlinger, V. M. Kao, F. Luckert, R. W. Martin, W. Walukiewicz, and C. T. Foxon, “Non-equilibrium GaNAs alloys with band gap ranging from 0.8-3.4 eV”, Phys. Status Solidi C, vol. 7, no. 7-8, pp. 1847-1849, May 2010.

[57] R. A. Arif, H. Zhao, and N. Tansu, “Type-II InGaN-GaNAs quantum wells for lasers applications”, Appl. Phys. Lett., vol. 92, no. 1, p. 011104, Jan. 2008.

[58] H. Zhao, R. A. Arif, and N. Tansu, “Self-consistent gain analysis of type-II ‘W’ InGaN-GaNAs quantum well lasers”, J. Appl. Phys., vol. 104, no. 4, p. 043104, Aug. 2008.

[59] T. Takayama, M. Yuri, K. Itoh, and J. S. Harris Jr., “Theoretical predictions of unstable two-phase regions in wurtzite group-III-nitride-based ternary and quaternary material systems using modified valence force field model”, *J. Appl. Phys.*, vol. **90**, pp. 2358-2369, 2001.

[60] MedeA-VASP, Material Designs Inc. Available at: http://www.materialsdesign.com. (Accessed. 4th December 2015).

[61] V. Fiorentini, and A.Baldereschi, “Dielectric scaling of the self-energy scissor operator in semiconductors and insulators”, Phys. Rev. B, vol. **51**, no. 23, pp. 17196-17198, Jun. 1995.

[62] C. K. Tan, D. Borovac, W. Sun, and N. Tansu, “First-principle electronic properties of dilute-P $GaN_{1-x}P_x$ alloy for visible light emitters”, Scientific Reports, 6, p. 24412, Apr. 2016.

[63] S. Schulz, M .A. Caro, and E. P. O'Reilly, "Impact of cation-based localized electronic states on the conduction and valence band structure of $Al_{1-x}In_xN$ alloys", *Appl. Phys. Lett.*, vol. **104**, p. 172102, 2014.

[64] M. Suzuki, and T. Uenoyama, "First-principles calculations of effective-mass parameters of AlN and GaN", Phys. Rev B, vol. **52**, no. 11, pp. 8132-8139, 1995.

[65] P.Carrier, and S. H. Wei, "Calculated spin-orbit splitting of all diamondlike and zinc-blende semiconductors: Effects of $p_{1/2}$ local orbitals and chemical trends", *Phys. Rev. B*, vol. **70**, p. 035212, 2004.

[66] S. F. Chichibu, et al, "Origin of defect-insensitive emission probability in In-containing (Al, In, Ga)N alloy semiconductors". *Nat. Material*, vol. **5**, pp. 810-816, 2006.

[67] X. Wu, E. J. Walter, A. M. Rappe, R. Car, and A. Selloni, "Hybrid density functional calculations of the band gap of $Ga_xIn_{1-x}N$", *Phys. Rev. B*, vol. **80**, p. 115201, 2009.

Chapter 9: Summary and Future Outlook

9.1. Summary

The research work completed in this dissertation are focused on the development of dilute-anion III-Nitride semiconductors for device applications in visible and deep ultraviolet (UV) spectral regime. The outcome of the research work involves 1) the design of dilute-anion GaN-based material and novel AlN-based materials for visible and deep UV applications respectively, 2) the design of novel nanostructures for visible light and deep UV emissions, and 3) the theoretical analysis of Auger non-radiative recombination processes in the III-Nitride materials. The original contributions in the field of III-Nitride semiconductor material and devices includes 1) Understanding the electronic properties of dilute-anion III-Nitride semiconductor materials, 2) Designing novel III-Nitride active region quantum well structure for visible and deep UV emitting applications, and 3) Evaluating the Auger recombination process in the dilute-As GaNAs and dilute-P GaNP materials. The future outlook of the research work is discussed afterwards.

9.1.1. Dilute-Anion III-Nitride Semiconductors for Visible and Deep UV Applications

By utilizing the first-principle density functional theory (DFT) calculation technique, the optoelectronic properties of the dilute-anion III-Nitride semiconductors were investigated. Comprehensive studies have been performed on the dilute-anion III-Nitride alloys for visible and deep UV applications. The III-Nitride materials that are extensively studied include dilute-As GaNAs, dilute-P GaNP, and dilute-As AlNAs. Dilute-As GaNAs and dilute-P GaNP semiconductors are investigated for visible light applications, while dilute-As AlNAs semiconductor is investigated for deep UV applications.

The electronic properties for the dilute-As GaNAs and dilute-P GaNP semiconductors were analyzed and compared. The band properties studied include the band structures, band gap energy, effective mass and also split-off band energy. The work showed that both dilute-As

GaNAs and dilute-P GaNP exhibit extraordinary characteristics, in which the band gap energy can be significantly reduced by incorporating a minute amount of anion-content in the GaN material. The ability to tune the band gap energy of GaN from 3.645 eV to 2.232 eV using dilute-As GaNAs material with only 12.5% As-content is advantageous in the field of solid state lighting, as compared to the InGaN semiconductor. The reason behind the significant reduction of energy band gap using the As-content is attributed to the As impurity level that is located close to the valence band maximum of the GaN. Similar characteristics were shown in the dilute-P GaNP alloys. These findings show strong potential of the dilute-anion GaN material as an alternative material for light emiting applications.

In addition, the investigations on the natural band alignment of dilute-As GaNAs material with respect to the GaN material were performed. The findings show that the valence band maximum position will move upwards significantly when As-content is added into the GaN. On the other hand, the conduction band minimum position is relatively unchanged even though the As-content in GaNAs is increased to 12.5%. The analysis indicate large valence band offset but small conduction band offset in the dilute-As GaNAs / GaN material system, which is significantly different from the InGaN / GaN material system. The significant change in the valence band offset is largely attributed to the position of the As-impurity in the energy band gap of GaN, in which the As-impurity level is fairly close to the valence band maximum of GaN. Based on the findings, the dilute-As GaNAs material can form a type-I heterostructure with GaN material, or type-II heterostructure with the InGaN by taking advantage of the unique band offset characteristics in the dilute-As GaNAs / GaN material system.

The studies in the electronic properties of the dilute-anion GaN material allows the utilization of the band parameters in relevant material and device simulations, and the potential in the dilute-As GaNAs material can be further evaluated. The investigations in the Auger recombination process lead to the evaluation of the Auger recombination rates in the dilute-As GaNAs material. The analysis shows that the Auger recombination rates in the dilute-As GaNAs material as two orders of magnitude lower than the InGaN material, attributed to the suppression of interband

Auger process in the GaNAs material. The reduction of Auger recombination rates in the GaNAs material is important, as the efficiency droop issue in the III-Nitride LEDs is related to the Auger recombination process. Similar findings have been obtained in the dilute-P GaNP alloy, showing that the band structure plays a key role in affecting the Auger recombination process. Consequently, the dilute-anion GaN material show strong potential as the next III-Nitride material for device applications especially in the field of solid-state lighting.

In the case of applications involving deep-ultraviolet emission, dilute-As AlNAs material has been suggested as one of the alternative materials to the AlGaN material. The electronic properties of the dilute-As AlNAs were investigated which include the band structures, band gap energy, effective masses of the electron and holes, split-off band energy. The effect of anion-content in the AlN is similar to that of in the GaN material. The incorporation of As-content in the AlN material leads to significant reduction of energy band gap, allowing the wavelength tuning from ~210 nm to ~320 nm with just 6% As-content in the AlN material. In addition, the findings on dilute-As AlNAs material reveal the possibility of addressing the valence band crossover issue in the AlGaN material. When the As-content stays less than 1%, the crystal field split-off band is on top of the heavy hole / light hole band, similar to that of AlN material. When the As-content goes beyond 1%, the crystal field split-off band will move below the heavy hole and light hole band. This implies that the valence band crossover issue in the deep UV AlGaN emitters could potentially be solved by using the dilute-As AlNAs material. This shows the strong potential of dilute-As AlNAs material as an alternative III-Nitride material for deep UV applications.

9.1.2. Novel III-Nitride Nanostructures for High-Efficiency LEDs and Lasers

Nanostructure engineering has been one of the most heated research direction in the field of solid-state lighting including light emitting diodes and lasers. The design of nanostructures especially in the active region structure directly impact the device performance. In this dissertation, the interface quantum well structure has been proposed for the visible light emitters. The interface quantum well structure was formed by using the InGaN layer and the dilute-As

GaNAs layer. The dilute-As GaNAs layer was inserted adjacent to the InGaN layer in the quantum well structure, sandwiched by the GaN layers as the barriers. By employing the interface QW structure, the electron-hole wavefunction overlap is significantly enhanced in comparison to that of conventional InGaN QW, even though the existence of polarization field in the QW leads to the band tilting. Based on the analysis, the high spontaneous emission rate can be achieved by using the InGaN-GaNAs interface QW structure for red color emission, while the spontaneous emission rate is much lower in the conventional InGaN QW for red emission. The insertion of dilute-As GaNAs layer in the QW structure allows the tuning of the emission wavelength, since the hole is deeply localized in the GaNAs layer. The findings show that the In-content in the InGaN layer can be kept low (~15-20%), which removes the barrier of the high In-content requirement for long-wavelengh emission. On the other hand, the tuning of As-content in the GaNAs layer leads to various emission wavelength from blue to red spectrum. The findings show that the spontaneous emission rate and optical gain of the InGaN-GaNAs QW structure are relatively similar across the visible spectrum regime, allowing a more uniform white light emission.

In the case of deep UV applications, AlInN has been suggested as a route to address the valence band crossover issue – specifically by using the structure in nanoscale system. The findings show that conventional AlInN QW can be used to removed the valence band crossover problem, with the tradeoff in the spontaneous emission rate. This is attributed to the significant reduction of electron-hole wavefunction overlap when the In-content increases in the AlInN QW. The AlInN-delta-GaN QW structure has been investigated to improve the spontaneous emission rate and also the optical gain of the conventional AlInN QW. The analysis shows that the insertion of delta-GaN layer in the AlInN QW leads to significant enhancement of the spontaneous emission rates, attributed to the strong confinement of electron and hole wavefunctions in the delta-GaN layer. This work show that the AlInN-delta-GaN QW can be potentially useful for the deep UV device applications.

9.1.3. Theoretical Analysis of Auger Process in III-Nitride Semiconductors

Auger recombination process is an important non-radiative recombination process naturally existing in the semiconductor material. The existence of Auger recombination process leads to lower efficiency of the light emitting device, since not all carriers are subjected to the radiative recombinations. In this dissertation, analytical model has been developed to evaluate the Auger recombination process in the III-Nitride semiconductors. The analytical model provides a closed-form analytical expressions, taking into account the intrabnad and interband Auger recombination processes. The analytical model has been applied to evaluate the Auger recombination coefficients for InGaN alloy and dilute-anion GaN-based semiconductor alloys. The findings show that the calculated Auger coefficients for InGaN alloy agrees considerably well with the reported InGaN Auger coefficient values in literature. One of the key advantage using the analytical model is the hassle-free calculation that involves much less computation power, in comparison to that of the numerical simulations. As a result, the analytical solutions could provide fast and intuitive estimation of how the Auger recombination process could play a role in the III-Nitirde semiconductor alloys.

On the other hand, numerical model has been developed for the Auger recombination process taking into consideration the interface roughness effect in the InGaN semiconductor. The concept of the Auger recombination process with interface roughness effect is described, and the corresponding calculation approach is presented. The development of numerical formulation of the Auger recombination process taking into account the interface roughness effect is also presented. The Auger recombination model holds high importance in the field of theory and simulations for nano-scale semiconductor device, since most of the devices using quantum wells as active region would contain interface roughness. The past theory and calculations assumes abrupt interface in the QW structure which is not the case in real QW structure. The findings based on the developed Auger model show that the Auger recombination without consideration of interface roughness yield $C_{Auger} \sim 10^{-34}$ cm^6s^{-1} for InGaN QW, which agrees well with the literature.

When the interface roughness of 1nm is included in the Auger calculation model for 3 nm InGaN QW structure, the C_{Auger} yields ~ 10^{-30} cm^6s^{-1} which is large enough to account for efficiency droop issue in the light emitting diode structure. The analysis shows that the increase of C_{Auger} is roughly four orders of magnitude in a thin InGaN QW, while the increase of C_{Auger} is only roughly two orders of magnitude in a thick QW. The findings suggest that the interface roughness plays a critical role in the semiconductor devices, especially when the device involves nanostructure with countable atomic layers.

9.2. Future Outlook

The breakthrough in the lighting technology occurred two decades ago, attributed to the realization of high efficiency light emitting diodes. The material innovations such as the material epitaxy, the use of phosphor for blue light conversion, and activation of p-type dopants for the GaN-based LED devices play a key role behind the technology breakthrough, prompting the switch from the era of conventional lighting technology into solid-state lighting technology. Such lighting revolution has been ongoing for years, and the solid state ligting technology has been well established in the industry and widely implemented in the consumer applications.

The breakthrough in lighting technology has since sprung numerous research directions, with the aim to enhance the white LED performance. While the progress is extremely promising and the white LEDs based on III-Nitride material and device technology become a norm in the society, the scientists and the engineers face a dilemma in that a bottleneck is seemingly reached within the technology. The ongoing limitations in current III-Nitride LED technology such as the efficiency droop, low efficiency at long wavelength, high In-content requirement that were discussed a decade ago are yet to be solved, and these have impeded the progress in III-Nitride lighting technology for a decade. It is however undoubtable that solid state lighting technology using III-Nitride materials will dominate in the short future, due to the high efficiency and high reliability features of the III-Nitride devices. Thus further evolution in the III-Nitride LED devices

could be based on further material and device innovations, which is the objective of this dissertation.

The vision and ideas described through this dissertation open up a new stand-alone direction in the III-nitride research area. In the past decades, the research work was primarily focused on InGaN material, attributed to the ease of realistic growth and 'high' emission rates. The fundamental drawbacks in the InGaN material prompted the hunt of alternative materials as a replacement, and dilute-anion III-Nitride materials have been considered now as a promising semiconductor class. The direction identified in the dissertation points out to the important areas and potential enabled by the dilute-anion III-Nitride semiconductors – beyond LEDs and lasers applications.

In this dissertation the investigation of electronic properties of the dilute-anion III-Nitride materials has provided the much needed information and laid the first step into the evaluation of the potential in the materials. The analysis in the dilute-anion III-Nitride material band structures provided the knowledge of band gap energy and related band parameters that are required for relevant material and device simulations. Further research discovers the advantages of using the dilute-anion III-Nitride materials for visible and deep UV light emitting applications. These include the suppression of the interband Auger process leading to reduction of Auger rates, enhanced spontaneous emission rate in red emission and uniform emission rate across the visible spectral regime, and removal of high In-content requirement in the III-Nitride quantum well for visible light applications. For deep UV applications, the advantage includes addressing the valence band crossover issue that persist in the III-Nitride light emitting devices.

However, it is important to point out that the research field in the dilute-anion III-Nitride materials and devices is still extremely limited, and the motivation in conducting research in this field is still lacking. Continuing research in the dilute-anion III-Nitride field for few decades is probably needed to drive the field forwards, and the work in this dissertation is just the beginning of this projected development.

The foundation of dilute-anion III-Nitride field has been established through the research work carried out in this dissertation. While the progress in these dilute-anion III-Nitride semiconductors are still in the early stage, further research and studies will expand the currently limited knowledge in these materials. With the ongoing research development, these dilute-anion III-Nitride semiconductors can one day be practically implemented in various device applications, providing unique features compared to the commonly known III-Nitride semiconductors.

CHEE-KEONG TAN

7 Asa Drive # 218 • Bethlehem, PA 18015 • USA
Phone (610) 758-4326 • Fax (610) 758-2605 • E-mail: ckt209@Lehigh.Edu

Information updated up to: ***July 2016***

Contact Information

Chee-Keong Tan
PhD Candidate and Research Assistant
Center for Photonics and Nanoelectronics
Department of Electrical and Computer Engineering
Lehigh University
7 Asa Drive, Bethlehem, PA 18015, USA
Email:ckt209@Lehigh.Edu
Cell Phone: (484) 725-4176, Fax: (610) 758-2605
Research Group: www.ece.lehigh.edu/~tansu

Birth Date and Place & Citizenship

July 1988, Georgetown, Penang State, Malaysia.

Education

July 2011 – present, ***Lehigh University (Bethlehem, Pennsylvania, USA)***

Ph.D. Candidate in Electrical Engineering, Department of Electrical and Computer Engineering

- **Expected Graduation: July 2016**
- Research Assistant, PhD Advisor: Prof. Nelson Tansu (ECE, Lehigh)
- Title: Dilute-Anion Nitride Semiconductor Materials and Nanostructures
- Research Areas: III-Nitride semiconductor materials and nanostructures for solid state lighting technologies.

Sep. 2008 – Jul. 2011, ***University of Sheffield (Sheffield, United Kingdom)***

Bachelor of Engineering (B.Eng.) in Electrical Engineering, Department of Electronic and Electrical Engineering

- Sheffield graduate award of University of Sheffield
- Thesis: Comparison of bulk and quantum well dilute nitride
- Graduate with First Class honors

Professional Experiences

July 2011 – present, ***Lehigh University (Bethlehem, Pennsylvania, USA)***

Ph.D. Candidate and Research Assistant

Department of Electrical and Computer Engineering (ECE)

P. C. Rossin College of Engineering and Applied Science & Center for Photonics and Nanoelectronics (CPN)

Ph.D. Advisor: Prof. Nelson Tansu

July 2010 – September 2010, ***University of Sheffield (Sheffield, United Kingdom)***

Undergraduate Research Assistant

Department of Electronic and Electrical Engineering (EEE)

Semiconductor materials and devices group

Advisor: Prof. John P.R. David

July 2009 – September 2009, ***Lehigh University (Bethlehem, Pennsylvania, USA)***

Undergraduate Research Assistant

Department of Electrical and Computer Engineering (ECE)

P. C. Rossin College of Engineering and Applied Science & Center for Optical Technologies (COT)

Advisor: Prof. Boon Siew Ooi

February 2008 – June 2008, Chung Hwa Confucian High School (Penang, Malaysia)
High School Teacher

Courses covered Mathematics, Mandarin and Malay Language, Sports, and Moral Education

Responsibilities included class-lecturing students, guiding and advising students, assist-coaching athletes

Research Interests

"Novel Semiconductor Materials Design and Nanostructure Engineering for Future Devices"

My research interests are related to the novel materials and nanostructure design for future devices. Specifically, my research areas are related to novel design of III-Nitride semiconductor materials and nanostructures for solid state lighting technologies. My research works cover mainly the aspect of computational design in III-Nitride semiconductors and nanostructures by using advanced computational techniques. My research interests include the development of new dilute-impurity nitride materials, novel nanostructure enginnering, the studies of efficiency droop of light emitting diodes in nitride material, fundamental electronic structures in nitride material and solar cell.

Leadership

2015-present	Lehigh Optics and Photonics Society (Vice President & Founding member)
2015-present	SPIE Lehigh University Student Chapter (Vice President)
2014-2015	SPIE Lehigh University Student Chapter (Treasurer)
2010-2011	SPIE University of Sheffield Student Chapter (Student Advisor)
2010-2011	University of Sheffield Electronic & Electrical Engineering Society (Secretary)
2009-2010	SPIE University of Sheffield Student Chapter (President & Founder)

Awards and Honors Received

- ***SPIE Optics and Photonics Education Scholarship*** (Aug 2016), Lehigh University
- ***Selected as the Winner for the Department of Energy (DOE) Solid State Lighting (SSL) R&D Workshop Poster Competition 2016 (National)***, US Department of Energy, United States, February 2016
- ***2015 CPN – Sherman Fairchild Fellowship*** (Sep 2015 – present), Lehigh University
- ***SPIE Optics and Photonics Education Scholarship*** (Aug 2015), Lehigh University
- ***Rossin Doctoral Fellow*** (April 2015 – present), Lehigh University
- ***Who's Who in America*** (Since 2015), Inducted in 2015.
- ***Lehigh University Dean's Teaching Assistantship*** (January 2015 – June 2015), Lehigh University
- ***Sherman Fairchild Fellowship*** (September 2014 – September 2015), Lehigh University
- ***Lehigh University Research Assistantship*** (June 2014 – present), Lehigh University
- ***Lehigh University Fellowship*** (January 2014 – June 2014), Lehigh University
- ***Lehigh University Research Assistantship*** (July 2011 – January 2014), Lehigh University
- ***Lehigh University Dean's Scholarship*** (July 2011 – September 2012), Lehigh University

- ***Sheffield Graduate Award*** (July 2011), University of Sheffield
- ***University of Sheffield Engineering International Scholarships*** (2008 – 2011), University of Sheffield
- ***Bronze Award in National Physics Competition*** (2007), Malaysia
- ***Distinction in National Chemistry Quiz*** (2007), Malaysia
- ***Distinction in Australia New South Wales Mathematic Competition*** (2007), Malaysia
- ***Distinction in National Physics Competition*** (2005), Malaysia
- ***Merit in Australia New South Wales Mathematic Competition*** (2005), Malaysia
- ***Olympiad Mathematic Contest*** (2002 - 2005), Malaysia

Professional Affiliations

2009 – 2011, Student Member, International Society for Optical Engineering (SPIE)
2014 – present, Student Member, International Society for Optical Engineering (SPIE)
2014 – present, Student Member, Institute of Electrical and Electronics Engineers (IEEE)
2014 – present, Student Member, American Physical Society (APS)

Technical Refereed Journal and Conference Publications

Refereed Journal Articles

- ✓ Publication Link: http://www.ece.lehigh.edu/~tansu/publications.html
  - ➢ **Total First Authorship Refereed Publications: 26; Total Refereed Journal Publications: 11**
  - ➢ **Additional Refereed Journals Currently Under Review / Submission (May 2016): 10**
- ✓ **Isi Web of Knowledge Record (as of July 2016): Total Citations = 201; h-index = 4**
  - ➢ **Publication Name Search in ISI Web of Knowledge: (Tan CK and Tansu)**
- ✓ **Google Scholar (as of July 2016): Total Citations = 245; h-index = 6**

Refereed Journal Publications

1. **C. K. Tan**, J. Zhang, X. H. Li, G. Y. Liu, B. O. Tayo, and N. Tansu, "First-Principle Electronic Properties of Dilute-As GaNAs Alloy for Visible Light Emitters", *IEEE / OSA Journal of Display Technology*, vol. 9, no. 4, pp. 272-279, April 2013. DOI: 10.1109/JDT.2013.2248342
2. G. Y. Liu, J. Zhang, **C. K. Tan**, and N. Tansu, "Efficiency-Droop Suppression by Using Large-Bandgap AlGaInN Thin Barrier Layers in InGaN Quantum Wells Light-Emitting Diodes", *IEEE Photonics Journal*, vol. 5, no. 2, Art. 2201011, April 2013. DOI: 10.1109/JPHOT.2013.2255028
3. **C. K. Tan**, and N. Tansu, "First-Principle Natural Band Alignment of GaN / Dilute-As GaNAs Alloy," *AIP Advances*, vol. 5, no. 1, p. 017129, January 2015. DOI: 10.1063/1.4906569
4. (**Invited Paper**) **C. K. Tan**, and N. Tansu, "Nanostructured Lasers: Electrons and Holes Get Closer," *Nature Nanotechnology*, vol. 10, no. 2, pp. 107-109, February 2015. DOI: 10.1038/nnano.2014.333

   http://www.nature.com/nnano/journal/v10/n2/full/nnano.2014.333.html
5. **C. K. Tan**, and N. Tansu, "Auger Recombination Rates in Dilute-As GaNAs Semiconductor", *AIP Advances*, vol. 5, no. 5, p. 057135, May 2015. DOI: 10.1063/1.4921394
6. P. F. Zhu, **C. K. Tan**, W. Sun, and N. Tansu, "Aspect Ratio Engineering of Microlens Arrays in Thin-Film Flip-Chip Light-Emitting Diodes", *Applied Optics*, vol. 54, no. 34, pp. 10299-10303, November 2015. DOI: 10.1364/AO.54.010299

7. **C. K. Tan**, D. Borovac, W. Sun and N. Tansu, "InGaN / Dilute-As GaNAs Interface Quantum Well for Red Emitters", *Scientific Reports* [Nature Publishing Group], vol. 6, Art. 19271, January 2016. DOI: 10.1038/srep19271.

   http://www.nature.com/articles/srep19271

8. **C. K. Tan**, D. Borovac, W. Sun and N. Tansu, "Dilute-As AlNAs Alloy for Deep Ultraviolet Emitters", *Scientific Reports* [Nature Publishing Group], vol. 6, Art. 22215, February 2016. DOI: 10.1038/srep22215

   http://www.nature.com/articles/srep22215

9. **C. K. Tan**, W. Sun, D. Borovac and N. Tansu, "Large Optical Gain AlInN-Delta-GaN Quantum Well for Deep Ultraviolet Emitters", *Scientific Reports* [Nature Publishing Group], vol. 6, Art. 22983, March 2016. DOI: 10.1038/srep22983

   http://www.nature.com/articles/srep22983

10. P. F. Zhu, H. Zhu, W. Qin, B. H. Dantas, W. Sun, **C. K. Tan**, and N. Tansu, "Narrow-Linewidth Red-Emission Eu^{3+}-Doped TiO_2 Spheres for Light-Emitting Diodes", *J. Appl. Phys.*, vol. 119, Art. 124305, March 2016.

11. **C. K. Tan**, D. Borovac, W. Sun, and N. Tansu, "First-Principle Electronic Properties of Dilute-P $GaN_{1-x}P_x$ Alloy for Visible Light Emitters", *Scientific Reports* [Nature Publishing Group], vol. 6, Art. 24412, April 2016. DOI: 10.1038/srep24412

    http://www.nature.com/articles/srep24412

✓ **More than 5 additional refereed journal papers in preparation for submission**

Refereed Conference Publications

1. **C. L. Tan**, H. S. Djie, **C. K. Tan**, V. Hongpinyo, Y. H. Ding, and B. S. Ooi, "The Effect of Multi Active Junctions on Broadband Emission from InAs/InGaAlAs Quantum-dash Structure", *The 22nd Annual Meeting of the IEEE Photonics Society (**IEEE PS'09**)*, Belek-Antalya, Turkey, (2009).
2. **C. L. Tan**, H. S. Djie, **C. K. Tan**, and B. S. Ooi, "Unique Lasing Mechanism of Localized Dispersive Nanostructures in InAs/InGaAlAs Quantum Dash Broad Interband Laser", *Novel In-Plane Semiconductor Lasers IX conference, **SPIE Photonics West 2010***, San Francisco, CA, USA, (2010).
3. C. L. Tan, **C. K. Tan**, H. S. Djie, and B. S. Ooi, "Absence of Quantized Energy-states Local Diffusion in Semiconductor Quantum Dash structures", *IEEE/OSA Conference on Lasers and Electro-Optics 2010 **(IEEE CLEO/QELS'10)***, San Jose, California, (2010).
4. **(Invited Conference Talk)** N. Tansu, J. Zhang, G. Y. Liu, **C. K. Tan**, P. F. Zhu, and H. P. Zhao, "Advances in III-Nitride Semiconductors for Energy Efficiency Applications," Proc. of the *KAUST-UCSB-NSF Solid State Lighting Workshop 2012*, Thuwal, Saudi Arabia, February 2012.
5. **(Invited Keynote Plenary Conference Talk)** N. Tansu, J. Zhang, G. Y. Liu, **C. K. Tan**, P. F. Zhu, and H. P. Zhao, "Physics and Technology of III-Nitride Semiconductors for Energy Efficiency Applications," Proc. of the *IUMRS-ICYRAM Conference 2012*, Material Research Society (MRS), Singapore, July 2012.
6. **(Invited Conference Paper)** J. Zhang, G. Y. Liu, **C. K. Tan**, P. F. Zhu, H. P. Zhao, and N. Tansu, "Engineering Nanostructures in Active Regions and Devices for High-Efficiency III-Nitride Light-Emitting Diodes – Epitaxy and Physics," Proc. of the *SPIE Optics + Photonics 2012*, NanoEpitaxy : Materials and Devices IV, San Diego, CA, August 2012.
7. **C. K. Tan**, J. Zhang, X. H. Li, G. Y. Liu, and N. Tansu, "Dilute-As GaNAs Semiconductor for Visible Emitters," *Proc. of the IEEE Photonics Conference 2012*, Burlingame, CA, September 2012.

8. G. Y. Liu, J. Zhang, **C. K. Tan**, and N. Tansu, "Characteristics of InGaN Quantum Wells Light-Emitting Diodes with Thin AlGaInN Barrier Layers," *Proc. of the IEEE Photonics Conference 2012*, Burlingame, CA, September 2012.
9. **(Invited Conference Paper)** N. Tansu, J. Zhang, G. Y. Liu, H. P. Zhao, **C. K. Tan**, and P. F. Zhu, "Physics of High-Efficiency III-Nitride Quantum Wells Light-Emitting Diodes," Proc. of the *Asian Communications and Photonics (ACP) Conference 2012*, Guangzhou, China, November 2012.
10. G. Y. Liu, J. Zhang, **C. K. Tan**, and N. Tansu, "InGaN-Delta-InN Quantum Well Light-Emitting Diodes with Carrier Transport Effect," Proc. of the *SPIE Photonics West 2013*, San Francisco, CA, February 2013.
11. **C. K. Tan**, J. Zhang, G. Y. Liu, and N. Tansu, "Effect of Interband Energy Separation on the Interband Auger Processes in III-Nitride Semiconductors," Proc. of the *SPIE Photonics West 2013*, San Francisco, CA, February 2013.
12. **(Tutorial Conference Paper)** N. Tansu, J. Zhang, G. Y. Liu, H. P. Zhao, **C. K. Tan**, and P. F. Zhu, "Internal and External Efficiency in InGaN-Based Light-Emitting Diodes," Proc. of the *Asian Communications and Photonics (ACP) Conference 2013*, Beijing, China, November 2013.
13. P. F. Zhu, **C. K. Tan**, and N. Tansu, "Extraction Efficiency Enhancement of Thin-Film Flip-Chip GaN Light-Emitting Diodes with Self-Assembled Microsphere Arrays," Proc. of the *International Conference on White LEDs and Solid State Lighting (WLED 5) Conference 2014*, Jeju, Korea, June 2014.
14. **C. K. Tan**, P. F. Zhu, and N. Tansu, "Investigation of Dilute-As GaNAs Active Regions for High Efficiency GaN-based Light-Emitting Diodes," Proc. of the *International Conference on White LEDs and Solid State Lighting (WLED 5) Conference 2014*, Jeju, Korea, June 2014.
15. **C. K. Tan**, P. F. Zhu, and N. Tansu, "Controlling the Interband Auger Recombination Mechanism in III-Nitride Based Ternary Active Regions," Proc. of the *SPIE Optics + Photonics 2014*, Thirteenth International Conference on Solid State Lighting and LED-based Illumination Systems, San Diego, CA, August 2014.
16. P. F. Zhu, **C. K. Tan**, and N. Tansu, "Comparison of Extraction Efficiency for Thin-Film Flip-Chip InGaN Light-Emitting Diodes with Microsphere and Microconcave Array Structures," Proc. of the *SPIE Optics + Photonics 2014*, Thirteenth International Conference on Solid State Lighting and LED-based Illumination Systems, San Diego, CA, August 2014.
17. P. F. Zhu, H. Y. Zhu, W. P. Qin, **C. K. Tan**, and N. Tansu, "Eu^{3+}-doped TiO_2 Nanospheres for GaN-based White Light-Emitting Diodes," Proc. of the *SPIE Optics + Photonics 2014*, Thirteenth International Conference on Solid State Lighting and LED-based Illumination Systems, San Diego, CA, August 2014.
18. P. F. Zhu, T. Toma, **C. K. Tan**, and N. Tansu, "Investigation of Solar Hydrogen Generation from the GaN and InGaN Thin Films," Proc. of the *SPIE Optics + Photonics 2014*, Solar Energy + Technology, San Diego, CA, August 2014.
19. **(Invited Conference Paper)** P. F. Zhu, W. Sun, **C. K. Tan**, and N. Tansu, "Light Extraction Efficiency Enhancement in GaN-Based LEDs with Self-Assembly Approach," Proc. of the *Progress In Electromagnetics Research Symposium (PIERS) 2014*, Guangzhou, China, August 2014.
20. **(Invited Keynote Conference Paper)** N. Tansu, **C. K. Tan**, P. F. Zhu, and W. Sun, "Physics of High Efficiency and Efficiency-Droop in III-Nitride Light-Emitting Diodes," Proc. of the *Progress In Electromagnetics Research Symposium (PIERS) 2014*, Guangzhou, China, August 2014.
21. **C. K. Tan**, and N. Tansu, "Dilute-P GaNP Semiconductor Alloy for Visible Light Emitter," Proc. of the *American Physical Society (APS) Annual March Meeting 2015*, San Antonio, Texas, USA, March 2015.
22. N. A. Lacroce, G. Y. Liu, **C. K. Tan**, R. A. Arif, S. M. Lee, and N. Tansu, "Effect of Dopant Activation on Device Characteristics of InGaN-based Light Emitting Diodes," Proc. of the *American Physical Society (APS) Annual March Meeting 2015*, San Antonio, Texas, USA, March 2015.

23. W. Sun, **C. K. Tan**, and N. Tansu, "Artifically-Engineered III-Nitride Digital Alloy for Solar Energy Harvesting," Proc. of the *American Physical Society (APS) Annual March Meeting 2015*, San Antonio, Texas, USA, March 2015.
24. **C. K. Tan**, and N. Tansu, "InGaN-GaNAs Active Region for Visible Light Emitters in Red Spectral Regime," *Proc. of the MRS International Conference on Materials for Advanced Technologies (ICMAT) 2015*, Singapore, Republic of Singapore, June 2015.
25. **C. K. Tan**, and N. Tansu, "Barrier Engineering in AlGaN-Delta-GaN Heterostructure for Deep UV Emitters," Proc. of the *MRS International Conference on Materials for Advanced Technologies (ICMAT) 2015*, Singapore, Republic of Singapore, June 2015.
26. **C. K. Tan**, and N. Tansu, "Design Analysis of InGaN-GaNAs Active Region for Long Wavelength Visible Emission," Proc. of the *SPIE Optics + Photonics 2015*, Fourteenth International Conference on Solid State Lighting and LED-based Illumination Systems, San Diego, CA, August 2015.
27. W. Sun, **C. K. Tan**, and N. Tansu, "Physics of Artificially-Engineered AlGaN and InGaN Based Digital Alloys," Proc. of the *SPIE Optics + Photonics 2015*, Low Dimensional Materials and Devices, San Diego, CA, August 2015.
28. N. A. Lacroce, G. Y. Liu, **C. K. Tan**, R. A. Arif, S. M. Lee, and N. Tansu, "Understanding the Dopant Activation for Improved Manufacturing Yield in InGaN-Based Light Emitting Diodes," Proc. of the *SPIE Optics + Photonics 2015*, Fourteenth International Conference on Solid State Lighting and LED-based Illumination Systems, San Diego, CA, August 2015.
29. **C. K. Tan**, Z. J. Zhao, and N. Tansu, "Using Dilute-P GaNP Alloy as Improved Visible Active Region," Proc. of the *SPIE Optics + Photonics 2015*, Active Photonic Materials, San Diego, CA, August 2015.
30. **C. K. Tan**, and N. Tansu, "Auger Recombination in Nanoscale III-Nitride Material System," Proc. of the *SPIE Optics + Photonics 2015*, Nanoengineering: Fabrication, Properties, Optics, and Devices XII, San Diego, CA, August 2015.
31. **(Invited Conference Paper)** N. Tansu, **C. K. Tan**, and J. Wierer, "Tutorial on III-Nitride Solid State Lighting and Smart Lighting", Proc. of the *IEEE Photonics Conference 2015*, Reston, VA, October 2015.
32. **C. K. Tan**, and N. Tansu, "Gain and Spontaneous Emission Characteristics of AlInN Quantum Well for Deep Ultraviolet Emitters", Proc. of the *IEEE Photonics Conference 2015*, Reston, VA, October 2015.
33. **C. K. Tan**, and N. Tansu, "Dilute-As AlNAs Semiconductor for Ultraviolet Emitters", Proc. of the *IEEE Photonics Conference 2015*, Arlington, VA, October 2015.
34. W. Sun, **C. K. Tan**, and N. Tansu, "Artificially Engineered InGaN-Based Digital Alloy for Optoelectronics", Proc. of the *IEEE Photonics Conference 2015*, Reston, VA, October 2015.
35. B. A. Krick, G. Zeng, **C. K. Tan**, and N. Tansu, "Surprisingly Low Wear Behaviour of Gallium Nitride", *2015 STLE Tribology Frontiers Conference*, Denver, CO, October 2015.
36. **(Invited Conference Paper)** **C. K. Tan**, and N. Tansu, "Dilute-As GaNAs Quantum Wells for Visible Lasers with Reduced Auger Recombination", Proc. of the *SPIE Photonics West 2016*, Novel In-Plane Semiconductor Lasers XV, San Francisco, February 2016.
37. **C. K. Tan**, D. Borovac, and N. Tansu, "Band Gap Narrowing with Dilute-Anion GaN Materials for Visible Emission", Proc. of the *SPIE Photonics West 2016*, Gallium Nitride Materials and Devices XI, San Francisco, CA, February 2016.
38. G. S. Zeng, **C. K. Tan**, B. A. Krick, and N. Tansu, "Investigation of Mechanical Wear Rates in III-Nitride Materials", Proc. of the *SPIE Photonics West 2016*, Gallium Nitride Materials and Devices XI, San Francisco, CA, February 2016.
39. W. Sun, **C. K. Tan**, and N. Tansu, "AlGaN Digital Alloys for Deep-Ultraviolet Application", Proc. of the *SPIE Photonics West 2016*, Physics and Simulation of Optoelectronic Devices XXIV, San Francisco, CA, February 2016.
40. I. Fragkos, **C. K. Tan**, V. Dierolf, Y. Fujiwara, and N. Tansu, "Rare-Earth Doped GaN Based Light Emitting Diode: A Model of Current Injection Efficiency", Proc. of the *SPIE Photonics West 2016*, Physics and Simulation of Optoelectronic Devices XXIV, San Francisco, CA, February 2016.

41. **(Invited – Student Award Winner)** **C. K. Tan**, W. Sun, D. Borovac, J. J. Wierer, Jr., and N. Tansu, "InGaN-GaNAs 'Interface Quantum Well' for Long-Wavelength Emission", DOE R&D Workshop on Solid State Lighting 2016, Raleigh, NC, USA, February 2016.
42. G. S. Zeng, **C. K. Tan**, N. Tansu and B. A. Krick, "Wear Mechanism of III-Nitride Semiconductor Materials", Proc. of the *Society of Tribologists and Lubrication Engineers Annual Meeting (STLE) 2016*, Las Vegas, NV, USA, May 2016.
43. G. S. Zeng, **C. K. Tan**, N. Tansu and B. A. Krick, "Humidity Effect on Wear Performance of Gallium Nitride", Poster Session Presented at: Proc. of the *Society of Tribologists and Lubrication Engineers Annual Meeting (STLE) 2016*, Las Vegas, NV, USA, May 2016.
44. G. S. Zeng, **C. K. Tan**, N. Tansu, and B. A. Krick, "Ultralow Wear of Gallium Nitride", The 58th Electronic Materials Conference (EMC), Delaware, DE, USA, June 2016.
45. **C. K. Tan**, W. Sun, D. Borovac, J. J. Wierer, and N. Tansu, "Electronics Properties of Dilute-Anion III-Nitride Semiconductors for Light Emitters", Proc. of the IEEE Lester Eastman Conference on High Performance Devices 2016, Bethlehem, PA, August 2016.
46. W. Sun, **C. K. Tan**, J. J. Wierer, Jr., and N. Tansu, "Miniband Engineering in III-Nitride Digital Alloy for Broadband Device Applications", Proc. of the IEEE Lester Eastman Conference on High Performance Devices 2016, Bethlehem, PA, August 2016.
47. I. E. Fragkos, **C. K. Tan**, Y. Zhong, V. Dierolf, Y. Fujiwara, and N. Tansu, "Understanding the Current Injection Efficiency in Rare-Earth Doped GaN:Eu Red-Emitting Light Emitting Diodes", Proc. of the IEEE Lester Eastman Conference on High Performance Devices 2016, Bethlehem, PA, August 2016.
48. **C. K. Tan**, W. Sun, D. Borovac, J. J. Wierer, and N. Tansu, "How Can Dilute-Anion III-Nitride Be Used for Light Emitters?", *Proc. of the International Workshop on Nitride Semiconductors 2016 (IWN 2016),* Orlando, FL, October 2016.

Patent or Invention Disclosures

1. Nelson Tansu, Wei Sun, and **Chee-Keong Tan**, New Solar Materials. (US Patent Pending)**.**
2. Nelson Tansu, and **Chee-Keong Tan**, Flexible Electronics. (US Patent Pending).
3. Nelson Tansu, and **Chee-Keong Tan**, New Deep UV Materials. (US Patent Pending).

Invited Seminar Talk

1. **C. K. Tan, "*Dilute-As GaNAs Semiconductor for Visible Light Emitters"*, University of Sains Malaysia, Penang, Malaysia, July 2015.**

Research Work Featured in Magazine / Newspapers

1. **"Toward More Vibrant LEDs" in *Lehigh News Center Highlight*, May 9th 2016.**
   http://www1.lehigh.edu/news/toward-more-vibrant-leds
2. **"Lehigh University's Chee-Keong Tan Makes Remarkable Achievement in Field of Solid State Lighting and LEDs" in *AZoOptics*, May 10th 2016.**
   http://www.azooptics.com/News.aspx?newsID=22537
3. **"Toward More Vibrant LEDs (Lehigh University)" in *World News Network*, May 9th 2016.**
   http://article.wn.com/view/2016/05/09/Toward_more_vibrant_LEDs_Lehigh_University/

Professional Services, Teaching and Educational Activities

National / International Level

1. ***Conference Presider (Session Chair)***, *SPIE Optics and Photonics 2015*, San Diego, CA, Nanoengineering: Fabrication, Properties, Optics, and Devices XII, Micro, Nano and Optical Materials, August 2015.

2. ***Conference Presider (Session Chair)***, *SPIE Optics and Photonics 2015*, San Diego, CA, Nanoengineering: Fabrication, Properties, Optics, and Devices XII, Nanometrology and Precision, August 2015.
3. ***Symposium Attendee (Invited)***, *International Year of Light 2015 Symposium hosted by National Science Foundation, National Academy of Sciences, American Institute of Physics, American Physical Society, Optical Society of America, IEEE Photonics Society, and SPIE*, Washington, DC, Light for a Better World: A Celebration of U.S. Innovation, September 2015.
4. ***Conference University Exhibitor***, *IEEE Photonics Conference 2015*, Reston, VA, October 2015.

University / Department Level

1. ***Research Undergraduate Student Mentor***, *NSF-supported Summer Experiences Research Program 2012*, Nicholas J. Stein (B.S., Lafayette College, United States), Lehigh University, Bethlehem, PA, June-August 2012.
2. ***Research Undergraduate Student Mentor***, *Summer Experiences Research Program 2015*, Breno H. Dantas (B.S., Universidade Federal de Pernambuco (UFPE), Brazil), Lehigh University, Bethlehem, PA, Summer 2015.
3. ***High School Student Mentor,*** **Milind Jagota (Liberty High School, Bethlehem),** Lehigh University, Bethlehem, PA, Summer 2015 – present.
4. ***Lehigh Undergraduate and Graduate Student Mentor (more than 15 students)*****,** Laboratory for Emerging Photonics and Nanostructures, Lehigh University, Bethlehem, PA, 2013 – present.
5. ***Substitute lecturer*** for ECE 450 course (Senior undergraduate / Graduate level), *Applied Quantum Mechanics for Engineers*, Lehigh University, Bethlehem, PA, Fall 2014.
6. ***Grader*** for ECE 126 course (Freshman / Sophomore undergraduate level), *Fundamentals of Semiconductor Devices*, Lehigh University, Bethlehem, PA, Spring 2015.
7. ***Visiting Lecturer Tour Organizer***, *SPIE Student Chapter at Lehigh University Technical Talk Event*, Prof. Mona Jarrahi (University of California Los Angeles, United States), Lehigh University, Bethlehem, PA, February 2015.
8. ***Visiting Lecturer Tour Organizer***, *SPIE Student Chapter at Lehigh University Technical Talk Event*, Prof. Eva M. Campo (Bangor University, United Kingdom), Lehigh University, Bethlehem, PA, June 2015.

Journal Reviewing

1. ***Scientific Reports*** (published by Nature Publishing Group)
2. ***Photonics*** (published by MDPI)
3. ***Sensors*** (published by MDPI)
4. ***IEEE/OSA Journal of Display Technology*** (published by IEEE / OSA)
5. ***IEEE Photonics Journal*** (published by IEEE)
6. ***Optical Materials Express*** (published by Optical Society of America)
7. ***Electronics*** (published by MDPI)
8. ***Journal of Photonics for Energy*** (published by SPIE)
9. ***Journal of Nanophotonics*** (published by SPIE)
10. ***Transactions on Components, Packaging and Manufacturing Technology*** (published by IEEE)
11. ***Applied Surface Science*** (published by Elsevier)
12. ***Journal of Materials*** (published by Hindawi)
13. ***International Journal of Photoenergy*** (published by Hindawi)